ADA042442

REPORT NO. FAA-RD-77-23

AIRCRAFT WAKE VORTICES: A STATE-OF-THE-ART REVIEW OF THE UNITED STATES R&D PROGRAM

U.S. Department of Transportation
Transportation Systems Center
Kendall Square
Cambridge MA 02142

Lockheed Missiles and Space Company, Inc.
Huntsville Research and Engineering Center
4800 Bradford Drive
Huntsville AL 35807

FEBRUARY 1977

FINAL REPORT

DDC
REPRODUCED
AUG 4 1977
C

DOCUMENT IS AVAILABLE TO THE U.S. PUBLIC THROUGH THE NATIONAL TECHNICAL INFORMATION SERVICE, SPRINGFIELD, VIRGINIA 22161

AD No.
DDC FILE COPY

Prepared for

U.S. DEPARTMENT OF TRANSPORTATION
FEDERAL AVIATION ADMINISTRATION
Systems Research and Development Service
Washington DC 20591

NOTICE

This document is disseminated under the sponsorship of the Department of Transportation in the interest of information exchange. The United States Government assumes no liability for its contents or use thereof.

NOTICE

The United States Government does not endorse products or manufacturers. Trade or manufacturers' names appear herein solely because they are considered essential to the object of this report.

Technical Report Documentation Page

1. Report No.	2. Government Accession No.	3. Recipient's Catalog No.
FAA-RD-77-23		

4. Title and Subtitle
AIRCRAFT WAKE VORTICES:
A STATE-OF-THE-ART REVIEW OF
THE UNITED STATES R&D PROGRAM

5. Report Date
February 1977

6. Performing Organization Code

7. Author(s)
J.N. Hallock* and W.R. Eberle, Editors

8. Performing Organization Report No.
DOT-TSC-FAA-77-4

9. Performing Organization Name and Address
*U.S. Department of Transportation
Transportation Systems Center
Kendall Square
Cambridge MA 02142

10. Work Unit No. (TRAIS)
FA705/R7126

11. Contract or Grant No.

12. Sponsoring Agency Name and Address
U.S. Department of Transportation
Federal Aviation Administration
Systems Research and Development Service
Washington DC 20591

13. Type of Report and Period Covered
Final Report.
Oct 1976 — Dec 1976.

14. Sponsoring Agency Code

15. Supplementary Notes
346 p.
†Lockheed Missiles and Space Company, Inc.
Huntsville Research and Engineering Center
4800 Bradford Drive
Huntsville AL 35807

16. Abstract

The report summarizes the current state-of-the-art understanding of the aircraft wake vortex phenomenon and the results of the United States program to minimize the restrictions caused by aircraft wake vortices in the terminal environment. The vortex phenomenon, vortex avoidance systems, and vortex alleviation techniques are discussed.

17. Key Words	18. Distribution Statement
Aircraft Wake Vortices, Vortices, Wake Decay, Wake Transport, Vortex Advisory System, Vortex Roll-Up	DOCUMENT IS AVAILABLE TO THE U.S. PUBLIC THROUGH THE NATIONAL TECHNICAL INFORMATION SERVICE, SPRINGFIELD, VIRGINIA 22161

19. Security Classif. (of this report)	20. Security Classif. (of this page)	21. No. of Pages	22. Price
Unclassified	Unclassified	346	

Form DOT F 1700.7 (8-72) Reproduction of completed page authorized

407082

Preceding Page BLANK - NOT FILMED

PREFACE

This report reviews the state of the art of the United States research and development program on the subject of aircraft wake vortices. The purpose of the report is to provide background material for the International Civil Aviation Organization in its deliberations on wake vortex effects. Although written for the aerodynamically trained or initiated reader, only the fundamentals of flight are assumed.

Many people participated in the preparation of the report. Summaries were prepared by the contributors listed below; the editors used the summaries in an attempt to present a unified depiction of the wake vortex program of the United States.

Section	Author, Organization
1	W. Wood, DOT/TSC
2	V. Gupta, Mitre Corp.
3	P. Lissaman, AeroVironment, Inc. E. Bate, AeroVironment, Inc. A. Bilanin, ARAP, Inc. A. Zalay, Lockheed-Huntsville W. Eberle, Lockheed-Huntsville L. Garodz, FAA/NAFEC
4	M. Barber, NASA/DFRC V. Rossow, NASA/Ames
5	I. McWilliams, DOT/TSC B. Tinling, NASA/Ames
6	D. Burnham, DOT/TSC H. Jeffreys, NASA/MSFC
7	T. Sullivan, DOT/TSC
8	J. Hallock, DOT/TSC
9	E. Spitzer, DOT/TSC
10	W. Wood, DOT/TSC J. Hallock, DOT/TSC

ACCESSION for
NTIS White Section
DDC Buff Section
UNANNOUNCED
JUSTIFICATION
BY
DISTRIBUTION/AVAILABILITY CODES
A

Two previously published reports supplement this state-of-the-art review and contribute to the complete story of the status of the United States program in aircraft wake vortices. "Aircraft Wake Vortices--An Annotated Bibliography (1923-1975)" was published in January 1976 as FAA-RD-76-43 and contains abstracts of relevant papers, reports, or other publications. "NASA Symposium on Wake Vortex Minimization" was published in October 1976 as NASA SP-409 and is the proceedings of a conference convened by NASA in February 1976 at which the various vortex alleviation devices and techniques were discussed.

A023 415

CONTENTS

Section		Page
1.	INTRODUCTION	1
2.	WAKE VORTEX ACCIDENTS HISTORY	5
	2.1 Overall Statistics	5
	2.2 Principal Vortex Accident Categories	11
	2.2.1 Landing/Landing: Same Runway Accidents	11
	2.2.2 Intersection Takeoff Accidents	12
	2.2.3 Parallel Runway Operations	13
	2.2.4 Missed Approach and Touch-and-Go Operations	13
	2.3 Landing/Landing: Same Runway Accidents	14
	2.3.1 Encounter Point Statistics	14
	2.3.2 Aircraft Types Involved	16
	2.3.3 Reported Wind Conditions	18
	2.3.4 Vortices Generated During Touch-and-Go Operations	20
	2.3.5 Distribution of Accidents by Airport Rank	20
3.	VORTEX PHENOMENA	22
	3.1 Introduction to the Generation of Aircraft Wake Vortices	22
	3.2 Vortex Structure	32
	3.2.1 Vortex Roll-up Phenomenon	34
	3.2.2 Models of Vortex Structure	51
	3.2.2.1 Rotational Structure of the Vortex	51
	3.2.2.2. Axial Structure of the Vortex	56
	3.2.3 Experimental Measurements of Vortex Structure	57
	3.2.4 Multiple Vortices	58
	3.3 Vortex Transport	76
	3.3.1 Vortex Descent Out of Ground Effect	78
	3.3.2 Vortex Transport by Mutual Induction in Ground Effect	87

CONTENTS (CONT'D)

Section			Page
	3.3.3	Wind Shear Effect on Vortex Transport	94
	3.3.4	Vortex Buoyancy	100
	3.3.5	Updated Vortex Transport Predictive Model	105
	3.3.6	Predictive Model Verification	109
3.4	Vortex Decay		112
	3.4.1	Dissipative Wake Vortex Decay	112
	3.4.2	Core-bursting	113
	3.4.3	Crow Instability	122
4.	AERODYNAMIC MINIMIZATION		131
4.1	Vortex Alleviation Criteria and Tests		131
	4.1.1	Vortex Alleviation Effectiveness Criterion	131
	4.1.2	Ground-based Testing Procedures	137
	4.1.3	Flight-Test Techniques	139
		Early Flight Tests	145
	4.1.4	*Unsuccessful Minimization* Techniques	148
4.2	Vortex Alleviation by Variations in Spanwise Wing Loading		148
	4.2.1	Reduction of Shed Vortex Strength	149
	4.2.2	Span Loading for Large Vortex Cores	149
	4.2.3	Flight-Test Results: Altered Span Loading	150
	4.2.4	Flight-Test Results: Turbulence Ingestion	152
	4.2.5	Flight-Test Results: Combinations of Mass and Turbulence Ingestion	152
	4.2.6	Flight-Test Results: Combinations of Span-loading Alteration-and-Turbulence Ingestion	153
5.	HAZARD DEFINITION		157
5.1	Analytic Methods of Calculating Vortex-induced Forces and Moments		158
5.2	Hazard Criteria Selection - Ground-based Flight Simulation		161

CONTENTS (CONT'D)

Section			Page
	5.2.1	Description of Simulations	161
	5.2.2	Test Program	163
	5.2.3	Results and Discussion	164
5.3		Other Vortex-Encounter Simulations	169
5.4		The TSC Vortex-Encounter Simulation	173
5.5		Hazard Volume	174
6.		VORTEX SENSORS	179
6.1		General Sensor Requirements	179
6.2		Sensor Characteristics	179
6.3		Description of Wake Vortex Sensors	181
	6.3.1	Mechanical Techniques	181
	6.3.1.1	Wind Sensors	181
	6.3.1.2	Pressure Sensors	190
	6.3.2	Acoustic Sensors	192
	6.3.2.1	Active Acoustic Sensors	193
	6.3.2.2	DAVSS	197
	6.3.2.3	MAVSS	204
	6.3.2.4	PAVSS	214
	6.3.2.5	Passive Acoustic Sensors	221
	6.3.3	Optical Techniques	223
	6.3.3.1	Passive Optical Techniques	223
	6.3.3.2	SLDVS	225
		6.3.3.2.1 SLDVS Historical Development	226
		6.3.3.2.2 JFK Installation	227
		6.3.3.2.3 SLDVS Hardware Description	228
		6.3.3.2.4 SLDVS Data Processing	235
	6.3.4	Electromagnetic Techniques	237
	6.3.5	Combination Techniques	241
	6.3.6	Future Sensor Development	241
6.4		Airborne Wake-Vortex Detection	242
7.		DATA-COLLECTION SITES	243
7.1		JFK Vortex Test Site	244

CONTENTS (CONT'D)

Section			Page
	7.2	DEN Vortex Test Site	246
	7.3	LHR Vortex Test Site	248
	7.4	ORD Vortex Test Site	251
	7.5	YYZ Vortex Test Site	256
8.		ANALYSIS OF LHR, JFK, AND DEN DATA	260
	8.1	Vortex Transport and Demise	261
		8.1.1 Safety Region	262
		8.1.2 Residence-Time Data	262
		8.1.3 Residence Times by Aircraft Type	263
		8.1.4 Residence Times - Wind Effects	266
		8.1.5 Residence Times - How Vortices Exit Safety Region	270
		8.1.6 Vortex Behavior at Various Sensor Baselines	270
		8.1.7 First and Second Vortex Crossings	271
		8.1.8 Residence Times - Cases Which Exceed 80 Seconds	272
	8.2	Vortex Decay	274
		8.2.1 Anemometer Data	274
		8.2.2 Monitoring Vortex Decay	280
9.		VORTEX AVOIDANCE SYSTEMS	286
	9.1	Vortex Advisory System	289
		9.1.1 VAS Design Details	290
		9.1.1.1 Meteorological Towers	290
		9.1.1.2 Meteorological Sensors	290
		9.1.1.3 Tower Data-Communication Subsystem	292
		9.1.1.4 Meteorological Data-preprocessing	292
		9.1.1.5 VAS Processor	294
		9.1.1.6 Controller Display	296
		9.1.2 VAS Performance-monitoring and Evaluation	298
		9.1.3 Suitability Tests	300
	9.2	Vortex-warning System	301
	9.3	Wake Vortex Avoidance System	304

CONTENTS (CONT'D)

Section		Page
10.	ON-GOING ACTIVITIES	308
	10.1 Joint DOT/NASA Flight Test	308
	10.1.1 Test Description	308
	10.1.2 Qualitative Summary of Results	310
	10.2 Alleviation Work by NASA	311
	10.3 Wake Vortex Predictive Model	312
	10.3.1 Three Baseline Data	313
	10.3.2 Extended Baselines	313
	10.4 Recategorization of Aircraft	314
	10.5 Takeoff Tests at Toronto	314
	10.6 VAS at O'Hare	315
11.	REFERENCES	316

ILLUSTRATIONS

Figure		Page
2-1	Breakdown of NTSB's Vortex-Related Accidents for the Ten-Year Period 1964-1973	7
2-2	Breakdown of Probable Vortex-Related Accidents for the Ten-Year Period 1964-1973	8
2-3	Yearly History of Vortex-Related Landing and Takeoff Accidents at Towered Airports	9
2-4	Rate of Vortex-Related Accidents at Towered Airports	10
2-5	Landing Weight Histogram for Accident Aircraft during Landing Accidents behind Landings on the Same Runway	17
2-6	Landing Weight Histogram for Vortex Generating Aircraft during Landing/Landing Accidents on the Same Runway	19
2-7	Distribution of Accidents by Airport Rank Based on Total Traffic	21
3-1	Spanwise Wing Loading for Illustrative Example	23
3-2	System of Bound and Trailing Vortices	25
3-3	Diagram of Wing Loadings used for Illustrative Examples	29
3-4	Vorticity Distribution and Stages of Vortex Wake for a Clean Wing	35
3-5	Vorticity Distribution and Stages of Vortex Wake for Wing with Flap and Thrust Effects	36
3-6	Lanchester's Concept of Tip Vortex Roll-up	37
3-7	Stretching of the Vortex Sheet During Roll-up	39
3-8	Point Vortex Computations where the Tip Spiral Structure is Modeled by a Single Point Vortex	42
3-9	The Roll-up of a Tip and Flap Vortex	43
3-10	The Flow Field in a Plane Normal to the Flight Direction	46
3-11	The Betz Roll-up Relations for a Simple Loaded Wing	49

ILLUSTRATIONS (CONT'D)

Figure		Page
3-12	Comparison of the Betz and Prandtl Models with Measurements made in the Wake of a C-5 Aircraft.....	50
3-13	Velocity and Pressure Distributions in a Viscous Vortex.....	52
3-14	Photographic Coverage (16mm Movie) of L-1011 Vortices.....	59
3-15	Vortex Structure of Boeing 747 in Takeoff Configuration.....	61
3-16	Vortex Structure of Boeing 747 in Holding Configuration.....	62
3-17	Vortex Structure of Boeing 747 in Landing Configuration.....	63
3-18	Vortex Structure of Lockheed L-1011 in Takeoff Configuration.....	64
3-19	Vortex Structure of Lockheed L-1011 in Landing Configuration.....	65
3-20	Vortex Structure of DC-9 in Takeoff and Landing Configurations.....	66
3-21	B-747 with Six Smoke Generators Illustrating Roll-up of Multiple Vortices.....	68
3-22	Representative Load Distribution of a Flapped Wing $\Gamma(y)$, Upper Curve, and Distribution of Shed Vorticity $d\Gamma/dy$ from Same Wing, Lower Curve..	70
3-23	The Wake of a Flapped Wing.....	72
3-24	Load Distribution which will Produce Three Vortices.	73
3-25	Normalized Load ($2\Gamma/U_\infty b$), Down Wash [$W(y)/U_\infty$], Sheet Strength ($1/U_\infty(d\Gamma/dy)$), and Acceleration Function ($bA/2U_\infty^2$) Distributions for a C-141 Aircraft in the Takeoff Configuration.....	75
3-26	Computed Wake Geometry for B-747 in the Landing Configuration.....	77
3-27	Viscous Effects on Vortex Cell.....	82

ILLUSTRATIONS (CONT'D)

Figure		Page
3-28	Vortex Cell Stages	85
3-29	Geometry of the Predictive Wake Vortex Transport Model	88
3-30	Vortex Structure in Crosswind Shear	95
3-31	Overhead View of AeroCommander 560F Wake Behavior in Wind Shear	98
3-32	Streamlines in the Vicinity of a Vortex Pair in Shear at Infinite Altitude and in Ground Effect	99
3-33	Schematic Representation of Observed Relationship between Atmospheric Stability and Wake Descent at Early Times	104
3-34	Vortices in Ground Effect	106
3-35	Comparison of Predictive Vortex Tracks with Photographic Data for NAFEC B-707 Run 17, 10/18/72.	110
3-36	Wake Vortex Trajectory Computed by the Predictive Wake Vortex Transport Model for a B-747 Tower Flyby	111
3-37	Vortex Structure with Dissipative Decay	114
3-38	Peak Recorded Tangential Velocity vs Age (All Configurations - B-747)	115
3-39	Peak Recorded Tangential Velocity vs Age (All Configurations - DC-9 - Series 10)	116
3-40	Vortex Breakdown Caused by Core-bursting	118
3-41	Estimated Vortex Breakdown Diagram	121
3-42	Mechanism of Crow Instability	123
3-43	Geometry of the Oscillating Vortex Pair	125
3-44	The Development of the Crow-linking Phenomenon from an Overhead Flying B-47	126
3-45	Time to Vortex Linking as a Function of Atmospheric Turbulent Dissipation Rate	128

ILLUSTRATIONS (CONT'D)

Figure		Page
3-46	Vortex Persistance as a Function of Ambient Windspeed and Height Above the Ground.....	130
4-1	Wake Vortex Pair Impinging on a Follower Wing.....	133
4-2	Roll Acceleration Parameter versus Separation Distance for a Learjet in a B-747 Wake.....	142
4-3	Probe Aircraft Flight Path during Velocity Profile Measurements of Vortex Wake.....	144
4-4	Vertical, Lateral, and Axial Velocity Components in the Wake of a B-747 in Landing Configuration....	146
4-5	Vertical, Lateral, and Axial Velocity Components in the Wake of a B-747 with Outboard Flap Retracted.	146
4-6	Spoilers on B-747 Airplane.....	154
5-1	Correlation of Assessment of Hazard with Roll Response Parameters.....	165
5-2	Comparison of Hazard Assessment for Learjet Vortex Encounters by Pilots Participating in Both Simulations.....	170
5-3	Vortex Hazard Boundaries Determined from Simulation.....	171
5-4	Maximum Induced Roll Angle as a Function of Distance from the Vortex Axis.....	176
5-5	Vortex Hazard Volume for Two Classes of Aircraft....	178
6-1	Theoretical Ground Level Crosswind vs. Lateral Position.....	184
6-2	GWVSS Data for a Boeing 707 Aircraft.....	186
6-3	Vortex Tracks from the Inner GWVSS Baseline at Heathrow Airport.....	187
6-4	GWVSS Time History Data from a Boeing 747 Aircraft in Holding Configuration.....	188
6-5	GWVSS Installation at Kennedy International Airport.....	189

ILLUSTRATIONS (CONT'D)

Figure		Page
6-6	Turbulence-scattering Cross Section vs Scattering Angle	195
6-7	Bistatic Acoustic Scattering Configurations	198
6-8	Monostatic Acoustic Scattering Configuration View Along the Flight Path	199
6-9	Avco DAVSS Bistatic Configuration	202
6-10	Avco DAVSS Monostatic Installation: View along the Flight Path	203
6-11	Monostatic DAVSS Vortex Tracks, Kennedy Airport, Runway 31R, DC-8 Aircraft	205
6-12	Narrow Beam Monostatic Acoustic Sensor	206
6-13	MAVSS Wake Velocity Profile	207
6-14	Expanded Scale Plots of the Data in Figure 6-13	209
6-15	Circulation vs. Radius for the Data in Figure 6-14.	210
6-16	MAVSS Vortex Tracks: DC-8 Aircraft, Kennedy Airport Runway 31R, 1 July 1974 at 1153 Hours	212
6-17	MAVSS Vortex Parameters vs Time for the Same Run as Figure 6-16	213
6-18	MAVSS Antenna	215
6-19	Simple PAVSS Configuration	216
6-20	PAVSS Signals for a B-747 Aircraft Landing on Runway 22L, Logan Airport, 3 June 1971	217
6-21	Vortex Location by the Intersection of Constant Time Delay Ellipses for two Transmitter-Receiver Pairs	219
6-22	Avco PAVSS Antenna	220
6-23	Vortex Tracks Obtained with the Avco PAVSS: B-727 Aircraft Landing on Kennedy Airport Runway 31R at 0810 Hours on 2 June 1975	222
6-24	Flow Visualization of Wake Vortices from a B-707 Aircraft	224

ILLUSTRATIONS (CONT'D)

Figure		Page
6-25	SLDVS Overall Block Diagram	229
6-26	Schematic Representation of the Basic Scanning Modes	231
6-27	SLDVS Telescope	233
6-28	Telescope and Scanning Mechanisms	234
6-29	Overall Block Diagram of Signal Processor for SLDVS	235
6-30	Sample Spectrum Output	238
6-31	Sample Time-Position Data Plot	239
6-32	Sample X, Y Data Plot	240
7-1	JFK Test Site	245
7-2	Overall Plan View of Sensor Locations at Stapleton Airport	247
7-3	Camera Field of View	249
7-4	The Site Layout of the Equipment on the Approach to Runway 28R at Heathrow	250
7-5	Field-of-View of the Movie Camera	252
7-6	Layout Map of Chicago O'Hare International Airport	253
7-7	Overall Plan View of Toronto Vortex Test Site	257
7-8	Camera Field of View	259
8-1	Probability of Finding a Vortex in the Safety Region	264
8-2	Probability of Finding a Vortex in the Safety Zone	265
8-3	Probability of Finding a Vortex in the Safety Zone for Specific Aircraft	267
8-4	Probability of Finding a Vortex in the Safety Zone for Various Crosswinds	269

ILLUSTRATIONS (CONT'D)

Figure		Page
8-5	Crossing Times for the First and Second Vortex.....	273
8-6	McGowan Vortex Lifetime Curve.....	276
8-7	Revised McGowan Vortex Lifetime Curve.....	277
8-8	Probability of a B-747 Vortex Existing Under Various Wind Conditions.....	278
8-9	Probability of a Trident Vortex Existing Under Various Wind Conditions.....	279
8-10	Vortex Decay via Linking with the Ground.....	282
8-11	Vortex Decay via Turbulent Diffusion.....	283
8-12	Vortex Decay via Core-bursting,.....	284
9-1	Approach Used in the Design of Wake Vortex Avoidance Systems.....	287
9-2	Locations of the VAS Meteorological Towers at Chicago O'Hare.....	291
9-3	Block Diagram of the VAS.....	293
9-4	The VAS Wind Criterion.....	295
9-5	The VAS Runway Monitor Display.....	297
9-6	The VAS Supervisor Display.....	299
9-7	Block Diagram of the Vortex-warning System.....	303
9-8	Block Diagram of a Wake Vortex Avoidance System....	306

TABLES

Table		Page
2-1	VORTEX ENCOUNTER POINT STATISTICS FOR LANDING ACCIDENTS BEHIND CONVENTIONAL LANDINGS ON THE SAME RUNWAY.....	15
3-1	COMPARISON OF VORTEX PROPERTIES FOR ELLIPTICAL WING LOADING AND LINEAR WING LOADING.....	33
3-2	INFLUENCE OF SPANWISE LOADING ON THE INITIAL VORTEX PARAMETERS.....	79
4-1	COMPARISON OF PREDICTED AND MEASURED ROLLING-MOMENT COEFFICIENTS.....	135
6-1	WAKE-VORTEX SENSOR CLASSIFICATION.....	182
7-1	DETAILED LOCATION OF THE METEOROLOGICAL TOWERS.....	254
7-2	DETAILED LOCATION OF GROUND-WIND VORTEX-SENSING SYSTEMS AT O'HARE.....	254
7-3	DETAILED LOCATION OF MONOSTATIC ACOUSTIC VORTEX-SENSING SYSTEMS AT O'HARE.....	255
8-1	COEFFICIENTS FOR PROBABILITY OF FINDING A VORTEX IN SAFETY ZONE.....	268

ABBREVIATIONS

AGL	Above Ground Level
ARTS	Automative Radar Terminal System
ATC	Air Traffic Control
CONUS	Conterminous United States
DAVSS	Doppler Acoustic Vortex Sensing System
DEN	Stapleton International Airport
DOT	Department of Transportation
FAA	Federal Aviation Administration
FSAA	Flight Simulator for Advanced Aircraft
GWVSS	Ground-Wind Vortex Sensing System
IFR	Instrument Flight Rules
ILS	Instrument Landing System
JFK	John F. Kennedy International Airport
LDVSS	Laser Doppler Vortex Sensing System
LHR	Heathrow International Airport
M&S	Metering and Sequencing
MAVSS	Monostatic Acoustic Vortex Sensing System
MSFC	Marshall Space Flight Center
MVDAF	Mobile Vortex Data Acquisition Facility
NAFEC	National Aviation Facilities Experimental Center
NAS	National Airspace System
NASA	National Aeronautics and Space Administration
NOAA	National Oceanic and Atmospheric Administration
NTSB	National Transportation Safety Board
ORD	O'Hare International Airport

PAVSS	Pulsed Acoustic Vortex Sensing System
PCM	Pulsed Code Modulation
SAW	Surface Acoustic Wave
SLDVS	Scanning Laser Doppler Vortex System
TSC	Transportation Systems Center
VAS	Vortex Advisory System
VFR	Visual Flight Rules
VWS	Vortex Warning System
WVAS	Wake Vortex Avoidance System
YYZ	Toronto International Airport.

METRIC CONVERSION FACTORS

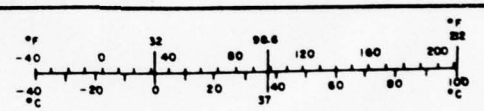
Approximate Conversions to Metric Measures

Symbol	When You Know	Multiply by	To Find	Symbol
		LENGTH		
in	inches	2.5	centimeters	cm
ft	feet	30	centimeters	cm
yd	yards	0.9	meters	m
mi	miles	1.6	kilometers	km
		AREA		
in^2	square inches	6.5	square centimeters	cm^2
ft^2	square feet	0.09	square meters	m^2
yd^2	square yards	0.8	square meters	m^2
mi^2	square miles	2.6	square kilometers	km^2
	acres	0.4	hectares	ha
		MASS (weight)		
oz	ounces	28	grams	g
lb	pounds	0.45	kilograms	kg
	short tons (2000 lb)	0.9	tonnes	t
		VOLUME		
tsp	teaspoons	5	milliliters	ml
Tbsp	tablespoons	15	milliliters	ml
fl oz	fluid ounces	30	milliliters	ml
c	cups	0.24	liters	l
pt	pints	0.47	liters	l
qt	quarts	0.95	liters	l
gal	gallons	3.8	liters	l
ft^3	cubic feet	0.03	cubic meters	m^3
yd^3	cubic yards	0.76	cubic meters	m^3
		TEMPERATURE (exact)		
°F	Fahrenheit temperature	5/9 (after subtracting 32)	Celsius temperature	°C



Approximate Conversions from Metric Measures

Symbol	When You Know	Multiply by	To Find	Symbol
		LENGTH		
mm	millimeters	0.04	inches	in
cm	centimeters	0.4	inches	in
m	meters	3.3	feet	ft
m	meters	1.1	yards	yd
km	kilometers	0.6	miles	mi
		AREA		
cm^2	square centimeters	0.16	square inches	in^2
m^2	square meters	1.2	square yards	yd^2
km^2	square kilometers	0.4	square miles	mi^2
ha	hectares (10,000 m^2)	2.5	acres	
		MASS (weight)		
g	grams	0.035	ounces	oz
kg	kilograms	2.2	pounds	lb
t	tonnes (1000 kg)	1.1	short tons	
		VOLUME		
ml	milliliters	0.03	fluid ounces	fl oz
l	liters	2.1	pints	pt
l	liters	1.06	quarts	qt
l	liters	0.26	gallons	gal
m^3	cubic meters	35	cubic feet	ft^3
m^3	cubic meters	1.3	cubic yards	yd^3
		TEMPERATURE (exact)		
°C	Celsius temperature	9/5 (then add 32)	Fahrenheit temperature	°F



1. INTRODUCTION

Although the phenomenon of aircraft wake vortices has been known since the beginnings of powered flight it is only recently that operational problems associated with the phenomenon have been experienced. All aircraft generate trailing wake vortices as a result of generating lift; however, the potential danger of encountering these wake vortices has only recently become apparent. Aircraft wake vortices now constitute one of the major problems confronting the air traffic control system.

Before 1970, landing aircraft maintained 3-nautical-mile separations under Instrument Flight Rule (IFR) conditions. The separation standard was based primarily on radar operating limits and to a lesser extent on runway occupancy limitations. There were no separation standards imposed because of vortex considerations.

With the introduction of the wide-bodied jets (B-747, DC-10, and L-1011) and the increasing number of aircraft operations at the major airports, the wake vortex problem has taken on increasing significance. The vortices from large aircraft can present a severe hazard to smaller aircraft which inadvertently encounter the vortices; the following aircraft can be subjected to rolling moments which exceed the aircraft roll control authority, to a dangerous loss of altitude, and to a possible structural failure. The probability of a vortex encounter is greatest in the terminal area where light and heavy aircraft operate on the same flight paths in close proximity and where recovery from an upset may not be possible because of the low aircraft altitude.

Accordingly, the solution implemented by the Federal Aviation Administration (FAA) in March 1970 was to increase the separation standards behind the Heavy jets (a Heavy jet has a maximum certificated takeoff weight in excess of 136,000 kilograms) to 4 nautical miles for a following Heavy aircraft and to 5 nautical miles for a following Non-Heavy aircraft. The United Kingdom took similar measures, and in April 1975 implemented a six-nautical-mile spacing

for Non-Heavy aircraft following a wide-body jet. The United States revised the separation standards in November 1975 by requiring the addition of an extra nautical mile separation for following aircraft with a maximum certificated takeoff weight less than 5670 kilograms. However, these increased separations led to additional delays and decreased the capacity and efficiency of the airport system through reduced runway utilization rates and increased fuel consumption.

The FAA has a broad objective to double the airport and airway system capacity by 1980 and to increase current capacity fivefold by 1995. Potential capacity relief through construction of more air carrier airports or additional runways at existing airports is not economically feasible. The need to increase the capacity of the nation's airports and to increase protection against accidents has led to a program by the FAA to develop an Upgraded Third Generation air traffic control system for the 1980's (ref. 1).

The success of this system is dependent upon the development of techniques for reducing the longitudinal separations required to avoid the hazard from trailing wake vortices, particularly behind Heavy aircraft during approach and landing. It appears that airports can achieve a twofold capacity increase with the Upgraded Third Generation improvements, such as dual runways, improved landing aids and data acquisition systems, reduced separation to 760 meters between parallel runways, and reduced longitudinal separations. Today, the technology exists to develop the necessary hardware/software which will substantially increase runway capacity; but the wake vortex problem must be solved before these advanced systems can be used to their full potential.

The wake vortex problem is being addressed by the FAA through two major concurrent programs. The National Aeronautics and Space Administration (NASA) in direct support of the FAA is concentrating on vortex alleviation through methods intended to hasten the demise of vortices. Among the many concepts being investigated are wing spoilers in various deployed configurations, mass injection, wingtip modifications, and the deployment of trailing devices.

Concurrently, the Transportation Systems Center (TSC), under the aegis of the FAA, is developing ground systems which will provide information on the presence or absence of potentially hazardous vortices in the approach corridor. The information will be provided to pilots via the air traffic controllers, and will permit reduced separations to be implemented whenever vortices are determined to be innocuous. The approach is predicated on the observation that separation criteria are overly conservative most of the time because the prevalent meteorological conditions cause vortices to dissipate or move out of the flight path of a following aircraft in a short period of time. A wake vortex avoidance system would also detect those conditions under which potentially hazardous vortices might persist in the flight corridor and would require the air traffic controller to impose the current separation standards for the time period for which such conditions might exist.

Wake vortices are not a major cause of aircraft accidents. The IFR/vortex separation standards are safe. However, the implementation of reduced separations to accommodate increased capacity will necessitate certification that the reduced separations are safe. The objective of the Wake Vortex Program in the United States is thus the increase of capacity of an airport while maintaining the current high level of safety.

It is the intent herein to summarize the results of the United States effort relative to both vortex avoidance and vortex alleviation. It is recognized that the effort includes significant support by both the United Kingdom Civil Aviation Authority and the Canadian Ministry of Transport, and their efforts will be identified in the appropriate sections of the report.

Section 2 examines the accidents attributed to wake vortices to gain a historical perspective of the wake vortex program. Section 3 describes in depth the phenomenon of aircraft wake vortices, including the formation, applicable models, and the transport and decay. NASA's program on the minimization of the vortex hazard by aerodynamic means is examined in Section 4.

In section 5, the mechanisms of how vortices affect aircraft which inadvertently penetrate a vortex are reviewed. To be able to collect information on vortices, various sensors were developed; Section 6 reviews the different approaches which were proposed or developed. Section 7 describes the various test sites which were or are used to collect data on vortex behavior.

Section 8 reviews the data from the recent extensive data collection programs; over 35,000 vortex tracks have been collected and analyzed. In Section 9, vortex avoidance systems which allow the tailoring of separations commensurate with prevailing meteorological conditions or vortex behavior are described. Finally in Section 10, the objectives and schedules of current vortex-related projects are described.

2. WAKE VORTEX ACCIDENTS HISTORY

A study of past vortex-related accidents (ref. 2) was undertaken with the objective of providing historical perspective, insight, and guidance to the Wake Vortex Program. The study was based on the National Transportation Safety Board (NTSB) data base and included 147 accidents in the conterminous United States (CONUS) during the 10-year period from 1964 to 1973 for which vortices were cited as a cause or a factor by the NTSB. NTSB reports on the vortex-related accidents were obtained for further study to categorize each accident by the flight phases of the accident aircraft and the vortex-generating aircraft, their relative runways of operation, and any other pertinent factors.

Reading the accident reports indicated that some of the accidents may not really have been vortex-related, and that they may have been classified as such only because the pilot, or the tower, or some witnesses made some vague references to "turbulence," "prop wash," "jet wash," or "vortices." The statistics on all of the 147 vortex-related accidents therefore provide a worst-case picture. Also to provide an additional more reasonable statistical picture, accidents which were thought unlikely to have been caused by vortices were eliminated to give a set of probable vortex-related accidents. However, these accidents may not all be genuinely vortex-related.

2.1 OVERALL STATISTICS

The following overall statistics of interest were revealed by the accidents study:

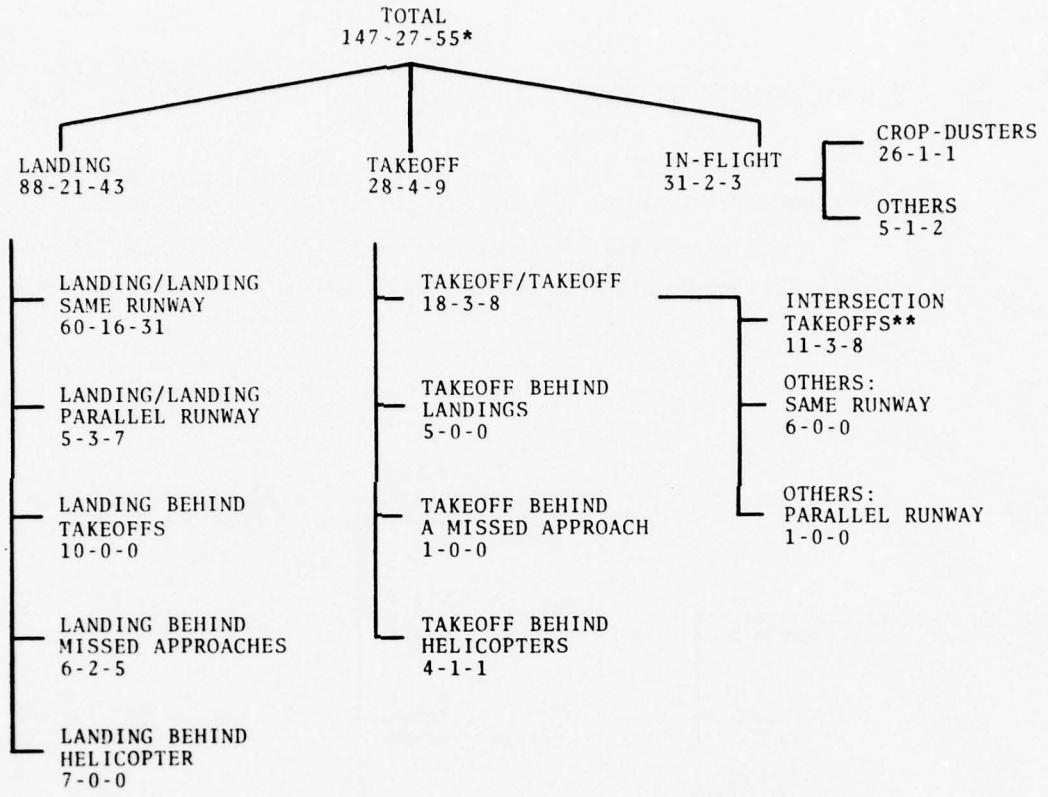
a. An average of 15 accidents per year have been classified by the NTSB as being vortex-related. The corresponding fatal accident rate is 3 per year with 6 fatalities. In comparison, single aircraft accidents of all types have occurred at an annual rate of roughly 4510 accidents, 540 fatal accidents and 1250 fatalities. Vortex-related accidents thus constitute less than 0.5 percent of all single aircraft accidents.

b. Twenty-seven (18 percent) of the 147 accidents were fatal and resulted in 55 fatalities (Fig. 2-1). Overall there were 88 landing accidents (21 fatal and 43 fatalities), 28 takeoff accidents (4 fatal and 9 fatalities), and 31 in-flight accidents (2 fatal and 3 fatalities). Twenty-six (84 percent) of the 31 in-flight accidents were, however, crop-dusters (one fatal with one fatality) involved in agricultural activities in close proximity to the ground.

c. The elimination of the apparently vortex-unrelated accidents (and the in-flight crop-duster accidents) leaves only 66 landing accidents (18 fatal with 38 fatalities), 18 takeoff accidents (3 fatal with 8 fatalities) and 2 in-flight accidents (1 fatal and 2 fatalities). These probable vortex-related accidents add up to a total of 86 accidents, 22 fatal accidents and 48 fatalities (Fig. 2-2).

d. The accidents were found to have occurred at airports with widely varying operations rates. Roughly 5/6 of the landing accidents and 3/4 of the takeoff accidents occurred at controlled airports. The overall accident rate over the 10-year period at towered airports is less than 1 per 3-million landings, and less than 1 per 10-million takeoffs. The air carrier accident rate is less than 1 per 40-million operations for both landings and takeoffs.

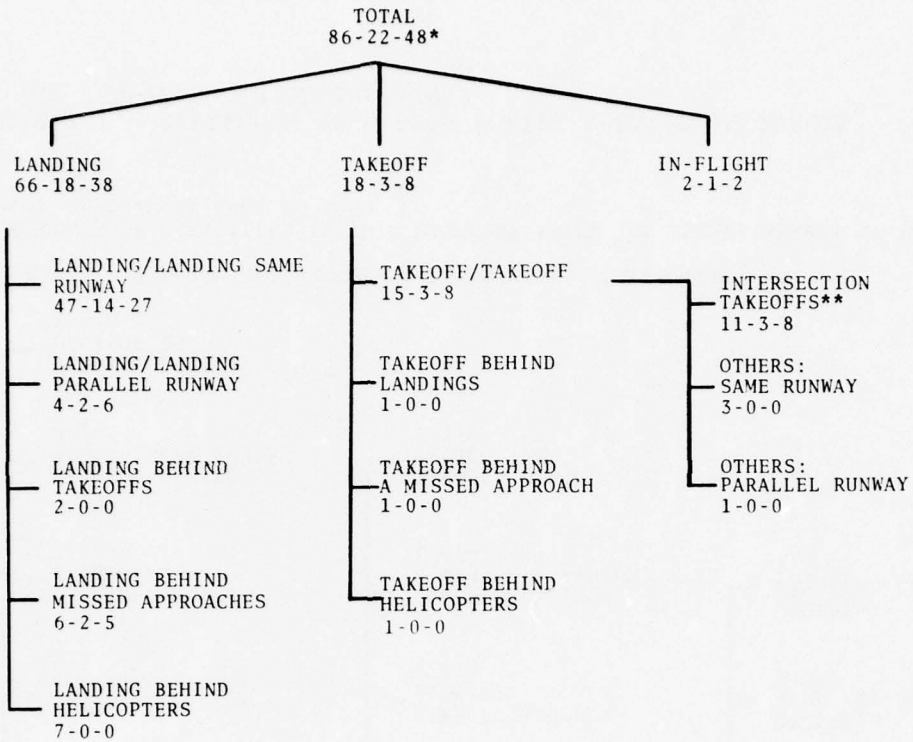
e. An unexpected finding of the study was that neither the number of vortex-related accidents per year (Fig. 2-3) nor the accident rate per million operations (Fig. 2-4) at towered airports have gone up with the introduction of wide-body jets in the late 60's and early 70's. A general aviation aircraft which weighs less than 5670 kilograms, and seems to have been the primary victim of the vortex problem in the past, may be expected to be almost as vulnerable to the vortices from an aircraft weighing 50,000 kilograms as to the vortices of an aircraft weighing more than 136,000 kilograms. The relatively small number of Heavies in the traffic mix so far, and the use of large separation standards behind them, have probably also contributed to this non-increase in the accident rates.



* # ACCIDENTS - # FATAL ACCIDENTS - # FATALITIES, RESPECTIVELY

** NO ACCIDENTS OR FATALITIES IN THIS CATEGORY AFTER THE ESTABLISHMENT OF THE 3-MINUTE SEPARATION RULE IN 1969

FIGURE 2-1. BREAKDOWN OF NTSB'S VORTEX-RELATED ACCIDENTS FOR THE TEN-YEAR PERIOD 1964-1973



NOTE: ALL IN-FLIGHT CROP-DUSTER ACCIDENTS HAVE BEEN EXCLUDED FROM THIS SET.

* # ACCIDENTS - # FATAL ACCIDENTS - # FATALITIES, RESPECTIVELY

** NO ACCIDENTS OR FATALITIES IN THIS CATEGORY AFTER THE ESTABLISHMENT OF THE 3-MINUTE SEPARATION RULE IN 1969.

FIGURE 2-2. BREAKDOWN OF PROBABLE VORTEX-RELATED ACCIDENTS FOR THE TEN-YEAR PERIOD 1964-1973

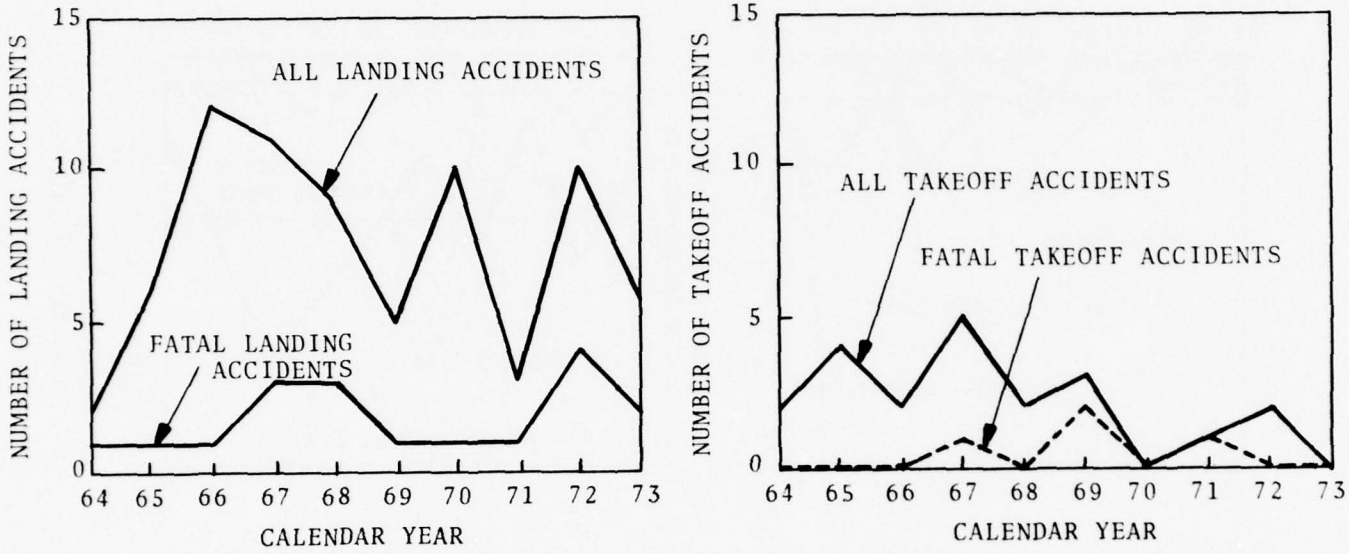


FIGURE 2-3. YEARLY HISTORY OF VORTEX-RELATED LANDING AND TAKEOFF ACCIDENTS AT TOWERED AIRPORTS

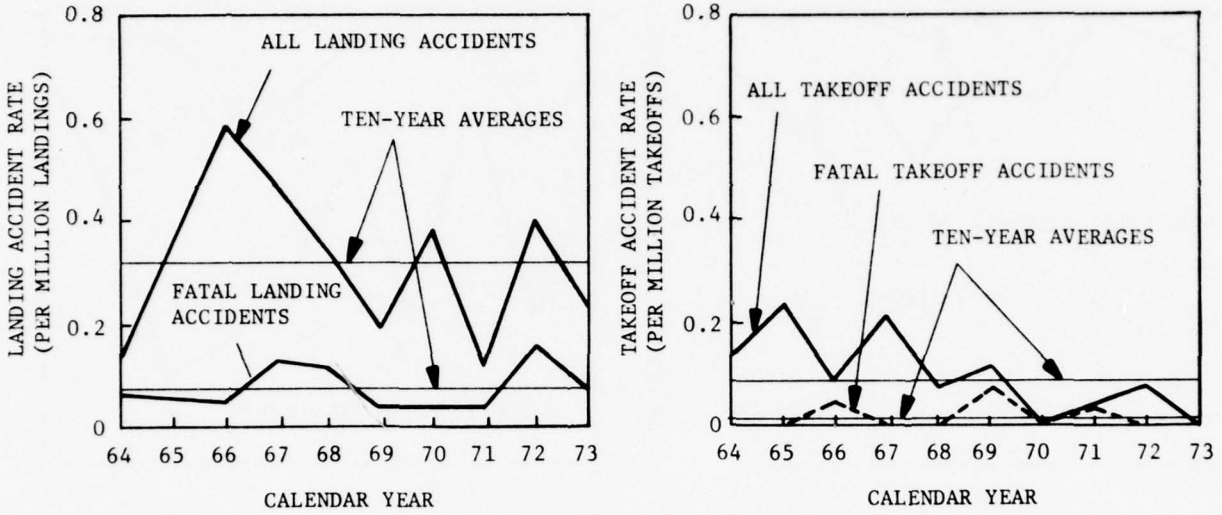


FIGURE 2-4. RATE OF VORTEX-RELATED ACCIDENTS AT TOWER AIRPORTS

f. All but 5 of the 147 accidents occurred under Visual Flight Rule (VFR) conditions when actual separations are in general less than those under IFR conditions. Four of the 5 IFR accidents were landing accidents, and one was an in-flight accident of the missed approach/missed approach type (the only accident of this type). Two of the IFR landing accidents, however, were probably not vortex-related. Moreover, the actual separations in the remaining IFR landing accidents were likely less than those required by IFR separation rules. There were thus no IFR landing accidents when full IFR separations were provided.

g. The vortex problem to date has been largely confined to small general aviation aircraft. More than 95 percent of the accident aircraft weighed less than 5670 kilograms. There have been only two air carrier accidents: one, a DC-9 landing accident (a training flight behind a DC-10) at Fort Worth, Texas; and the other, a DHC-6 (Twin Otter) takeoff accident at the J.F. Kennedy International Airport (JFK), New York, New York. The latter, however, an intersection takeoff accident (a situation which is now recognized to be particularly hazardous), involved an aircraft weighing less than 5670 kilograms.

h. As for vortex-generating aircraft, an unexpected finding of the study is that vortex-related accidents have been caused by air carrier (and military) aircraft of all sizes. Many accidents were caused by aircraft weighing less than 35,000 kilograms.

2.2 PRINCIPAL VORTEX ACCIDENT CATEGORIES

Figures 2-1 and 2-2 showed the detailed breakdown of vortex accidents by the flight phases of the accident aircraft and the vortex-generating aircraft. A brief discussion of some of the important categories is given below.

2.2.1 Landing/Landing: Same Runway Accidents

Landing behind another landing aircraft on the same runway was found to be by far the most frequent type of vortex-related accident. Sixty such accidents occurred behind conventional aircraft (47 probable) and 7 occurred behind landing helicopters

(all probable). This category thus accounts for more than 82 percent of the landing accidents and about 63 percent of all probable vortex-related accidents.

Landings also happen to be the operation where airport capacity is most critical in terms of delays. "Landing/Landing: same runway" is therefore an important category of vortex accidents and is discussed in greater detail in Section 2.3.

2.2.2 Intersection Takeoff Accidents

Intersection takeoffs (mid-runway takeoffs behind regular air carrier takeoffs) constitute the second largest category of vortex accidents. Eleven accidents fall into this category (all probable), and constitute approximately 13 percent of all probable vortex-related accidents. All of these accidents occurred at towered airports.

Apart from intersection takeoffs, the "takeoff/takeoff: same runway" situation (with both aircraft starting their roll from the threshold) seems to be free of the vortex problem. There have been only 3 probable accidents in this category in a 10-year period, none of them at a towered airport. Thus, the vortex problem is practically nonexistent at controlled airports in the ordinary takeoff/takeoff phase where both aircraft start their takeoff roll at the runway threshold. There may be three reasons to explain this: First, unlike landing aircraft which cannot afford to swerve from their rather constrained path towards the runway threshold, the takeoff aircraft can afford to move away from the vortex problem area if the need arises. Second, the engines are under full power during takeoffs as opposed to idling engines during landings. And third, the most important reason is that the takeoff rolls of various aircraft types vary roughly in direct proportion to their size. As a result, smaller aircraft lift off earlier and fly a higher altitude profile as compared with a heavier aircraft. This provides natural separation (in the correct direction from the point of view of the vortex problem) between aircraft of different weight classes.

The pattern of natural separation is, however, disturbed when a small aircraft makes an intersection takeoff. For a dangerous vortex encounter to occur, it is not really necessary for the small aircraft's lift-off point to be beyond that of the large aircraft. Even when the small aircraft lifts off before the lift-off point of the large aircraft, the altitude separation between the flight paths of the two aircraft may not be sufficient if the two lift-off points are too close.

It is of interest to note that no intersection takeoff accident has occurred after the JFK air carrier accident in 1969. The separation rule for intersection takeoffs was changed from 2 to 3 minutes in October 1969 after the JFK accident. These facts further tend to confirm the speculation that the takeoff/takeoff situation is free from a vortex problem except in the case of intersection takeoffs. However, the latter can be handled procedurally either by increasing separation standards as was done in 1969 or by allowing intersection takeoffs behind landings only.

2.2.3 Parallel Runway Operations

The number of accidents attributed to the vortices generated by an aircraft operation on a parallel runway is rather small (7), and the runways centerline spacing in most of these cases was about 200 to 300 meters. However, almost 40 percent of the landing/landing accidents in the same runway category occurred on one of a pair of parallel runways (with centerline spacing 760 meters in most cases). The NTSB reports on most of the vortex accidents are sketchy; the possibility exists that some of the latter accidents may really have been caused by a generator aircraft operating on a parallel runway. Therefore, a definitive statement cannot be made from accidents history about the relative vortex hazard of parallel runway operations.

2.2.4 Missed Approach and Touch-and-Go Operations

In many of the "landing/landing: same runway" accidents, the lead aircraft actually executed a touch-and-go. Also, there were six landing accidents and one takeoff accident behind missed

approaches. The accident history suggests that the vortices produced during missed approaches and touch-and-go landings by large aircraft may be particularly hazardous to small aircraft operations.

2.3 LANDING/LANDING: SAME RUNWAY ACCIDENTS

In view of the large number of accidents in this category and its implications with respect to arrival separation standards and capacity, these accidents were studied in a greater level of detail. Seven of these accidents were behind landing helicopters. These accidents were categorized separately because the vortex-generation phenomenon in helicopters is different from that of fixed-wing aircraft. Also, many times the landing operation of helicopters is really hovering. Helicopters also tend to land on one side of a runway, which is thus really equivalent to landing on a parallel runway. Also, in three of the seven cases, the helicopters were really making a touch-and-go landing. These accidents have not been included in the following statistics.

2.3.1 Encounter-Point Statistics

It is of obvious interest to find the location along the approach path at which the vortex encounter (leading to an accident) occurred after the accident aircraft had turned final. For further detail, the accidents were grouped by the location of their first vortex encounter with respect to the runway threshold.

Table 2-1 gives the resulting encounter point statistics and shows that 37 percent of the encounters took place after the victim aircraft had crossed the threshold. Another 34 percent of the accidents took place after the accident aircraft was less than 450 meters away from the threshold. Another 12 percent of the encounters occurred between 450 and 1050 meters from the runway, while the remaining 17 percent of the encounters occurred more than 1 nautical mile away from the runway end. These percentages remain substantially the same even after the elimination of accidents expected to be unrelated to the vortex problem, except that all accidents in

TABLE 2-1. VORTEX ENCOUNTER POINT STATISTICS FOR LANDING ACCIDENTS BEHIND CONVENTIONAL LANDINGS ON THE SAME RUNWAY

ENCOUNTER LOCATION	ALL ACCIDENTS FROM NTSB DATA BASE			AFTER ELIMINATION OF ACCIDENTS UNRELATED TO THE VORTEX PROBLEM		
	# ACCIDENTS-FATAL ACCIDENTS -FATALITIES-SERIOUS INJURIES-OCCUPANTS, RESPECTIVELY	PERCENT-AGE	CUMULATIVE PERCENTAGE	# ACCIDENTS-FATAL ACCIDENTS -FATALITIES-SERIOUS INJURIES-OCCUPANTS, RESPECTIVELY	PERCENT-AGE	CUMULATIVE PERCENTAGE
AFTER TOUCHDOWN	4- 0- 0- 0- 14	7	7	NONE	0	0
AFTER THRESHOLD BUT BEFORE TOUCHDOWN	18- 2- 5- 3- 34	30	37	15- 2- 5- 3- 26	32	32
0-150 M FROM RUNWAY	8- 1- 2- 0- 13	13	50	6- 1- 2- 0- 11	13	45
150-450 M FROM RUNWAY	13- 3- 7- 3- 25	21	71	12- 3- 7- 3- 24	25	70
450-1050M FROM RUNWAY	7- 4- 5- 6- 13	12	83	7- 4- 5- 6- 13	15	85
1050-1850 M FROM RUNWAY	NONE	0	83	NONE	0	85
MORE THAN 1850 METERS FROM RUNWAY	10- 6-12- 4- 48	17	100	7- 4- 8- 3- 13	15	100
TOTAL	60-16-31-16- 147	100	100	47-14-27-15- 87	100	100

the "after touchdown" category are eliminated. The table thus shows that the vortex problem in the landing phase (behind another landing aircraft) is concentrated in the immediate neighborhood of the touchdown zone.

The accidents with encounters more than 450 meters away (particularly those with encounters more than 1050 meters away) from the runway seem to have characteristics of their own. Many of these encounters seem to be rather random encounters occurring only because the small aircraft are approaching low, while at the same time their lateral navigation is poor. They manage in this way to encounter the vortices even when the vortices have been blown away from the extended centerline.

Table 2-1 also indicates that the percentage of fatal accidents increases steadily from 9 percent for encounters over the runway to 60 percent for encounters more than a mile away from the runway end, the trend remaining the same also after the elimination of accidents expected to be unrelated to the vortex problem. The probable explanation is that the vertical component of the impact velocity may be expected to be large with a large encounter altitude. Damage to the aircraft and injuries to the occupants may also be expected to be related to the sink velocity of the aircraft at the point of impact. Hence, more fatalities, and in general more damage, may be expected as the encounter altitude increases. It should be recognized that higher encounter altitude possibly also provides space in which to recover, which is possibly a partial explanation of why comparatively few accidents result from encounters at high altitudes.

2.3.2 Aircraft Types Involved

Figure 2-5 shows a landing weight histogram for accident aircraft involved in landing accidents behind conventional aircraft landings on the same runway. It is at once clear that small general aviation aircraft are the primary victims of the vortex problem. About 85 percent of the accident aircraft weighed less than 1800 kilograms while almost 97 percent weighed less than 5000 kilograms.

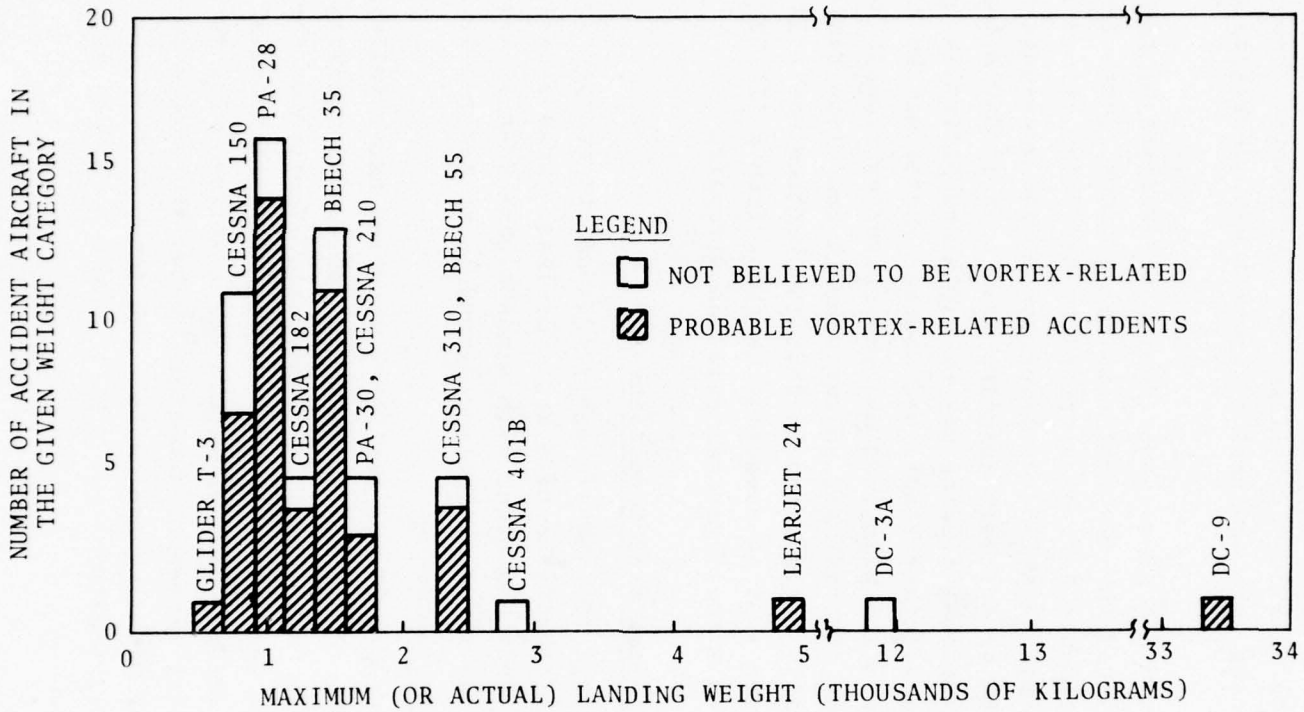


FIGURE 2-5. LANDING WEIGHT HISTOGRAM FOR ACCIDENT AIRCRAFT DURING LANDING ACCIDENTS BEHIND LANDINGS ON THE SAME RUNWAY

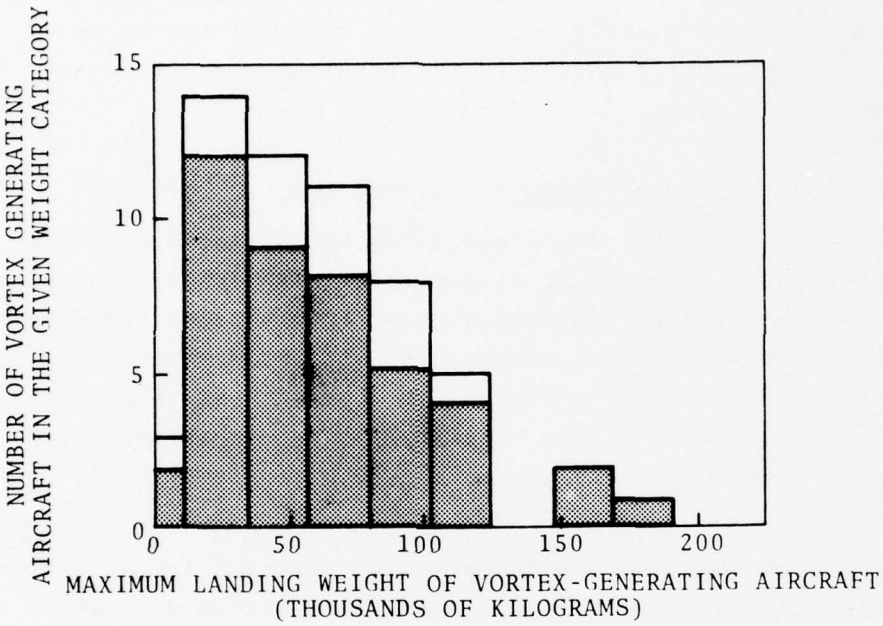
As for vortex-generating aircraft which caused these accidents, the largest number of accidents (12) were found to have been caused by B-707's, followed by 6 accidents caused by B-727's. In four cases, the generating aircraft was identified only as a jet.

Figure 2-6 gives some idea of the weights of the aircraft which produced the accident-causing vortices. More than 90 percent of the accidents have been caused by Non-Heavy air carrier aircraft weighing less than 136,000 kilograms. Some accidents have even been caused by aircraft weighing less than 12,000 kilograms. This highly surprising finding may be explained partially by the weight mix of the aircraft fleet, and another factor may be that the general aviation pilots do not expect vortex trouble behind small air carrier aircraft and so may come in too close behind them. A very probable explanation is that the vortices of a 50,000-kilogram aircraft are just as dangerous as those from a 150,000-kilogram aircraft to a small general aviation aircraft.

2.3.3 Reported Wind Conditions

A large majority (roughly 2/3) of the accidents occurred under wind conditions of 5 knots or less. Some accidents in the NTSB data base did occur with winds higher than 10 knots. Most of these accidents were, however, found to be not really related to the vortex problem.

About 1/4 of the accidents occurred under tailwind conditions. The actual number of operations under tailwind conditions is probably much less than 25 percent. Therefore, the tailwind conditions seem to be more dangerous than the headwind conditions from the vortex point of view. For a vortex below the flight path of a landing aircraft, a headwind blows the vortex further from the flight path, whereas a tailwind tends to blow the vortex back on the flight path.



LEGEND

NOT BELIEVED TO BE VORTEX-RELATED

PROBABLE VORTEX-RELATED ACCIDENTS

NOTE: "UNIDENTIFIED JETS" NOT INCLUDED IN THIS HISTOGRAM

FIGURE 2-6. LANDING WEIGHT HISTOGRAM FOR VORTEX GENERATING AIRCRAFT DURING LANDING/LANDING ACCIDENTS ON THE SAME RUNWAY

2.3.4 Vortices Generated During Touch-and-Go Operations

In about 10 percent of the cases, the accident-causing aircraft made a touch-and-go landing. There is reason to believe that the actual number of touch-and-go operations by air carrier aircraft is much less than 10 percent. Therefore, landing behind the touch-and-go operations of air carrier aircraft may be more dangerous from the vortex point of view than landing behind full-stop landings.

2.3.5 Distribution of Accidents by Airport Rank

Figure 2-7 shows the distribution of the 57 accidents which occurred at towered airports by airport rank. A similar distribution is also shown for the 45 remaining accidents after the elimination of the vortex-unrelated cases. The airport rank is based on the total traffic level in 1973. The figure shows that the vortex-related accidents of the "landing/landing on the same runway" category occur under widely varying total traffic-level conditions.

It is noted that many of the airports with the largest number of aircraft operations are primarily general aviation airports (e.g., Van Nuys and Long Beach airports in California). These airports do not appear to have a large number of vortex-related accidents in proportion to their number of operations. Vortex-related accidents tend to occur at airports which are primarily air carrier airports.

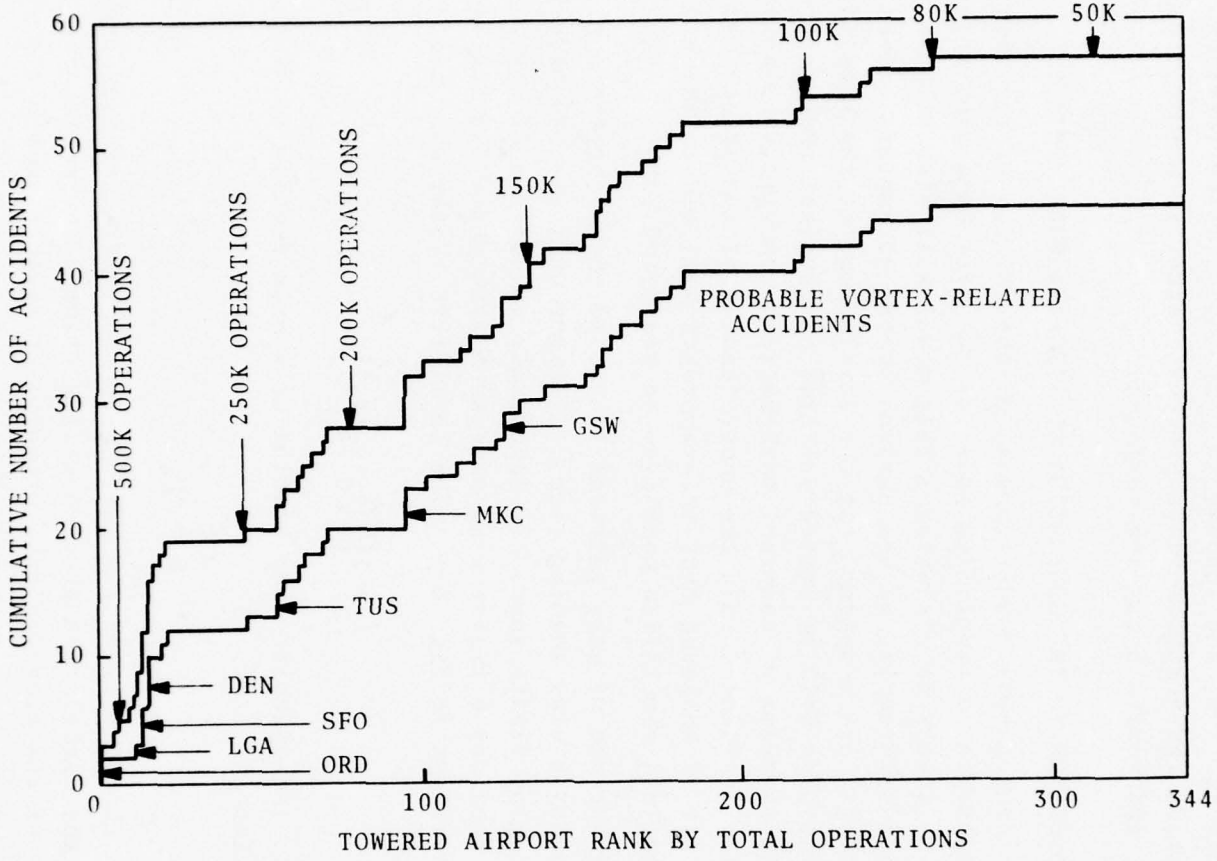


FIGURE 2-7. DISTRIBUTION OF ACCIDENTS BY AIRPORT RANK BASED ON TOTAL TRAFFIC

3. VORTEX PHENOMENA

In this section, the fundamental physics by which vortices are generated, the vortex roll-up process, vortex structure, vortex transport, and vortex decay are reviewed.

3.1 INTRODUCTION TO THE GENERATION OF AIRCRAFT WAKE VORTICES

To present a basic understanding of the physics of the wake vortex phenomenon, a simplified model of the lift on a wing using lifting-line theory is presented. This model will also help in gaining an understanding of how various system parameters affect vortex strength and movement. In the development of the simplified model, principles will be stated in terms of physical phenomena rather than in terms of abstract mathematical concepts. Numerical examples are included to aid the understanding of the principles involved. It is believed that this approach will aid in the understanding of less simplified models to be presented later.

The existence of wake vortices is caused solely by the non-uniform spanwise wing loading (i.e., lift per unit span denoted by ℓ) of a wing of finite span. To illustrate the origin of wake vortices, consider a finite wing of span b with three distinct wing loadings as shown in Fig. 3-1. The total lift of the wing is

$$L = 2\left[\frac{b}{6}\left(\ell_0+\ell_1+\ell_2\right)\right] \quad . \tag{3.1}$$

In general, the spanwise wing loading of a wing section is (Kutta-Joukowski theorem, ref. 3)

$$\ell = \rho U_\infty \Gamma', \tag{3.2}$$

where ρ is the density of the air, U_∞ is the aircraft flight speed, and Γ' is the circulation about a wing section. Therefore, the total lift of the wing (in this example) is related to the circulation at the given wing sections as

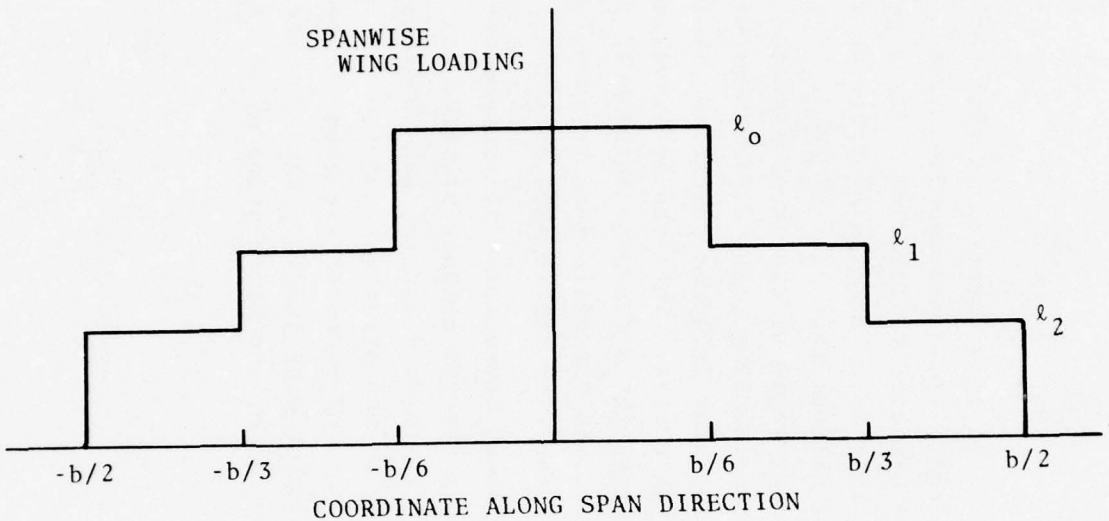


FIGURE 3-1. SPANWISE WING LOADING FOR ILLUSTRATIVE EXAMPLE

$$L = b \rho U_\infty \left(\Gamma_o' + \Gamma_1' + \Gamma_2'\right)/3 \quad , \tag{3.3}$$

and may be related to the lift coefficient by ($\bar{c}$ is the mean wing chord)

$$C_L = \frac{2}{3} \left(\Gamma_o' + \Gamma_1' + \Gamma_2'\right)/\bar{c}U_\infty \quad . \tag{3.4}$$

The interpretation of this equation is that the lift coefficient is a nondimensional (i.e., nondimensionalized by the mean chord and flight speed) average circulation. For a given wing shape, the lift coefficient is a function of angle of attack only. Since $\ell_2 < \ell_1 < \ell_o$, it follows that $\Gamma_2' < \Gamma_1' < \Gamma_o'$. Since vorticity (or circulation) cannot begin or end in an inviscid fluid, the difference in circulation (e.g., the differences between Γ_o' and Γ_1') cannot merely disappear in space. Instead, it is shed from the wing as a trailing vortex. This can be visualized, as shown in Fig. 3-2. Likewise, the difference between Γ_1' and Γ_2' is shed as a trailing vortex, and the difference between Γ_2' and zero circulation outboard of the wing tip is shed as a trailing vortex.

Figure 3-2 shows three horseshoe-shaped vortices. Each vortex is infinitely long (in the absence of viscosity), has a constant circulation over its entire length, and consists of two trailing vortices parallel to the airstream and a bound vortex attached to the wing. The trailing vortices are shed at the points on the wing at which the spanwise wing loading changes. The circulation at the wing root is made up of the circulation of all three horseshoe vortices. Thus

$$\Gamma_o' = \gamma_o + \gamma_1 + \gamma_2 \quad , \tag{3.5}$$

$$\Gamma_1' = \gamma_1 + \gamma_2 \quad , \tag{3.6}$$

$$\Gamma_2' = \gamma_2 \quad . \tag{3.7}$$

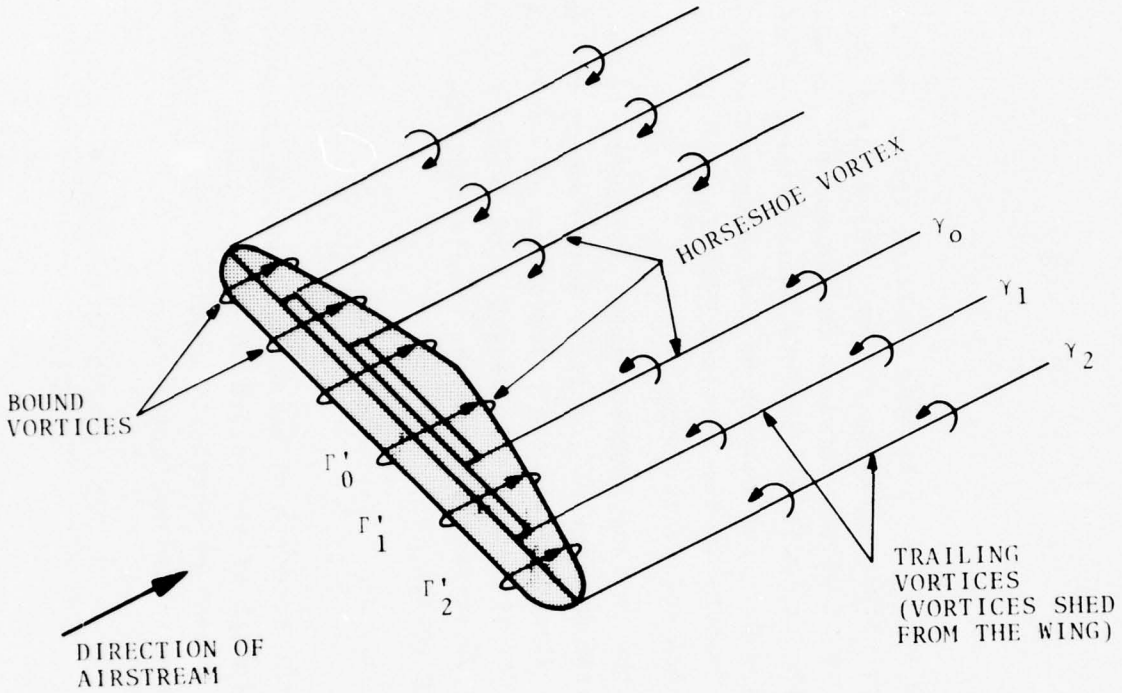


FIGURE 3-2. SYSTEM OF BOUND AND TRAILING VORTICES

Alternatively stated, the circulation of each shed vortex γ is equal to the change in circulation on the wing at the point at which the vortex is shed. Thus,

$$\gamma_0 = \Gamma_0' - \Gamma_1' , \tag{3.8}$$

$$\gamma_1 = \Gamma_1' - \Gamma_2' , \tag{3.9}$$

$$\gamma_2 = \Gamma_2' . \tag{3.10}$$

As seen from Fig. 3-2, each trailing vortex is in the flow field of every other trailing vortex. For a first approximation assume that the trailing vortices on one end of the wing do not interact with the trailing vortices on the other end of the wing. However, the mutual interaction of the three vortices on each end of the wing results in the vortices "rolling up" into a single vortex for each end of the wing.

During the roll-up process, total vorticity is conserved. Also, the first moments of vorticity with respect to the span and the vertical direction and the polar moment of vorticity are all conserved. For the example presented here (Figs. 3-1 and 3-2), conservation of vorticity gives the result that the circulation in the rolled-up vortex is

$$\Gamma = \gamma_o + \gamma_1 + \gamma_2 = \left(\Gamma_o' - \Gamma_1'\right) + \left(\Gamma_1' - \Gamma_2'\right) + \left(\Gamma_2' - 0\right) = \Gamma_o' . \tag{3.11}$$

(Γ' denotes the strength of bound vorticity on the wing and Γ denotes the strength of the rolled up shed vortex.) By conservation of the first moment of vorticity about the center of the wing, the centroid of the rolled-up vortex is

$$\bar{y} = \frac{\gamma_0(b/6) + \gamma_1(b/3) + \gamma_2(b/2)}{\gamma_0 + \gamma_1 + \gamma_2} . \tag{3.12}$$

Some of the important characteristics of aircraft wake vortices are now examined; in particular, the effect of aircraft weight, aircraft speed, and spanwise wing loading on the vortex strength (circulation) of the rolled-up vortex are derived.

For fixed relative loadings of the wing sections, a weight increase requires a corresponding increase in spanwise wing loading which necessitates an increase in the circulation about the wing (equation 3.3). Physically, this is accomplished by increasing the angle of attack to move the stagnation point down on the leading edge of the wing. Equations (3.2) and (3.1) show that for a fixed wing and fixed relative spanwise wing loading, the strength (circulation) of the rolled-up vortex is directly proportional to the aircraft weight.

Equation (3.2) also shows that a decrease in airspeed necessitates a corresponding increase in circulation about the wing. Physically, this is accomplished by increasing the angle of attack to move the stagnation point down on the leading edge of the wing. Alternatively, it could also be accomplished by the deployment of flaps although this would change the relative spanwise wing loading. For a fixed aircraft weight and fixed spanwise wing loading, equations (3.2) and (3.1) show that the rolled-up vortex strength is inversely proportional to airspeed.

For the effect of spanwise wing loading, note from equation (3.11) that the strength of the rolled-up vortex is Γ_o' which is a function of the spanwise wing loading at the wing root. This means that all of the bound vorticity at the wing root must be shed. However because total lift is constrained to be a constant, any decrease in wing loading toward the wing tip requires a corresponding increase in wing loading toward the wing root and an increase in shed vortex strength. To illustrate the effect, assume a uniform wing loading for an aircraft weight, W_A. In Fig. 3-1, this would give

$$\ell_o = \ell_1 = \ell_2 = W_A/b \ , \tag{3.13}$$

which implies

$$\Gamma = \Gamma_o' = W_A/\rho b U_\infty \ . \tag{3.14}$$

For a contrasting example, let the spanwise wing loading be non-uniform so that

$$\ell_1 = 0.8\ \ell_o \quad , \tag{3.15}$$

$$\ell_2 = 0.5\ \ell_o \quad , \tag{3.16}$$

then, from equation (3.1),

$$\ell_o = 1.3\ W_A/b \quad , \tag{3.17}$$

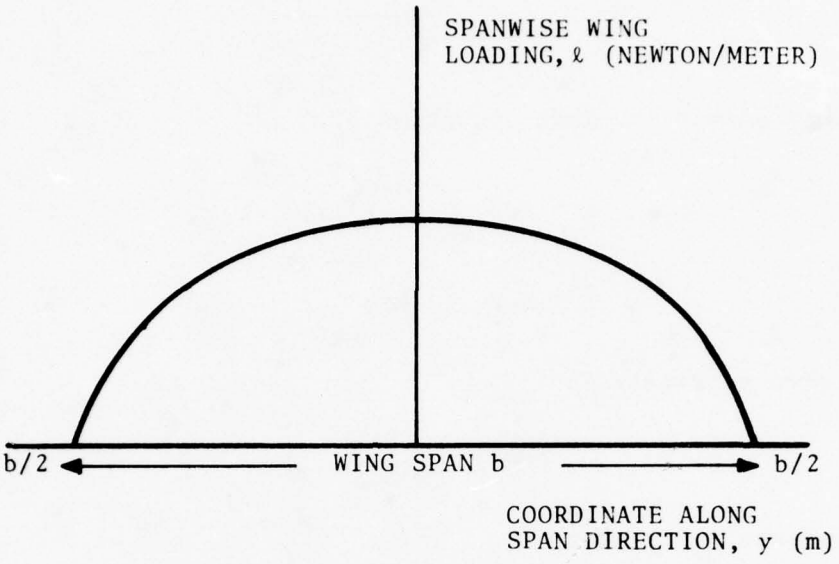
and

$$\Gamma = \Gamma_o' = 1.3\ W_A/\rho b U_\infty \tag{3.18}$$

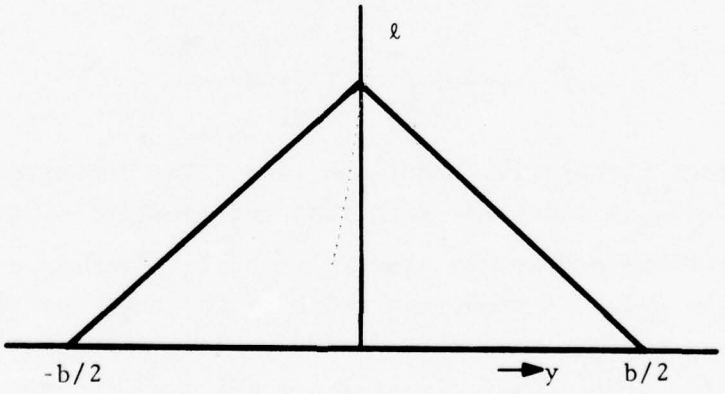
Thus the vortex strength increases as the deviation from a uniform wing loading increases. In particular, the use of flaps increases the inboard wing loading and thereby decreases the outboard wing loading since total lift is constant. This causes an increase in the strength of the rolled-up vortex.

For aerodynamic calculations using lifting-line theory, the principles described in the foregoing discussion are valid. In the practical use of lifting-line theory, the number of sections into which the wing is divided (cf., Figs. 3-1 and 3-2) is increased significantly. In the limit as the number of sections increases to infinity, the spanwise wing loading (cf., Fig. 3-1) becomes a smooth curve. The three trailing vortices on each end of the wing in Fig. 3-2 become a very large number of very small shed vortices. In the limit, these small vortices form a vortex sheet of shed vortices which rolls up into a single vortex near the wing tip. The process is discussed later.

To conclude the introduction to the generation of aircraft wake vortices, the derivation of trailing vortex strength, vortex separation, and vortex downward velocity for an elliptically loaded wing will be outlined. To show the effects of spanwise wing loading distribution, similar data for a linear spanwise loading will also be derived. Diagrams of the two wing loadings are shown in Fig. 3-3. For the derivations, integration is used in place of summation for presenting the concepts which have been derived in



(a) ELLIPTICAL WING LOADING



(b) LINEAR WING LOADING

FIGURE 3-3. DIAGRAM OF WING LOADINGS USED FOR ILLUSTRATIVE EXAMPLES

the previous few pages. For the elliptical loading, the circulation about the wing is:

$$\Gamma'(y) = \Gamma'_o \sqrt{1 - 4y^2/b^2} \ . \tag{3.19}$$

The summation for the lift (equation 3.3) is

$$L = 2\rho U_\infty \int_o^{b/2} \Gamma'(y)dy \ , \tag{3.20}$$

$$L = \pi\rho U_\infty \Gamma'_o \, b/4 \ , \tag{3.21}$$

or the shed vorticity is

$$\Gamma = \Gamma'_o = \frac{4L}{\pi\rho U_\infty b} \ . \tag{3.22}$$

For reference, note that

$$C_L = \frac{2}{(b/2)} \int_o^{b/2} \Gamma'(y)dy \Big/ \bar{c}U_\infty \ , \tag{3.23}$$

where

$$\frac{1}{(b/2)} \int_o^{b/2} \Gamma'(y)dy$$

is the average circulation about the wing. The interpretation of equation (3.23) is identical with that for equation (3.4).

As described previously, the value of Γ'_o given by equation (3.22) is the value of the circulation of the shed vortices

$$\Gamma = -\int_o^{b/2} \left(\frac{d\Gamma'}{dy}\right)dy = -\left[\Gamma'(b/2) - \Gamma'(o)\right] = \Gamma'_o \ , \tag{3.24}$$

since there is no bound circulation at the wing tip. Equation (3.24) is analogous to equation (3.11). The negative sign is caused by the fact that an increase in shed vorticity is effected by a decrease in bound vorticity along the positive spanwise direction.

The first moment of shed vorticity is

$$\Gamma_y = -\int_0^{b/2} y\left(\frac{d\Gamma'}{dy}\right) dy \ , \tag{3.25}$$

$$\Gamma_y = -\Gamma_o' \int_0^{b/2} \left[4y^2/b^2 \sqrt{1 - 4y^2/b^2}\right] dy = \Gamma_o' b\pi/8 \ . \tag{3.26}$$

Therefore, the centroid of vorticity is

$$\bar{y} = \Gamma_y/\Gamma = \pi b/8 \ . \tag{3.27}$$

From the well known vertical speed for a vortex pair separated by distance $2\bar{y}$ (a negative value is descent),

$$\frac{d\bar{z}}{dt} = -\frac{\Gamma}{2\pi(2\bar{y})} = -\frac{8L}{\pi^3 \rho U_\infty b^2} \ . \tag{3.28}$$

For comparison, consider similar results for a linear spanwise lift distribution. The circulation about the wing is

$$\Gamma'(y) = \Gamma_o' \ (1-2y/b) \ . \tag{3.29}$$

The lift is

$$L = 2\rho U_\infty \int_0^{b/2} (1-2y/b)dy = \rho U_\infty \Gamma_o' b/2 \ , \tag{3.30}$$

or

$$\Gamma = \Gamma_o' = 2L/\rho U_\infty b \ , \tag{3.31}$$

which is the strength of the trailing vortices. Then

$$\Gamma_y = \int_0^{b/2} 2\Gamma_o' y/b \ dy = \Gamma_o' b/4 \ , \tag{3.32}$$

or

$$\bar{y} = b/4 \quad . \tag{3.33}$$

The vertical speed of the rolled-up vortex is

$$\frac{d\bar{z}}{dt} = - 2L/\pi\rho b^2 U_\infty \quad . \tag{3.34}$$

Values of vortex properties calculated from the above expressions are shown for comparison in Table 3-1. The weight and wing span are the maximum landing weight and wing span for the Boeing 707-320C.

From these results it may seen that for a given form of the lift distributions, the strength of the shed vortex is directly proportional to aircraft weight and inversely proportional to both aircraft speed and wing span. Vortex separation is directly proportional to wing span only. The descent rate is proportional to aircraft weight and is inversely proportional to aircraft speed and to the square of the wing span.

The purpose of the foregoing discussion is the description (in a simplified manner) of the physical principles and processes which cause the formation of wake vortices and determine their strength. With these principles in mind, a more detailed description of the roll-up process is presented.

3.2 VORTEX STRUCTURE

In this section, the structure of aircraft wake vortices is discussed. Both analytical models of vortex structure and experimental measurements of vortex structure are presented. Any discussion of vortex structure necessitates a discussion of viscous effects, particularly within the vortex core. However, a complete description of the contribution of viscosity to vortex decay and bursting is reserved until a later section. For most of this section, vortex structure will be described from the viewpoint of a single pair of vortices. The case of multiple pairs of vortices is discussed in the last part of the section.

TABLE 3-1. COMPARISON OF VORTEX PROPERTIES FOR ELLIPTICAL WING LOADING AND LINEAR WING LOADING

PARAMETER	ELLIPTIC WING LOADING	LINEAR WING LOADING
Aircraft Weight, W_A, kg	111,891	111,891
Wing Span, b, m	44.42	44.42
Airspeed, U_∞, m/sec	69.5	69.5
Vortex Strength, Γ, m^2/sec	369	579
Distance Between Vortices, $2\bar{y}$, m	34.89	22.21
Rolled-up Vortex Descent Rate, $d\bar{z}/dt$, m/sec	-1.68	-4.14

3.2.1 Vortex Roll-Up Phenomenon

The wake vortex originates in the vorticity shed from the generating wing. The vorticity can be resolved into streamwise and cross stream components. The streamwise portion (consisting of vorticity oriented with the flight direction) is the manifestation of the lift on the wing and its associated bound vortex field (the vorticity embedded in the lifting surface). This vorticity forms the trailing vortices. The other component of vorticity (which was not described in the previous section), the cross stream component, is alined essentially normal to the flight path and is initially in the plane of the wing. This component is associated with the viscous profile drag of the wing and represents the wake momentum deficit associated with the profile drag. This component causes an axial velocity to be imposed upon the vortex, and thereby, contributes to vortex decay and bursting. It does not otherwise affect the tangential velocity component of the vortex. In an ideal flow (the hypothetical case where the wing has no viscous drag), only the first contribution (the streamwise vorticity) would exist and would eventually organize itself into a pair of trailing vortex systems.

The general development of the wake vortex system occurs in a series of stages. For simplicity, first consider the simplest case of a clean wing with no areas of abrupt changes in lift or drag (Fig. 3-4). The wing vorticity (both streamwise and cross streamwise) is first shed in an approximately flat sheet of width roughly corresponding to the wing span (the planar sheet stage). The sheet commences to form a self-induced scroll-like shape (the vortex roll-up stage). The roll-up process continues until most of the wing vorticity is concentrated in two approximately circular vortex cores (the viscous vortex pair stage). Various interactions may occur in these cores creating instabilities which can cause the wake to break up rapidly. If the catastrophic instabilities do not occur, the final regular decay takes place. Here under the influence of both atmospheric and aircraft-induced turbulence, the cores expand to fill an approximately elliptical region of vorticity (the decaying impulse state). Many of the significant aerodynamic

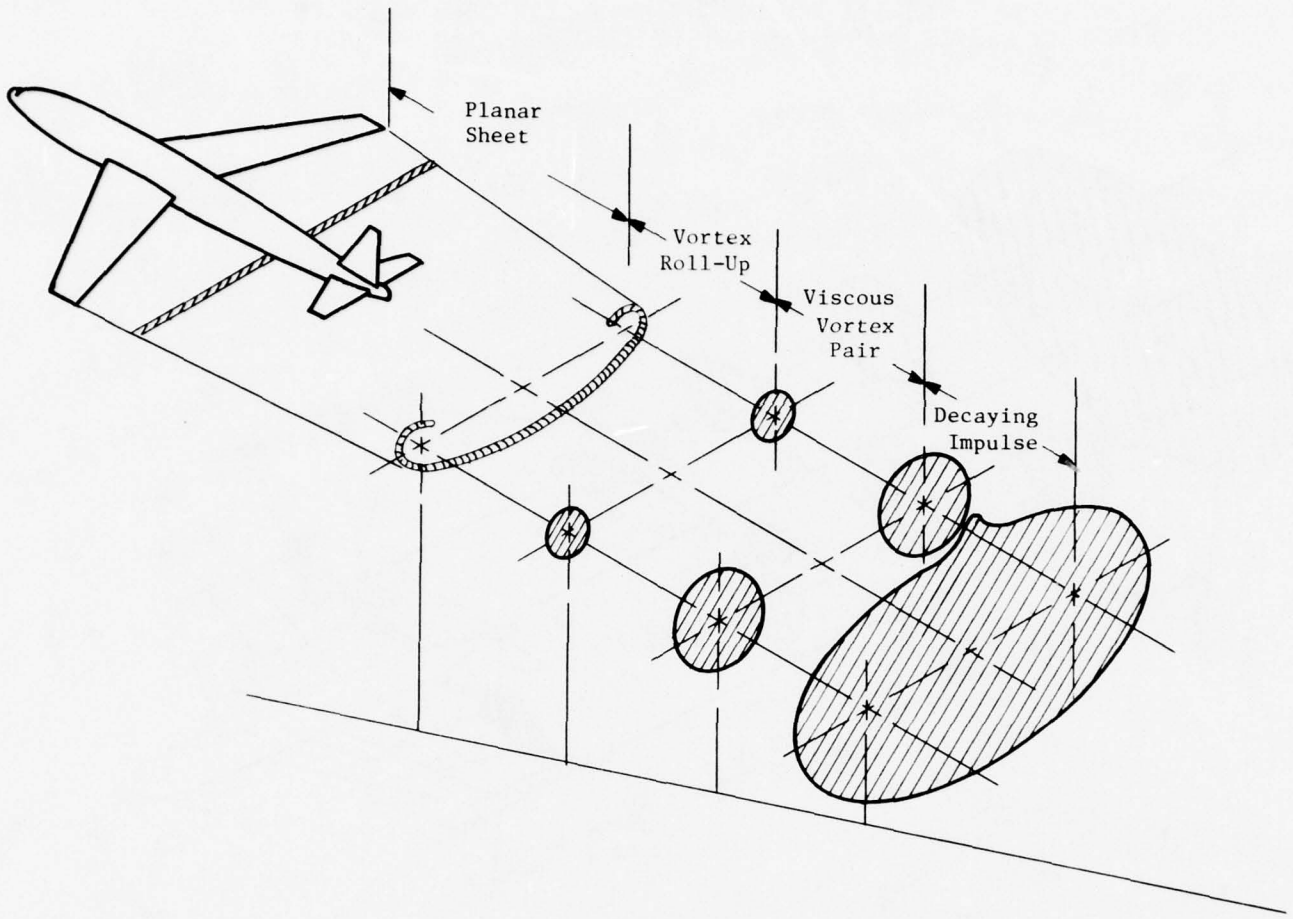


FIGURE 3-4. VORTICITY DISTRIBUTION AND STAGES OF VORTEX WAKE FOR A CLEAN WING

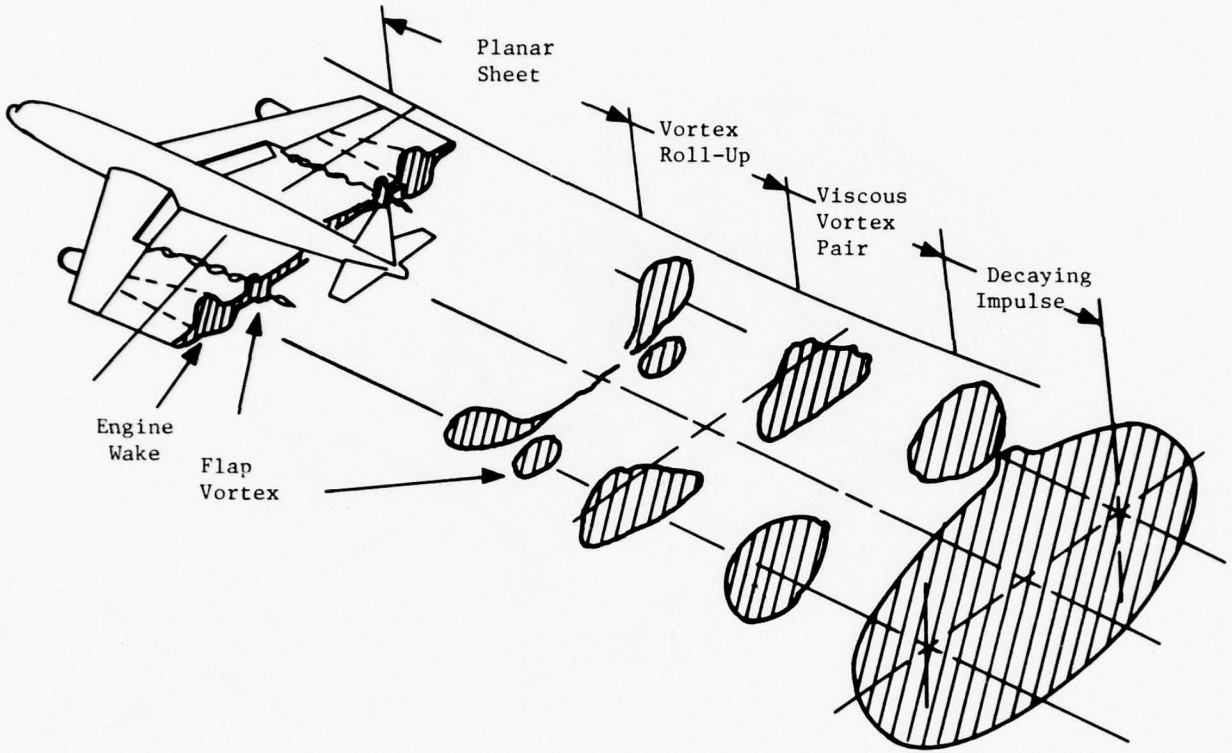


FIGURE 3-5. VORTICITY DISTRIBUTION AND STAGES OF VORTEX WAKE FOR WING WITH FLAP AND THRUST EFFECTS

effects occur between the roll-up stage and the decaying impulse stage when the system is in its viscous vortex-pair state. Thus, this is the domain to which most attention is devoted in this section.

If the wing contains significant regions of concentrated streamwise or cross stream perturbations, then there may be more than one vortex pair, and the various stages may develop with different time scales compared with the clean case; the different phases may be delayed or accelerated. Such a situation frequently occurs in the important cases of aircraft in the landing or take-off configurations. There, strong disturbance effects occur because of flaps, jet engine thrust, and landing gear. A representation is shown in Fig. 3-5 where the flap vortex remains isolated, so that there are two vortex pairs while the engine-induced turbulence apparently accelerates the decay process.

A description of the fundamental principles of the roll-up process is now presented. This is the process by which the planar sheet evolves into the viscous vortex pair. As described in the previous section, a vortex sheet is trailed from a finite aspect ratio wing as a consequence of the nonuniform spanwise lift of the wing. The roll-up of the sheet into discrete vortices as a result of a convective motion was recognized as early as 1907 by Lanchester (see Fig. 3-6). Since then, there have been numerous studies to describe this complicated phenomenon. This section will briefly review roll-up and the subsequent vortex-vortex interactions in the wake. The material presented here has, for the most part, been taken from ref. 4.

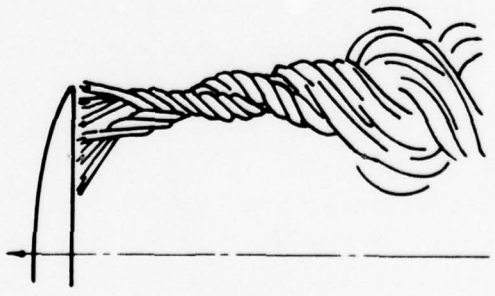


FIGURE 3-6 - LANCHESTER'S CONCEPT OF TIP VORTEX ROLL-UP

The discussion of aircraft vortex wake roll-up quite appropriately begins at the trailing edge of a lifting wing with an attempt to estimate at what distance downstream the wake may be considered essentially rolled up. In the roll-up process, the vortex sheet is stretched and rolled up in a spiral as shown in Fig. 3-7. The spiral structure is sketched in Fig. 3-7 where points A, B, and C are shown at the wing trailing edge and after roll-up has proceeded for some time. The downwash velocities in the wake are of the order of Γ_o'/b, the downwash velocity at the wing root being exactly $\Gamma_o'/2b$ from lifting-line theory. An estimate of the downstream distance at which roll-up is complete is obtained by noting that roll-up requires a redistribution of trailed vorticity over the length of the order of b. For example, the vorticity generated at the wing root must be transported out to near the wing tip. The velocity of transport is on the order of Γ_o'/b. Therefore, the time required for the redistribution must be the order of b^2/Γ_o' or, in terms of the downstream distance, the order of $U_\infty b^2/\Gamma_o'$. The nondimensional distance which characterizes the roll-up phenomenon is x/b which is of the order of AR/C_L where AR and C_L are the wing aspect ratio and life coefficient, respectively. For an aspect ratio 7 wing at a cruise C_L of 0.4, the downstream distance is on the order of 20 wingspans. In the take-off and landing configurations, roll-up occurs more quickly because of higher values of C_L. As will become apparent, more accurate estimates of the distance downstream at which roll-up is complete must be obtained by detailed calculation.

Details of the roll-up phenomenon, other than of a qualitative nature obtained from flow visualization studies, have been difficult to obtain. Clearly, the three-dimensionality of the flow field has hindered both theoretical and experimental investigations. However with the advent of high lift wings where wake geometry becomes a factor in determining the downwash at the wing, and with the realization that wake vortices from large aircraft can pose a hazard to other aircraft, the study of the roll-up problem received new impetus. The calculation of the downstream development of a vortex wake from a flat sheet is a formidable task, and estimates are made

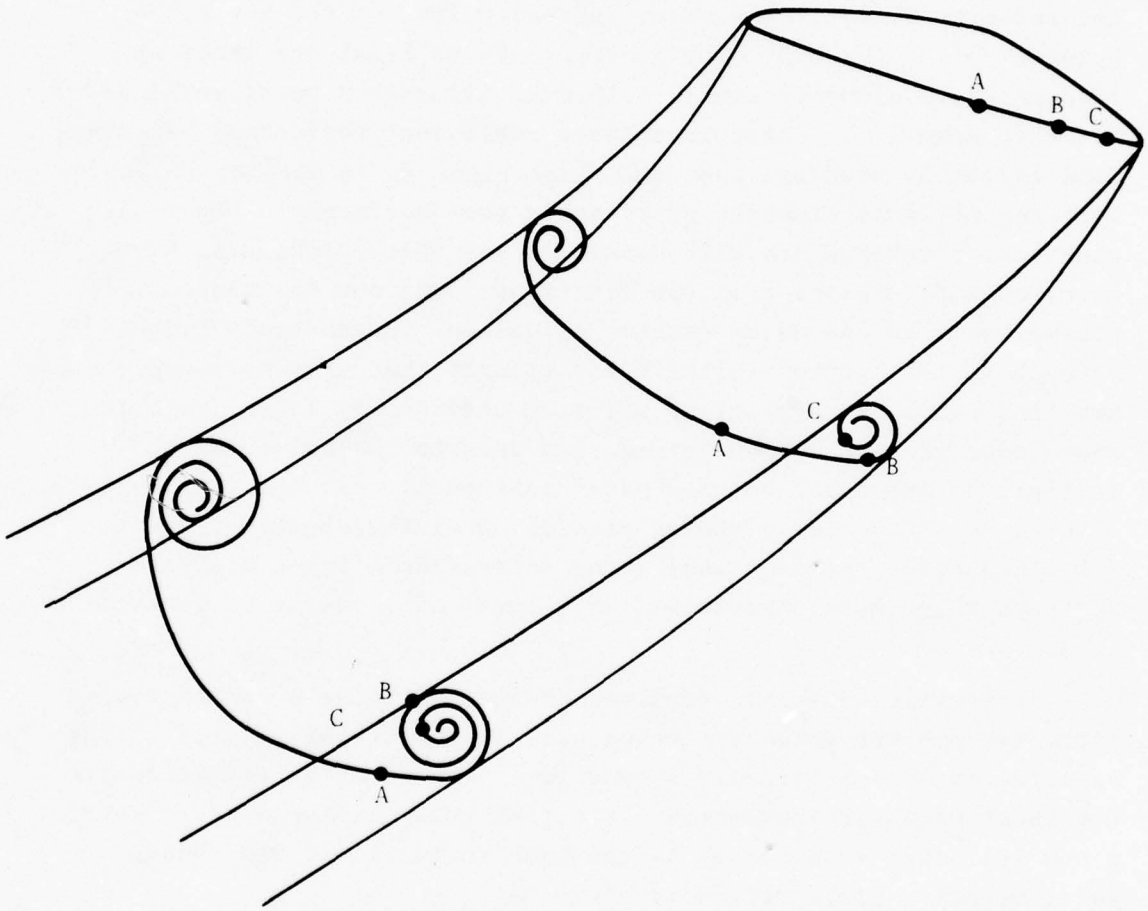


FIGURE 3-7. STRETCHING OF THE VORTEX SHEET DURING ROLL-UP

from approximate models. With recent advances in numerical computation procedures and as computers become larger, the numerical solution of the entire vortex wake is nearly possible. However to date, a description of roll-up is obtained by considering the motion of an initially plane two-dimensional vortex sheet of strength

$$\gamma = - \frac{d\Gamma'}{dy} = \int_{-\infty}^{\infty} \zeta \, dz \quad , \tag{3.35}$$

where ζ is the axial or trailed vorticity (i.e., the gradient of the velocity field). The sheet initially lies in the x-y plane between $-b/2 \leq y \leq b/2$. The procedure is to break the sheet up into discrete elements (refs. 5 through 11) with n point vortices, and then numerically calculate their subsequent positions. In the discretization process, some ambiguity rises as to whether to choose vortices of equal strength or to space them uniformly. Other discretization schemes are also possible, and these procedures have received wide treatment in the literature. Of course, the correct scheme would be one which exactly calculates the unsteady velocity at each vortex. However, there is evidence that this may never be possible since the similarity solution obtained by Kaden (ref. 12) shows that the arc length between two neighboring points on the initially plane sheet become spaced arbitrarily far apart as roll-up proceeds. The never-ending stretching of the sheet (cf., Fig. 3-7), and hence the ever-increasing separation between discrete vortices which model the sheet, is a continuing source of frustration.

Apparently, discrete vortices cannot model the wing tip region correctly and two fixes are being used to render the results of the calculation more physically appealing. The first is to discretize the sheet with vortices which are not singular at the center (refs. 8 and 10). One such vortex is the Lamb vortex whose well known swirl velocity distribution is given by

$$v = \frac{\Gamma}{2\pi r} \left[1 - \exp \left(- \frac{r^2}{r_c^2} \right) \right] . \tag{3.36}$$

The radial distance r is measured from the center of each vortex and the parameter r_c, which has the dimensions of length, can be chosen to set the level of the maximum tangential velocity in the vortex. The effect of nonzero r_c is to introduce an artificial viscosity into the computation, and therefore, to slow down or dampen the roll-up. Unfortunately, the calculations are somewhat sensitive to the value of r_c used, and no rigorous procedure to determine its value exists. The question of whether the roll-up phenomenon is being modeled accurately, or if the calculation merely looks correct, remains.

The second technique is to dispense with any hope of modeling the spiral structure of the tip region (ref. 9). The discrete vortices are deleted from the calculation as they become part of the spiral and become separated from their neighbor by more than some prescribed arc length. As the vortices are removed from the calculation, they are added back by increasing the circulation of one tip vortex by the appropriate amount. The results of such a calculation are shown in Fig. 3-8. Again the question of whether the roll-up phenomenon is being modeled accurately, or if the calculation merely looks correct, is yet to be resolved.

Although discrete vortex calculations have shortcomings, they have proven to be extremely useful in providing insight into the initial deformation of the vortex sheet from which subsequent development may be inferred. As an illustration, Fig. 3-9 shows the roll-up of a sheet into what appears to be two pairs of discrete vortices. The roll-up of two or more pairs of discrete vortices occurs quite frequently because of flaps.

When the exact details of the actual roll-up are not required, two models which describe the inviscid structure of the vortex wake have been developed. The first model, after Prandtl (ref. 13), has been based on the conservation of mechanical energy. Unfortunately, the model requires an arbitrary choice of the swirl velocity distribution, being only constrained by circulation at large radius from the vortex center and an integral constraint on kinetic energy.

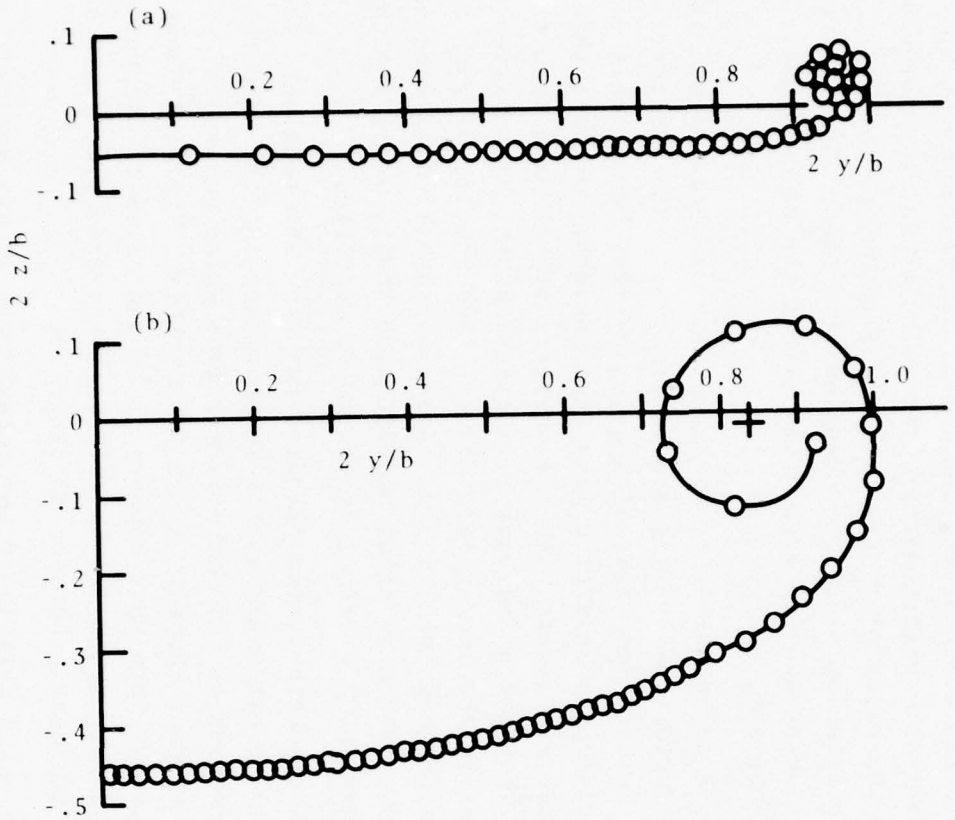


FIGURE 3-8. POINT VORTEX COMPUTATIONS WHERE THE TIP SPIRAL STRUCTURE IS MODELED BY A SINGLE POINT VORTEX

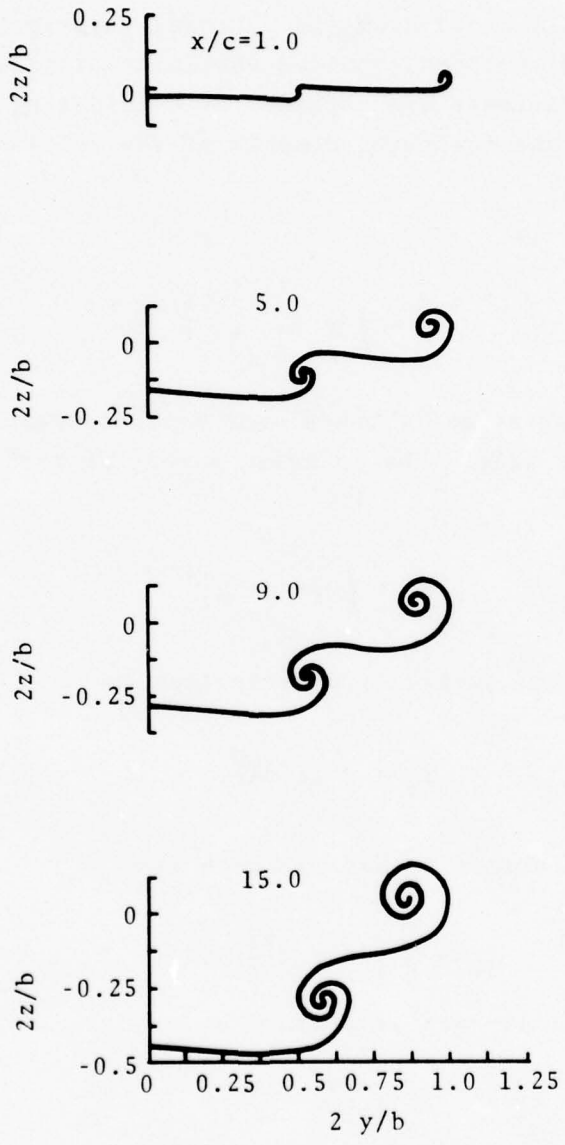


FIGURE 3-9. THE ROLL-UP OF A TIP AND FLAP VORTEX

The second model developed by Betz (ref. 14) overcomes the arbitrariness inherent in the Prandtl calculation. Since the Betz model and recent extensions have explained many of the observed details of vortex structure, it is appropriate to give a somewhat more complete elaboration of its basis.

The Betz model evolved from the integral invariants of an incompressible, two-dimensional bounded vorticity distribution. The global integral invariants are obtained by considering the time rates of change of the following moments of the vorticity distribution:

The total vorticity is

$$\Gamma = \int \zeta \, dA \quad , \tag{3.37}$$

where the area integration is taken over a plane area at a fixed distance behind the wing. The spanwise moment of vorticity distribution is

$$\Gamma_y = \int y\zeta \, dA \quad . \tag{3.38}$$

The vertical moment of vorticity distribution is

$$\Gamma_z = \int z\zeta \, dA \quad . \tag{3.39}$$

The polar moment of vorticity distribution is

$$\Gamma_r = \int \left(y^2 + z^2\right)\zeta \, dA \quad , \tag{3.40}$$

where ζ is the vorticity and is defined by

$$\zeta = \frac{\partial W}{\partial y} - \frac{\partial V}{\partial z} \quad . \tag{3.41}$$

Using the continuity equation,

$$\frac{\partial V}{\partial y} + \frac{\partial W}{\partial z} = 0 \quad , \tag{3.42}$$

and the vorticity equation,

$$\frac{\partial \zeta}{\partial t} + V \frac{\partial \zeta}{\partial y} + W \frac{\partial \zeta}{\partial z} = \nu \left(\frac{\partial^2 \zeta}{\partial y^2} + \frac{\partial^2 \zeta}{\partial z^2} \right) , \tag{3.43}$$

(where ν is the viscosity) it is not difficult to show that the time derivatives of equations (3.37) through (3.40) are zero. It has been customary to define the centroid of vorticity when Γ is non-zero as

$$\bar{y} = \frac{\Gamma_y}{\Gamma} , \tag{3.44}$$

$$\bar{z} = \frac{\Gamma_z}{\Gamma} . \tag{3.45}$$

The polar moment of the vorticity distribution Γ_r divided by Γ defines a length squared, or

$$D = \left[\frac{\Gamma_r}{\Gamma} \right]^{1/2} , \tag{3.46}$$

which represents the dispersion of the vorticity about the centroids $\bar{y}$ and $\bar{z}$ and is also an invariant of the motion. Howard (ref. 15) has elegantly shown that no other invariants of the flow exist.

Behind an aircraft, the flow field in a plane normal to the flight direction is shown in Fig. 3-10. In 1932, Betz investigated the moments of the vorticity distribution over the half plane, $y \geq 0$, using systems of point vortices in an inviscid fluid. The Betz result in a viscous fluid for distributed vorticity can be generalized. The time rate of change of equations (3.36) through (3.39) is

$$\frac{d\Gamma}{dt} = -\nu \int_{-\infty}^{\infty} \left.\frac{\partial \zeta}{\partial y}\right|_{y=0} dz \quad , \tag{3.47}$$

$$\frac{d\Gamma_y}{dt} = 0 \quad , \tag{3.48}$$

$$\frac{d\Gamma_z}{dt} = -\int_{-\infty}^{\infty} \left[\left.\frac{W^2}{2}\right|_{y=0} + \nu z \left.\frac{\partial \zeta}{\partial y}\right|_{y=0} \right] dz, \tag{3.49}$$

$$\frac{d\Gamma_r}{dt} = -\int_{-\infty}^{\infty} (z-\bar{z}) \left.\frac{W^2}{2}\right|_{y=0} dz + 2\nu\Gamma \quad , \tag{3.50}$$

where the integrals which define Γ, Γ_y, Γ_z, and Γ_r are carried out over the area defined by $y \geq 0$.

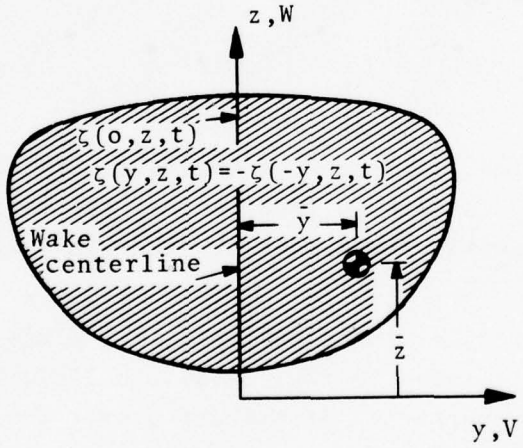


FIGURE 3-10. THE FLOW FIELD IN A PLANE NORMAL TO THE FLIGHT DIRECTION

Since the wake centerline is a streamline, the time rate of change of the circulation can result solely from the diffusion of vorticity across the centerline as shown in equation(3.47). The constancy of Γ_y is related to the invariance of the vertical impulse of the fluid motion.

When viscous effects are ignored, the rate of descent of the centroid of the wake is given by

$$\frac{d\bar{z}}{dt} = \frac{1}{\Gamma}\frac{d\Gamma_z}{dt} = -\frac{1}{\Gamma}\int_{-\infty}^{\infty}\frac{W^2}{2}\bigg|_{y=0} dz \ . \tag{3.51}$$

For a trailing pair of irrotational vortices of strength Γ separated by spacing b', it is not difficult to show (cf., Section 3.3.1) the well-known result

$$\frac{d\bar{z}}{dt} = -\frac{\Gamma}{2\pi b'} \ , \tag{3.52}$$

and the descent rate is constant. This is not necessarily the case when the wake is made up of two or more vortex pairs.

The polar moment of the dispersion length D is a measure of the spread of the vorticity. As can be seen from equation (3.50), the time rate of change is related to the symmetry of the function $W^2(0,z,t)$ about $\bar{z}$ and is increased by viscous diffusion. In the absence of viscosity and when the vorticity is symmetric about $z = \bar{z}$, which is the case when the vorticity distribution is a sheet or that of a rolled-up trailing vortex, $d\Gamma_r/dt = 0$. Betz reasoned that Γ_r should not in fact change significantly during roll-up, and then, made the assumption that not only should Γ_r be constant when defined over the half-plane but should be approximately correct locally as well. In this manner, he replaced the difficult computation of the precise details of the inviscid roll-up of the vortex sheet with a local axisymmetric distribution of vorticity, so constituted and so located that "proper" consideration is given to the conservation of vorticity and moments of vorticity behind each half of the wing.

If the second moment of the vorticity is to hold locally as well as globally, Betz reasoned

$$-\int_{y}^{b/2} \frac{d\Gamma(\eta)}{d\eta}\left[\eta-\bar{y}(y)\right]^2 dy = \int_{0}^{r} \zeta^2 \frac{d\Gamma(\zeta)}{d\zeta}\, d\zeta \ , \tag{3.53}$$

$\bar{y}(y)$ is defined by

$$\bar{y}(y) = -\frac{1}{\Gamma(y)}\int_{y}^{b/2} \frac{d\Gamma(\eta)}{d\eta}\, \eta\, d\eta \ , \tag{3.54}$$

and is the centroid of the vorticity trailed between the wing station y and the wing tip at y - b/2. Equation (3.53) is approximate and can be manipulated to allow physical interpretations of the underlying assumptions.

When equation (3.53) is combined with a statement of Kelvin's theorem

$$\Gamma(y) = -\int_{y}^{b/2} \frac{d\Gamma(\eta)}{d\eta}\, d\eta = \int_{0}^{r} \frac{d\Gamma(\zeta)}{d\zeta}\, d\zeta = \Gamma\ (r). \tag{3.55}$$

Donaldson et al. (ref. 16), Rossow (ref. 17), and Jordan (ref. 18) have independently shown the surprisingly simple result that the relationship between r and y is

$$r = \bar{y}(y) - y \ . \tag{3.56}$$

This result, taken with equation (3.55), states that the value of the circulation at wing station y is the value of the circulation at radial distance r in an axisymmetric vortex. Referring to Fig. 3-11, the radial distance r is equal to the distance from y to the centroid $\bar{y}$ of all the trailed vorticity outboard of y. When all the vorticity can be considered rolled up, the vortex center is located at $y = \bar{y}(0)$ to preserve the vertical impulse of the flow. Since, at this point, r also equals $\bar{y}(0)$, the circular regions containing vorticity just touch along the aircraft centerline.

The Betz model has been checked against measurements made behind model and full-scale aircraft. In Fig. 3-12, the computed

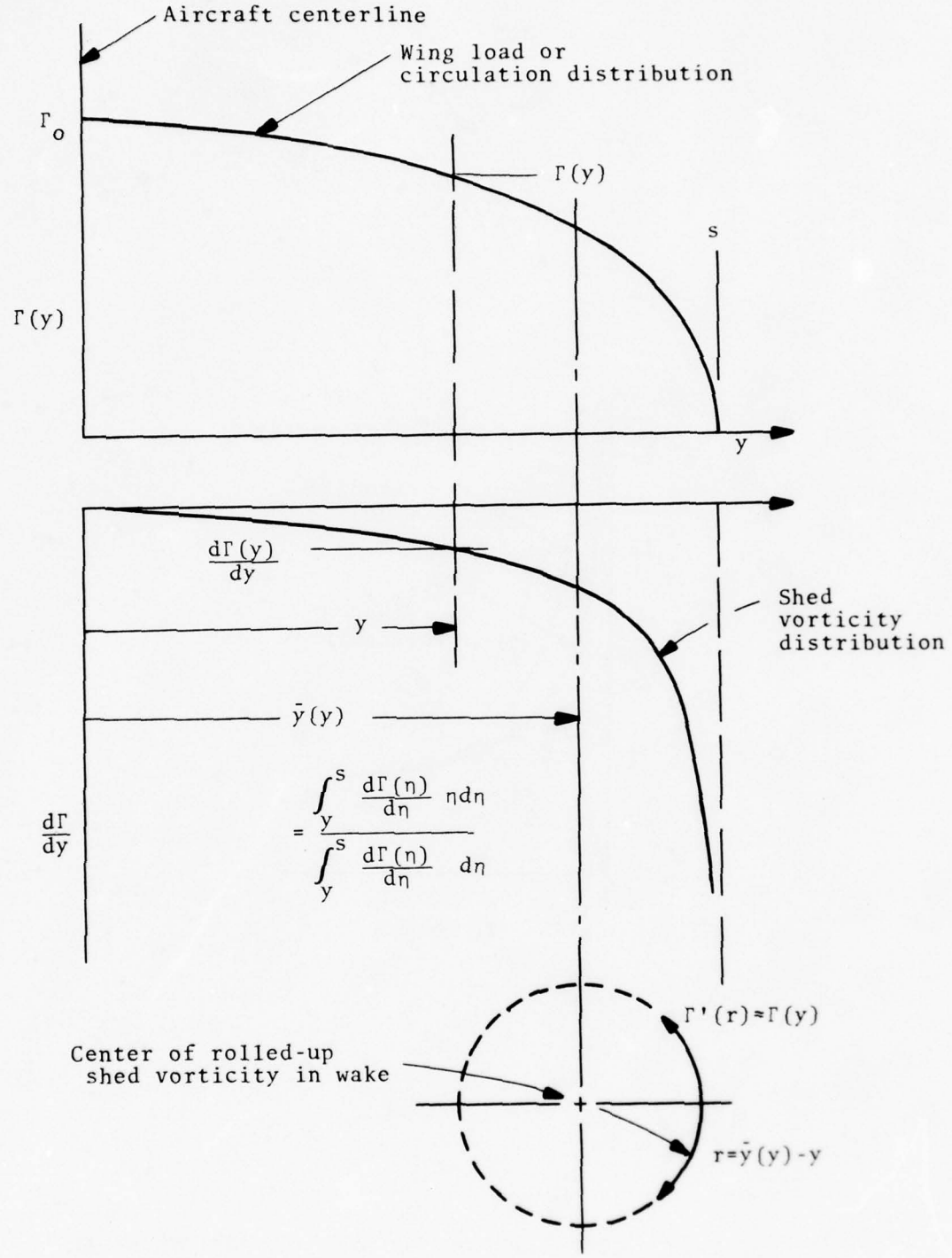


FIGURE 3-11. THE BETZ ROLL-UP RELATIONS FOR A SIMPLE LOADED WING

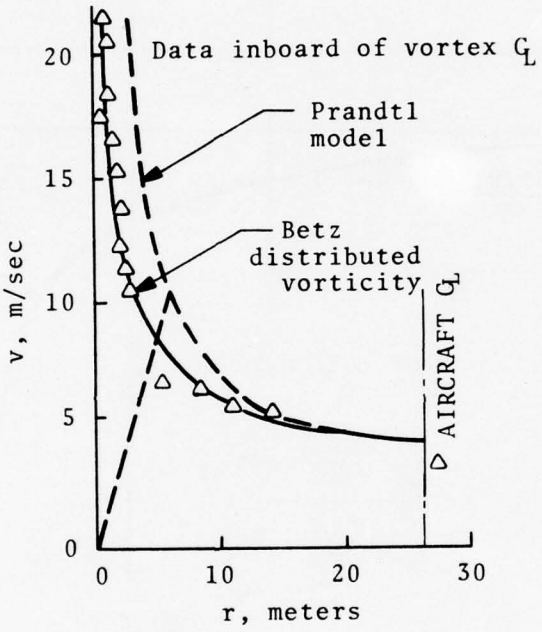


FIGURE 3-12. COMPARISON OF THE BETZ AND PRANDTL MODELS WITH MEASUREMENTS MADE IN THE WAKE OF A C-5 AIRCRAFT

swirl velocity distribution is compared with measurements made by Verstynen and Dunham (ref. 19) behind a C-5A aircraft. As can be seen, the Betz model predicts distributions which are in far better agreement than the Prandtl model.

3.2.2 Models of Vortex Structure

The Betz model described in the previous section is entirely inviscid and gives excellent correlation with data from flight tests for aircraft with continuous flaps (DC-7, DC-9, C-141, etc.). However, aircraft with segmented flaps (B-727, L-1011, DC-10, B-747, etc.) produce individual interior vortices when the flaps are extended and do not show as good agreement with measured vortex profiles (ref. 20). The merging of the multiple vortices is a turbulent interaction process and thus will require a viscid analysis. Nevertheless, it is desirable to use simpler models of the rolled-up vortex in many aspects of vortex analysis, including the effects of viscosity. Although many models representing vortex structure have been proposed, only a few are presented here. There is no general agreement on the equations describing the core structure. In fact, it appears that both viscous and inviscid models fit the test data reasonably well.

3.2.2.1 Rotational Structure of the Vortex - The general flow field of the viscous vortex is shown in Fig. 3-13. The dominant velocity is a swirling flow field having approximately circular streamlines. The tangential velocity along these streamlines varies from zero at the center to some maximum which may be 50 percent of the flight speed, and then, decreases approximately inversely with increase in radius. Thus, in the outer region, the flow corresponds to that of a potential vortex and is irrotational. The inner portion contains rotational flow with distributed vorticity.

In the literature the term core radius is used to define some characteristic distance from the vortex center. There are two natural definitions. First is to define the core radius as the radius at which the maximum tangential velocity occurs, the second is to define the core radius as the effective edge of the distributed

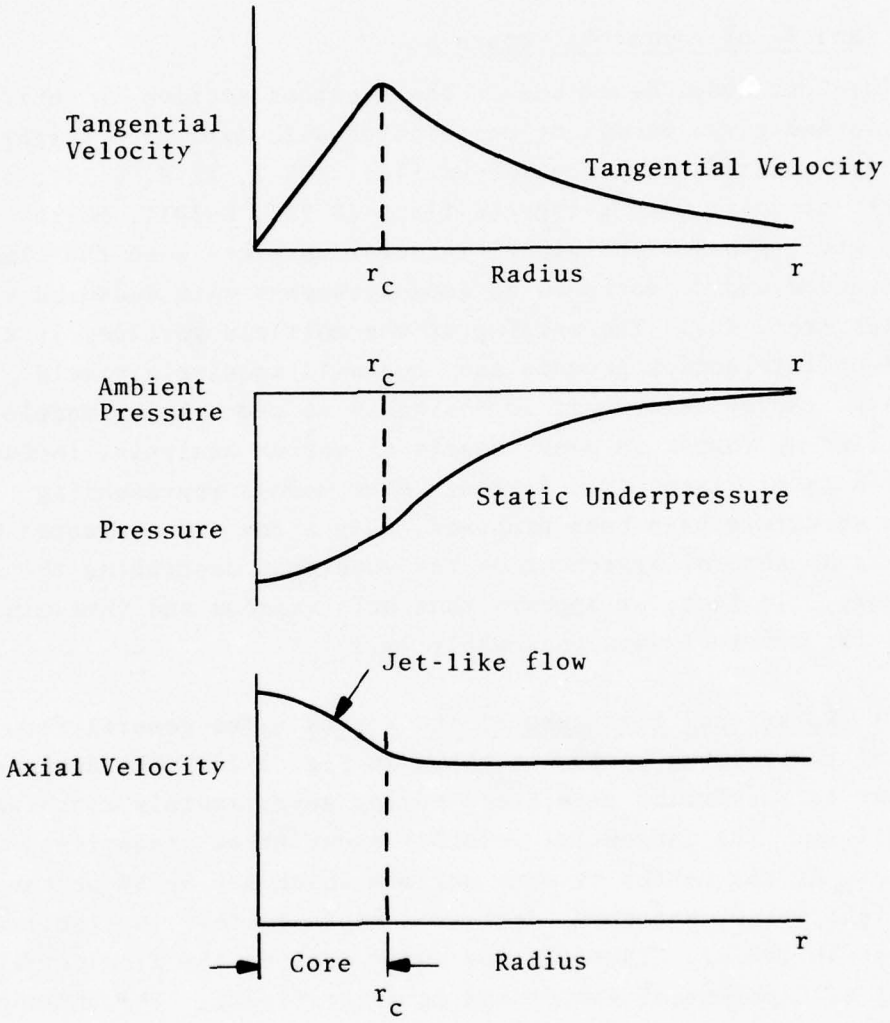


FIGURE 3-13. VELOCITY AND PRESSURE DISTRIBUTIONS IN A VISCOUS VORTEX

vorticity; i.e., beyond the core radius the flow is irrotational. Both definitions are useful, the first is the natural applied aerodynamics definition used to identify vortex hazard or an experimental velocity measurement, and the second is helpful in setting up theoretical fluid mechanical models of the flow.

The pressure gradient in the core is generated primarily by the centrifugal forces developed because of the tangential swirling flow. As a consequence, it is a function of the radial distribution of the tangential velocity. In general, the core pressure is lower than atmospheric (an underpressure); in the outer part, the pressure behaves like the inverse of the radius squared, while near the vortex center the effect is reduced by the slower tangential velocities. The underpressure also causes the air density in the vortex to be less than that in the ambient air.

The total pressure is constant in the irrotational portion of the flow where it is noted that the equilibrium relation between tangential velocity and pressure gradient implies an invariant total pressure for a potential vortex. In the inner region however, where the tangential velocity reduces to zero, a reduction in total pressure occurs. This is associated both with the dissipative process during the vortex development behind the wing as well as the fact that low-energy air from the wing boundary layer initially formed the vortex.

The simplest conceptual model for the trailing vortex is that of the potential vortex where the tangential velocity varies inversely as the radius. This is adequate in the outer irrotational portion of the flow, but gives unrealistic singularities near the vortex center. The most obvious method of removing the singularity is to consider a Rankine vortex. Here the tangential velocity varies as the radius for the inner portion and inversely as the radius for the outer region. If v_c is the tangential velocity at core radius r_c,

$$v(r) = v_c \, r/r_c \quad r < r_c \ , \tag{3.57}$$

and

$$v(r) = v_c \, r_c/r \qquad r \geq r_c \quad , \tag{3.58}$$

which is an irrotational vortex. All of the vorticity is contained within the core, and

$$\Gamma = 2\pi \, r_c \, v_c \quad . \tag{3.59}$$

The Rankine model does give regular velocity fields. It contains singularities in higher derivatives and gives a greatly over simplified vorticity distribution, but one which does contain some of the dominant features of vortical flow near the center with irrotational flow in the outer portion.

An improvement on the Rankine model is that given by Lamb in 1897 and represents the exact solution of the viscous Navier-Stokes equations for a two-dimensional line vortex in a laminar flow. The model is analytic; that is, all derivatives exist, and it forms a useful basic model. The tangential velocity distribution is

$$v = \frac{\Gamma}{2\pi r} \left[1 - \exp\left(-r^2/r_c^2\right)\right]. \tag{3.60}$$

The strength of the vortex at radius r is

$$\Gamma(r) = \Gamma \left[1 - \exp\left(-r^2/r_c^2\right)\right] . \tag{3.61}$$

The maximum tangential velocity occurs at $r = r_c$. For this model, the vorticity is not contained within a finite radius as in the Rankine model. Note that 63.2 percent of the vorticity is contained within $r = r_c$, and 98.2 percent of the vorticity is contained within $r = 2r_c$. The model suffers from its inherent assumption of constant viscosity. Experimental data show that portions of a vortex are turbulent with a greatly increased effective viscosity associated with turbulent flow.

The model of Owen (ref. 21) introduces an approximate model for the development of self-induced turbulence with time by making a number of rational assumptions relating to turbulence generation in the annulus dividing the irrotational from the rotational flow. Although a simple model containing a number of relations between turbulence mechanisms for which rather arbitrary constants have necessarily been defined, it seems to be supported by tests of widely varying scale. It should be noted that the method of Owen, although defining a core structure which does show development with time, does not contain terms which would give a temporal decay in vortex strength.

The dimensionless decay of maximum rotational velocity is predicted to vary inversely as the square root of time in Owen's model; recent tests (ref. 22) have indicated such a decay. However, Brown (ref. 23) suggests that the maximum rotational velocity should vary inversely as the one-third root of time for a vortex formed from a typical wing. The data of ref. 22 has sufficient scatter that it apparently could equally support this hypothesis.

A further model, also reasonably well supported by experiment, is that developed by Kuhn and Nielsen (ref. 24), where a turbulent core profile having a similar form to the profile of a turbulent two-dimensional boundary layer is developed. Based on the data of Hoffman and Joubert (ref. 25), the regions are defined as an inner region analogous to the laminar sublayer, an intermediate region with logarithmic circulation distribution (analogous to the law of the wall), and an outer region having a defect law analogous to the outer region of a turbulent boundary layer. The tangential velocity distribution is

$$v = v_c\left(r_c/r\right)\left[1 + \ell n\left(r/r_c\right)\right] \quad . \tag{3.62}$$

It is noted that this vortex model cannot apply over the whole range of r since setting r equal either to zero or a very large number lead to impossible results.

In comparing the various models, it must be remembered that the viscous transfer mechanisms within the vortex are still

improperly understood. It appears that frequently the flow is laminar near the center, but that there is an annular region of turbulence near the position of maximum core velocity. It is possible that the reason for conflicting results on turbulent and laminar flow regions is that these regions change as the vortex develops and that the initial turbulence as well as the ambient turbulence changes the initial core character for different configurations of a generating wing.

The importance of the core models is that they are necessary to provide quantitative predictions of the magnitude of the velocities induced by a vortex. It is well known that as the vortex ages these velocities reduce, but evidently in a nonlinear way with respect to time. For example, current test data imply that there is an initial plateau period during which the vortex velocities remain virtually constant for approximately 40 spans downstream distance. There is then a steady reduction in this velocity for about 80 spans, followed by a much more rapid decay.

The dispersion, dissipation, and decay must be driven by viscous and turbulent transfer mechanisms, within the core as well as in the ambient fluid surrounding the vortex. For any quantitative predictions some model of these mechanisms must be postulated. Thus, the turbulence structure in the core is of significant interest.

3.2.2.2 Axial Structure of the Vortex - The axial flow perturbation is generally small compared with the flight speed. Near the center of the vortex, there may be perturbations of the order of 15 percent of the flight speed. Perturbations in either direction have been observed, those in which the axial flow exceeds the flight speed (jet-like) as well as those in which the axial flow is lower than the flight speed (wake-like). For example, Marchman and Marshall (ref. 26) report experimental observations of a jet-like axial flow at high angles of attack and a wake-like flow at lower angles. This can be accounted for by the observation that, at least during the early states of vortex development, the

jet-like flow is connected with the induced drag while the wake-like flow (or velocity deficit) is associated with the profile drag. A simple equation relating the axial components caused by these different drag terms has been given by Brown (ref. 23). Theories have been proposed in which both jet- and wake-like axial flows occur at the same cross section at different radii, and there is limited evidence from flight tests with flow visualization that this situation can occur. It appears that the magnitude and sign of the axial perturbation depend upon complicated interactions related basically to the relative magnitude of the induced and profile drag of the wing. It is also apparent that the axial component can change from a jet-like to a wake-like flow and as the vortex ages it is always wake-like. The effect of axial flow on vortex transport and decay is secondary in importance to the tangential flow.

3.2.3 Experimental Measurements of Vortex Structure

It was determined early in 1970 that there was a need to investigate the vortex wake characteristics of large jet transport airplanes in conditions representative of terminal area operations. An investigation was conducted as a joint operation involving the Federal Aviation Administration's (FAA) National Aviation Facilities Experimental Center (NAFEC), the National Aeronautics and Space Administration (NASA), the Boeing Company, and the United States Air Force. The airplanes involved, flight test techniques used, and details of the results obtained are described in refs. 27-29.

NAFEC's part in the investigation included the acquisition of quantitative data on vortex structure for the Boeing 707, 727 and 747; McDonnell-Douglas DC8 and DC9; and the Lockheed C5A, using tower flyby and flow visualization. At the time of these early tests, a very limited number of sensors was available for the measurement of vortex airflow velocities. However, in view of the then-accepted theory of trailing vortices of fixed-wing airplanes (ref. 30), namely that the vortex core diameter was initially equal to 15 percent of the wingspan, the available instrumentation appeared to suffice for achieving the objective of the planned tests. It was subsequently shown in ref. 31 and in other literature

(including the individual reports for each aircraft type tested at NAFEC) that the vortex core diameter was frequently much smaller, especially in clean configurations, and the need for further testing using closer sensor spacing became apparent. Accordingly, further tower flyby tests were run using 3-, 1.2-, and 0.3-meter sensor spacing on the following airplanes: Boeing 707, 727, and 747; Lockheed C141, C5A, and L-1011; McDonnell-Douglas DC-9 and DC-10; and Convair 880. Tests were also run on the Douglas DC-7 using 1.2-meter sensor spacing. Flow visualization was also employed, using aircraft- and tower-mounted smoke generators. These tests have been reported individually (refs. 32 through 38), covering the airplanes listed (with the exception of the Lockheed C141, C5A and L-1011, on which only unpublished material exists).

Typical vortex visualization with tower-mounted smoke generators is shown in Fig. 3-14. Vortex tangential velocity data are shown in Figs. 3-15 through 3-20. It is noted that the landing configuration of the Boeing 747 gives a very large vortex core. In general, the tests showed that this characteristic is typical for aircraft with four wing-mounted engines. It is not so pronounced for the Lockheed L-1011 for which the two wing-mounted engines are located close to the fuselage. The effect is probably the result of wing loading caused by the absence of flaps behind the engines rather than by the effects of the engines.

3.2.4 Multiple Vortices

Up to this point, the discussion has considered the case of two trailing vortices - one for each wing tip. In the takeoff and landing configurations, additional vortices are generated from the flaps. In general, multiple vortices roll up into a single pair a short distance behind the generating aircraft. The effect is shown in Fig. 3-21. Therefore, the existence of a single pair of trailing vortices (as discussed in previous sections) is the condition of primary interest. However, it is instructive to examine the conditions which cause multiple vortices as well as the roll-up process for multiple vortices.

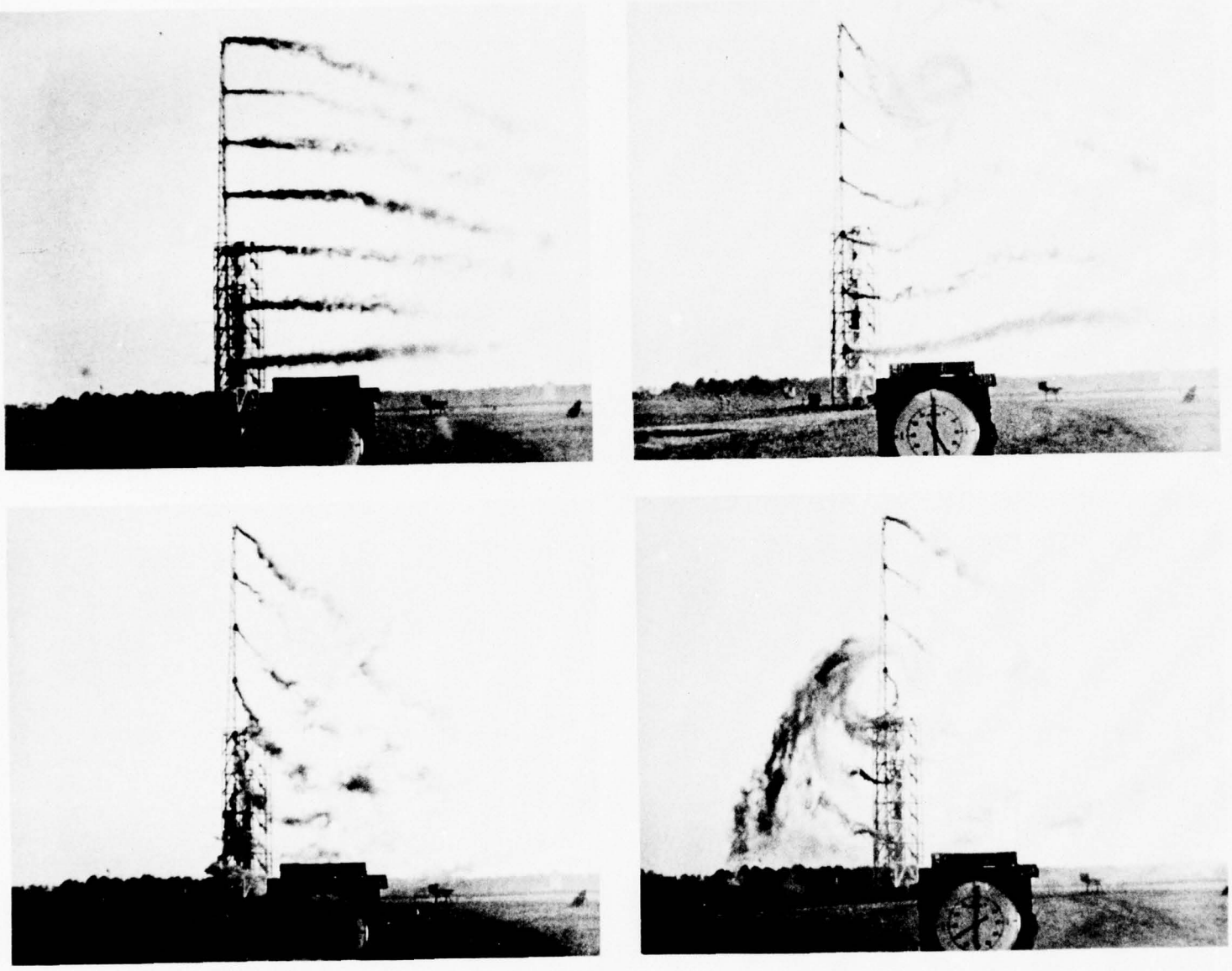


FIGURE 3-14. PHOTOGRAPHIC COVERAGE (16mm MOVIE) OF L-1011 VORTICES

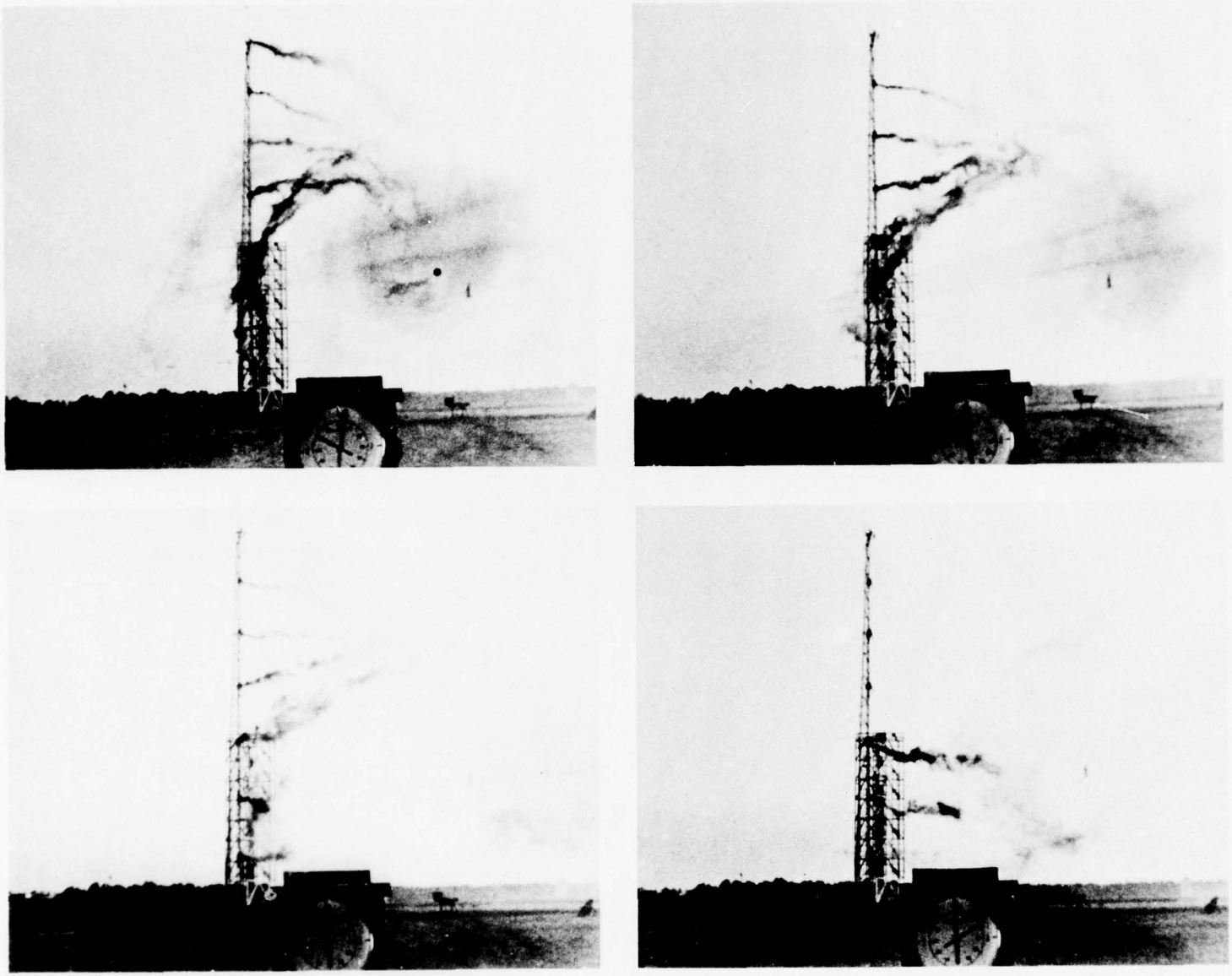


FIGURE 3-14. PHOTOGRAPHIC COVERAGE (16mm MOVIE) OF L-1011 VORTICES (CONCLUDED)

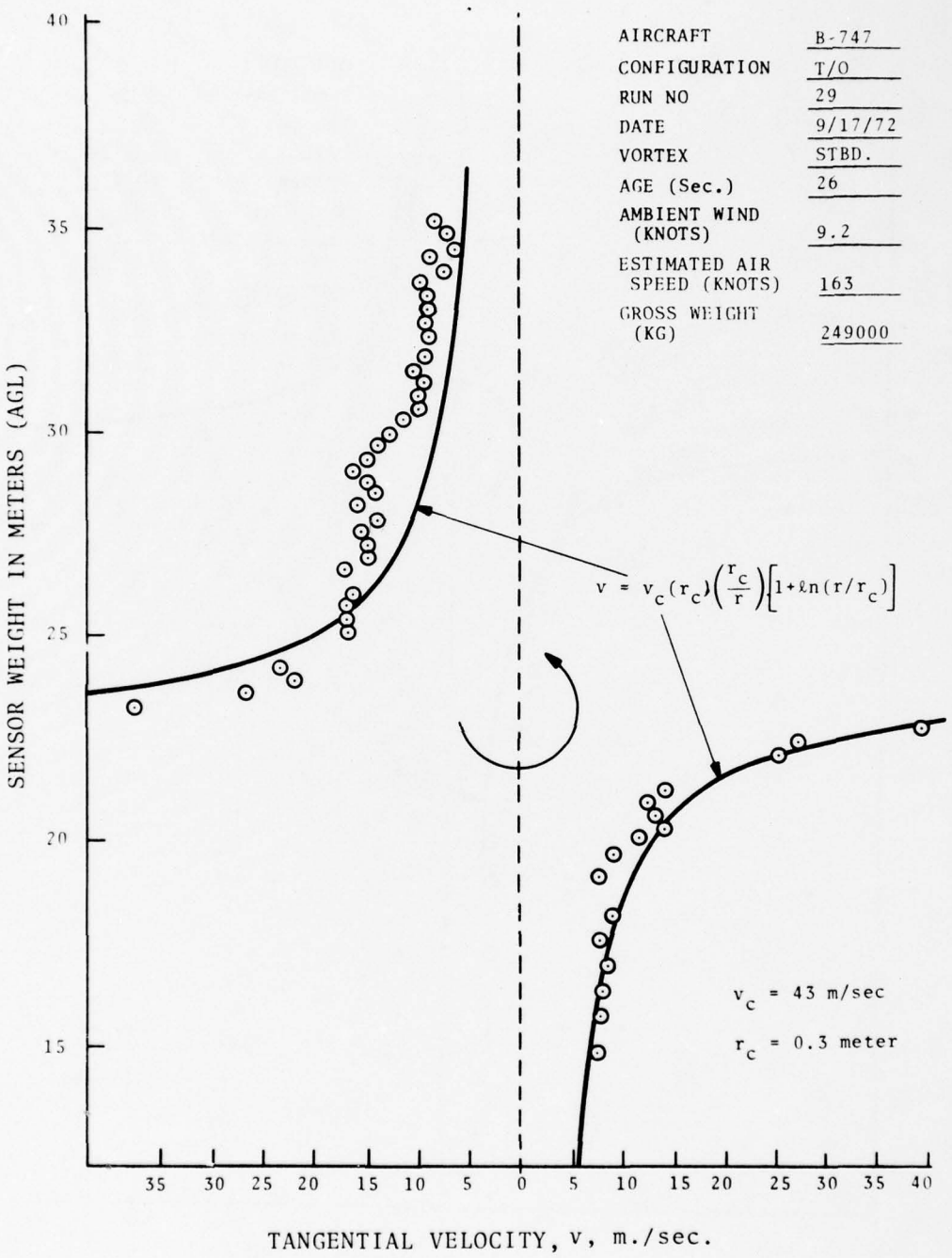


FIGURE 3-15. VORTEX STRUCTURE OF BOEING 747 IN TAKEOFF CONFIGURATION

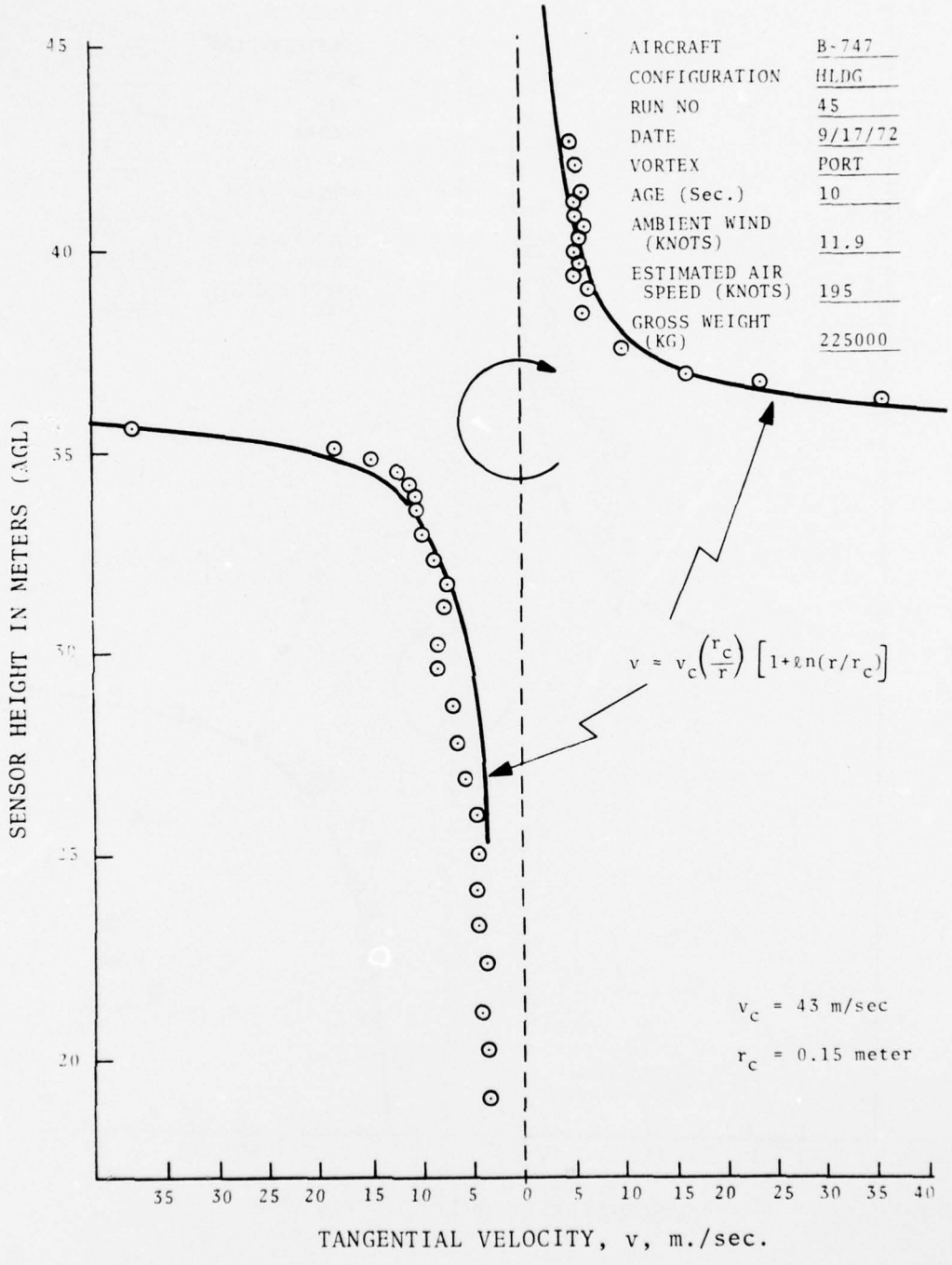


FIGURE 3-16. VORTEX STRUCTURE OF BOEING 747 IN HOLDING CONFIGURATION

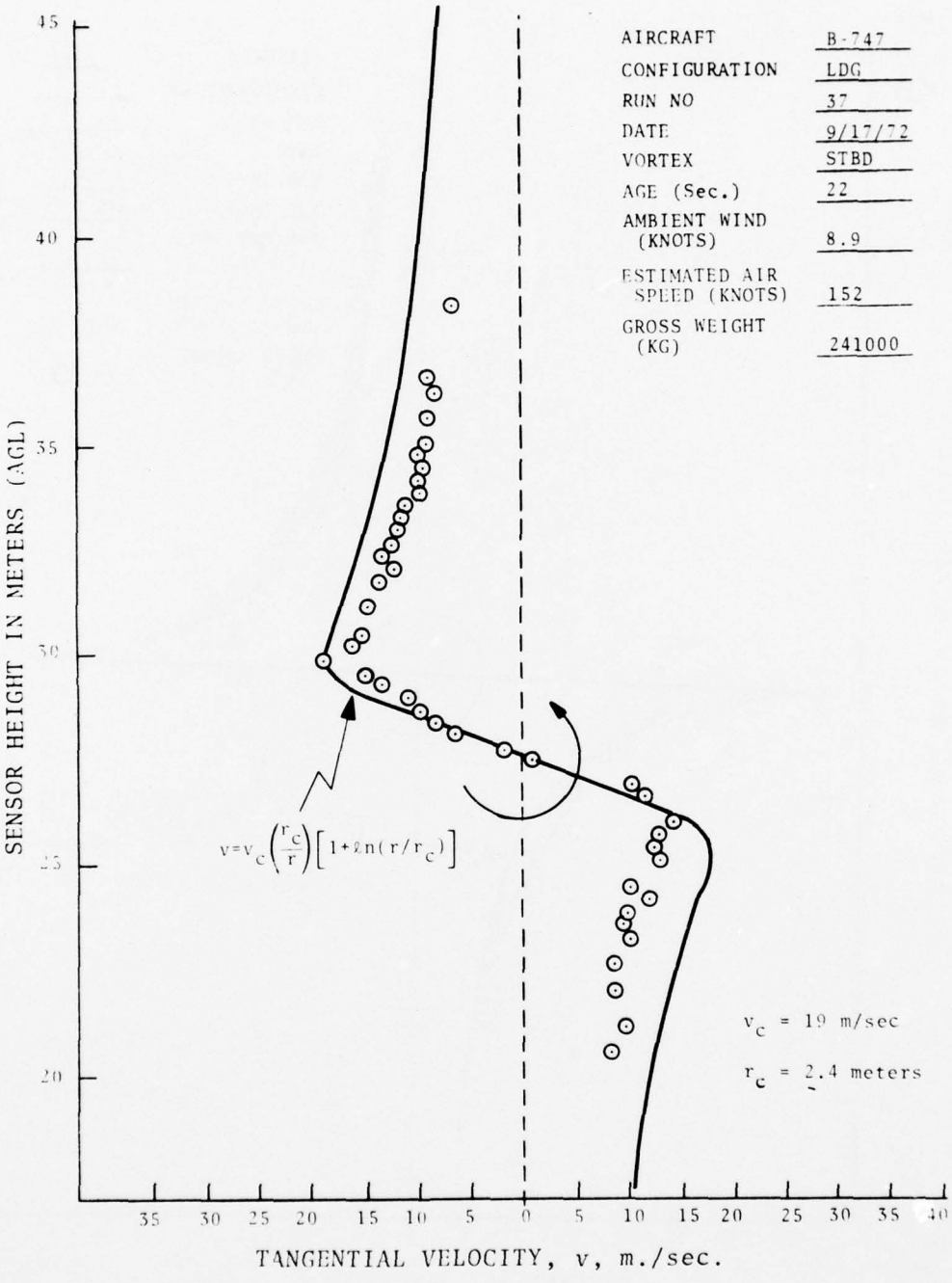


FIGURE 3-17. VORTEX STRUCTURE OF BOEING 747 IN LANDING CONFIGURATION

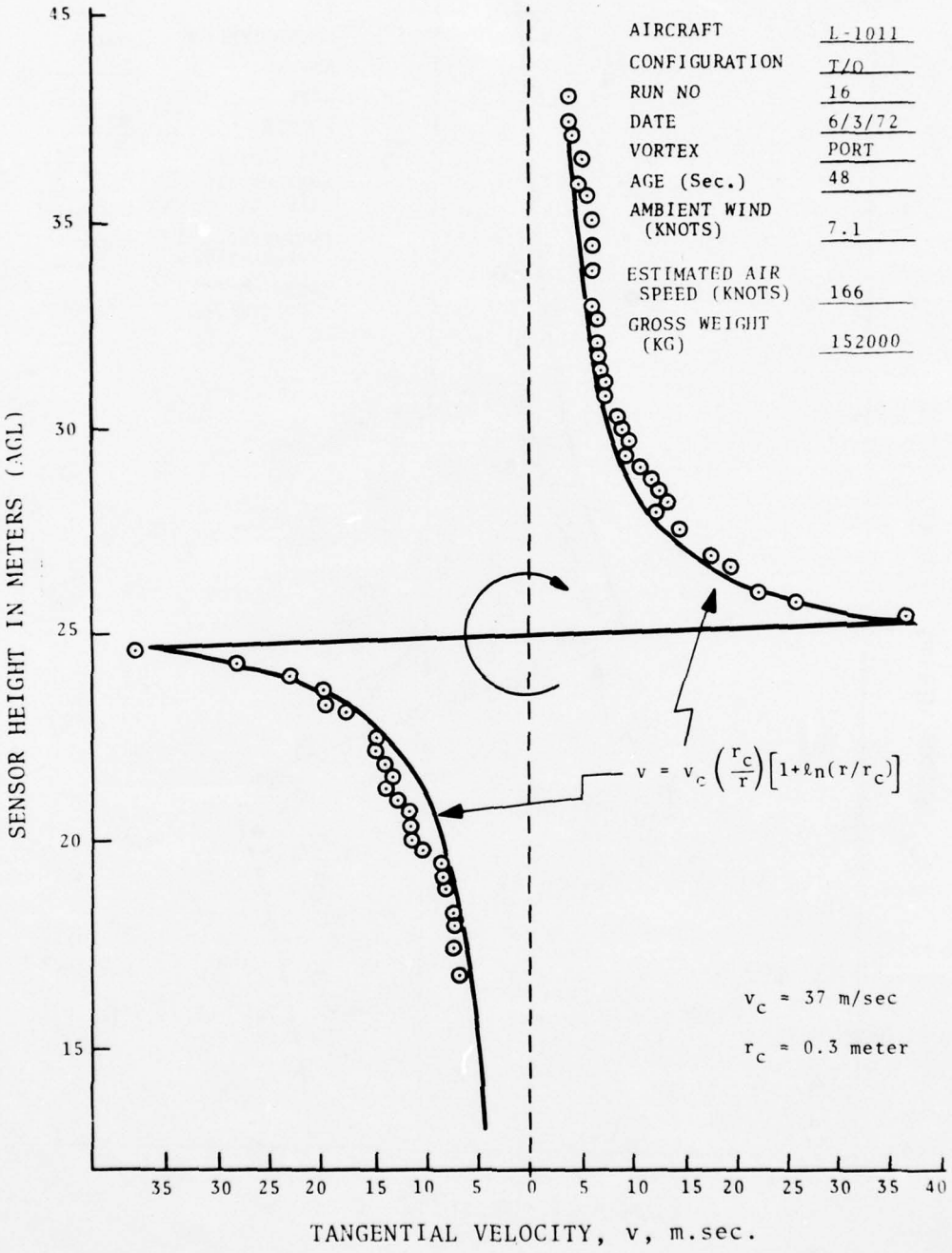


FIGURE 3-18. VORTEX STRUCTURE OF LOCKHEED L-1011 IN TAKEOFF CONFIGURATION

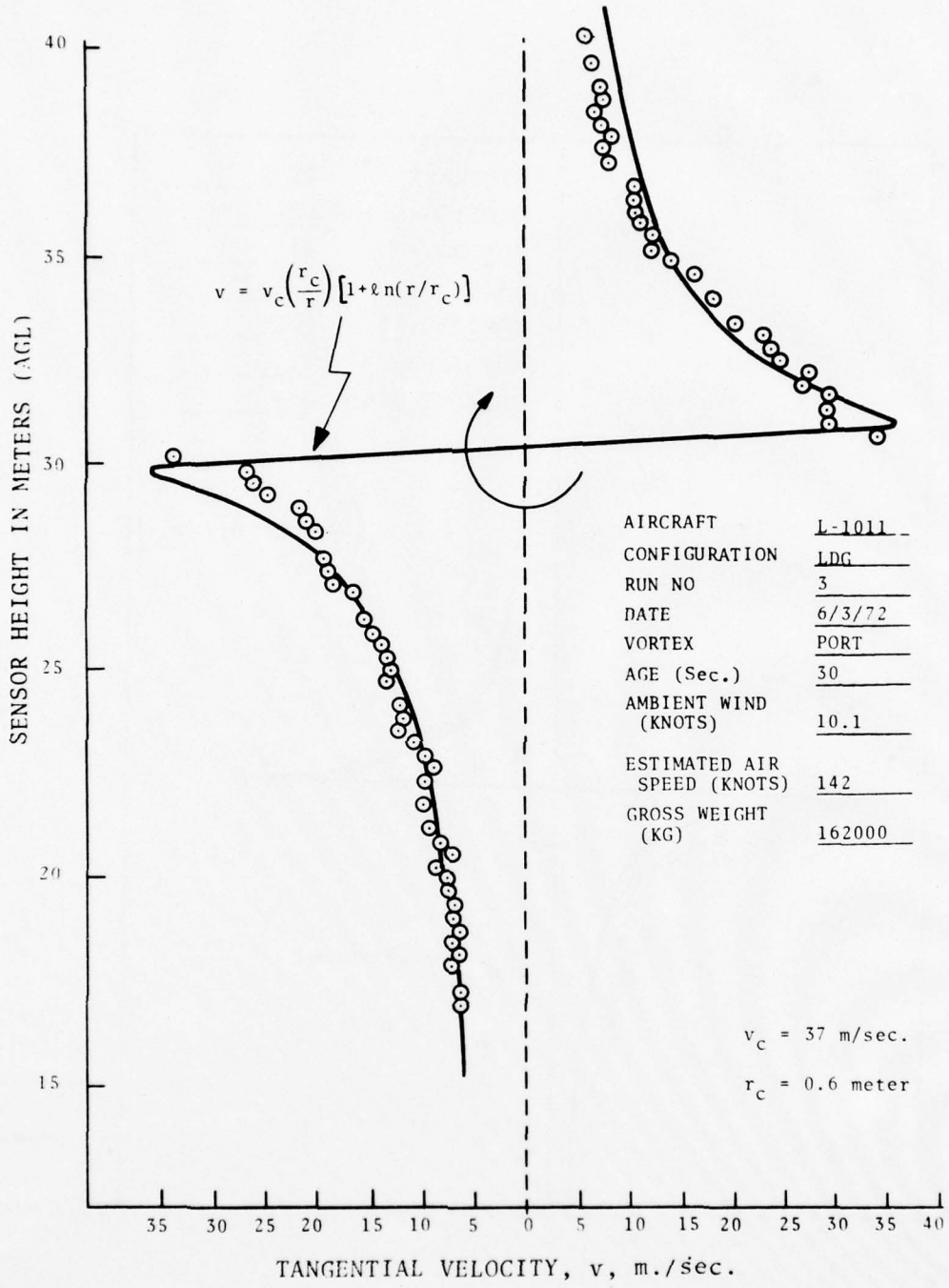


FIGURE 3-19. VORTEX STRUCTURE OF LOCKHEED L-1011 IN LANDING CONFIGURATION

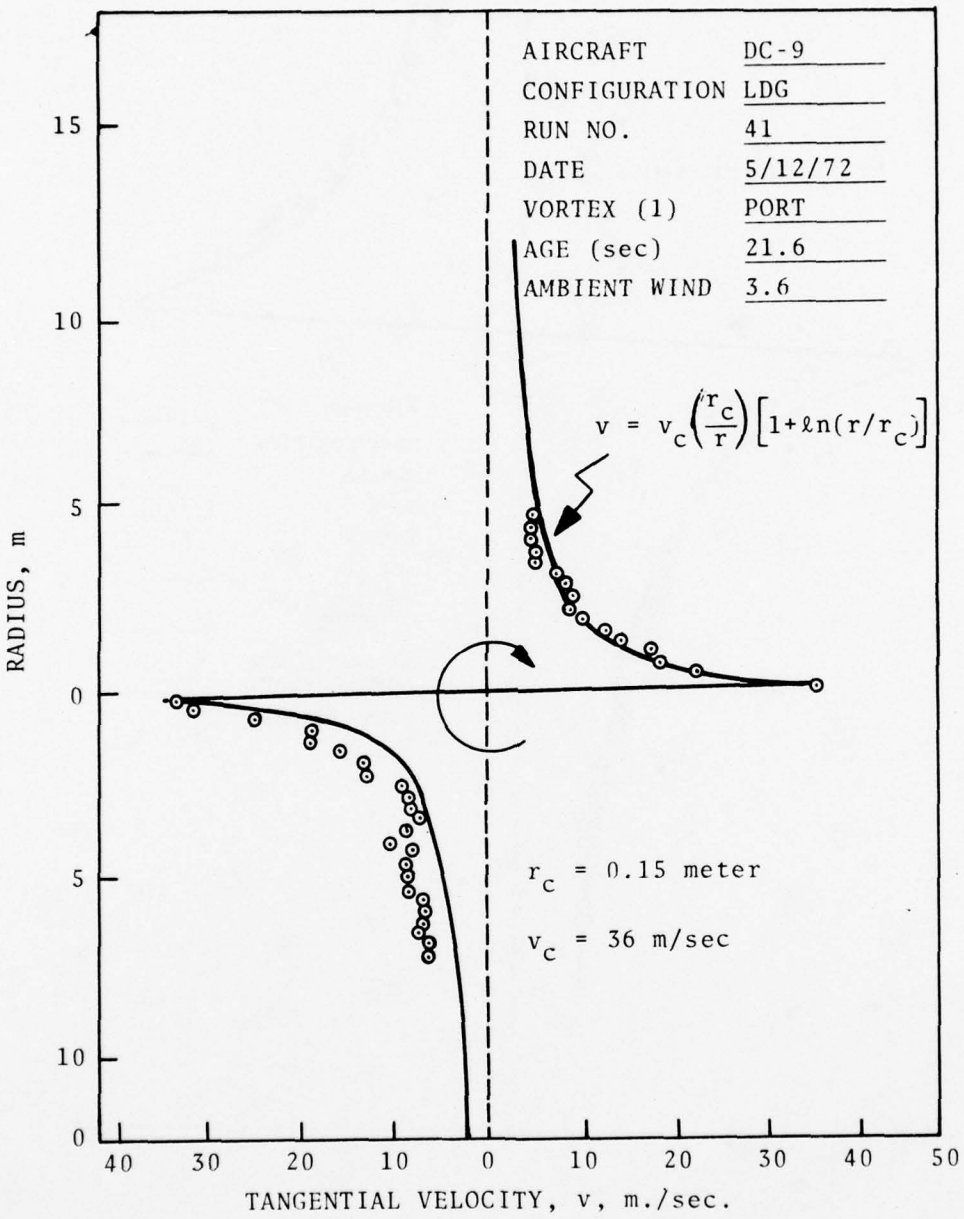


FIGURE 3-20. VORTEX STRUCTURE OF DC-9 IN TAKEOFF AND LANDING CONFIGURATIONS

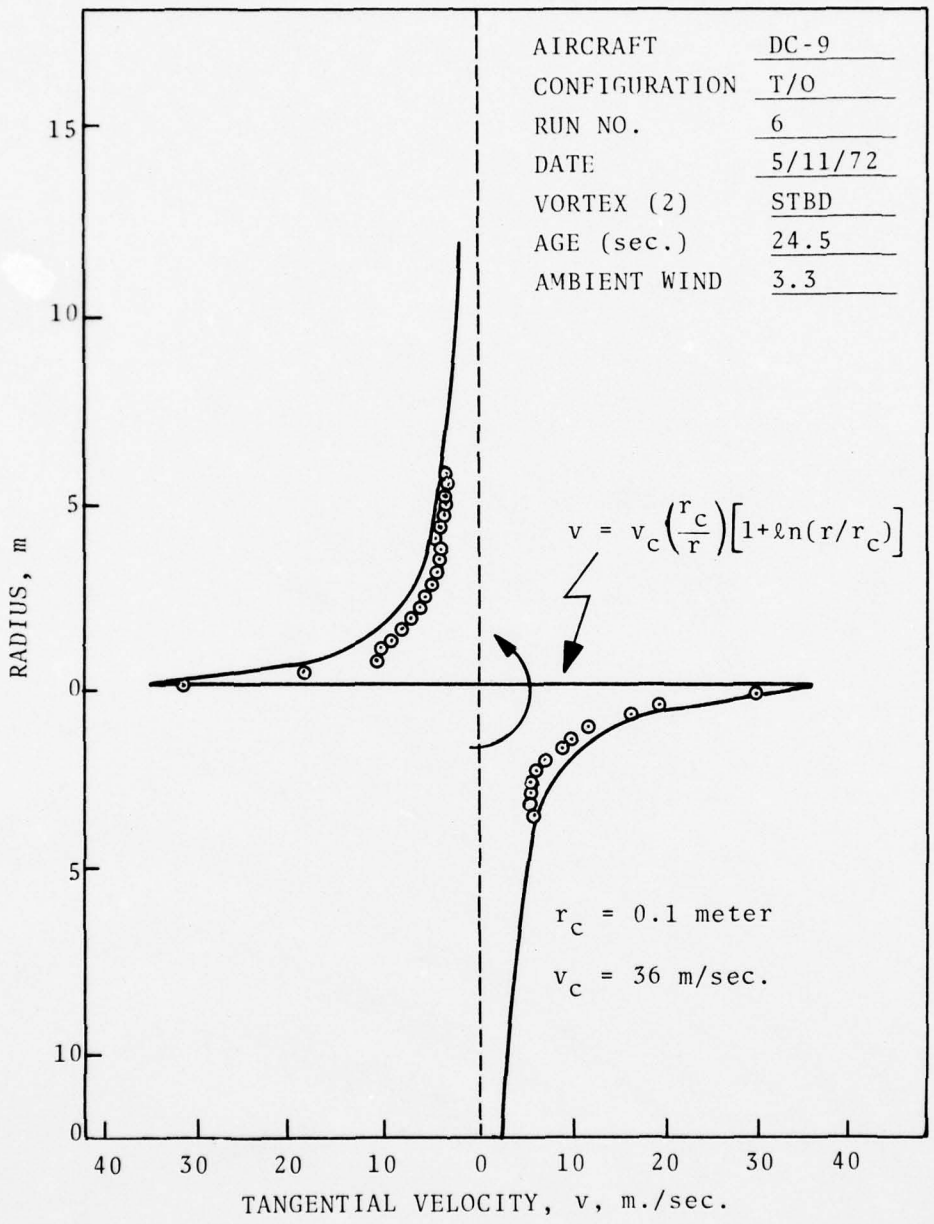


FIGURE 3-20. (CONTINUED)



FIGURE 3-21. B-747 WITH SIX SMOKE GENERATORS ILLUSTRATING ROLL-UP OF MULTIPLE VORTICES

The discussion of the roll-up phenomenon in Section 3.2.2 has considered wing load distributions whose trailed vortex sheets proceed to roll up from the tip with $r = \bar{y}(y) - y$ a monotonic function of y in the interval $0 \leq y \leq b/2$. This may not always be the case when the aircraft is in an unclean configuration (during landing and takeoff when flaps and gear are deployed). That r may not be a single-valued function of y is easily shown by a geometric argument. First, calculate the rate of change of r as y is varied. Differentiating equation (3.56) with respect to y yields

$$\frac{dr}{dy} = \frac{d\bar{y}}{dy} - 1 \quad , \tag{3.63}$$

and $d\bar{y}/dy$ is obtained from the definition of $\bar{y}$ in equation (3.54). Substituting into equation (3.29) yields

$$\frac{dr}{dy} = - \frac{(\bar{y}-y)}{\Gamma'} \frac{d\Gamma'}{dy} - 1 \quad . \tag{3.64}$$

To have a conventional roll up as y decreases from the tip, r increases. Therefore, a conventional rollup is possible if

$$- \frac{\bar{y} - y}{\Gamma'} \frac{d\Gamma'}{dy} < 1 \quad . \tag{3.65}$$

In Fig. 3-22, a load distribution typical of a flapped wing is shown. If the tangent to the load distribution at point P is drawn, it is easy to see that the line intersects the $\Gamma = 0$ axis at $y = y^*$. The distance $|y^* - y|$ is given by

$$|y^* - y| = \left| \frac{\Gamma'}{d\Gamma'/dy} \right| \tag{3.66}$$

The location of the centroid of the vorticity outboard of point P is $\bar{y}(y)$. Comparing the ratio of $|\bar{y} - y|$ and $|y^* - y|$ and equation (3.64), it is clear that

$$\left| \frac{\bar{y} - y}{\Gamma'} \frac{d\Gamma'}{dy} \right| = \left| \frac{\bar{y} - y}{y^* - y} \right| \quad . \tag{3.67}$$

A conventional roll-up has $y^* > \bar{y}$. Also $\bar{y} > y$ and $d\Gamma'/dy < 0$, so that

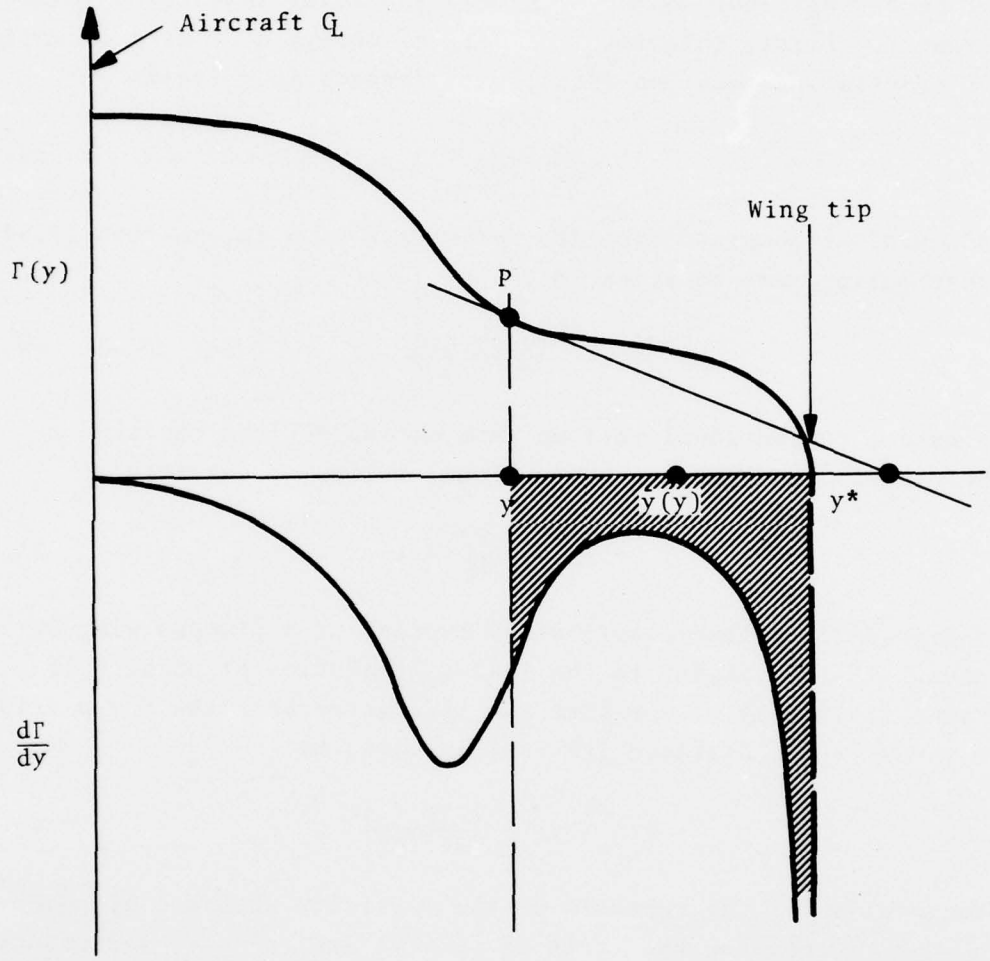


FIGURE 3-22. REPRESENTATIVE LOAD DISTRIBUTION OF A FLAPPED WING $\Gamma(y)$, UPPER CURVE, AND DISTRIBUTION OF SHED VORTICITY $d\Gamma/dy$ FROM SAME WING, LOWER CURVE

$$- \frac{\bar{y} - y}{\Gamma} \frac{d\Gamma'}{dy} = \frac{\bar{y} - y}{y^* - y} < 1 \ . \qquad (3.68)$$

Therefore, the condition for a single roll-up is seen to be that $y^*(y)$ always remains outboard of $\bar{y}(y)$ and y decreases from the tip.

For the load distribution in Fig. 3-22 any attempt to apply the roll-up relations much inboard of point P will result in multi-valued behavior of the function r(y). For this case, the behavior may be avoided if the roll-up of not one but two vortices is considered. In Fig. 3-23, the wake which will result from the flapped load distribution shown in Fig. 3-22 is sketched. If the Betz method is to be modified to compute the structure of "interior" vortices, it is clear from the sketch that some questions must be resolved; namely,

> Where does the roll-up originate? Or what portion of the sheet forms the center of the "interior" vortex? And where does the vortex sheet trailed from the wing divide itself into tip and "interior" vortices?

The answer to the "origin of roll-up" question is the station at which the sheet strength $-|d\Gamma'/dy|$ is maximum. Or, the maximum sheet strength corresponds to a maximum in vorticity which becomes the center of the vortex. The next answer, however, is not as straightforward. As an engineering approximation, the locations at which the minimums of the absolute value of sheet strength occur are taken to be the locations at which the vortex sheet divides itself. The assumptions are shown in Fig. 3-24, where the load distribution shown is one which will produce three vortices. Roll-up proceeds from the maximums of sheet strength at wing stations y_{mC}, y_{mB}, and b/2, and the sheet divides itself at the local minima of $|d\Gamma'/dy|$. The vorticity shed between points B and C rolls up into a fuselage vortex, between points A and B into a flap vortex, and outboard of A into a tip vortex.

The rule of thumb for dividing the lift distribution has been checked by Yates (ref. 39) who has calculated the initial inplane accelerations of a two-dimensional vortex sheet. His results are

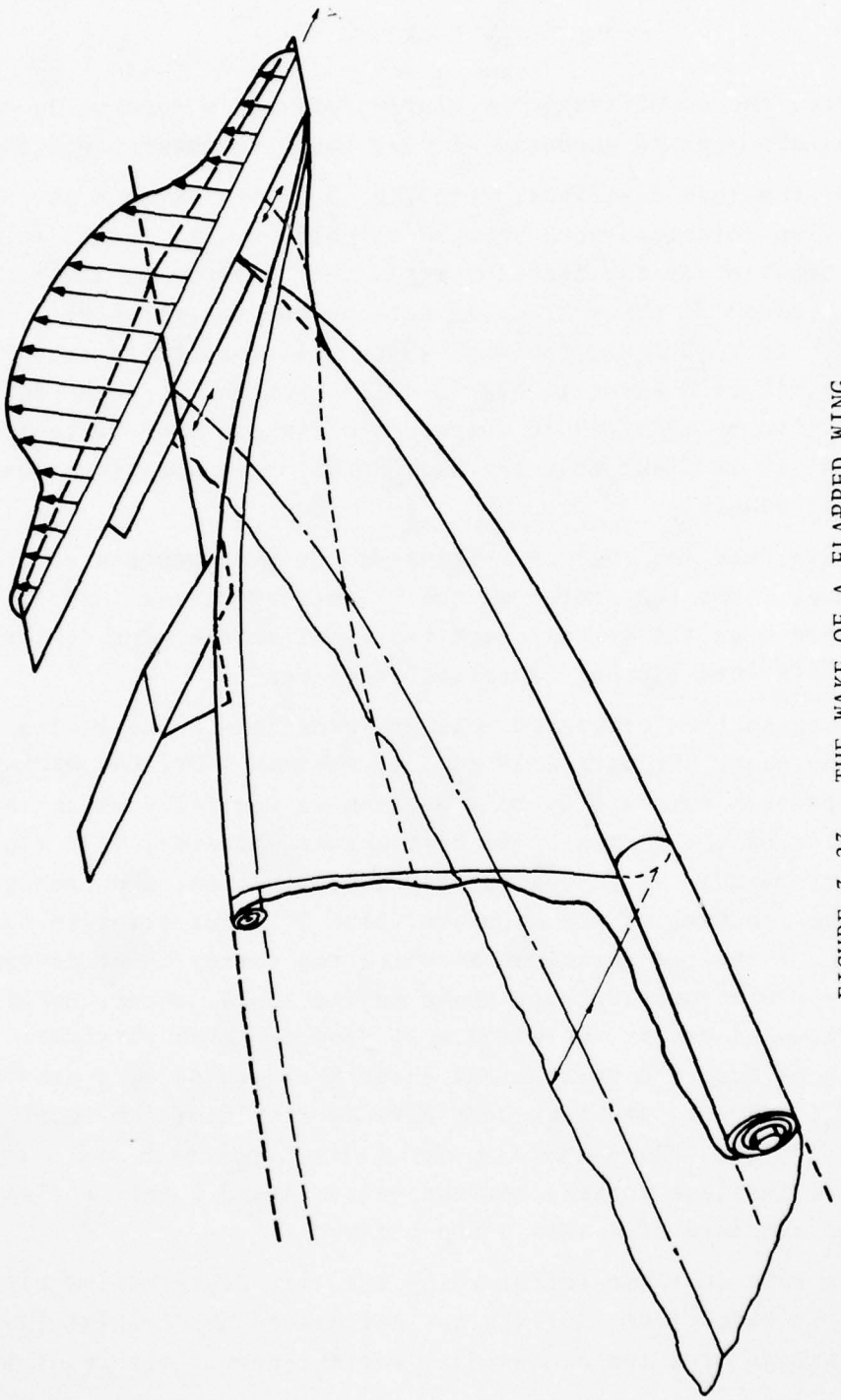


FIGURE 3-23. THE WAKE OF A FLAPPED WING

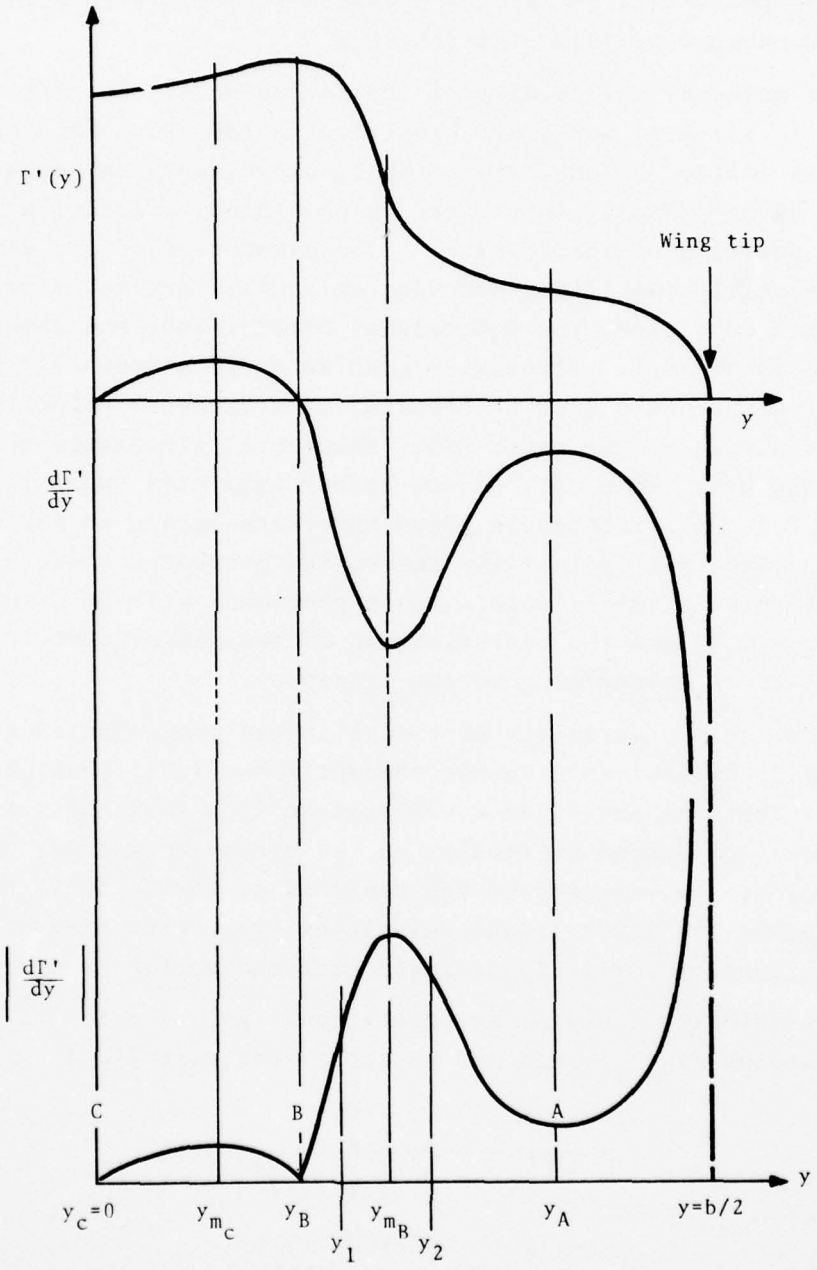


FIGURE 3-24. LOAD DISTRIBUTION WHICH WILL PRODUCE THREE VORTICES

given in Fig. 3-25 where it is shown that the centers of roll-up are in exact agreement. The locations at which the sheet divides are predicted within the accuracy generally associated with the computation of wing load distributions.

The mathematical details of the inclusion of the "interior" roll-up in the Betz model are presented in ref. 23. Each discrete vortex is modeled by one irrotational, two-dimensional point vortex insofar as one is only interested in obtaining information regarding the position of the vortices. The assumption of two-dimensionality is easily justified, provided streamwise gradients are small. Under this condition, the equivalence between time and downstream distance is $x = U_\infty t$. Streamwise gradients are necessarily of the order of W/U_∞, where W is a characteristic downwash velocity in the wake and is of the order Γ/b. Therefore, streamwise gradients are of the order of C_L/AR and are safety neglected under most circumstances. A qualification is added here with regard to the phenomenon of sinusoidal instability and vortex breakdown where axial gradients play a subtle role. These phenomena will be discussed in Section 3.4, and the approximation of two-dimensionality appears appropriate in determining vortex transport.

Treating the vorticity as though it was concentrated at a point is a somewhat more subtle concept whose justification lies in the fact that the motion of a vortex tube with straight vortex lines does not depend critically on the cross section of the tube. In addition, the velocity of the centroid of vorticity is proportional to the irrotational velocities from other discrete distributions of vorticity averaged with the vorticity over the area.

The velocity field of an irrotational point vortex of strength Γ at position (y_1, z_1) relative to the vortex centroid is

$$V = -\frac{\Gamma}{2\pi}\left[\frac{(z-z_1)}{(y-y_1)^2 + (z-z_1)^2}\right] , \tag{3.69}$$

$$W = \frac{\Gamma}{2\pi}\left[\frac{(y-y_1)}{(y-y_1)^2 + (z-z_1)^2}\right] . \tag{3.70}$$

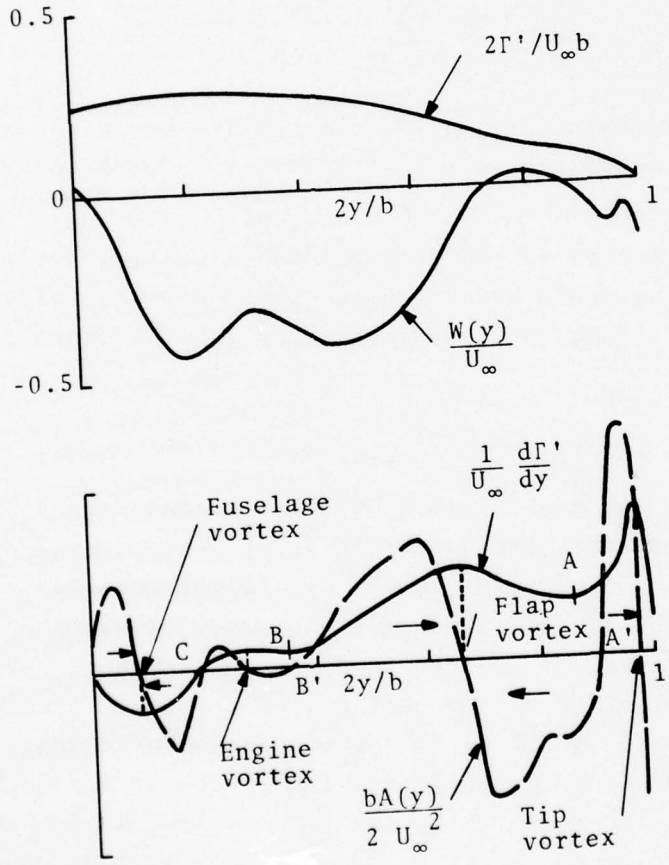


FIGURE 3-25. NORMALIZED LOAD ($2\Gamma/U_\infty b$), DOWN WASH [$W(y)/U_\infty$], SHEET STRENGTH ($1/U_\infty(d\Gamma/dy)$), AND ACCELERATION FUNCTION ($bA/2U_\infty^2$) DISTRIBUTIONS FOR A C-141 AIRCRAFT IN THE TAKEOFF CONFIGURATION

Therefore, the motion of the j^{th} vortex (equivalently, the centroid of the j^{th} vortex) in a system of n point vortices is given by

$$\frac{dy_j}{dt} = -\frac{1}{2\pi} \sum_{i(\neq j)}^{n} \frac{\Gamma_i (z_j - z_i)}{r_{ij}^2} , \tag{3.71}$$

$$\frac{dz_j}{dt} = \frac{1}{2\pi} \sum_{i(\neq j)}^{n} \frac{\Gamma_i (y_j - y_i)}{r_{ij}^2} , \tag{3.72}$$

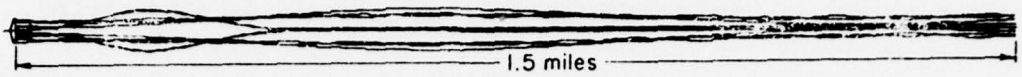
where $r_{ij}^2 = (y_i - y_j)^2 + (z_i - z_j)^2$. The exclusion in the summation is a consequence of the fact that a vortex induces no motion on its own centroid.

The calculation of the interaction of multiple vortices requires numerical computations. A computed wake geometry for a B-747 in the landing configuration (C_L = 1.2) is shown in Fig. 3-26.

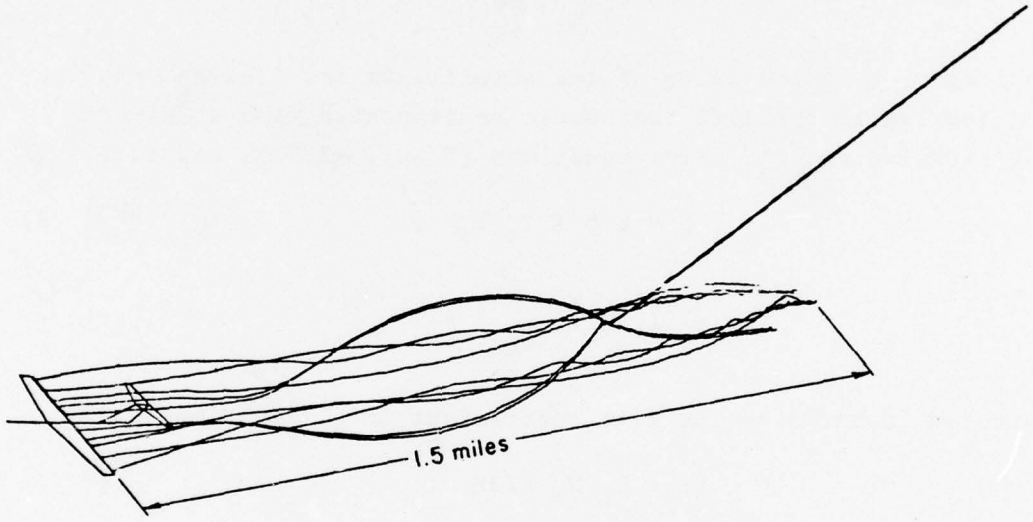
3.3 VORTEX TRANSPORT

There are two mechanisms by which a vortex pair ceases to reside in the flight corridor. The first - and most frequent - is the transport of the vortex out of the flight corridor caused by advection by the ambient wind or by interaction with the ground. The second mechansim is vortex aging and/or breakup. After roll-up is complete, viscous decay begins. The rate of decay is very slow during the first 30 to 60 seconds and accelerates thereafter. In this section it is assumed that the vortex is non-decaying (in the sense that the vortex strength is constant) during the transport process. The demise of the vortex pair will be considered in the next section.

The foundation for the discussion on vortex transport is set by reviewing vortex transport out of ground effect. Then the stages of vortex development are reviewed to determine the maximum time for which the assumption of constant vortex strength is



Top View



Oblique View

FIGURE 3-26. COMPUTED WAKE GEOMETRY FOR B-747 IN THE LANDING CONFIGURATION

reasonable. With this background, a simple model of vortex transport is presented. Phenomena which cause perturbations of the basic model are then discussed; these include the effects of wind shear and vortex buoyancy.

3.3.1 Vortex Descent Out of Ground Effect

Returning to the concepts presented in Section 3.1, a spanwise loading coefficient is defined as (cf., equation (3.23))

$$K = \frac{2}{b\,\Gamma_o'} \int_o^{b/2} \Gamma'(y)dy \quad . \tag{3.73}$$

Physically, K is the ratio of the actual lift for a given spanwise wing loading to the lift that would be generated with a uniform wing circulation, Γ_o'. From equations (3.20), (3.22), and (3.23),

$$L = \rho\, b\, K\, \Gamma_o'\, U_\infty \quad , \tag{3.74}$$

or

$$\Gamma_o' = \frac{W_A}{\rho\, b\, K\, U_\infty} = \Gamma. \tag{3.75}$$

Expressed in terms of the lift coefficient (cf., equation (3.23))

$$\Gamma = C_L\, U_\infty\, \bar{c}/2K \quad , \tag{3.76}$$

and the separation distance between the two vortices is

$$b' = 2\bar{y} = Kb \quad . \tag{3.77}$$

Therefore, the vertical speed for the vortex pair is

$$\frac{d\bar{z}}{dt} = -\frac{\Gamma}{2\pi(2\bar{y})} = -C_L\, U_\infty/4\pi\, K^2\, AR \quad . \tag{3.78}$$

$K = \pi/4$ for an elliptically loaded wing, and $K = 0.5$ for the linear spanwise wing loading example discussed in Section 3.1. Representative values of vortex parameters for selected aircraft are shown in Table 3-2. The time, t_s, shown in Table 3-2 will be discussed later.

TABLE 3-2. INFLUENCE OF SPANWISE LOADING ON THE INITIAL VORTEX PARAMETERS

Aircraft	Config.	U_∞ (m/sec)	C_L	K	b' (m)	$d\bar{z}/dt$ (m/sec)	t_s (sec)
B747	Takeoff	83	1.02	0.74	44.2	-1.8	195
AR = 6.96	Holding	113	0.66	0.80	47.8	-1.3	282
b = 59.7 m	Landing	75	1,23	0,70	41,8	-2,1	153
L-1011	Takeoff	85	1.07	0,78	36.8	-1,7	169
AR = 6.95	Approach	81	1.20	0.74	35.0	-2.0	134
b = 47.2 m	Landing	73	1,51	0,71	33,5	-2,5	104
DC-10	Takeoff	78	1,21	0.63	29.8	-2.8	83
AR = 6.95	Approach	74	1.20	0.62	29.3	-2.7	85
b = 47.2 m	Landing	70	1.37	0.62	29.3	-2.9	78
B-727	Takeoff	66	1.59	0.70	23.0	-2.4	77
AR = 7.20	Holding	105	0.60	0.67	22.1	-1.6	112
b = 32.9 m	Landing	64	1.64	0.67	22.1	-2.6	67

For the basic vortex transport calculations, the Rankine vortex model is used:

$$v(r) = \Gamma\, r/2\pi r_c^2 \qquad r < r_c \quad , \tag{3.79}$$

and

$$v(r) = \Gamma/2\pi r \qquad r \geq r_c \quad . \tag{3.80}$$

The basic assumption of vortex transport is that the transport velocity of each vortex is the velocity of the surrounding velocity field evaluated at the centroid of the vortex. The velocity field is composed of ambient wind and the velocity imposed by other vortices. Thus, equation (3.80) can be used to calculate the mutual induction of vortices upon each other if r_c is less than the separation distance between the vortices. Equation (3.78) comes from the Rankine vortex assumption. The vertical velocity of each vortex of the pair is given by the tangential velocity field of the other vortex at $r = 2\bar{y}$, the separation distance between the vortices.

Before proceeding to develop the equation of vortex transport by the mutual induction of the vortex pair, first examine vortex development to ascertain the time period for which the constant vortex strength assumption is reasonably valid. After the wing vortex sheet has rolled up, the trailing system consists of a pair of vortices of finite rotational core area, but with a core radius a relatively small fraction of the vortex span. If the vortex pair is immersed in a still, homogeneous inviscid flow, the pair is convected downward at a velocity $\Gamma/2\pi b'$. The classical analysis shows that there is a closed recirculating mass of air, of roughly oval proportions, associated with the concentrated vortex pair, and that the cell is convected downward at a uniform speed. Flow exterior to the cell never enters it. Thus a long vortex pair, which may be regarded as substantially two-dimensional, will move downward in an unbounded fluid with constant velocity for all times.

In real flows, this situation does not persist indefinitely, and most experiments show that the rate of descent decreases and

finally approaches zero (even out of ground effect). This is caused by diffusion of core vorticity by some combination of laminar and turbulent viscosity, and it will occur even in homogeneous (unstratified) flows. Much effort has gone into explaining and quantifying the effect, but the subject still remains controversial. A rational interpretation of the effect, coupled with careful observations, which greatly assists explanation of the effect, has been put forward by Maxworthy (ref. 40).

Maxworthy conducted experiments with vortex rings in water, using various visualization techniques to identify where the flow went. When the vorticity was relatively well distributed in the ring he observed that the outer flow was entrained into the back of the cell, causing an increase in the cell volume. At the same time a portion of the cell vorticity was shed into the wake, removing both vorticity and momentum from the cell. The combined effect was to increase the cell size and to reduce its propagation velocity.

The mechanism of mass entrainment is important for further development of the vortex transport. Figure 3-27 shows a sketch of the vortex flow field, in coordinates fixed at the core centers, so that the outer flow is represented by a uniform but unsteady flow from below. The cell has a well defined stagnation point, A, and over the front portion, a well defined cell boundary, A-B. Across this boundary, the pressure and velocity fields of inner and outer flows are continuous, the only discontinuity being between the inner vortical fluid and the outer irrotational flow. Because of both laminar and turbulent effects, the vorticity of the inner vortical flow is transferred to the outer flow, and as a consequence the total pressure of the flow is reduced. Thus after passing the maximum velocity point near B, the outer flow, contained approximately by the stream tube DC, is unable to recover sufficient velocity to rejoin the outer flow at the rear, but remains as part of the stationary cell. Thus, the cell size is increased. At the same time, a neighboring stream tube EF acquires a smaller amount of vorticity and suffers less pressure reduction

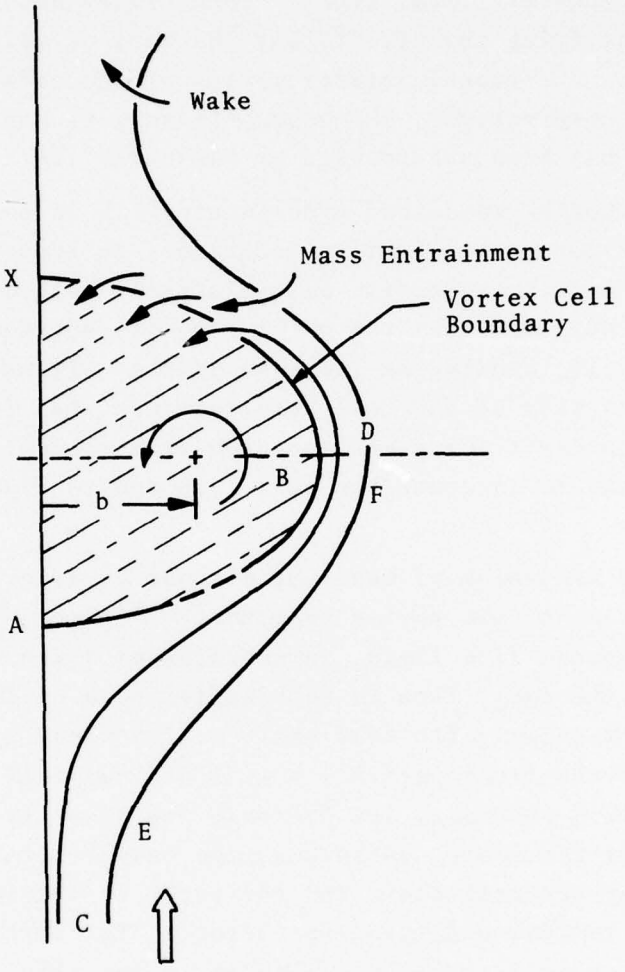


FIGURE 3-27. VISCOUS EFFECTS ON VORTEX CELL

so that it does depart from the cell at the rear, but at a lower than free stream total pressure. This portion develops into a wake behind the cell.

Thus, the same process causes entrainment of the outer flow into the cell and a detrainment (removal) of some of the cell vorticity and momentum. A further process occurs on the centerline of the cell, AX. Here vorticity is annihilated by diffusion from the left and right cells. Thus, three vorticity transfer mechanisms occur and the overall effect controls the cell dynamics.

Maxworthy showed that initially the vortex shedding to form the wake was extremely weak since the cell vorticity at the boundary was quite weak. Thus although the cell grew in size, it did not lose momentum, and the impulse was conserved. In these circumstances, the main vorticity loss occurred along the centerline and was small, and there was minimal wake momentum loss. During the later stages in growth, when more vorticity is present near the boundary between the inner and outer flows, the wake develops. Vorticity and momentum are shed from the cell and thus the momentum in the cell decreases while the cell size increases. Both of these effects contribute to the reduction in speed and the final complete annihilation of the cell momentum for the two-dimensional vortex observed by Maxworthy. It is noted that for a three-dimensional vortex pair such as an aircraft wake, vortex annihilation caused by three-dimensional effects almost always precedes the two-dimensional vortex annihilation.

It must be noted that Maxworthy's experiments were conducted with vortex rings at extremely low Reynolds numbers for which the flow was certainly laminar. However, further unpublished flow visualization tests with finite wings also exhibited a detrained wake. These experiments were also performed at very low Reynolds numbers. It is, however, possible that during the later stages of development of an aircraft trailing vortex system that similar processes of mass entrainment and momentum detrainment occur. For laminar transfer, the time scales would be too long to be of interest, but if the transfer is assumed turbulent, it may be possible to account for some of the observed effects. Thus, it

appears very probable that the later development of a vortex pair follows qualitatively the stages described by Maxworthy but with an additional initial stage. The three stages are postulated as shown in Figure 3-28.

Stage I - The Inviscid Cell: Here the vorticity is confined to well within the cell boundary. The cell boundary is defined as the streamline between the flow which remains with the vortex pair and that which remains with the ambient air. On the boundary itself there will be no laminar mass or momentum transfer (since there is no distortion) and turbulent transfer will have no net effect since both inner and outer flow have the same total pressure. In these circumstances, the core size is less than the cell size and the inviscid cell model will be a good representation of the dynamics. The time rates of change of cell size and vortex strength are zero; the propagation velocity $d\bar{z}/dt$ is constant.

Since the inviscid cell model (equation (3.58)) is the basic model to be used in the model for vortex transport in ground effect, it is important to make an approximation of the time for which the inviscid cell model is valid. Experimental measurements (refs. 19 and 41) indicate that the vortex core grows because of turbulent diffusion at the core boundary and can be predicted from Lamb's turbulent vortex model for the core growth as

$$r_c(t) = \left(r_c^2(0) + 5.04\ t\ \nu_T\right)^{1/2} \quad , \tag{3.81}$$

where $r_c(0)$ is the initial core radius and ν_T is the turbulent eddy kinematic viscosity. It follows that the time required for the core to grow sufficiently such that the cores overlap each other and vorticity detrainment is initiated is

$$t_s = \frac{\left(\frac{b'(t)}{2}\right)^2 - r_c^2(0)}{5.04\ \nu_T} \quad . \tag{3.82}$$

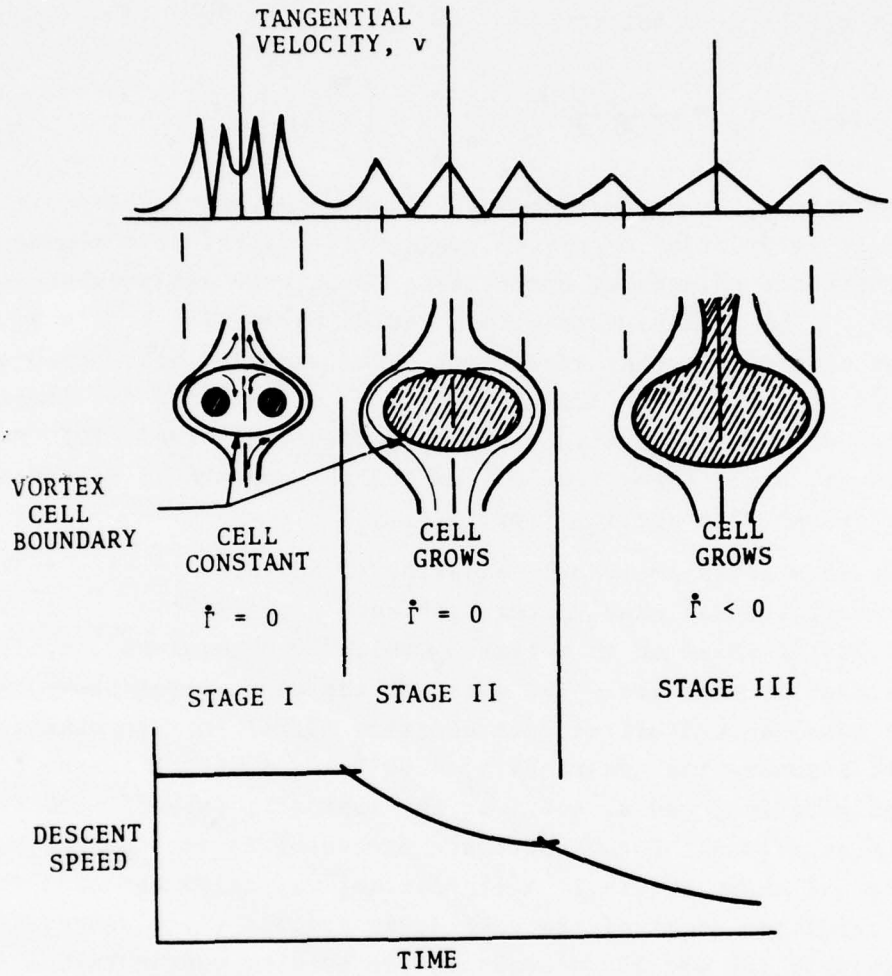


FIGURE 3-28. VORTEX CELL STAGES

This expression can be reduced further using equations (3.76) and (3.77) and the empirical expressions relating the eddy kinematic viscosity coefficient and initial vortex core radius, $a_1 = \nu_T/\Gamma$ and $a_2 = r_c(0)/\bar{c}$, to obtain

$$t_s = \frac{K^3 b\, AR}{10.08\, a_1\, C_L\, U_\infty} \left[1 - \left(\frac{2a_2}{K\, AR} \right)^2 \right] . \qquad (3.83)$$

The parameter a_1 is approximately 10^{-3} based on model tests (ref. 41) and is an order of magnitude smaller for flight test measurments where the effects of atmospheric turbulence are present (ref. 19). The initial vortex core radius parameter, a_2, is a function of aircraft characteristics. For example, measurements conducted using the C-5A indicate that $a_2 \sim 0.1$ and 0.2 for flaps-up and flaps-down flight configurations, respectively (ref. 19). For the DC-9, a_2 also ranges from 0.1 to 0.2 but appears to be independent of the flap setting (ref. 37).

The relationship given by equation (3.83) demonstrates that the constant initial wake vortex sink rate given earlier in equation (3.78) is valid up to a time t_s which is determined largely from aircraft parameters. The onset of the wake vortex slow down process has been calculated from equation (3.83) for representative aircraft assuming the constants $a_1 = 10^{-3}$ and $a_2 = 0.1$ in the holding configuration, and $a_2 = 0.2$ in the approach, takeoff, and landing configurations. The results are presented in the last column in Table 3-2 shown earlier. A significant variation can be noted in the predicted onset of the wake decay process which ranges from approximately 100 and 300 seconds in the holding configuration to 80 to 200 seconds in the landing, takeoff, and approach configurations for the aircraft considered. The times are sufficiently long so that vortex strength may be considered to be constant for the transport process. However, if the vortex persists in the flight corridor for times greater than t_s in Table 3-2, vorticity decay must be included in any consideration of vortex transport past t_s.

Stage II - The Entraining Cell: As the core vorticity diffuses and approaches the cell boundary, the first process (of mass entrainment) occurs, and the cell grows; $\dot{\Gamma} = 0$. The propagation velocity reduces slightly from the inviscid value because of greater vortex separation resulting from cell growth.

Stage III - The Decaying Cell: During the later stages, substantial mass entrainment and momentum and vorticity shedding occur, causing a wake to develop behind the vortex pair. Of course, various catastrophic instabilities usually develop before the complete decay has occurred.

3.3.2 Vortex Transport by Mutual Induction in Ground Effect

The primary mechanism of vortex transport is mutual induction – vortex motion caused by each vortex being immersed in the velocity field of the other vortex. The ground effect is included by "image vortices" as shown in Fig. 3-29. The image vortices are imaginary vortices whose presence creates the same effect as the ground plane, thereby obviating the need to otherwise model the ground plane.

The notation adopted is that Γ_1, Γ_2, Γ_3 and Γ_4 are the circulations of the vortices and (Y_1, Z_1), (Y_2, Z_2),..., are the spatial coordinates of the vortices. The cross runway freestream velocity component is V_∞. The coordinate system is a right-hand coordinate system with the positive x-axis out of the plane of the paper. Therefore Γ_1 is negative and Γ_2 is positive.

By definition, for the image vortices

$$\Gamma_3 = -\Gamma_1 \quad , \tag{3.84}$$

$$\Gamma_4 = -\Gamma_2 \quad , \tag{3.85}$$

$$Z_3 = -Z_1 \quad , \tag{3.86}$$

$$X_3 = X_1 \quad , \tag{3.87}$$

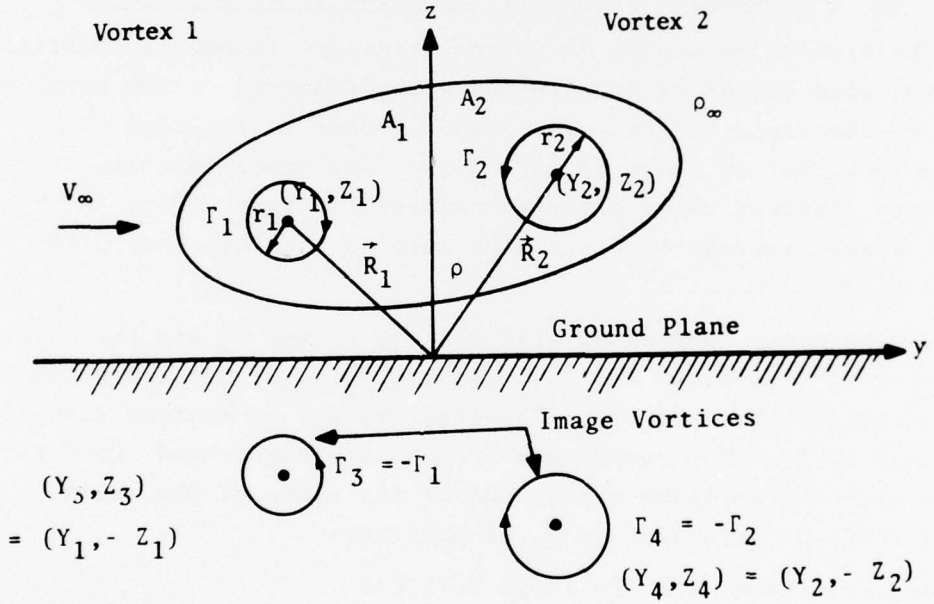


FIGURE 3-29. GEOMETRY OF THE PREDICTIVE WAKE VORTEX TRANSPORT MODEL

$$Z_4 = - Z_2 \quad , \tag{3.88}$$

$$X_4 = X_2 \quad . \tag{3.89}$$

The advection of each vortex is caused by each vortex being immersed in the velocity field of the other vortices. Let V and W be the velocity components in the vortex field in the y and z directions, respectively. Both V and W are functions of position in the velocity field. The contribution to the velocity field by each vortex is given by the Rankine model (equation (3.79)). The velocity field at any point is given by the sums of the velocity fields of the individual vortices. A vortex does not contribute to the velocity field at its centroid. The contribution to the velocity field at the centroid of vortex 1 by vortex 3 is

$$V = \Gamma_3/2\pi\left(Z_1 - Z_3\right) = \Gamma_1/4\pi Z_1 \quad , \tag{3.90}$$

$$W = 0 \quad . \tag{3.91}$$

The contribution to the velocity field at the centroid of vortex 1 by vortex 2 is

$$V = \left[\frac{\Gamma_2}{2\pi\left(\left(Z_2-Z_1\right)^2 + \left(Y_2-Y_1\right)^2\right)^{1/2}}\right] X \left[\frac{Z_2 - Z_1}{\left(\left(Z_2-Z_1\right)^2 + \left(Y_2-Y_1\right)^2\right)^{1/2}}\right] . \tag{3.92}$$

The term in the first set of brackets is the tangential velocity (cf., equation (3.79)), and the term in the second set of brackets is the cosine of the angle between the tangential velocity and the positive y-axis. Similarly,

$$W = \left[\frac{\Gamma_2}{2\pi\left(\left(Z_2-Z_1\right)^2 + \left(Y_2-Y_1\right)^2\right)^{1/2}}\right] X \left[\frac{-\left(Y_2 - Y_1\right)}{\left(\left(Z_2-Z_1\right)^2 + \left(Y_2-Y_1\right)^2\right)^{1/2}}\right] . \tag{3.93}$$

The term in the first set of brackets is the tangential velocity and the term in the second set of brackets is the cosine of the angle between the tangential velocity and the positive z-axis.

Similarly, the contribution to the velocity field at vortex 1 by vortex 4 (remembering $Y_4 = Y_2$ and $Z_4 = -Z_2$ and $\Gamma_3 = \Gamma_2$) is

$$V = \left[\frac{-\Gamma_2}{2\pi\left(\left(Z_2+Z_1\right)^2 + \left(Y_2-Y_1\right)^2\right)^{1/2}}\right] \times \left[\frac{-\left(Z_1+Z_2\right)}{\left(\left(Z_2+Z_1\right)^2 + \left(Y_2-Y_1\right)^2\right)^{1/2}}\right], \tag{3.94}$$

and

$$W = \left[\frac{-\Gamma_2}{2\pi\left(\left(Z_2+Z_1\right)^2 + \left(Y_2-Y_1\right)^2\right)^{1/2}}\right] \times \left[\frac{-\left(Y_2-Y_1\right)}{\left(\left(Z_2+Z_1\right)^2 + \left(Y_2-Y_1\right)^2\right)^{1/2}}\right]. \tag{3.95}$$

Therefore, the total induced velocity field at the centroid of vortex 1 is

$$V_1\left(Y_1,Z_1\right) = \frac{\Gamma_1}{4\pi Z_1} + \frac{\Gamma_2}{2\pi}\left[\frac{Z_2 - Z_1}{\left(Z_2-Z_1\right)^2 + \left(Y_2-Y_1\right)^2} + \frac{Z_1 + Z_2}{\left(Z_2+Z_1\right)^2 + \left(Y_2-Y_1\right)^2}\right], \tag{3.96}$$

and

$$W_1\left(Y_1,Z_1\right) = \frac{\Gamma_2}{2\pi}\left[\frac{-\left(Y_2-Y_1\right)}{\left(Z_2-Z_1\right)^2 + \left(Y_2-Y_1\right)^2} + \frac{Y_2 - Y_1}{\left(Z_2+Z_1\right)^2 + \left(Y_2-Y_1\right)^2}\right]. \tag{3.97}$$

Similarly, for the velocity field at the centroid of vortex 2,

$$V_2\left(Y_2,Z_2\right) = \frac{\Gamma_2}{4\pi Y_2} - \frac{\Gamma_1}{2\pi}\left[\frac{Z_1 + Z_2}{\left(Z_2+Z_1\right)^2 + \left(X_2-X_1\right)^2} - \frac{Z_2 - Z_1}{\left(Y_2-Y_1\right)^2 + \left(X_2-X_1\right)^2}\right], \tag{3.98}$$

and

$$W_2\left(Y_2,Z_2\right) = \frac{\Gamma_1}{2\pi}\left[\frac{Y_2 - Y_1}{\left(Z_2+Z_1\right)^2 + \left(Y_2-Y_1\right)^2} - \frac{Y_2 - Y_1}{\left(Z_2-Z_1\right)^2 + \left(Y_2-Y_1\right)^2}\right]. \tag{3.99}$$

Note that

$$\dot{Y}_1 = V_1(Y_1,Z_1) + V_\infty \quad , \tag{3.100}$$

$$\dot{Z}_1 = W_1(Y_1,Z_1) \quad , \tag{3.101}$$

$$\dot{Y}_2 = V_2(Y_2,Z_2) + V_\infty \quad , \tag{3.102}$$

$$\dot{Z}_2 = W_2(Y_2,Z_2) \quad . \tag{3.103}$$

It is noted that V_∞ may be a function of altitude. The vortex trajectories are obtained by integrating equations (3.100) through (3.103) with the initial values of the coordinates being the coordinates at which the roll-up process is completed. The integration forms the basic wake vortex transport predictive model. In the basic model equations (3.100) through (3.103) are integrated using a fourth-order Runge-Kutta technique to determine vortex position as a function of time.

In the absence of wind shear, the vortices are of equal strength and descend together. Thus

$$\Gamma_2 = -\Gamma_1 = \Gamma \quad , \tag{3.104}$$

and

$$Z_2 = Z_1 = Z \quad , \tag{3.105}$$

Therefore,

$$\dot{Z}_1 = \dot{Z}_2 = \frac{-\Gamma}{2\pi\left(Y_2-Y_1\right)} + \frac{\Gamma}{2\pi}\left[\frac{\left(Y_2-Y_1\right)}{\left(2Z\right)^2 + \left(Y_2-Y_1\right)^2}\right] \quad , \tag{3.106}$$

$$\dot{Z}_1 = \dot{Z}_2 = \frac{\Gamma}{2\pi\left(Y_2-Y_1\right)}\left[\frac{-\left(2Z\right)^2}{\left(2Z\right)^2 + \left(Y_2-Y_1\right)^2}\right] \quad . \tag{3.107}$$

The downward velocity goes to zero as Z goes to zero (i.e., near the ground), and equation (3.107) becomes the classic equation for vortex descent out of ground effect (equation (3.78)) as Z becomes large. Similarly, the horizontal component of vortex motion is

$$\dot{Y}_1 = V_\infty - \frac{\Gamma}{4\pi Z}\left[\frac{(Y_2-Y_1)^2}{(2Z)^2 + (Y_2-Y_1)^2}\right] \quad , \tag{3.108}$$

$$\dot{Y}_2 = V_\infty + \frac{\Gamma}{4\pi Z}\left[\frac{(Y_2-Y_1)^2}{(2Z)^2 + (Y_2-Y_1)^2}\right] \quad . \tag{3.109}$$

Y_1 and Y_2 approach V_∞ as altitude, Z, becomes large. These equations also show the phenomenon of vortices stalling in the flight corridor.

It has been observed that vortices tend to descend to an altitude of one half of their initial separation distance, b'. Near the ground, the vortices tend to separate, so that

$$(Y_2-Y_1)^2 >> (2Z)^2 \quad . \tag{3.110}$$

The vortex can be expected to stall in the flight corridor (i.e., $\dot{Y}_1 = 0$ or $\dot{Y}_2 = 0$) if

$$V_\infty \cong \pm\frac{\Gamma}{4\pi Z} = \pm\frac{\Gamma}{2\pi b'} \quad . \tag{3.111}$$

The vortex can be expected to stall in the flight corridor if the crosswind is approximately equal to the initial descent speed.

In the absence of a crosswind (i.e., $V_\infty = 0$), the vortex trajectory is a hyperbola. In this condition, the vortex descent is symmetric with respect to a vertical plane. Hence,

$$Y_2 = -Y_1 = Y \quad . \tag{3.112}$$

From equations (3.107) and (3.109)

$$\dot{Y}/\dot{Z} = -(2Y)^3/(2Z)^3 \quad , \tag{3.113}$$

or

$$dZ/Z^3 = -dY/Y^3 \quad , \tag{3.114}$$

and hence,

$$1/Y^2 + 1/Z^2 = \text{Constant} = C \quad , \tag{3.115}$$

which is the equation of the hyperbola representing the vortex trajectory in the absence of a crosswind.

This result can be used to calculate the time for which a vortex remains in a flight corridor of width $2y_b$ for a constant crosswind. The coordinate system is referenced to the wind with the origin in the y-direction taken as the aircraft axis at the time of aircraft passage. The origin coincides with the runway centerline at the time of aircraft passage. Since the coordinate system is fixed on the wind, the crosswind is zero relative to the coordinate system. From equations (3.109) and (3.112)

$$\dot{Y} = \frac{\Gamma}{4\pi Z}\left[\frac{Y^2}{Z^2+Y^2}\right] . \tag{3.116}$$

Using equation (3.115) for Z,

$$\dot{Y} = \frac{\Gamma}{4\pi C}\left[\frac{CY^2-1}{Y^2}\right]^{3/2} , \tag{3.117}$$

where the value of C is calculated from equation (3.115) using the initial values of Y and Z (e.g., Y=b'/2 and Z = aircraft altitude). Integrating equation (3.117) gives

$$t + D = \frac{4\pi}{\Gamma C}\left[\frac{CY^2-2}{(CY^2-1)}1/2\right] , \tag{3.118}$$

where D is the constant of integration determined by Y=b'/2 at t=0. If the lateral boundaries of the flight corridor are at $\pm\, y_b$ at t=0, at later time, t, the boundaries of the flight corridor (referenced to the wind-based coordinate system) are at

$$Y = -V_\infty t \pm y_b \quad , \tag{3.119}$$

with a + or - denoting downwind or upwind flight corridor boundaries, respectively. Inserting equation (3.119) in (3.118)

$$\frac{(\pm\, y_b - Y)}{V_\infty} + D = \frac{4\pi}{\Gamma C}\left[\frac{CY^2-2}{(CY^2-1)^{1/2}}\right] . \qquad (3.120)$$

Let

$$F(Y) = \frac{4\pi}{\Gamma C}\left[\frac{CY^2-2}{(CY^2-1)^{1/2}}\right] - D + \frac{Y \mp y_b}{V_\infty} . \qquad (3.121)$$

Physically, F(Y) is the difference in the time at which the vortex reaches position Y and the time at which the boundary reaches position Y. The various solutions are found by starting with $Y=\pm b'/2$ as the initial solutions and performing a Newton iteration on equation (3.121). For the downwind vortex (Y>0) and downwind boundary, there is only one solution. For the upwind vortex (Y<0) crossing the upwind boundary, a solution may or may not exist (depending upon the magnitude of V_∞). Care must be taken when considering the upwind vortex crossing the downwind boundary; depending upon the magnitude of V_∞ either one solutuon exists or (for small V_∞) no solutions or two solutions exist.

3.3.3 Wind Shear Effect on Vortex Transport

The tilting or banking of the plane containing the vortex pair has been observed experimentally at altitude (ref. 42) and in ground effect (ref. 43), as well as in operational situations (refs. 44 and 45). Occasionally in the light aircraft tests, long segments of the wake were observed to roll past the vertical resulting in bank angles exceeding 90 degrees. As will be shown below, it appears that crosswind shear or crosswind shear gradients are responsible for the observed rolling tendency of wakes.

The geometry of vortex transport in wind shear is shown in Fig. 3-30. Crosswind shear (change in crosswind with respect to altitude) in the vicinity of the wake implies an ambient, coherent vorticity field alined parallel with the vorticity associated with the vortex pair. Interactions between the two vortical flows could produce opposite changes in the circulations of the counter-rotating vortices. Thus, the velocities induced by each vortex on the other (the descent speeds) would be unequal and wake roll, manifesting itself as an altitude mismatch between vortices, could occur for the descending pair.

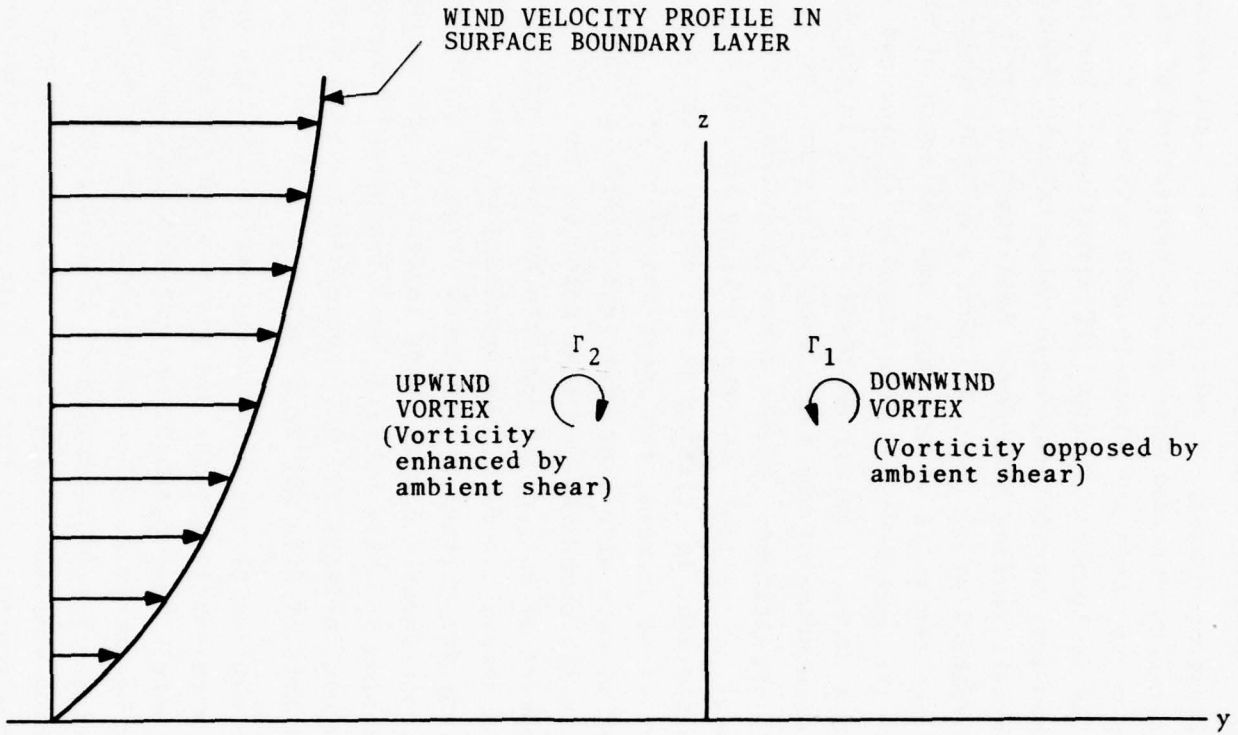


FIGURE 3-30. VORTEX STRUCTURE IN CROSSWIND SHEAR

There is, however, a lack of definitive experimental evidence or agreement about which direction the wake will roll under given shear conditions -- apparently because of the relatively weak deterministic influences of shear on wake roll. For light shear, it is possible that random vertical atmospheric convection of each of the vortices could overwhelm any shear-induced motions, resulting in atmospherically influenced, random roll directions. For increasing shear however, any deterministic shear effects should produce definite wake-rolling behavior. Full-scale aircraft wake measurements by Tombach et al (ref. 43) show a definite negative correlation between the sense of the shear and the sense of the tilting, so that the upwind vortex (the shear being produced in the sense of that of a boundary layer) descends relative to the downwind vortex a large percentage of the time, especially when the shear strength becomes significant. On the other hand, measurements reported by Brashears et al (ref. 45) show tilting in both directions, with a preference for tilting in the opposite sense to that noted by Tombach et al whenever the shear was relatively strong. The Brashears et al data also show, for weak shears, a tendency toward tilting in the same sense as that noted by Tombach. In this case however, random effects could dominate the weak deterministic influence of the shear. In fact, the Brashears et al data show the least tendency for tilting at a nonzero value of shear, where the opposite strong shear and weak shear tendencies are balanced out. An explanation for this behavior is not apparent however. Variations in ground effects and differences in aircraft scale between the two sets of data may be a factor.

Wind shear may not be the only causal factor for this phenomenon. Perhaps more subtle effects are responsible for the observed tilting of the wake. For instance, non-uniform shears or shear gradients might be involved. This creates an unsteady situation in which the necessary redistribution of ambient vorticity because of its interaction with the vortex pair is difficult to conceptualize and model analytically. A simple finite element computer model was devised by Burnham (ref. 44) for vortex tilt in the shear layer near the ground. The tilting of the vortices produced by this

model was a function of the vertical shear gradient rather than the shear itself. The direction of tilt in the Burnham model agrees with the data of Tombach et al.

In addition to the tilting, another dramatic (and operationally more significant) aspect to wake behavior occurs simultaneously. Whenever the wake banks, the upper (generally downwind) vortex appears to break up (decay) well ahead of the other vortex, often leaving one vortex drifting alone for some time before it decays. In the overhead view in Fig. 3-31, the upper vortex shows signs of decay at 15 seconds and has completely broken down by 30 seconds; the lower vortex still persisted, apparently unmodified, when the last picture in the sequence was taken, at 45 seconds. The single remaining vortex does not attempt to link with its image below the ground as has been observed when both vortices approach the ground, but rather invariably experiences vortex breakdown.

Analytical studies of the mechanisms involved in wake tilting and in wind shear effects on wakes have not produced conclusive results. Potential flow analysis of a vortex pair at infinite altitude has shown that, in a uniform crosswind shear, the recirculating cell about the upwind vortex cell (the cell whose vorticity is enhanced by the shear) enlarges and the downwind cell (the cell whose vorticity is opposed by the shear) contracts, as shown in Fig. 3.32. Continued analysis along these lines (ref. 45) showed that additional cell contraction around the downwind vortex was brought about by the proximity of the ground. For a sufficiently large amount of cell contraction about the downwind vortex, the interior flow (and vorticity) could presumably be detrained, resulting in the rather abrupt dissipation of that vortex. The upwind vortex would be further isolated from the exterior flow by the enlargement of its cell, and hence, its vorticity would be "protected." These effects (if in fact real) are in qualitative agreement with experimental observations of vortex breakup in shear flow (ref. 43) such as in the example in Fig. 3-31.

Both of the analyses modeled the steady potential flow in the vicinity of a vortex pair resulting from superposition of vortex-induced motion, crosswind shear, and, in the case of ground effect,

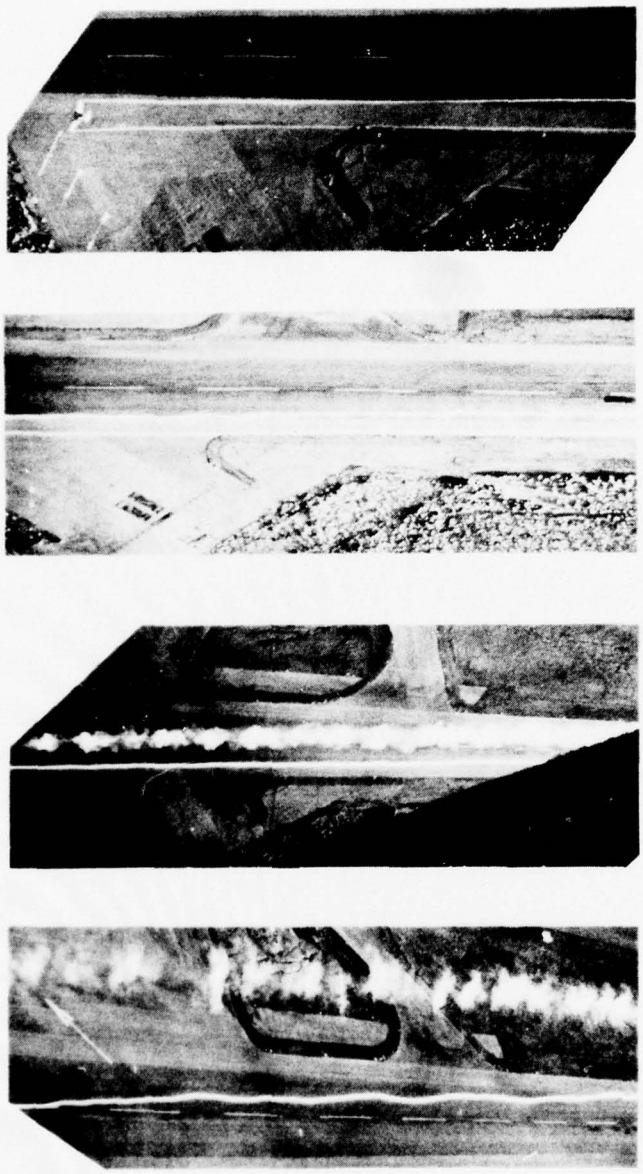
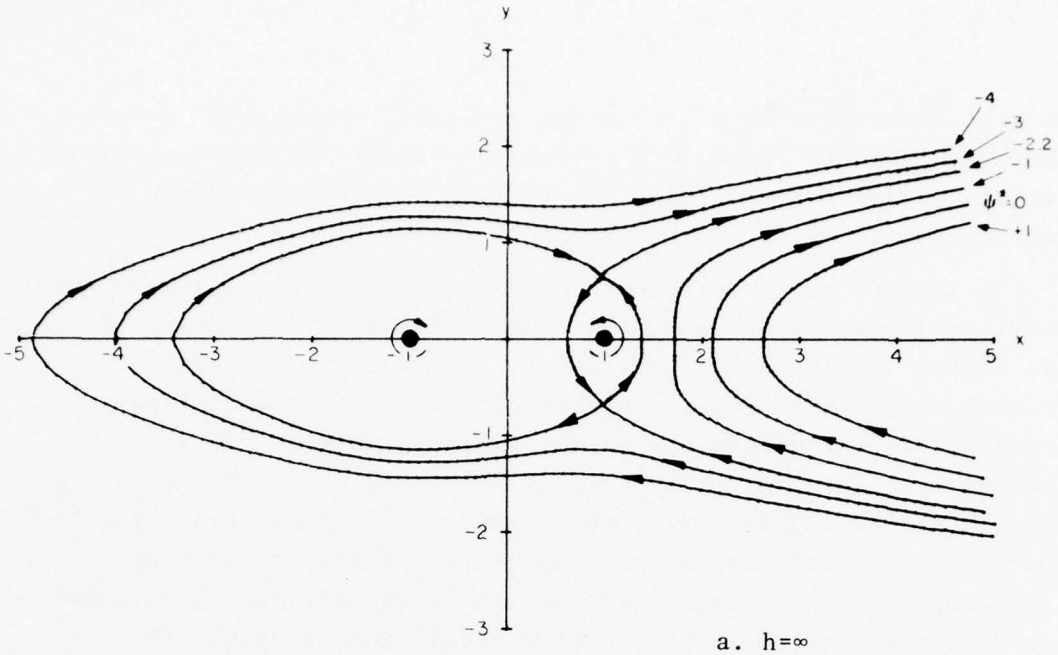
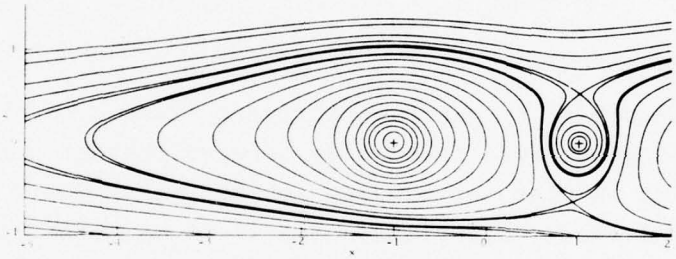


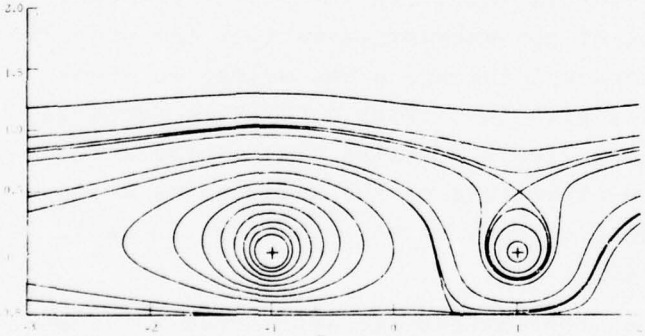
FIGURE 3-31. OVERHEAD VIEW OF AEROCOMMANDER 560F WAKE BEHAVIOR IN WIND SHEAR. WAKE GENERATED ONE SPAN ABOVE GROUND. WIND SHEAR 0.08 S^{-1}; WIND FROM AIRCRAFT'S LEFT; I.E., FROM BOTTOM OF PICTURE. THE LEFT VORTEX DESCENDS TOWARD THE GROUND; THE RIGHT ONE RISES AND BREAKS UP. THE PHOTOGRAPHS WERE TAKEN FROM AN AIRCRAFT CIRCLING OVERHEAD, THUS THE ANGLE OF OBSERVATION IS SLIGHTLY DIFFERENT IN EACH PICTURE.



a. h=∞



b. h=0.5 b_v



c. h=0.25 b_v

FIGURE 3-32. STREAMLINES IN THE VICINITY OF A VORTEX PAIR IN SHEAR AT (A) INFINITE ALTITUDE, AND (B,C) IN GROUND EFFECT. FOR SHEAR IN THE SENSE OF A BOUNDARY LAYER FLOW, THE CROSSWIND IS FROM THE LEFT. THE "DOWNWIND" VORTEX RECIRCULATION CELL BECOMES SMALLER THAN THE UPWIND CELL FOR SUCH A SITUATION.

from the induced flows of the image vortices. Resulting streamlines were calculated and mapped. The wake tilting is an unsteady phenomenon however, and thus, the limitations of such steady analyses should be recognized.

It appears that the factors causing vortex tilting are neither intuitively obvious nor have they been sufficiently illuminated by full-scale, atmospheric flight tests, or theoretical analysis. The most significant aspect of wake tilting from an operational standpoint is the occurrence of the solitary vortex. It is undoubtedly some manifestation of flow asymmetry associated with wind shears, turning flight, etc., which produces the conditions for the creation of the solitary vortex, which so far has eluded proper understanding. Such long-lived vortices could present operational hazards since they appear to be rare events and, as such, the conditions for their occurrence may not be predictable.

3.3.4 Vortex Buoyancy

Vortex buoyancy is the aerostatic force imposed on the vortex by virtue of the difference in density between the air contained within the vortex and the surrounding ambient air. There are three sources of this density difference: The first is a result of the static underpressure of the vortex (cf., Fig. 3-13). The second is the result of entrainment of hot exhaust gases from the engines. The third is the result of descent through a non-adiabatic atmosphere. The first two effects give the vortex a positive (upward) buoyancy force. The third may give a positive or negative force depending on the temperature-lapse rate of the surrounding atmosphere. The magnitude of these effects on vortex motion is small compared with mutual induction.

Positive buoyancy causes the vortices to approach each other. The Kutta-Joukouski force on a body with circulation and velocity through a fluid gives

$$F = -\rho(\dot{Z}-W)\,\Gamma \qquad (3.122)$$

where the force is in the positive z-direction, and $\dot{Z} - W$ is the velocity of the vortex relative to the surrounding air. Therefore

since Γ_1 is negative (Fig. 3-29), the force resulting from buoyancy is in the positive y-direction. Similarly, the force on vortex 2 is in the negative y-direction.

For the first effect, the momentum equation for cylindrical flow gives

$$\frac{dp}{dr} = \frac{\rho v^2}{r} = \frac{\rho \Gamma^2}{4\pi^2 r^2} \quad , \tag{3.123}$$

where the second part of the equation is valid outside the core for the Rankine vortex (equation 3.80)). Assuming adiabatic conditions in the core,

$$p\rho^{-k} = p_\infty \rho_\infty^{-k} = \text{Constant} \quad , \tag{3.124}$$

where k is the ratio of specific heats, and

$$\frac{k p_\infty \rho^{k-1}}{\rho_\infty^k} \, d\rho = \frac{\rho \Gamma^2}{4\pi^2 r^3} \, dr \quad . \tag{3.125}$$

Integrating between the limits of infinity and r,

$$\rho(r) = \left[\rho_\infty^{k-1} - \frac{k-1}{k} \frac{\rho_\infty^k}{p_\infty} \frac{\Gamma^2}{2\pi r^2} \right]^{\frac{1}{k-1}} \quad . \tag{3.126}$$

As an example of the magnitude of the effect, for the flight conditions for a landing B-727 (Table 3-2) and an assumed core radius of 0.6 m, the density is 0.72 kg/m^3 compared with an ambient density of 1.23 kg/m^3. The upward buoyant force is

$$F = 2\pi g \int_0^\infty \left(\rho_\infty - \rho(r) \right) r \, dr \quad . \tag{3.127}$$

In practice the integral would be taken from the core radius, r_c, because equation (3.123) is based upon the Rankine vortex assumption, and therefore, is only valid for $r \geq r_c$.

Engine-exhaust extrainment is another aircraft variable which can affect the vortex transport process through variations in the

vortex buoyancy. The density variation caused by exhaust entrainment is

$$\rho = \rho_\infty T_\infty / T \quad , \tag{3.128}$$

where T is the temperature of the air in the core of the vortex and T_∞ is the ambient air temperature. The buoyant force produced by exhaust entrainment is also given by equation (3.127).

The third cause of buoyancy is vortex descent through a non-adiabatic atmosphere. The interface between the wake fluid and the exterior atmosphere is only a dividing streamline; it does not support shear or pressure. In the presence of atmospheric turbulence or turbulence in the wake, the streamline is perturbed, and some mixing between the interior wake fluid and the exterior atmosphere occurs. When the mixing is small, as it is when the wake is young and the turbulence is low, the wake fluid retains its identity and its physical properties as it moves about through the atmosphere. One consequence is the creation of aerostatic forces as the wake moves into regions of varied temperature and density. For example, an upward (or buoyant) force is developed on those segments of a wake descending into stably stratified atmosphere if there is little or no mixing of the ambient air with the wake fluid. Results of experiments on wake buoyancy are presented by Tombach (ref. 46) in which he showed that a wake descending into a stable atmosphere acquired buoyancy, until at some later time, turbulent mixing between the wake and the atmosphere became significant enough to erode the temperature difference between them. Increasing ambient turbulence shortened the period during which buoyancy was acquired, and as a consequence of more rapid mixing, resulted in more rapid decay of both buoyancy and vortex descent.

The aerostatic forces are a result of an increase in the temperature of the fluid in the wake oval, caused by adiabatic compression as the oval descends into a denser atmosphere. An atmospheric temperature stratification other than adiabatic (neutral) will result in a temperature difference, and hence, a density difference between the wake and the atmosphere. Buoyancy will thus be created for wakes descending into a stable atmosphere

(the most common situation) with no mixing. Theoretical models with no mixing (ref. 47) indicate that the buoyancy so acquired accelerates wake descent and decreases vortex-spacing. The experimental observations discussed above indicate, however, the possibility of a retarding tendency caused by buoyancy, but may be a consequence of entrainment rather than of buoyancy.

Overall, the effects of aerostatic forces on vertical wake motions appear to be of smaller order than the dissipative mechanisms associated with turbulence, which could overwhelm the buoyancy effect, and thus, result in the difficulties experienced in properly isolating the buoyancy influence. A comprehensive discussion of both theoretical and experimental observations on the descent of a wake in a stratified fluid is given in ref. 47.

The predominant effect of atmospheric stability appears to be the indirect one associated with the vertical air currents resulting from atmospheric mixing. In a stable atmosphere, this mixing is suppressed, resulting in reduced vertical air motions and reduced effects on vertical wake motions. In unstable conditions, vertical atmospheric activity and resulting wake motions are amplified. Such motions may be either upward or downward, thus unpredictable wake ascent or descent can result under such unstable atmospheric conditions.

The effects of atmospheric stratification on initial wake descent rates are shown schematically in Fig. 3-33. For a stable atmosphere, the wake descends initially at a speed which is consistent with the inviscid analytical model. Random influences become more evident for less stable conditions. The figure applies only to vertical wake motion during the first few moments after the wake has been fully formed. Subsequent vertical wake motions are influenced by buoyancy, turbulence, and the continued random action of vertical air motions (which are accentuated for less stable conditions). Not all of these factors can be quantified presently however.

Vertical air motions often become quite pronounced under the influence of thermal activity near the ground. Extreme vertical convolutions of wakes can occur because of convection by these air

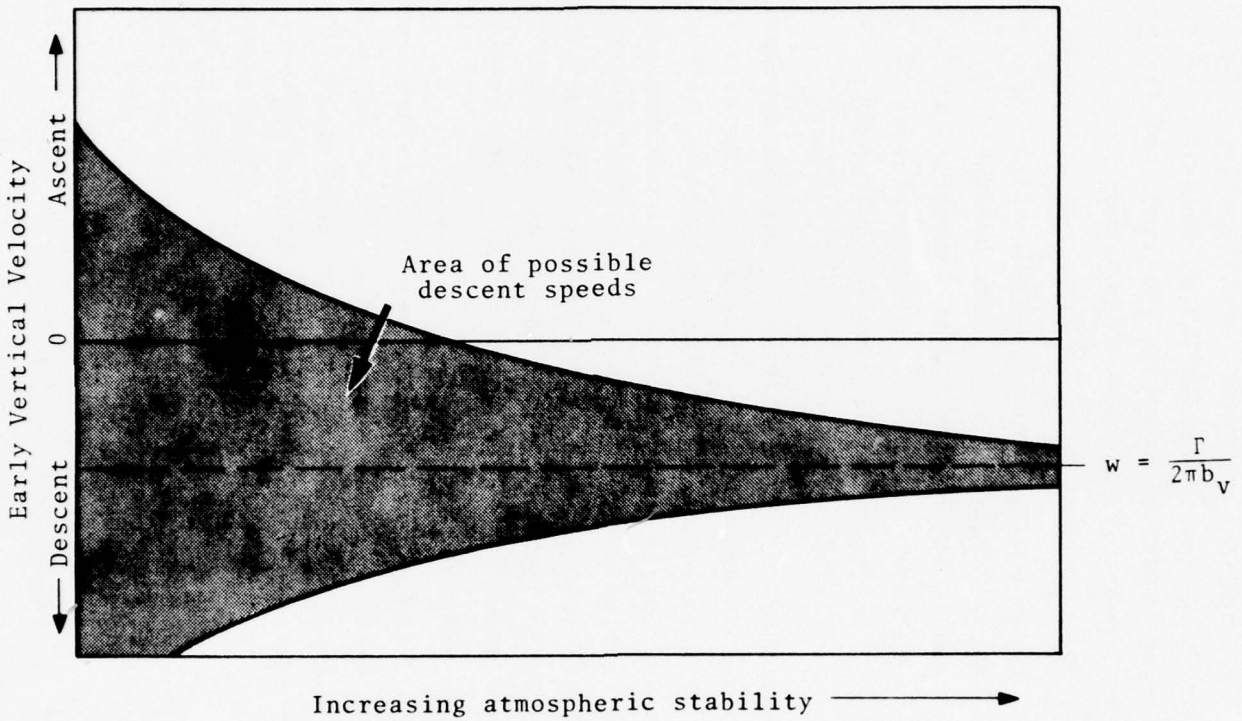


FIGURE 3-33. SCHEMATIC REPRESENTATION OF OBSERVED RELATIONSHIP BETWEEN ATMOSPHERIC STABILITY AND WAKE DESCENT AT EARLY TIMES. IN UNSTABLE CONDITIONS, THE DESCENT IS RELATIVELY INDETERMINATE, PROGRESSIVELY INCREASING STABILITY RESULTS IN DESCENT MORE CLOSELY APPROACHING THE VORTEX INDUCED WAKE SPEED.

motions. Under these conditions, the wake (and the vortex pair) is stretched and distorted into a highly nonlinear configuration where mutual and self-induced vortex velocities act to amplify the process. Figure 3-34 shows such a wake generated near the ground under conditions of high atmospheric thermal activity. The impossibility of dealing with such a resultant wake structure on anything but a statistical basis is clearly evident. However, it remains to be shown that such a convoluted wake could pose a hazard in operational conditions.

All wake motions near the ground do not exhibit such extreme behavior. Under stable atmospheric conditions and reduced thermal activity, the wake and the vortex pair undergo more orderly motions which are fairly well understood and can be approximated analytically. These conditions are also the ones of greatest operational interest because these same factors are conducive to wake persistence. Wakes generated or moving into ground effect are subjected to the influences of the induction velocities generated by the underground or image vortices. The vertical motion of the wake gradually and predictably slows and eventually stops at about one-half the vortex spacing above the ground, and simultaneously, the vortices move apart.

3.3.5 Updated Vortex Transport Predictive Model

When buoyancy conditions are present (i.e., the density of the vortex cell differs from that of the ambient atmosphere), there are two forces which impose an acceleration on the vortex. The resulting velocity causes the vortex transport velocity to differ from that described in Section 3.3.2. The updated vortex transport predictive model is a modification of the predictive model presented in Section 3.3.2. It calculates the vortex transport velocity resulting from the acceleration and superimposes that velocity on the vortex transport velocity because of mutual induction.

The mass of the vortex per unit length is

$$\iint_{A_1} \rho \, dA = \bar{\rho} \, A_1 \, , \qquad (3.129)$$



FIGURE 3-34. VORTICES IN GROUND EFFECT.

where A_1 is the cell cross-sectional area associated with the vortex and $\bar{\rho}$ is the average mass density within A_1. The first force is the buoyancy force given by

$$F = (\rho_\infty - \bar{\rho}) A_1 \, g \quad , \tag{3.130}$$

and acts in the positive vertical direction. The second force is the Kutta-Joukowski force which is the force caused by a body with rotation moving relative to a fluid. Let V_1 and W_1 be the components of the sum of the velocity fields of vortices 2, 3, and 4 (cf., Fig. 3-29) at the centroid of vortex 1. Let $\dot{Y}_1$ and $\dot{Z}_1$ be the transport velocity components of vortex 1. For pure advection presented in the basic vortex transport predictive model, $\dot{Y}_1 = V_1 + V_\infty$ and $\dot{Z}_1 = W_1$; this will not always be true in the generalized case considered in the updated predictive model. Let V_2, W_2, Y_2, and $\dot{Z}_2$ have similar meanings for vortex 2.

The vector form for the Kutta-Joukowski force is

$$\bar{F} = \rho_\infty \, \bar{V}_r \times \bar{\Gamma} \quad , \tag{3.131}$$

where $\bar{V}_r$ is the free-stream velocity relative to the vortex. The horizontal component of the Kutta-Joukowski force on vortex 1 is

$$F_h = \rho_\infty \left(W_1 - \dot{Z}_1 \right) \Gamma_1 \quad . \tag{3.132}$$

(Γ_1 is negative.) The vertical component is

$$F_v = - \rho_\infty \left[\left(V_1 - V_\infty \right) - \dot{Y}_1 \right] \Gamma_1 \quad . \tag{3.133}$$

Similarly for vortex 2, the buoyancy force is

$$F = \left(\rho_\infty - \bar{\rho} \right) A_2 \, g \quad . \tag{3.134}$$

The horizontal component of the Kutta-Joukowski force is

$$F_h = \rho_\infty \left(W_2 - \dot{Z}_2 \right) \Gamma_2 \quad , \tag{3.135}$$

where Γ_2 is positive, and the vertical component is

$$F_v = - \rho_\infty \left[\left(V_2 + V_\infty \right) - Y_2 \right] \Gamma_2 \quad . \tag{3.136}$$

The change in the transport velocity of a vortex over a time period Δt is caused by three effects: (a) acceleration caused by application of buoyancy and Kutta-Joukouski's forces, (b) displacement of the vortex within the velocity fields of the other vortices, and (c) change in the velocity field of the other vortices because of their displacement. The second and third effects are the mutual advection effects discussed in Section 3.3.2. Let starred quantities denote vortex transport parameters because of buoyancy and Kutta-Joukowski forces. The star denotes vortex transport because of the first transport effect only. Then

$$\ddot{Y}_1^* = \frac{\rho_\infty \left(W_1 - \dot{Z}_1\right) \Gamma_1}{\bar{\rho} A_1} \quad , \tag{3.137}$$

and

$$\ddot{Z}_1^* = \frac{\left(\rho_\infty - \bar{\rho}\right) A_1 \, g \, - \, \rho_\infty \left[\left(V_1 + V_\infty\right) - Y_1\right] \Gamma_1}{\bar{\rho} A_1} \quad . \tag{3.138}$$

Then in the numerical integration process, both the velocity caused by the first transport effect and the total transport velocity are calculated

$$\dot{Y}_1^* \, (t+\Delta t) = \dot{Y}_1^* \, (t) + \ddot{Y}_1^* \, (t)(\Delta t) \quad , \tag{3.139}$$

and the total vortex transport velocity is

$$\dot{Y}_1 \, (t+\Delta t) = \dot{Y}_1^* \, (t+\Delta t) + V_1 \, (t) + V_\infty \quad , \tag{3.140}$$

and the vortex position is

$$Y_1 \, (t+\Delta t) = Y_1 \, (t) + \dot{Y}_1 \, (t) \, \Delta t \quad . \tag{3.141}$$

Similarly,

$$\dot{Z}_1^* \, (t+\Delta t) = \dot{Z}_1^* \, (t) + \ddot{Z}_1^* \, (t)(\Delta t) \quad , \tag{3.142}$$

$$\dot{Z}_1 \, (t+\Delta t) = \dot{Z}_1^* \, (t+\Delta t) + W_1 \, (t) \quad , \tag{3.143}$$

and

$$Z_1 (t+\Delta t) = Z_1 (t) + \dot{Z}_1 (t) \Delta t . \qquad (3.144)$$

In practice, these equations are integrated with a fourth-order Runge-Kutta integration technique. In the absence of buoyancy, the starred quantities become zero, and equations (3.140) and (3.143) become equations (3.100) and (3.101), respectively. Similar equations are also written for vortex 2.

It is noted that the Kutta-Joukowski force cannot exist without buoyancy. The Kutta-Joukouski force results from a relative velocity between the vortex and the air in which it is immersed. The only mechanism in the model by which such a relative velocity can be generated is buoyancy since the basic assumption of the transport model is that the vortex transport velocity is identical to the velocity field at the vortex centroid.

3.3.6 Predictive Model Verification

A wake-vortex predictive model based on the phenomena described in the preceding sections has been formulated (refs. 48 and 49). The most important of these phenomena is mutual induction which includes image vortices to provide for the effect of the ground. A comparison of predicted vortex tracks and vortex tracks obtained from photographic data of smoke entrained in the vortex is presented in Fig. 3-35 (ref. 50). The crosswind profiles assumed for the predictive track are a mean power-law model based on data measured before aircraft passage, a linear interpolation based on data measured before aircraft passage, and a linear interpolation based on data measured after aircraft passage.

Figure 3-36 shows the importance of proper input of aircraft parameters as initial conditions to the integration of equations (3.100) through (3.103). The measured vortex positions are the same for the top and bottom. The predicted vortex track for the top uses an assumed value of spanwise loading coefficient of $\pi/4$, the value for an elliptically loaded wing. The predicted vortex track for the lower figure uses the more appropriate value (calculated from actual spanwise loading) of 0.63.

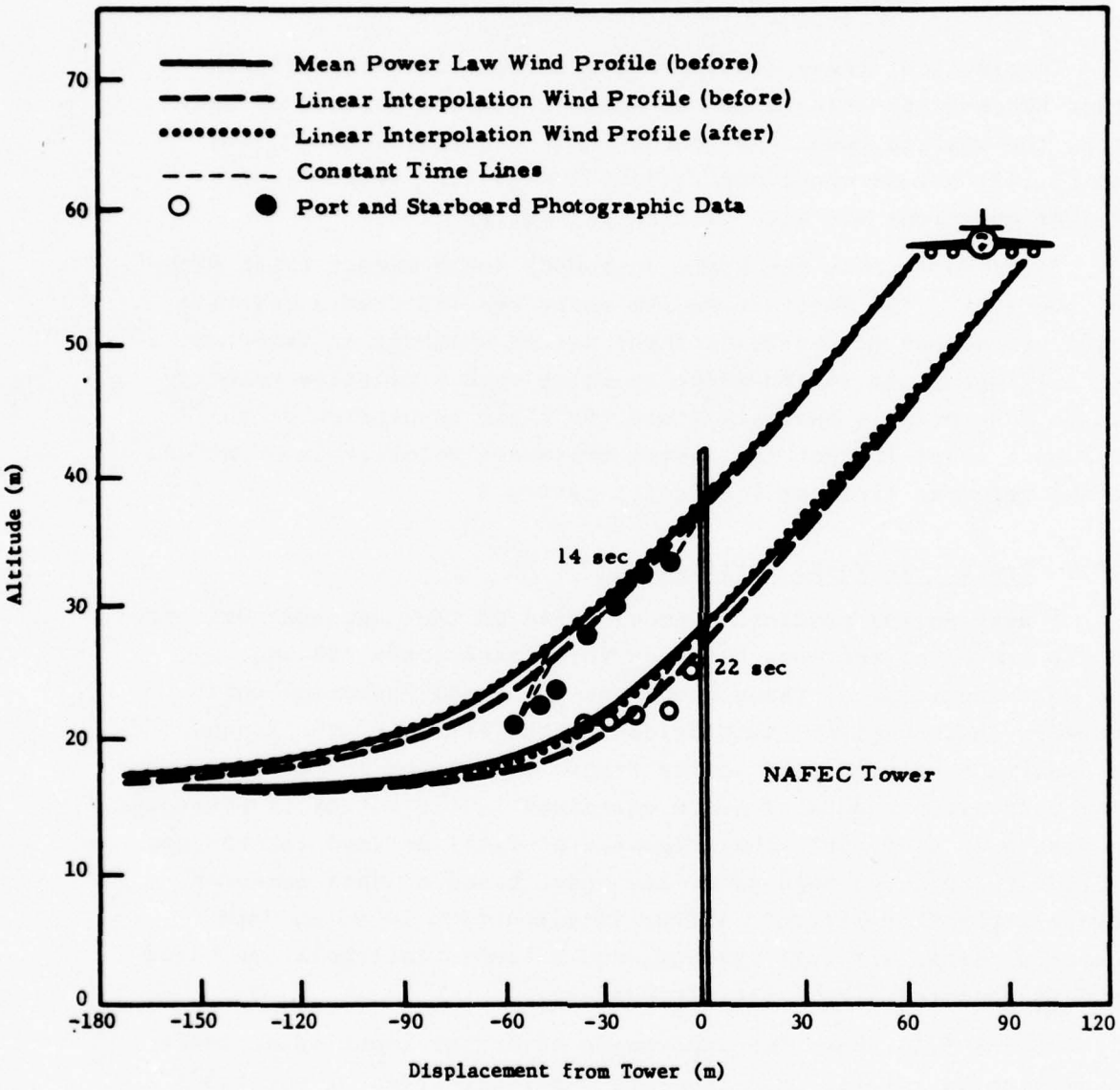


FIGURE 3-35. COMPARISON OF PREDICTIVE VORTEX TRACKS WITH PHOTOGRAPHIC DATA FOR NAFEC B-707 RUN 17, 10/18/72.

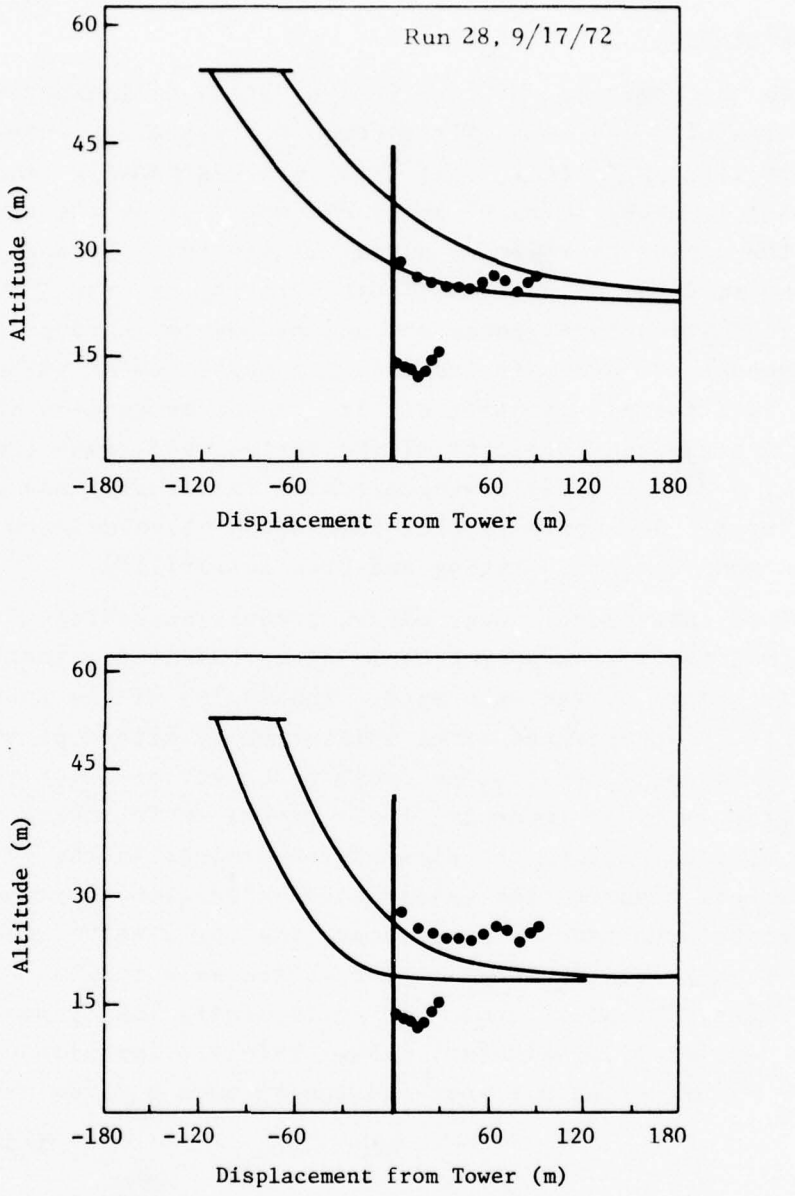


FIGURE 3-36. WAKE VORTEX TRAJECTORY COMPUTED BY THE PREDICTIVE WAKE VORTEX TRANSPORT MODEL FOR A B-747 TOWER FLYBY (NAFEC RUN 28 9/17/72) WITH ELLIPTIC LOADING (TOP K = $\pi/4$) AND WITH FLAP EFFECTS (BOTTOM K = 0.63)

3.4 VORTEX DECAY

From the beginning of its life, a vortex pair experiences three forms of decay. The first form is dissipative wake decay caused by viscous forces. This decay would gradually lead to vortex demise if other forms of decay did not destroy the vortex first; the vortex pair almost always is destroyed by one of two catastrophic decay mechanisms - core bursting or Crow instability. In the real atmosphere, decay mechanisms develop through coupling with atmospheric, aircraft-induced, and self-induced turbulence as well as with normal viscosity of air. These mechanisms effectively alter the organized vorticity of the vortex pair, such that the encounter hazard to a following aircraft is abruptly and dramatically reduced. Such catastrophic wake decay is associated with the two phenomena of core bursting and Crow instability.

Before catastrophic wake decay, gradual weakening of the circulation of the vortex pair because of turbulent dissipation of vorticity occurs as the wake ages. The demise of the vortex is significantly accelerated after initiation of either of the two catastrophic decay modes. The decay modes act to alter the geometry of the vortices (reducing their danger to following aircraft), as well as accelerating the dissipation process in the residual wake, further reducing the danger associated with an encounter. Regardless of the mode of wake decay, the turbulent transport of vorticity away from the core region of the wake results in a weakening of the wake as it ages. At sufficiently long times, the wake is completely dissipated. Thus, harmless turbulence is the ultimate result of an aircraft passage through a given parcel of air.

3.4.1 Dissipative Wake Vortex Decay

Although not considered a significant decay mechanism by itself, the dissipation or annihilation of vorticity caused by real fluid effects can have important consequences on the motion (and hence, the predicted location) of the wake before decay has occurred. For this reason, the dissipation process and its resultant effects

on wake transport must be properly understood to develop a reliable predictive model for vortex behavior. This is particularly true in ground effect. Here, shear generated by vortex velocities at the ground can produce vorticity which mixes with and drastically affects the subsequent motion of a vortex.

The initial decay mechanism is one in which viscous forces cause the vortex core to expand without affecting vortex strength (c.f., discussion associated with Figs. 3.27 and 3.28 in Section 3.3.1). The vortex structure changes from that shown in Fig. 3.37a to that shown in Fig. 3-37b. The vortex strength is the same for both figures. The expansion of the core with constant vortex strength causes a decrease in the peak tangential velocity as shown by Fig. 3-37b as well as by the equation for vortex strength of the Rankine vortex (equation (3.59)).

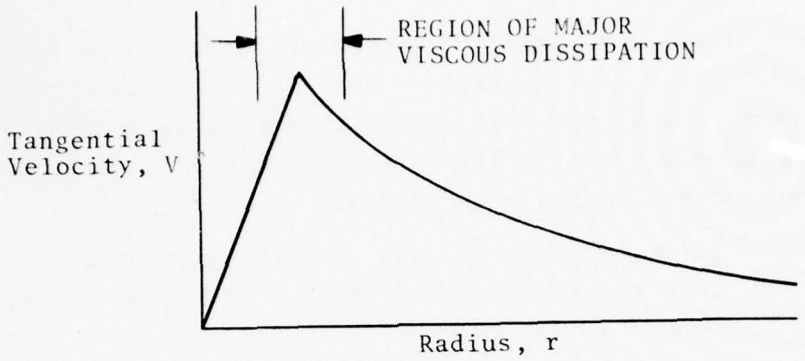
$$\Gamma = 2\pi\, r_c\, v_c \quad . \tag{3.59}$$

The decrease in peak velocity with vortex age from experimental measurements is shown in Figs. 3-38 and 3-39. The measurements were made at NAFEC. It is noted that the numbers shown are peak-recorded velocity for anemometers at 0.3-meter increments. For the B-747, the fact that peak velocities are higher for takeoff and holding configurations than for the landing configuration is supported by the vortex structures (particularly the core size) shown in Figs. 3-15, 3-16, and 3-17.

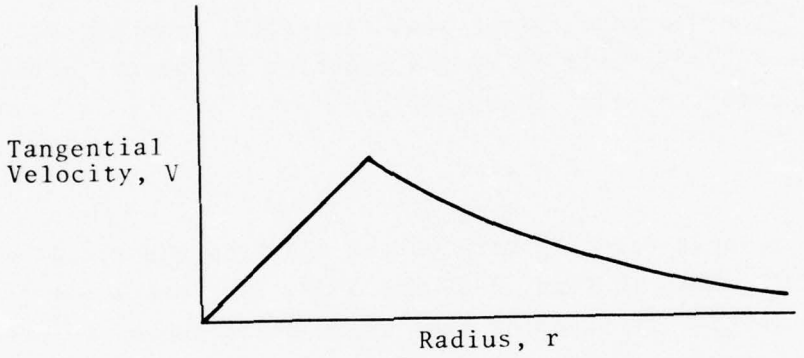
Figure 3-38 shows theoretical curves for the decay of maximum tangential velocity. The inverse of the square root of time is from the model of Owens (ref. 21). The negative exponential form is based on the assumption that the derivative of the velocity with respect to time is proportional to the velocity.

3.4.2 Core-bursting

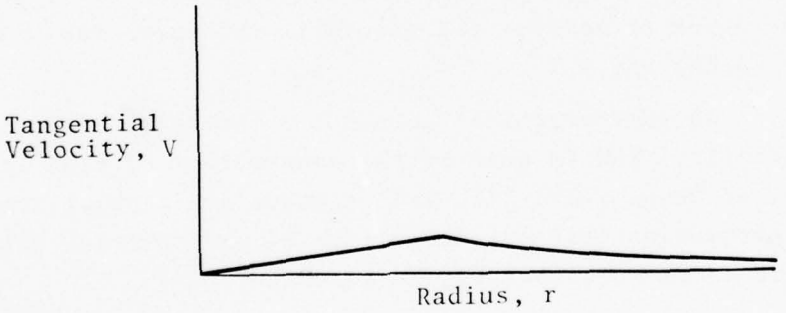
One major form of vortex instability is core-bursting or vortex breakdown. This mode consists of a sudden abrupt widening of the vortex core; in the case of a smoke-marked aircraft vortex,



(a) Vortex Structure After Vortex Roll-Up



(b) Vortex Structure After Dissipative Decay



(c) Vortex Structure After Vorticity Detrainment
Stages of Vortex Dissipative Decay

FIGURE 3-37. VORTEX STRUCTURE WITH DISSIPATIVE DECAY.

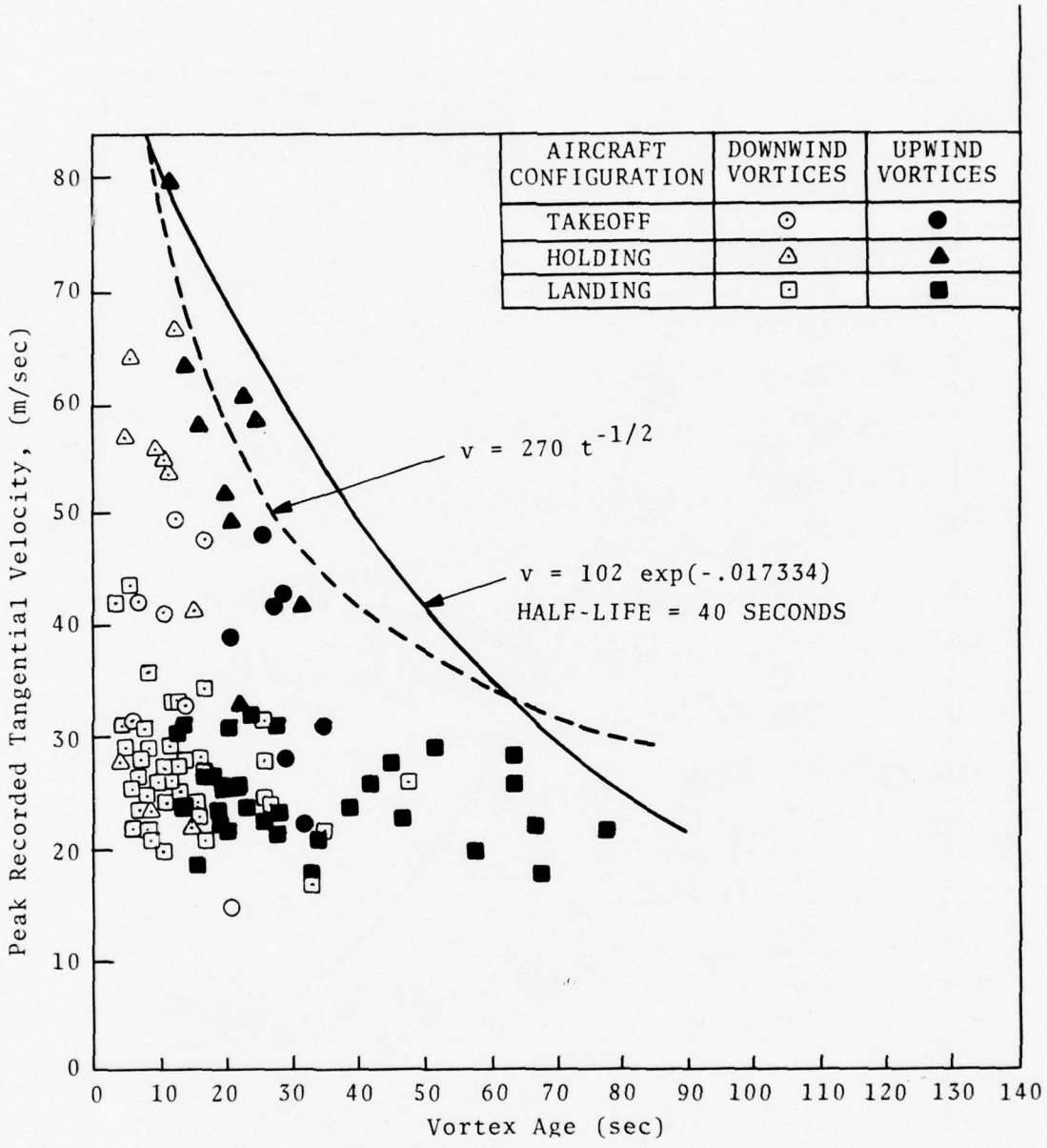


FIGURE 3-38. PEAK RECORDED TANGENTIAL VELOCITY VS AGE (ALL CONFIGURATIONS - B-747)

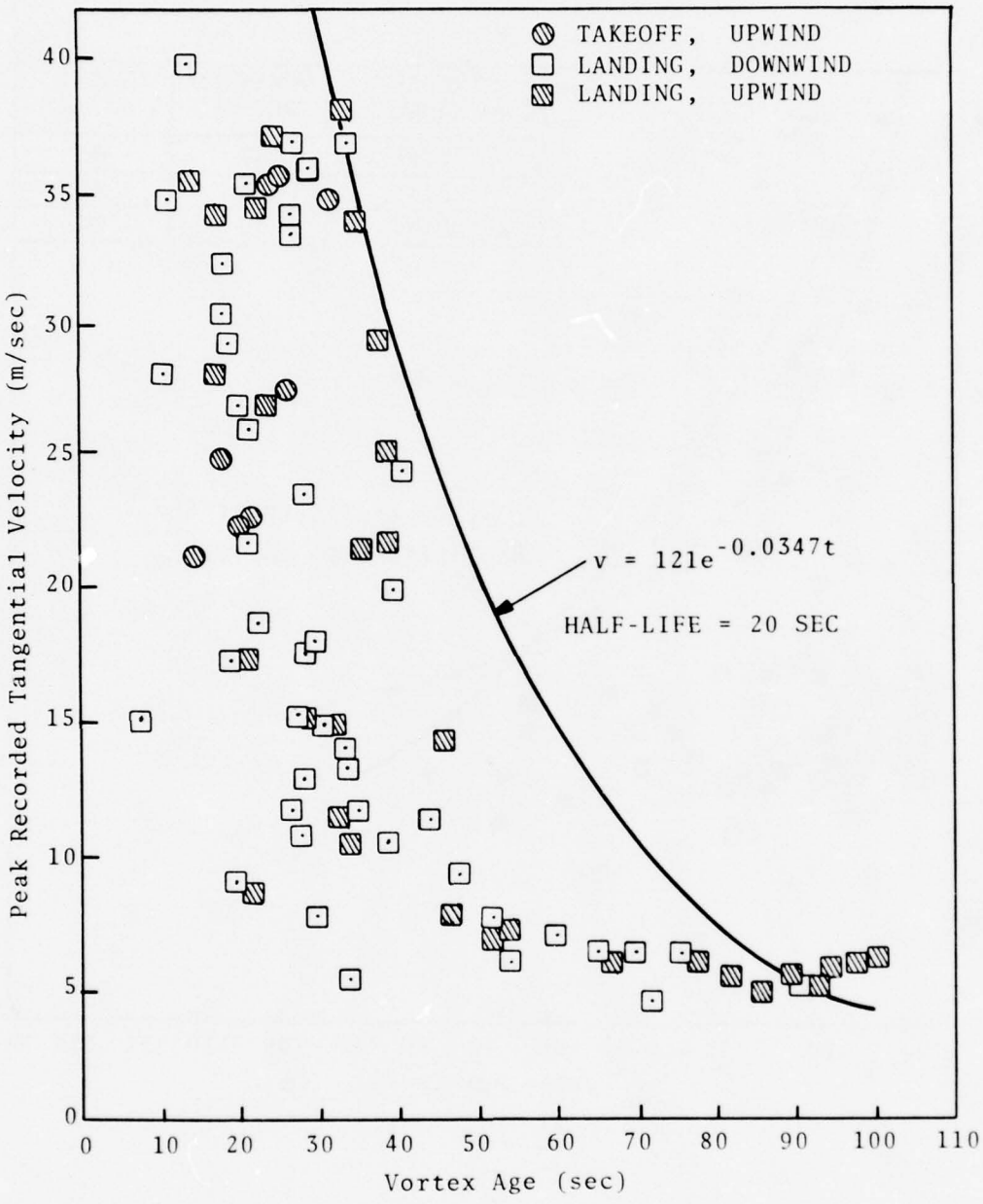


FIGURE 3-39. PEAK RECORDED TANGENTIAL VELOCITY VS AGE (ALL CONFIGURATIONS - DC-9 - SERIES 10)

the widening is manifested by the disappearance of the tracer elements. The phenomenon has been observed in the laboratory and in flight tests.

Core-bursting has been observed under many different full-scale flight conditions (for example, ref. 42) although the reasons for its occurrence are not yet fully understood (ref. 51). Figure 3-40 shows an axially moving burst (vortex breakdown) from a field experiment. Smoke was injected into the vortex core from the generator aircraft for flow visualization.

Core-bursting manifests itself as a localized "burst," or sudden increase, in diameter of the vortex core, followed by rapid travel of a conical parcel of smoke down the vortex (vortex breakdown). There is usually little or no smoke left behind the traveling region, while the density of smoke within it increases as it moves down the core. This suggests that at least some of the smoke initially in the core is swept up by it. Core-bursting often occurs spontaneously at many positions along a vortex. The axially moving bursts then quickly consume the remaining vortex segments. Initiation of core-bursting is apparently unrelated to the ambient meteorological conditions such as turbulence, stability, etc.

The qualitatively details of the breakdown are still quite obscure. In the laboratory experiments of Sarpkaya (ref. 52), the first effect seemed to be an axisymmetric disturbance under which the core expanded and contracted smoothly. Downstream a distinct spiral disturbance appeared which was then followed by a disorganized but roughly axisymmetric core widening, the final breakdown. In Tombach's flight test experiments (ref. 53), the same sequence of events seems to take place although the initial smooth axisymmetric bulging is not as distinct.

Several explanations of vortex breakdown have been proposed, and include the stagnation of the axial velocity (refs. 54 and 55), the conjugate jump theory (ref. 56), and a stability approach (ref. 57). None of these are entirely satisfactory, yet all contain common elements and all seem partially supported by experiment. It appears agreed that the rapid enlargement of the vortex core is

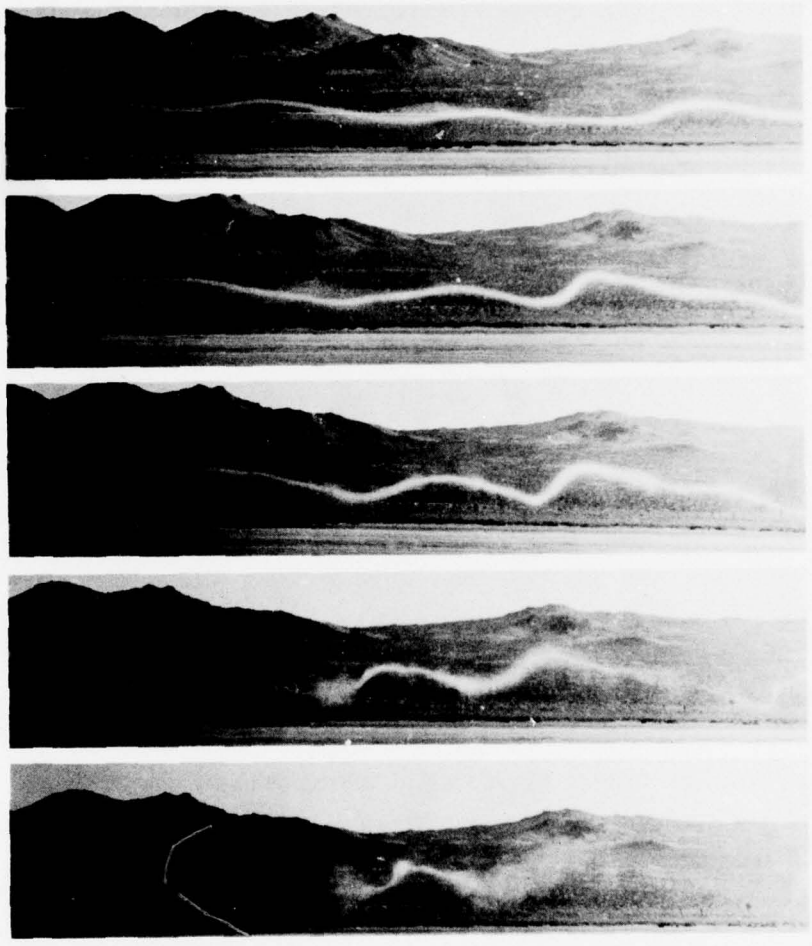


FIGURE 3-40. VORTEX BREAKDOWN CAUSED BY CORE-BURSTING

accompanied by axial pressure gradients, and that the breakdown can only occur when the flow approaches a certain critical combination of axial and tangential flow profiles. Apparently, the magnitude of the triggering adverse pressure gradient required depends upon the proximity of the flow to its critical state. It is generally agreed that dissipation and core development will cause the core to approach the critical state, so that in most cases, the core will eventually develop to a state capable of breakdown.

It appears likely that the critical state can be described crudely as a function of the axial velocity on the centerline and the swirl ratio. The swirl ratio is the ratio of the maximum tangential velocity to the freestream speed. Core-bursting seems to be strongly related to the axial velocity in the vortex core. If the critical axial tangential flow combination could be determined, then the breakdown prediction problem would reduce to testing for the critical state after computing the core development.

It appears that the core-bursting phenomenon is not related to an interaction between the left and right elements of the vortex pair, but rather to the development of the core itself, and this development is a function of the kinematic viscosity controlling the core development. Observations by Tombach (ref. 42) have shown that, at the scale of his flight test in which vortices were generated by a single engine light airplane (Cessna 170), core-bursting occurred before Crow instability in light atmospheric turbulence, while in high ambient turbulence the Crow instability invariably terminated the vortex life (because of the effect of turbulence on the onset of the Crow instability, rather than the effect of turbulence on core-bursting).

Thus, it is possible that at the same turbulence level, the time scales for core-bursting and Crow instability are related to some function of the airplane Reynolds number, which could be defined as $U_\infty b/\nu$, where U_∞ and b are the flight speed and span, and ν the kinematic viscosity. On this basis, the vortices from small slow aircraft might be expected to dissipate principally because of core bursting while those from large fast aircraft are caused by Crow

instability. Some supportive evidence is that most small-scale laboratory tests exhibit core-bursting (although Crow instability can certainly be excited), while very large-scale flight tests usually show sinuous instability.

Thus, it is possible (although not definitely substantiated) that Crow instability is the most frequent mode of decay for vortices characteristic of large transport aircraft. However under unusual or artificially perturbed circumstances, core-bursting may be important. Core-bursting is certainly the cause of vortex demise when a vortex pair tilts (e.g., because of wind shear, Section 3.3.4) and one vortex lingers after the other has been destroyed. As discussed in the next section, Crow instability requires the interaction of both vortices.

The nature and precise mechanism of vortex breakdown is still controversial. It is generally agreed that the breakdown is always associated with adverse pressure gradients, and apparently these may be either cause or effect. The conditions for breakdown to occur are related principally to the swirl ratio and the magnitude of the axial flow. No general agreement on this critical function has been reached, but both Benjamin (ref. 56) and Mager (ref. 58) give similar results which can be represented as in Fig. 3-41. The axial velocity has been expressed as the ratio of the mean core axial velocity to the free-stream flow.

It should be noted that both supercritical and subcritical states are driven by dissipation toward the critical condition, so that in general, most cores will approach the breakdown state. Note that Mager defines a further dividing line in the swirl-number axial-velocity ratio diagram above which no breakdown is possible. If the proper conditions for breakdown were known, then it would still be necessary to be able to calculate core development to determine the core state. One of the controversial factors of the calculation is the viscous transfer constant and whether it is turbulent or laminar. It is certainly extremely important in any prediction scheme since turbulent dissipation would cause breakdown an order of magnitude more rapidly than laminar flow.

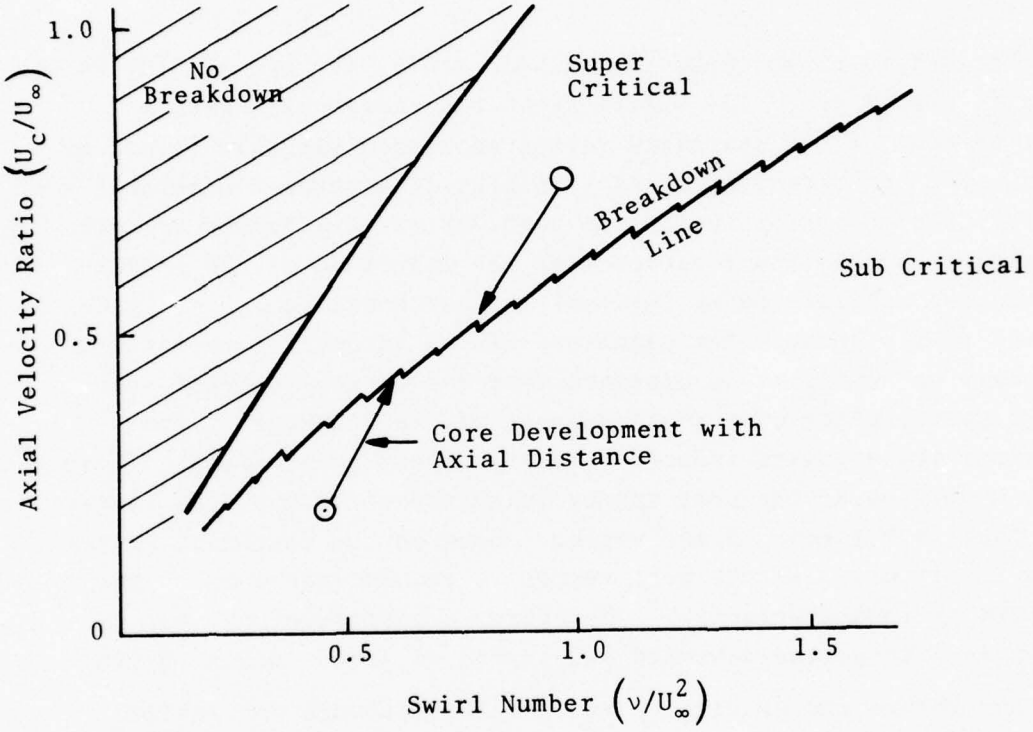


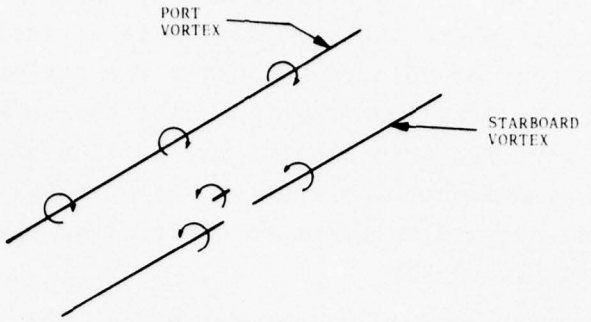
FIGURE 3-41. ESTIMATED VORTEX BREAKDOWN DIAGRAM

3.4.3 Crow Instability

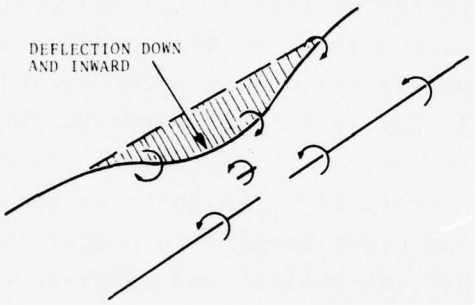
The Crow or sinuous instability is a better understood vortex-annihilation phenomenon than is core-bursting. The mutual and self-induced velocity fields associated with a perturbed pair of vortices result in a periodic, sinusoidal oscillation of the pair which is unstable with time. The initial perturbation of the vortex pair is provided by atmospheric turbulence, which continues to act as an energetic forcing function to the instability during its growth.

The origin of the Crow instability (refs. 47, 57, and 59) is shown in Fig. 3-42a. The figure shows the vortex pair with a small segment of the starboard vortex perturbed slightly inward by atmospheric turbulence. Vortex transport is a three-dimensional process; the motion of the entire port vortex is affected by each segment of the starboard vortex with the magnitude of the effect between two segments being inversely proportional to the distance between them. Because the magnitude of the tangential velocity is inversely proportional to distance from the vortex centroid, the inward perturbation of a small segment of the starboard vortex increases the downward induced velocity at the port vortex. Therefore, a portion of the port vortex is transported down at a faster rate than is the rest of the vortex. Because the starboard vortex field is circular, as the port vortex is transported down it encounters an inward velocity. Therefore, a portion of the port vortex is transported downward and inward as shown in Fig. 3-42b.

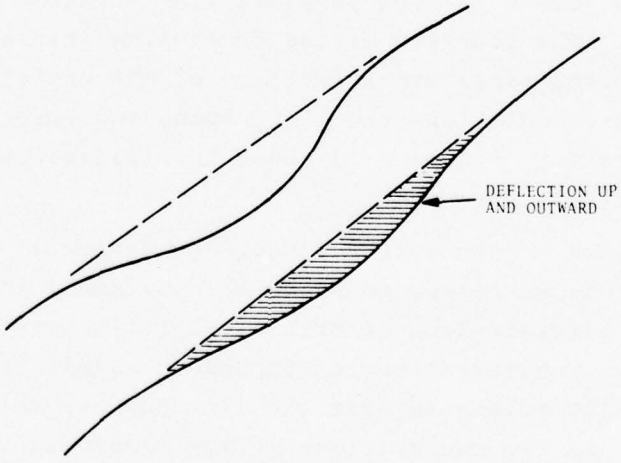
Now remove the original perturbation (although not really necessary) and examine the effect of the deflection of the port vortex upon the starboard vortex. The distance between the port and starboard vortices at the point where the port vortex is deflected is greater than that for the undisturbed vortex. Therefore, the induced downward velocity (on the starboard vortex) is smaller opposite the deflected portion of the port vortex than it is where the vortices are undisturbed. In addition, the velocity field at the starboard vortex is outward and downward at the position opposite the deflected port vortex. Thus, in comparing the induced velocity field on the starboard vortex by the deflected and



(a) ORIGINAL VORTEX PAIR WITH SMALL PORTION OF STARBOARD VORTEX PERTURBED BY ATMOSPHERIC TURBULENCE



(b) EFFECT OF PERTURBATION OF STARBOARD VORTEX UPON PORT VORTEX



(c) EFFECT OF DEFLECTION OF PORT VORTEX UPON STARBOARD VORTEX (WITH ORIGINAL PERTURBATION REMOVED)

FIGURE 3-42. MECHANISM OF CROW INSTABILITY

undeflected portions of the port vortex: (1) there is an outward component of velocity where the port vortex is deflected, and (2) the downward component of velocity opposite the deflected portion of the port vortex is less than that opposite the undeflected portion of the port vortex. Accordingly, the portion of the starboard vortex opposite the deflected portion of the port vortex is deflected upward and outward relative to the rest of the starboard vortex as shown in Fig. 3-42c.

Although the initial deflections are small, the process continues in an unstable manner, causing the magnitude of the deflection to grow. The resulting instability manifests itself as a (roughly) sinusoidal oscillation of each of the two vortices. The two vortices oscillate in planes inclined at approximately 45 degrees to the vertical, roughly resembling a "V"-shaped trough, as shown in Figure 3-43. As the instability develops with time, the vortices move closer together at the bottom of the trough and further apart at the top. Eventually, the vortices touch at the bottom (called "linking") and cross connect such that they mutually annihilate themselves at the link points, and discreet vortex rings are formed from the remaining portions of the vortices between adjacent link points. Thus, because of the instability, the wake has been changed from a pair of parallel line vortices to a series of vortex rings. The geometry of the developing instability and the resulting vortex rings are a function of the undisturbed vortex pair spacing and circulation (the lift, span, and speed of the generating aircraft). Figure 3-44 shows the initiation and the formation of vortex rings.

Upon formation of the vortex rings, the danger associated with vortex encounter is much reduced since the sustained rolling moment on an encounter aircraft because of a straightline vortex is no longer possible. Subsequent vortex breakdown within the rings themselves (usually initiated near the link points) quickly causes the dissipation and the overall loss of any remaining wake identity.

The time required for operation of the catastrophic decay modes (after passage of the generator aircraft) has been examined experimentally (ref. 51). The general results of these experiments

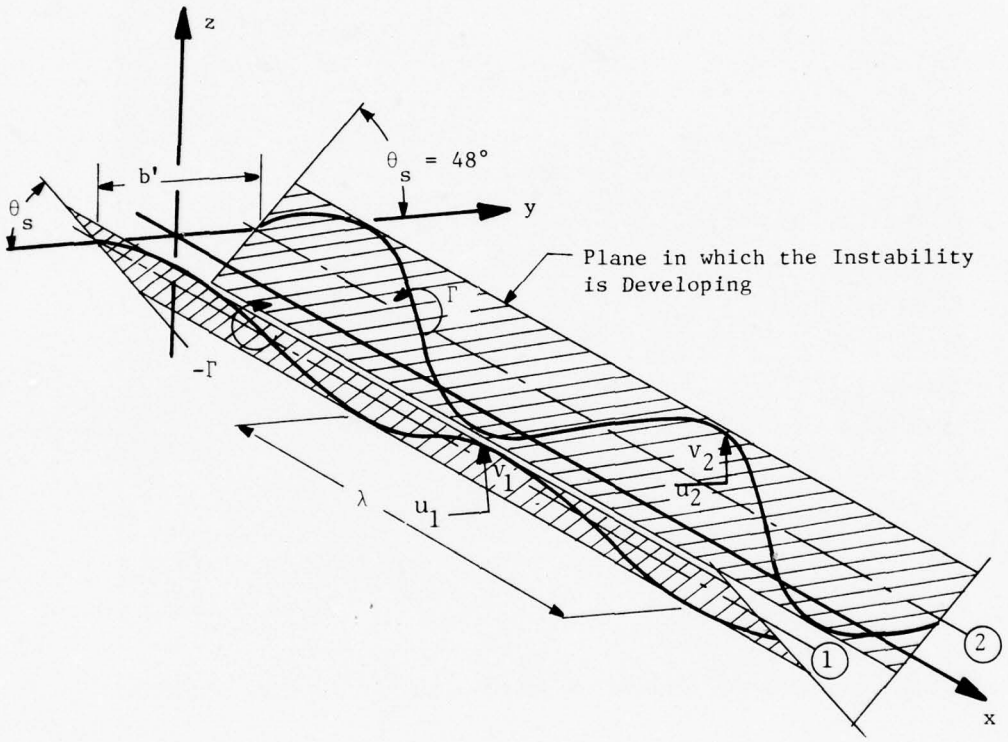


FIGURE 3-43. GEOMETRY OF THE OSCILLATING VORTEX PAIR. THE VORTICES ARE VIEWED FROM ABOVE, AND THE GENERATING AIRCRAFT LIES BEYOND THE UPPER LEFT-HAND CORNER OF THE FIGURE

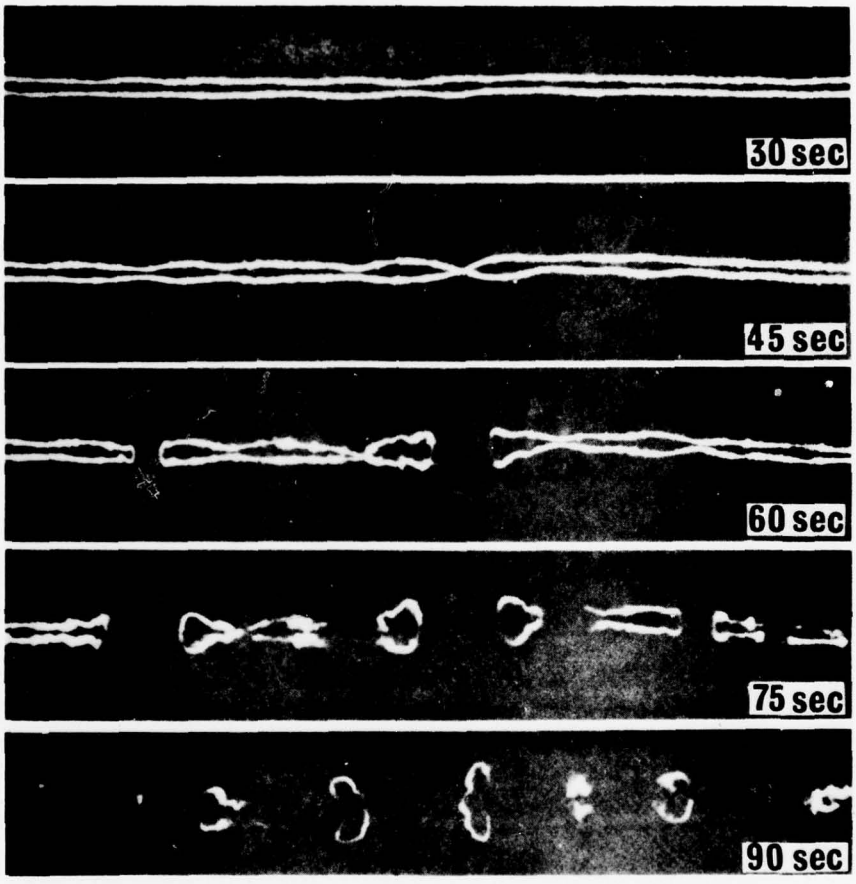


FIGURE 3-44. THE DEVELOPMENT OF THE CROW-LINKING PHENOMENON FROM AN OVERHEAD FLYING B-47

showed that core-bursting is apparently unrelated to ambient meteorology, while the time at which linking occurred for the Crow instability is a strong function of atmospheric turbulence, and corresponded well to the theory of Crow and Bate (ref. 59). In all cases, the Crow instability sets the upper limit on wake lifetime and hence is probably operationally significant. Turbulence hastens vortex demise through Crow instability by two mechanisms. First, turbulence causes an unsteady lift on the wing which results in a non-uniform vortex in the axial direction. Second, atmospheric turbulence provides the initial perturbation to start the Crow instability.

The time to link for the Crow decay modes can be expressed as a function of the properties of the undisturbed wake and the level of atmospheric turbulence, expressed as the rate of dissipation of turbulent energy, ε. Since atmospheric turbulence initiates the instability, the time to link may be expected to be a strong function of atmospheric turbulence. Thus for a given generator aircraft (fixed wake properties), the time to link can be directly determined from knowledge of ε in the region of interest.

Figure 3-45 shows representative times and distances downstream from various aircraft at which linking will occur. It should be mentioned that the values shown correspond only to the situation at which linking is just initiated and the vortex rings are formed. The additional short time required for complete destruction of the wake because of vortex breakdown on the rings has not been included. Also the values were computed at infinite altitude, so that ground effects were not included. The gross weight and speed of the aircraft were assumed for landing configuration although the vortex separation was for an unflapped, elliptically loaded wing. The numbers presented in the figure should thus be considered representative of vortex linking only and should not be interpreted to signify the termination of encounter danger. The values shown were derived using the theory of Crow and Bate, and therefore, do not represent actual measurements. In general, the Crow-Bate theory shows that, in a given boundary layer, the net effect of ground proximity is to shorten wake lifetime, but by no more than 10 percent.

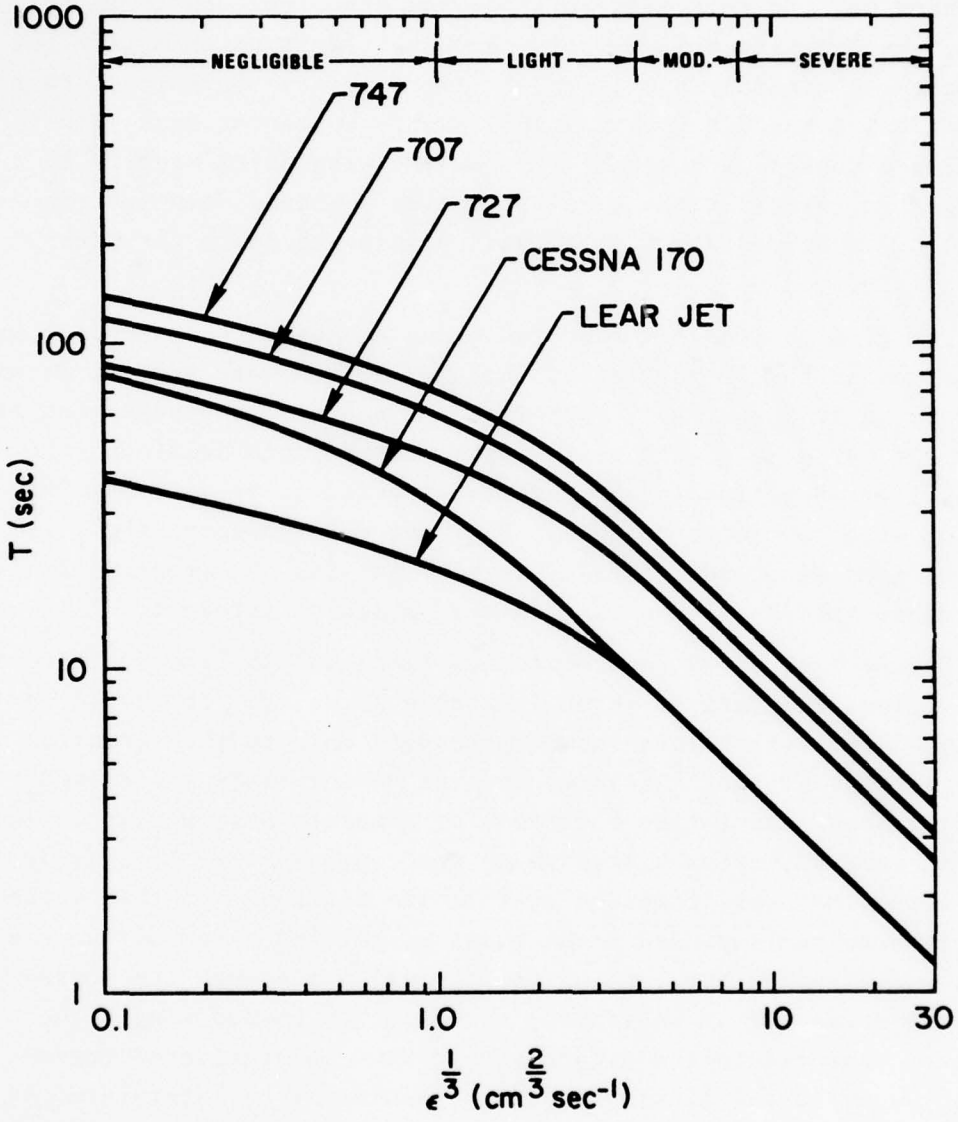


FIGURE 3-45. TIME TO VORTEX LINKING, T, AS A FUNCTION OF ATMOSPHERIC TURBULENT DISSIPATION RATE, $\varepsilon^{1/3}$.

In general, turbulence increases as wind speed increases. Therefore, vortex lifetime may be expected to decrease as the wind speed increases. Such a criterion has been postulated by McGowan (ref. 60) and is shown in Fig. 3-46. Superimposed on the plot are B-747 (from ref. 27) and CV-880 data points (ref. 34). It is believed that the envelope is very conservative as the altitude is reduced, particularly for the downwind vortex in ground effect. (Section 8 examines the McGowan curve in the light of new data.)

It should be noted that wake decay near the ground is a complicated phenomenon which currently cannot be expressed analytically. Surface winds, wind shear, and turbulence sometimes act in concert to distort and stretch the vortices into highly convoluted shapes. The mutual interactions of the vortices and their images along with ground-generated dissipation and decay because of core-bursting and Crow instability further complicate the behavior of the vortices. (Recent measurements of vortex decay near the ground are discussed in Section 8.) Figure 3-34 showed an example of a situation during a low pass near the ground during an experimental field test with smoke-marked vortices. It can be seen that the prediction of the location and strength of the vortices at any given ground station along the aircraft flight path would be difficult to express in an analytical form. For this reason, the statistical analysis of the wake behavior will be quite important in the formulation of a reliable predictive model.

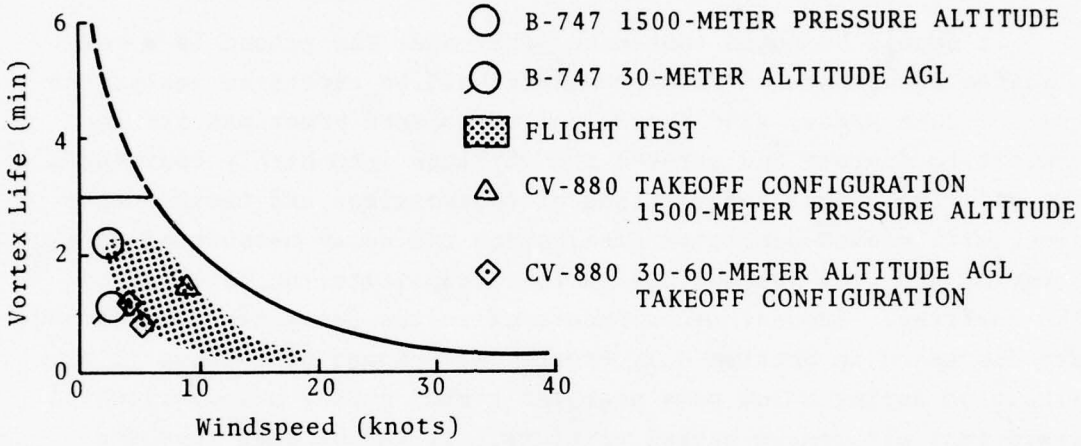


FIGURE 3-46. VORTEX PERSISTENCE AS A FUNCTION OF AMBIENT WINDSPEED AND HEIGHT ABOVE THE GROUND

4. AERODYNAMIC MINIMIZATION

Aerodynamic Minimization is the general term used to describe modifications made to the airframe of the generating aircraft for the purpose of decreasing the effect of trailing vortices upon a following aircraft. The goal of aerodynamic minimization is to decrease the allowable longitudinal spacing between aircraft by modifying the vortex structure in such a way that if a vortex encounter does occur, the resulting upset will not exceed the control authority of the following aircraft. Aerodynamic alleviation is achieved by modification of the spanwise wing loading or by the generation of turbulence behind the generating aircraft. The major techniques of aerodynamic alleviation are outlined in this section. For a complete discussion on the various alleviation techniques, see the recently released "NASA Symposium on Wake Vortex Minimization" published by NASA as SP-409.

4.1 VORTEX ALLEVIATION CRITERIA AND TESTS

Most of the vortex-wake alleviation work in the United States has been conducted by NASA. A reasonably consistent set of effectiveness criteria and test procedures have evolved.

4.1.1 Vortex Alleviation Effectiveness Criterion

A simple and reasonably accurate criterion is needed to compare alleviation techniques as well as to evaluate the rolling moment hazard posed by wakes of existing aircraft. A vortex alleviation effectiveness criterion (ref. 61) which is approximated fairly well by inviscid theory is the estimation of the rolling moment on a wing of a following aircraft as it encounters a wake vortex of a generating aircraft. For wind-tunnel tests and analytical evaluations, the parameter which is used as an indicator of the severity of upset is the ratio of the rolling moment imposed upon the following aircraft by the vortex divided by the maximum rolling moment which can be generated by the following aircraft at full aileron deflection. The aircraft is assumed to be controllable if

the ratio is less than unity, and uncontrollable if the ratio is greater than unity. For the maximum degree of upset, the following aircraft is placed in the vortex so that the axis of the aircraft coincides with the axis of the vortex. For in-flight vortex encounter tests, the encounter criterion is the ratio of the vortex-imposed angular acceleration to the angular acceleration of the following aircraft at full aileron deflection.

The NASA studies related to wake vortex alleviation have been primarily restricted to axial penetrations of the vortex; cross-vortex penetrations were rarely studied. A cross-vortex encounter is not necessarily less hazardous than an axial encounter, but the entry into the vortex along the axis is the most likely to occur during landing and takeoff operations. If the flight path of the following aircraft is along or only slightly off axial, the flow field is approximated by steady-state theories.

The schematic diagram in Fig. 4-1 indicates the way in which the rolling moment on the following wing is analyzed. The axial or streamwise velocity is assumed equal to the free-stream velocity. The vertical components of the circumferential velocities in the vortices are used as the upwash or downwash on the follower wing by adding the contributions of the one or more pairs of vortices in the wake. The torque on the following wing is then reduced to coefficient form by

$$C_{m_f} = \frac{\text{rolling moment}}{(1/2)\rho U_\infty^2 S_f b_f} \quad , \tag{4.1}$$

where S_f and b_f are the wing area and wing span of the follower aircraft, respectively. The torque or rolling moment on the encountering wing may be calculated (ref. 62) by: two-dimensional strip theory, strip theory with empirical lift-curve slope correction, or vortex-lattice theory (flat-wake approximation).

The two-dimensional strip theory for the rolling moment assumes that the lift on each spanwise wing element is given by its two-dimensional value or

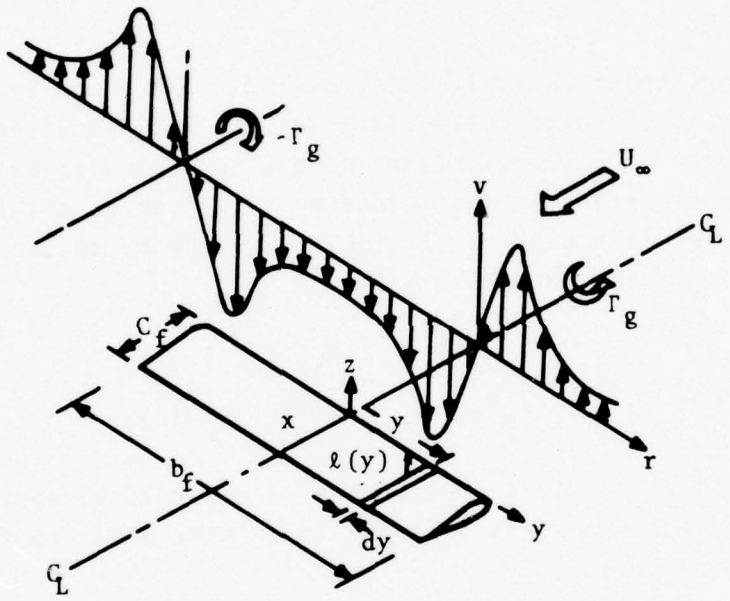


FIGURE 4-1. WAKE VORTEX PAIR IMPINGING ON A FOLLOWER WING.

$$\ell(y) = C_{L_\alpha} (\sin \alpha) \frac{1}{2} \rho U_\infty^2 c(y) \quad , \tag{4.2}$$

where C_{L_α} is the two-dimensional lift-curve slope of the airfoil section at the spanwise station y, $\sin \alpha \approx W/U_\infty$ is the flow inclination, and c(y) is the local chord of the wing. When the quantity $y\ell(y)$ is integrated across the span of a rectangular wing, the rolling-moment coefficient becomes

$$C_{m_f} = \frac{C_{L_\alpha}}{b_f^2} \int_{-b_f/2}^{b_f/2} (W/U_\infty) y \, dy \quad . \tag{4.3}$$

The values presented in Table 4-1 (ref. 62) were found by integrating equation (4.3) numerically after setting W/U_∞ equal to the sum of the measured v/U_∞ contributions of the left- and right-hand vortices. A different form of equation (4.2) can be obtained when only one vortex is acting on the following wing by setting $W/U_\infty = v/U_\infty = \Gamma/2\pi r U_\infty$ and with y = r:

$$C_{m_f} = 2 \left(\frac{C_{L_\alpha}}{2\pi} \right) \left(\frac{b_g}{b_f} \right)^2 \int_0^{b_f/2b_g} \left[\frac{\Gamma}{b_g U_\infty} \right] d\left(\frac{r}{b_g} \right) \quad . \tag{4.4}$$

Although equation (4.4) is sometimes more convenient, equation (4.3) is used because it is believed to be more accurate for the wakes being considered.

For two-dimensional wings, the theoretical value of C_{L_α} is usually used ($C_{L_\alpha} = 2\pi$). As noted in Table 4-1, the predictions made with $C_{L_\alpha} = 2\pi$ are generally too high because it does not account for the induced angles of attack near the wing tips and near the vortex centerline. An empirical relationship for the lift-curve slope to be used in the calculation of torque may be obtained by use of the formula introduced by Jones and Cohen (ref. 63)

$$C_{L_\alpha} = \frac{2\pi \, AR}{P \cdot AR + 2} \quad , \tag{4.5}$$

TABLE 4-1. COMPARISON OF PREDICTED AND MEASURED ROLLING-MOMENT COEFFICIENTS

Configuration	α deg	C_{L_g}	b_f/b_g	AR_f	Normalized Rolling Moment, C_{m_f}/C_{L_g}			
					Measured	Strip Theory		Vortex-Lattice Theory
						$C_{L_\alpha} = 2\pi$	Empirical C_{L_α}	Flat-Wake Approximation
Flaps 0°	8	0.75	0.29	5.84	0.092	0.222	0.110	0.109
Flaps 0° plus spoiler	8	0.70	---	---	0.053	0.184	0.091	0.085
Landing	6	0.85	---	---	0.081	0.243	0.120	0.117
Landing plus spoiler	8	0.86	---	---	0.081	0.163	0.081	0.071
Tailored	10	0.82	---	---	0.105	0.246	0.122	0.111
Flaps 0°	8	0.75	0.14	2.82	0.099	0.317	0.101	0.090
Flaps 0° plus spoiler	8	0.70	---	---	0.023	0.154	0.049	0.038
Tailored	10	0.82	---	---	0.074	0.173	0.055	0.042

where AR is the aspect ratio and P is semiperimeter/span. Comparing the rolling moment calculated by vortex-lattice theory and by strip theory with several versions of equation (4.5); it is concluded that the span, aspect ratio, and perimeter in equation (4.5) should be interpreted on the basis of half a wing when the vortex and wing center are alined. It is reasoned that each half-wing then acts as a separate wing, and equation (4.5) should be interpreted accordingly. For the rectangular wings studied here, equation (4.5) then becomes

$$C_{L_\alpha} = \frac{2\pi\ AR_f}{AR_f + 6} \quad . \tag{4.6}$$

The strip-theory predictions corrected for C_{L_α} by equation (4.6) are noted in Table 4-1 to be in good agreement with the vortex-lattice theory and in fair agreement with experiment. The vortex-lattice theory used is a version of Hough's (ref. 64) and of Maskew's (ref. 65) methods adapted to the present situations. The differences which occur between the vortex-lattice theory and experiment may be caused by any of the following: differences in the interpretation of the measured rolling moments; differences in the vortex velocity data (e.g., large axial velocities), a combination of both, or unsteady aspects of the wind-tunnel measurements because of meander of the vortex which were assumed negligible. Nevertheless, the foregoing results indicate that either the vortex lattice theory or the simple strip theory with C_{L_α} determined by the Jones-Maskew formula provides reasonable estimates for the rolling moment induced by a vortex on a follower wing.

With the empirically adjusted strip theory, the rolling moment and lift on a wing can be calculated for the aircraft axis located at any point in the wake. Calculation of rolling moment and lift for a large number of points (i.e., position of the aircraft axis with respect to the vortex axis) enables generation of contours of equal rolling-moment coefficient and lift (ref. 61). The maximum rolling moment occurs when the encountering wing is centered approximately on the vortex. Aircraft typically have the control capability to create a rolling-moment coefficient of 0.04 to 0.06, so

that any imposed torque by a vortex which causes C_{m_f} to exceed about 0.06 will cause the encountering aircraft to roll even when full counter-roll control is imposed. Large values of positive and negative lift are induced on the follower by the vortex wake, depending on its location relative to the vortex pair. The shapes of the curves of constant torque and lift change with both the vortex structure and with the span of the follower. The dependence of the rolling moment on distance behind the generating aircraft is not discussed because downstrean changes in the structure of a two-vortex-developed wake depend largely on viscosity and turbulence.

4.1.2 Ground-based Testing Procedures

The purpose of ground-based vortex testing is to evaluate the many devices and concepts which have been proposed to alter vortex formation and decay (ref. 66). NASA decided that evaluation testing should be limited to those facilities which can recreate, in model scale, an actual vortex-penetration situation. It was further decided that the facilities should have common models, a standard measurement and technique, and be capable of providing a model Reynolds number based on the generating model chord on the order of 0.5 million or greater. The facilities selected included the 12- by 24-meter wind tunnel at NASA's Ames Research Center, the V/STOL wind tunnel at Langley Research Center and the Hydronautics Ship Model Basin in Laurel, Maryland.

In addition, the inactive 550-meter towing basin at Langley was modified with a new overhead carriage system to provide a towing system using air as the test medium in lieu of water as is used at the Hydronautics facility. The models selected include a 0.03-scale Boeing 747 transport as the generating aircraft and two trailing wing models representing, in span and aspect ratio, a small jet transport and a business jet as the follower aircraft. Each facility has the capability to generate a vortex system and to measure directly the induced rolling moment of the vortex on the trailing models.

The standard test procedure involved generation of a vortex system in the ground facility and surveying the flow field at various distances downstream using a roll balance equipped following model as a sensor. Although it is recognized that the technique represents only one of many types of penetrations likely to occur in a real situation, it does represent the one judged to be most hazardous from a pilot/control standpoint. It is also believed safe to assume that large reductions in the induced rolling moment measured by this technique are indicative of reductions in the severity of other upset situations. The generating aircraft are mounted in the V/STOL and 12- by 24-meter tunnels in the most forward position of the test section and the probe model surveys the vortex field at discrete downstream locations.

Because the generating models are stationary and the airstream is moving, the probe model can sense the vortex at a given position over a long period of time. Typical sample periods ranged from 10 to 40 seconds. Rolling-moment data in the V/STOL tunnel were sampled once per second and averaged over the sample period while the 12- by 24-meter tunnel data selected only the highest peak within the sample period. Comparison of the two analysis techniques, using data from the V/STOL tunnel taken at 7.5 span lengths downstream with the large probe model, indicated approximately 10-percent higher values using the peak measurements over the averaged measurements. It would be expected that the difference measured with the smaller model or at greater distances downstream with either model would be greater because of the meandering of the vortex.

In the towing facilities, both models are moving and the data-recording time is limited. A normal test run in the Hydronautics facility was approximately 25 seconds which provided about 15 seconds for a single vertical survey through the vortex. In the vortex-flow facility, the probe model is positioned prior to the run, and the sample time is approximately two seconds. In both the Hydronautics and vortex-flow facilities, the highest peak data per sample were used.

4.1.3 Flight-Test Techniques

Flight tests have played an important role in the coordinated research program to develop wake vortex alleviation techniques. The contribution of flight testing to the program lies in three important areas: to verify that the more flexible and less expensive ground-based research facilities are suitable for the development of vortex alleviation devices and techniques; to identify, under full-scale conditions, shortcomings of any alleviation technique which might not have been evident in the small-scale test environment; and to assess the operational feasibility of the developed techniques. The operational feasibility phase has two facets. The first is the influence of the alleviation device on the operation of the generating aircraft. The second is to demonstrate the level of alleviation attained in the operational situation. Primary emphasis has been placed on the latter.

Recent flight experience has emphasized the importance of flight tests in complementing and focusing the research efforts in the ground-based facilities. As a result of wind-tunnel studies at Ames and Langley Research Centers, it was discovered that raising the outboard flap segment in the landing configuration of a Boeing 747 markedly reduces the rolling moments induced on a following model (ref. 67). Flight tests confirm that the vortex-induced upset can be reduced substantially through this flap modification. However, the flight-test results show that the alleviation is greatly diminished when the landing gear is extended (ref. 68). The effect of gear was unexpected, and hence, had been overlooked in the wind tunnels. The flight test, therefore, had two important effects; i.e., confirming that the wind-tunnel test results were meaningful, and focusing future research on configurations which provide alleviation in the presence of a lowered landing gear.

Three flight-test techniques for wake turbulence research have evolved. The development of these techniques was initiated before the vortex-wake alleviation program, so that the hazards associated with the vortex systems could be documented from a number of jet

aircraft. The three techniques are flow visualization, upset measurements of encountering aircraft, and velocity profile measurements.

Flow visualization is useful in comparisons of various alleviation configurations. However, the primary value of flow visualization is to make it feasible for the pilot of a probe aircraft to locate the vortex and to penetrate its core so that the other two techniques can be applied. Historically, the first flow visualization simply relied on the entrainment of the jet exhaust in the vortices. This system was marginally successful for the tightly rolled-up vortex systems generated by transport aircraft in the cruise configuration and, for some aircraft, in the landing configuration. However, for most aircraft in the landing configuration with or without alleviation, specially developed flow-visualization techniques must be used. As might be expected, the more effective an alleviation technique is in eliminating or spreading the organized flow within the wake, the more difficult it becomes to mark the wake effectively.

Measurements taken to derive the moments induced on an aircraft subjected to wake vortices have become known as "upset measurements." Actually, it is necessary to measure more than simply the upset of the probe aircraft. The control inputs, angular rates, airspeed, and angles of attack and sideslip must be known to account for those angular accelerations resulting from the aerodynamic characteristics of the probe aircraft. The separation distance between the two aircraft and the encounter altitude are also required to correlate the data.

Upset measurements are taken with the flight path of the probing aircraft nominally parallel to the vortex axes (hence, the name "parallel probes"). When probing the wake of an unfamiliar configuration, the initial encounter with the wake is made at a separation distance large enough to ensure that the resulting forces will not severely load the structure of the aircraft. As the probe aircraft encounters the wake, the pilot performs his task in one of two modes. He can hold the controls fixed, allowing the upset to remove the aircraft from the wake, or he can attempt to hold the

probe airplane as nearly centered in a vortex as possible. Either action produces the desired data, but the pilot may obtain more subjective information by using a combination of the two. The procedure is repeated several times at each separation distance to increase the probability that the maximum possible induced accelerations of the probe aircraft were achieved.

The instrumentation used to obtain the data required to derive the induced moments is, generally, that which would be typical for a study of handling qualities. The three-dimensional aircraft dynamics are measured by angular accelerometers, rate and attitude gyros, and linear accelerometers. The deflections of the control surfaces are measured as are airspeed, altitude, angles of attack and sideslip, and separation distance.

A roll-acceleration parameter, convenient for comparative purposes, was developed to relate the vortex-induced roll acceleration, $\dot{P}_{vortex}$, to the maximum roll-acceleration capability of the aircraft using maximum aileron deflection $\dot{P}_{\delta a_{max}}$. The ratio $\dot{P}_{vortex}/\dot{P}_{\delta a_{max}}$ indicates the magnitude of the induced moment. The physical meaning of this parameter is that, when a value of unity is reached, the pilot could exactly counter the vortex-induced roll acceleration with maximum deflection of the ailerons. Similar parameters can be determined for accelerations in the pitch and yaw axes. For each encounter behind a given configuration, the peak values of the roll-acceleration parameter are plotted against the separation distance at which they occurred as in Fig. 4-2. Assuming that the highest values at each distance represent the maximum upset expected at that location, an upper bound to the data is constructed. The separation distance defined by the intersection of that boundary and the line for a unity roll-acceleration parameter is used in comparisons with values obtained in a similar manner from data obtained during tests of other aircraft or configurations.

The need for more definitive information on the wake vortex phenomenon led to the development of another flight-test technique. Use of this technique results in measurements of the velocity profiles in the wake, which will allow comparisons of the wake

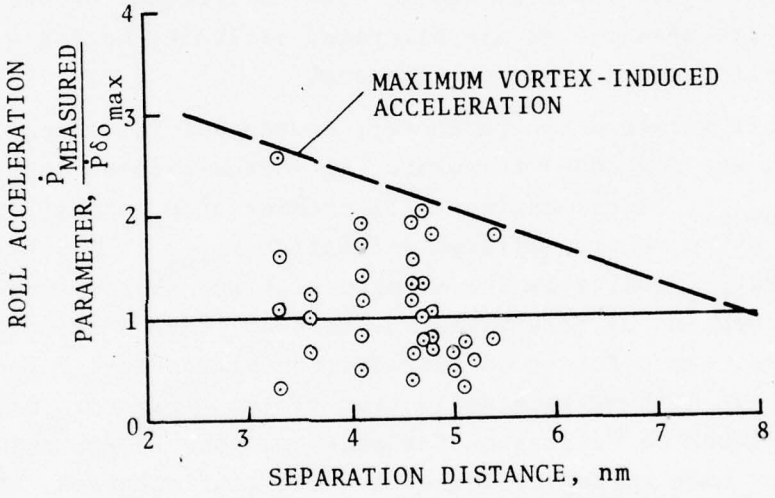


FIGURE 4-2. ROLL ACCELERATION PARAMETER VERSUS SEPARATION DISTANCE FOR A LEARJET IN A B-747 WAKE; B-747 WITH FLAPS DOWN, GEAR UP, THRUST FOR LEVEL FLIGHT, C_L = 1.4

structure with theories. This can be especially useful in the wake alleviation work by more clearly defining the changes in the wake structure caused by an alleviation technique.

The measurements require a completely different technique in procedure, instrumentation, and data reduction. The flow velocities must be measured by sensors with higher frequency-response characteristics than normally used in handling qualities research, and the aircraft motion must be measured for use in correcting the velocity data. The separation distance is again required to correlate the data.

The flight test procedure used to obtain velocity profile data is considerably different from that used during upset measurements (Fig. 4-3). The flight path of the probing aircraft is across the wake to traverse effectively the flow field with the velocity-measuring probe. Ideally, the flight path should be in a plane perpendicular to the wake axes to minimize the motion excursions for which corrections must be made. The limited capability of the flow visualization systems to mark the wake results in an inability to see the wake well enough from right angles to enable the pilot of the probe aircaft to penetrate the vortex cores consistently. As the crossing angle is reduced, the apparent density of the flow-visualization medium is increased, thereby allowing consistent core penetrations. Local atmospheric conditions and the angle of the sun relative to the two aircraft affect visualization as well. Experience has shown that crossing angles of from 25 to 45 degrees are adequate for the task. The lower crossing angles have the additional advantage of allowing a shorter time between crossings because a turn of only 50 to 90 degrees is required to traverse back across the wake. The saving of time between wake crossings allows more data to be obtained in the amount of time allowed by the flow-visualization system.

As with the upset-measurement procedures, wake encounters are begun at separation distances large enough to assure safe operations. A zigzag flight path is flown while the separation distance is continually reduced until a predetermined minimum separation

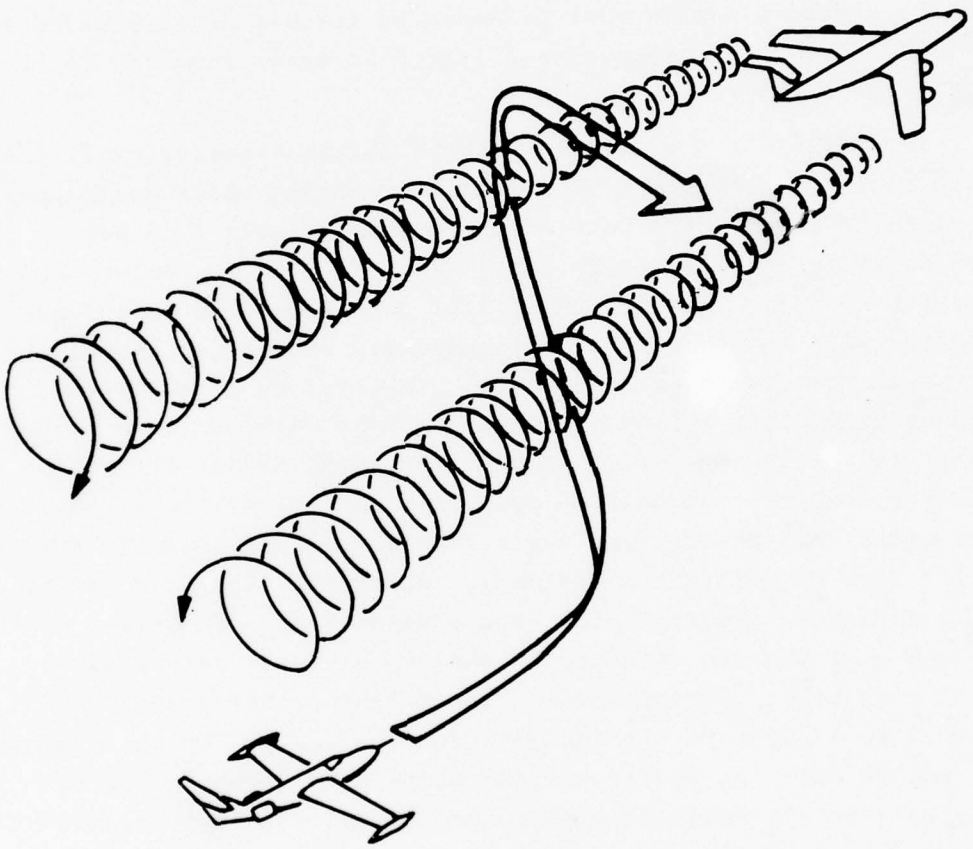


FIGURE 4-3. PROBE AIRCRAFT FLIGHT PATH DURING VELOCITY PROFILE MEASUREMENTS OF VORTEX WAKE

distance is reached. This minimum separation distance is set for safety reasons and, as for upset measurements, is based on computed loads, extrapolated load measurements, or probe pilot decisions. Once the minimum separation distance is reached, a 360-degree turn which sets the probe aircraft up for additional data at a larger separation distance is initiated. The procedure is repeated several times until adequate data are acquired for that vortex-generating aircraft configuration.

The velocity profile measured at a separation distance of 2.9 nautical miles behind a B-747 in its normal landing configuration is presented in Fig. 4-4. All three components of velocity are shown, the top one being the vertical velocity component defined as positive upward, the middle trace is the lateral component defined as positive to the left, and the bottom trace is the axial velocity component defined positive toward the aircraft which generated the wake. Comparing these data with those of the next figure demonstrates the ability of the system to show the effects of vortex-wake alleviation in the measured flow field. A comparison of Figs. 4-4 and 4-5 indicates the reduction in the three components of velocity in the wake of the B-747 at 2.2 nautical miles with the outboard flaps retracted.

Early Flight Tests - A Boeing B-747, a Lockheed L-1011, a McDonnell-Douglas DC-10, and an Air Force C-5A made flights in 1970 past FAA-instrumented towers at Idaho Falls, Idaho, and at the FAA's NAFEC installation in Atlantic City, New Jersey. The size and intensity of the wake vortices generated by aircraft ranging in size from the Lear jet to the C-5A and B-747 were studied to determine the effects of aircraft configuration, weight, speed, and atmospheric parameters. Colored smoke was used to make the vortices visible while sensitive instrumentation attempted to measure the size and strength of the wake vortices near the ground. Some of these measurements have been reported (refs. 27, 32, 34, 36, and 38).

High-altitude penetrations of wake vortices were performed by the FAA at NAFEC using C-141's and CV-880's in the late 1960's

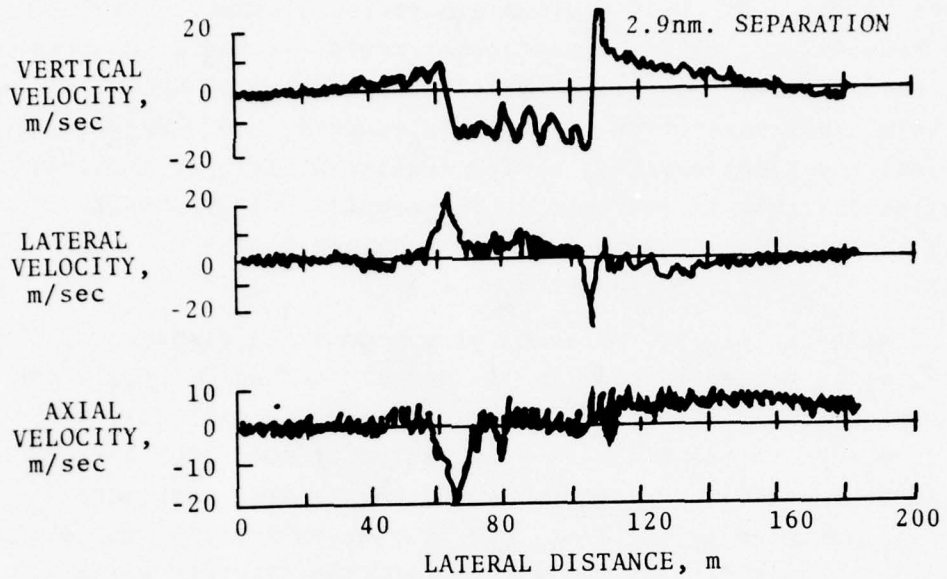


FIGURE 4-4. VERTICAL, LATERAL, AND AXIAL VELOCITY COMPONENTS IN THE WAKE OF A B-747 IN LANDING CONFIGURATION

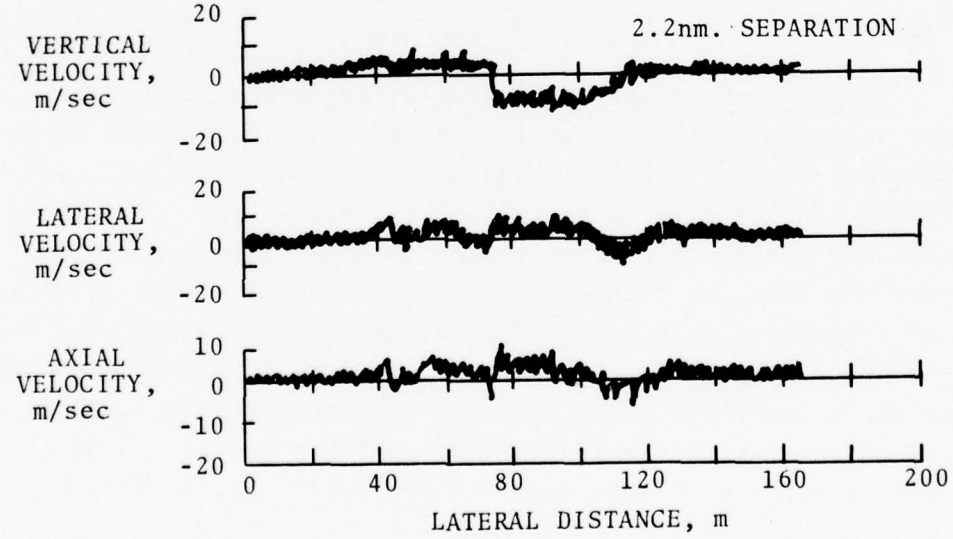


FIGURE 4-5. VERTICAL, LATERAL, AND AXIAL VELOCITY COMPONENTS IN THE WAKE OF A B-747 WITH OUTBOARD FLAP RETRACTED

(ref. 69). Flight at high altitudes has a natural advantage in that contrails automatically mark the vortex trail, but operating conditions at high altitudes are not representative of the conditions which prevail for terminal area operations involving takeoff and landing. Early attempts to conduct wake vortex penetrations during actual landing approach involved considerable risk, so subsequent investigations were performed at altitudes above the ground which were safe yet permitted the operational conditions which exist at takeoff and landing to be duplicated.

The first major program of this type was conducted in early 1970 at the NASA Flight Research Center at Edwards Air Force Base. The flight-test program was intended to make determinations in flight of the effects of the vortices on following airplanes. Carefully instrumented probe airplanes, such as the DC-9, Cessna 210, CV-990, Learjet, and F-104, flew into the vortices behind the C-5A and CV-990 at various weights, speeds, and configurations. The probe airplane responses served to measure vortex strength and made it possible to determine the effect of the vortex wake on airplane control and pilot response in all axes.

The second major flight-test program focused on the wide-bodied trijets and was conducted by an FAA/NASA/Air Force/industry test group in November of 1972. The strength of the vortices generated by a wide-bodied trijet, the DC-10-40, was compared with the strength of the vortices generated by a previously investigated C-5A. The wakes were probed by an instrumented DC-10-10, a L-1011, a DC-9, and a Learjet 23.

The third major flight-test program in the series was intended primarily to investigate changes in the wake vortex characteristics because of the higher initial rate of descent associated with two-segment noise-abatement approaches (ref. 70). A Boeing 727-200 equipped with two-segment approach instrumentation was used as the generator aircraft. The probe aircraft were the Learjet and PA-30 aircraft.

The fourth test program (ref. 71) involved probing the wake of a B-747 with a Learjet and a T-37B. The T-37B had the instrumentation to measure airplane/pilot response and, for the first time in the wake vortex tests, it was equipped with strain gages to determine the actual loads imposed on the aircraft structure in flight. The primary objective of this program was to obtain full-scale data for comparison with wind-tunnel and water-channel tests conducted at the NASA Ames and Langley Research Centers, which predicted that the wake vortex strength of the B-747 could be alleviated if greater inboard flap and lesser outboard flap deflections were used to obtain the same lift coefficient.

4.1.4 Unsuccessful Minimization Techniques

A number of active devices have been tested to determine their suitability in aircraft wake vortex minimization. Here, the vortices are altered by the emission of a sheet or jet of air at various positions along the wing. In various tests, it was found that the blowing technique does indeed alter the vortex by decreasing the peak tangential velocity; however, no apparent reduction in rolling moments was found. Another class of active devices is the incorporation of a cyclic disturbance into the shed vortex sheet to trigger an instability; but all devices tested to date have not yielded an operationally useful technique.

Passive devices attached to a wing to alter the flow about the wing have been tested. End plates, winglets, and ogee tips do alter the vortex structure, but do not significantly appear to reduce the induced rolling moments on a following aircraft.

4.2 VORTEX ALLEVIATION BY VARIATIONS IN SPANWISE WING LOADING

The primary method of vortex alleviation is design or operational modifications to the wing of the generator aircraft. This includes changes in the spanwise wing loading by airfoil modification or modifications in the use of flaps or spoilers. The intent of some of the techniques is to decrease the strength of the generated vortices, while the intent of others is to promote the mutual

interaction and mutual annihilation of multiple vortices shed from the wing.

4.2.1 Reduction of Shed Vortex Strength

Recalling equations (3.73) through (3.76), the strength of the shed vortex is

$$\Gamma = \frac{W_A}{\rho b K U_\infty} = C_L U_\infty \bar{c}/2K \quad , \tag{4.7}$$

where K is the spanwide loading coefficient

$$K = \frac{2}{b\Gamma_o'} \int_o^{b/2} \Gamma'(y)\, dy \quad . \tag{4.8}$$

From equation (4.7), it is seen that the strength of the shed vortex can be reduced by increasing the spanwise loading coefficient. This result is obtained by reducing the lift at the wing root or aircraft centerline as much as possible while the total lift coefficient is held fixed. A modified wing loading may be obtained by a flap which does not extend to the wing root. In that case, a set of vortices are shed from the ends of the flap, but are of opposite sign, so they tend to cancel each other. This leaves the net shed vorticity less than that with a monotonically decreasing spanwise wing loading.

4.2.2 Span Loading for Large Vortex Cores

A variety of wing shapes have been considered experimentally and theoretically as a means to reduce the high circumferential velocity in lift-generated vortices. These configurations were studied because it was thought that enlarging the vortex core would reduce the swirl velocity and the rolling moment associated with a given lift. The direct relationship between span loading and vortex structure provided by the Betz roll-up theory suggested that wing platform, twist, or camber be shaped to produce a loading which sheds vortices with large cores. Many of these span loadings had the characteristic that they tapered gradually to zero at the

wing tips from an increased centerline loading. The properties of these loadings is illustrated by considering a so-called tailored loading (ref. 72) which produces a vortex sheet which rotates as a unit rather than rolling up from its edges.

In this particular case, the velocity distribution in the wake was specified, and the corresponding strengths of the vortex sheet and of the span loading were then found. When the vortex structure was compared with that for elliptic loading, it was found that the higher centerline lift required to maintain a given lift on the generator leads to a larger value of shed vortex strength, and thereby, produces higher rolling moments when the span of the follower wing is more than about 0.2 of the span of the generating wing.

The effect of tailored loading on the maximum tangential velocity is largest in the near wake but is negligible in the far wake. This suggests that a span loading designed primarily for the generation of large vortex cores is not the proper direction for wake alleviation because these wings require higher centerline loadings. The corresponding decrease in the spanwise loading coefficient, K, associated with these loadings also suggests that a direct span-loading vortex core design is not a good direction to proceed and that another approach should be tried.

4.2.3 Flight-Test Results: Altered Span Loading

Span loadings were altered in flight by varying the deflections of the inboard and outboard flaps on the B-747 aircraft (ref. 71). Seventeen flights were flown by the B-747 airplane to complete the tests, and the Cessna T-37B and Learjet-23 (LR-23) aircraft were used as the probe aircraft. Both parallel and cross-track probes were performed during the test series.

The results of the tests conducted with a retracted outboard flap on the B-747 airplane (called the 30/1 configuration) show that a significant amount of attenuation was provided. These data agree with wind-tunnel data obtained from a model which did not have a landing gear. When the landing gear on the airplane was extended, a significant amount of the attenuation was lost.

With the outboard flap extended, the dominant vortex is the vortex shed from the outboard edge of the outboard flap. With the outboard flap retracted, the dominant vortex is that shed from the outboard edge of the inboard flap. In both cases, the wingtip vortex interacts with the dominant vortex. The effects of configuration on vortex life were compared visually: The unattenuated vortex persists for at least 45 seconds while the attenuated vortex disappears completely in 30 seconds. After these tests, the vortex-marking system was modified to include smokers at the inboard edge of the inboard flap to try to determine why the landing gear reduced the attenuation. The photographs show that the landing gear diffuses a powerful vortex at the inboard edge of the inboard flap, significantly reducing the attenuation provided by the 30/1 flap configuration. Though not available in the photographic record, visual observations of the inboard vortex showed that it intermingled with the vortex off the outboard edge of the inboard flap when it was not diffused by the landing gear.

Although interesting from a research standpoint, the vortex attenuation afforded by the 30/1 flap configuration was disregarded for obvious operational reasons when the degrading effects of the landing gear were discovered. It should be noted that the configuration also imposed a center-of-gravity limitation on the B-747 airplane.

A flight evaluation of the vortices 4 to 6 nautical miles behind the B-747 airplane in the 5/30 configuration (inboard flaps set at 5 degrees, and the outboard flaps at 30 degrees) was short and conclusive. Whereas the 30/1 flap configuration produced marked attenuation, the 5/30 vortex resulted in T-37B encounters which were even more violent than those caused by the conventional 30/30 landing configuration at 6 nautical miles. One encounter at 6 nautical miles produced a violent double snap roll which far exceeded the capability of the roll-rate data-acquisition system and also caused an engine flameout. These tests showed the correct approach to vortex attenuation to be increasing the inboard span loading.

4.2.4 Flight-Test Results: Turbulence Ingestion

The ingestion of turbulence into the vortices in flight was accomplished by mounting splines on the wingtips of a C-54G aircraft. A Piper Cherokee (PA-28) airplane was used as the probe aircraft for the tests. The data showed that the PA-28 airplane has insufficient roll-control power to overcome the vortices of the basic C-54G airplane at a separation distance of approximately 4 nautical miles, and that maximum roll-control power is never required to oppose the vortex attenuated by splines. The data generally correlate with the pilots' opinions of the attenuation, which was that roll control became insufficient approximately 2.5 nautical miles behind the unattenuated C-54G airplane but that it was sufficient throughout the entire range of separations tested for the attenuated configuration (ref. 71).

The effects of the splines on the performance, handling qualities, and noise of the C-54G airplane were also measured. It was concluded that although the splines significantly reduced the rate of climb of the C-54G airplane, the airplane's four-engine performance was acceptable for the test program. (It should be noted that the splines were not retractable as they would be for any configuration seriously proposed for operation.) The splines caused no noticeable changes in the handling qualities of the C-54G airplane. Finally, the maximum overall sound-pressure level of the C-54G airplane during landing approach with splines on was approximately 4 decibels higher than with splines off.

4.2.5 Flight-Test Results: Combinations of Mass and Turbulence Ingestion

Flight tests were conducted with the B-747 airplane to evaluate the effects of engine thrust on vortex attenuation. In general, most of the B-747 testing has been conducted with thrust for level flight at altitudes of approximately 3000 meters because a level flightpath makes it easier for the probe pilots to find and encounter the vortices. However, considerable testing has been performed for all the attenuated and unattenuated configurations wherein the thrust was reduced from that required for level flight to

that required for a -3 degrees flightpath angle and further to flight idle (approximately -6 degrees flightpath angle, depending on spoiler, flap, and gear configuration). To date, a detailed comparison of the pilots' qualitative assessment of the effects of engine thrust with quantitative data has not been completed. In general however, it appears that reducing the thrust from that required for level flight to flight idle adds approximately 2 nautical miles to the required separation distance. The generalization is true for both the 30/30 and 30/1 flap configurations.

Tests wherein the inboard and outboard engine thrust levels have been varied alternately have been conducted, but the data are not yet available. Tests to determine the effects of engine thrust on the attenuation provided by deflecting various spoiler segments are yet to be completed.

4.2.6 Flight-Test Results: Combinations of Span Loading Alteration and Turbulence Ingestion

Wind-tunnel tests made as early as 1969 indicated that the character of the trailing vortex system could be changed significicantly by adding a spoiler to the wing in the area of the vortex formation (ref. 73). Flight tests of a spoiler on the wingtip of a CV-990 aircraft were conducted in 1970 as a result of these wind-tunnel tests. Unfortunately, at that time in-flight vortex-marking systems were not available, and therefore the tests were rather inconclusive.

More recently however, wind-tunnel tests have shown that extending various combinations of the B-747 spoilers is effective in attenuating its vortices (ref. 74). The four outboard spoiler panels on the B-747 airplane are in the vicinity of the outboard flap, where the dominant vortex is shed (see Fig. 4-6). Therefore, it is not surprising that extending these spoilers affects the resulting vortex system.

The flight tests were paced by the wind-tunnel tests (ref. 74). In flight, the spoilers were deflected in various combinations. The deflection angles were chosen as a result of the flight crew's

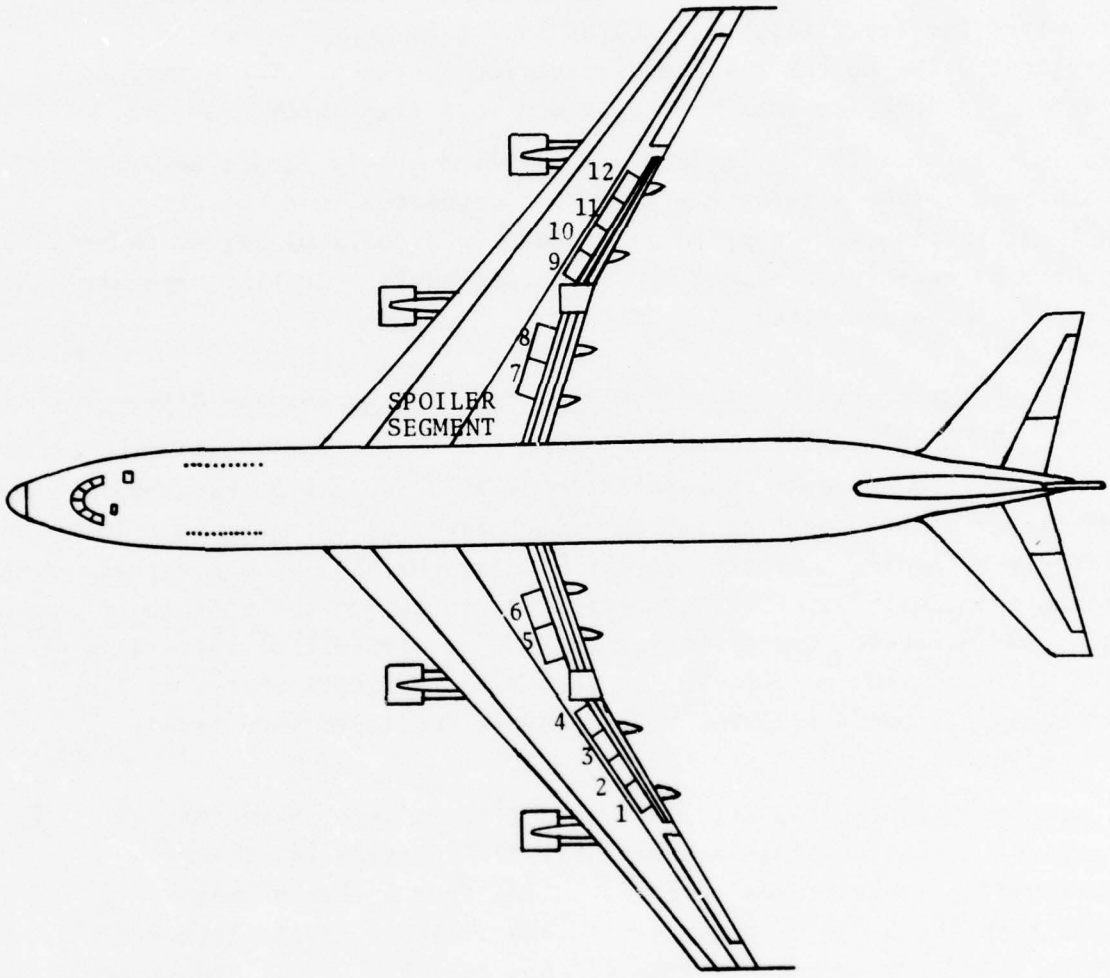


FIGURE 4-6. SPOILERS ON B-747 AIRPLANE

concern about the level of buffet induced by the spoilers and limitations of the control system on the production B-747 airplane. The 37-degree deflection for spoilers 3, 4, 9, and 10, and the 41-degree deflection for spoilers 1, 2, 11, and 12 were used because of the crew's concern about the safety of accepting a higher level of buffet. The 25-degree limit for the deflection of spoilers 1, 2, 11, and 12 was established because it caused the highest buffet level that the flight crew felt passengers would tolerate. The 45-degree deflections for the spoiler combinations (1, 4, 9, 12) and (2, 3, 10, 11) were limited primarily by the control system. It is interesting to note that the flight crew felt that the buffet level with a spoiler deflection of 45 degrees was excessive for spoiler combination (2, 3, 10, 11), but acceptable for the spoiler combinations (1, 4, 9, 12).

The pilots' qualitative separation requirements from the spoiler flight test indicate that with spoilers 1, 2, 11, and 12 deflected 41 degrees, significantly more attenuation is provided than with any other configuration. In fact, it would appear that the 41-degree deflection of spoilers 1, 2, 11, and 12 could be proposed as an operational configuration which would allow light aircraft to be spaced as close as 3 nautical miles behind heavy aircraft. Therefore, a series of tests was developed to investigate the operational feasibility of using this configuration. The investigation was to include actual landings of the B-747 airplane with the spoilers extended and probes of its vortex at landing flare altitudes by the T-37B airplane.

The proposed low-altitude probes with the T-37B airplane required a re-evaluation of the criteria on which probing was based at altitude. The probe pilots used as a criterion the level of upsets which would force them to abandon an approach either in instruments or after breaking out at the bottom of an overcast. Among other factors, a bank-angle limit of approximately 30 degrees for the T-37B airplane at altitude was considered as a baseline (with lower limits for aircraft with larger wingspans). The adequacy of this partial criterion was questioned, however, when actual landings were proposed; lower control power, proximity to

stalls or spins at low altitude, and the thrust required to overcome the downwash of the generating airplane became additional items of concern.

Intentional probes of the downwash area between the B-747 vortices were made with the B-747 airplane with spoilers 1, 2, 11, and 12 deflected. The T-37B airplane probed this area to less than 2 nautical miles and found only light to moderate turbulence with an incremental downwash of approximately 150 meters per minute. The problem of adequate climb performance at low speeds in the landing configuration had to be considered, even when roll-control power was adequate to overcome the vortex-induced roll. An additional unknown was the variation of vortex strength and life as a function of altitude and ground effect. Tests using ground-based sensors were conducted to evaluate the normal and attenuated vortex characteristics (see Section 10), but the results are not yet available.

Another question pertinent to the problem of separation distance is the effectiveness of attenuating devices for following aircraft which have considerably larger wingspans than the T-37B and LR-23 airplanes. Wind tunnel and water tank tests on a McDonnell-Douglas DC-9 scale model indicate a definite reduction in induced roll, but not as large a reduction as models of smaller wingspan experienced. This effect is caused by the better fit of an airplane with a larger wingspan in the larger attenuated vortex.

5. HAZARD DEFINITION

The purpose of the study of hazard definition is to define the conditions in terms of vortex and aircraft parameters under which a vortex wake is a hazard to specific classes of following aircraft. It is also desirable to define the spacial extent of the region of hazard. An ideal solution to the problem of hazard definition would be to run a series of flight tests in which several types of instrumented aircraft would probe known vortex flow fields. In these tests, the encounter upset would be measured as a function of vortex strength and encounter geometry. Unfortunately in this type of experiment, it is very difficult to control all of the important variables. Nevertheless, a significant quantity of information can be gleaned from data measured during encounter flight tests.

NASA has conducted a series of flight tests to evaluate the response of probe aircraft to vortex-wake encounters as was outlined in the previous section. The wake-generating aircraft included C-5A, B-747, DC-10, CV-880, B-727, and DC-9 while the list of probe aircraft included the DC-10, DC-9, T-37B, Learjet, and the Cessna 210. Vortex encounter probes were made at distances ranging from 1 to 15 nautical miles behind the generator aircraft. Roll response was found to be the principal effect in vortex encounters. Analysis of the data showed good correlation between the separation distance at which roll acceleration just exceeded the roll-control capability and the minimum-separation distance which the test pilots judged as necessary for safety.

There are serious limitations to relying solely on flight test for hazard definition. For the sake of safety, the encounter probes took place at an altitude of approximately 3000 meters above ground level (AGL). If there is a significant difference in the time scale of vortex decay between 3000 meters AGL and 150 meters AGL, then the separation distances found in the flight tests are not directly applicable to approach and landing operations which constitute the most important concern of the wake vortex program.

It has not been possible to measure the vortex flow field and the probe aircraft response simultaneously. The distance behind the generator aircraft has been used as a parameter which relates to the vortex strength. In addition, all of the probes were central encounters; i.e., the probe aircraft were flown into the visual center of the vortex (as marked by a smoke trail), and consequently, there is only qualitative information on the spatial extent of the hazard region. It is also not clear that the encounter response for an unintentional encounter is the same as that when the pilot's task is to enter and remain in the vortex.

The remainder of this section is an explanation of a methodology for the definition of hazard as it will apply to various vortex avoidance system concepts. "Hazard Definition," as the term is used here, is a means of determining if an aircraft on a given flight path will be sufficiently disturbed by a vortex in the vicinity of the flight path so that it could be dangerous to continue the mission. There are four basic steps to the hazard-definition process:

a) Determination of the relevant vortex parameters (as discussed in Section 3).

b) Derivation of an analytic method for calculating the forces and moments on an aircraft encountering a vortex.

c) Selection of hazard criteria to judge if a given degree of upset is hazardous.

d) Derivation of methods for calculating the dynamic response of aircraft in the vortex flow field.

5.1 ANALYTIC METHODS OF CALCULATING VORTEX-INDUCED FORCES AND MOMENTS

In the consideration of aircraft upset because of a vortex encounter, the induced rolling moment is the most important consideration. Yaw, pitch, and sideforce may be significant, and can be calculated using strip theories as is done in refs. 75-78. Jenkins and Hackett (ref. 79) discuss the effect of induced lift on the yawing moment which may be important for some configurations.

The problem of calculating rolling moments has been explored in some detail by Barrows (ref. 80). A number of possible approaches can be used to calculate lift and roll on an aircraft encountering an arbitrary downwash field. The most prominent of these are:

a) Modified strip theory

b) Reciprocal relations (reverse flow theorems)

c) Weissinger theory

d) Vortex-lattice theory.

If a quick estimate of the vortex-induced rolling moment is required, a modified strip integration is recommended. The rolling moment coefficient may be calculated (ref. 80) as follows:

$$C_\ell = \frac{m a_o}{\bar{c}\, U_\infty} \left(\frac{2}{b}\right)^2 \int_{-b/2}^{b/2} W\, c\, y\, dy \,, \tag{5.1}$$

where m is an aspect ratio correction, a_o the two-dimensional lift curve slope, $\bar{c}$ the average chord, W the downwash velocity, and c the wing chord. The theoretical value for a_o is 2π, but in practice a somewhat lower value is generally obtained. A value of 5.67 is recommended in the absence of data for the particular airfoil making up the wing. For unswept tapered wings, the aspect ratio correction may be computed from

$$m = \frac{1}{1 + \left(\frac{2a_o}{\pi AR}\right)(1+\varepsilon)} \,, \tag{5.2}$$

where

$$\varepsilon \approx \frac{3\lambda - 1}{3(1+\lambda)} \,, \tag{5.3}$$

and λ is the taper ratio (tip chord/root chord).

If both computational efficiency and accuracy are desired, the most appropriate approach is to use a reciprocal relation as presented by Heaslet and Spreiter (ref. 81), which relates the rolling moment on a wing in an arbitrary downwash field to that of a

fictitious wing in steady rolling motion. The theorem may be stated as follows: The rolling moment on a wing encountering an arbitrary downwash field is equal to the integral over the span of the product of the local angle of attack and the sectional lift at the corresponding spanwise station of a flat-plate wing of identical planform which is rolling at a rate p = 2V/b. Essentially the theorem states that a modified strip integration may be used to compute the rolling moment (ref. 82).

For swept wings, Weissinger theory can be used although it has several disadvantages:

1) It generally requires a computer program with a large number of matrix elements which must either be calculated from a complicated integral or loaded by hand.

2) It is not accurate for either very large or very small aspect ratio.

3) The calculation of a rolling moment for a given downwash field involves a matrix multiplication, rather than a simple integration. (This may give rise to difficulties if it is important to bring computation time to a minimum as in real-time dynamic simulations.)

4) Although the theory is good for predicting the onset of stall, it is not clear what modifications should be made to correct for stall when it occurs over a limited span of the wing.

Vortex-lattice theory, while uniformly accurate for all values of aspect ratio, is the most time consuming of all the methods, and thus, is poorly suited for real-time simulations. There is such a large degree of uncertainty associated with wake vortex encounters that it is not possible to use effectively the potential accuracy available from this method of calculation.

5.2 HAZARD CRITERIA SELECTION - GROUND-BASED FLIGHT SIMULATION

Two piloted simulations were conducted at Ames Research Center in a joint NASA/FAA program to establish hazard criteria for wake vortex encounters. The objectives of the first simulation were to: (a) determine if vortex encounters can be simulated on piloted, moving-base simulators with sufficient realism to permit determination of hazard criteria; and (b) determine the parameters that best correlate with pilot opinion of hazard. The second simulation was conducted to determine hazard boundaries for both IFR and VFR landing approaches for jet aircraft in the 5600-kilogram and 136,000-kilogram classes.

5.2.1 Description of Simulations

The first simulation was conducted on the Ames Six-Degree-of-Freedom Motion Simulator. This simulator is equipped with a one-man cab that was configured to approximate the Ames Learjet that had previously been employed in intentional encounters of the marked wake of a number of large jet aircraft. The cab was equipped with hydrualically-actuated control loaders for the wheel and column and spring-loaded pedals for the rudder controls. The hydraulic loaders were programmed to provide the Learjet control gradients, dead bands, and hysteresis.

Visual cues were provided by a landing approach scene displayed on a black and white television monitor. The visual scene was generated by a computer-driven, six-degrees-of-freedom television camera that duplicates the aircraft motion with respect to the landing approach scene.

The second simulation was conducted on the Flight Simulator for Advanced Aircraft (FSAA). This simulator differs from the Ames Six-Degrees-of-Freedom Motion Simulator principally in the translation motion limits and in the realism of the visual scene. The vertical and horizontal translational limits are considerably less than those of the Six-Degrees-of-Freedom Motion Simulator, but the lateral travel is greater by a factor of more than five. The large lateral freedom provides greater fidelity to the rolling and

lateral acceleration cues which are considered to be important to the realism of a simulated wake vortex encounter. The visual scene in the FSAA is collimated and in color, contributing further to realism.

The aerodynamic models used during the simulation represent the Gates/Learjet Model 23 and the Boeing 707/720. The models duplicated the aircraft control-system characteristics and provided for clean-up and go-around for an aborted landing.

The vortex was represented by a pair of two-dimensional vortices. The parameters which characterize the flow field in each case were: vortex spacing, core diameter, and circulation strength. The axes of the two vortices from the generating airplane were assumed to be straight lines, and to be separated by 25.6 and 45.7 meters for the Learjet and Boeing 707/720 simulations, respectively, corresponding to observed spacing for the Boeing 727 and the Boeing 747 in the landing configuration.

The conduct of an efficient simulation program required that the encounter geometry could be specified to obtain repeatable upsets at the given altitude. For the simulation, the angle of penetration relative to the vortex axis was a variable, but the aircraft center of gravity was always required to pass close to a vortex core. The required relationship was maintained by translating and rotating the vortex coordinates, so that the flight path remained fixed relative to the vortex regardless of aircraft motion. Just prior to penetration, the vortex coordinates were frozen in inertial space, so that the aircraft could be then maneuvered relative to them. The location of the freeze point was chosen to be close enough to the vortex to ensure penetration regardless of pilot maneuvering.

The forces and moments caused by the presence of the vortex flow field were calculated by strip theory. In brief, the procedure divides the wing, horizontal tail, and vertical tail into N-number of chordwise strips. (For this case, the wing was divided into 20 strips per semi-span, while the horizontal and vertical tails were each divided into 6 strips per panel for each aircraft.) The local

velocity, angles of attack and slideslip, and forces and moments (referred to the airplane center of gravity) induced by the vortex were calculated for each strip. These incremental forces and moments were summed with estimated fuselage contributions to give the net forces and moments on the airplane due to the vortex.

5.2.2 Test Program

The simulation was limited to vortex encounters during the landing approach. The piloting task was to fly either an IFR or a VFR approach on a 3-degree glideslope. Each approach was initiated at an altitude of about 250 meters with the aircraft trimmed on the glideslope and localizer at the proper airspeed. The pilot was instructed to continue to a landing following an encounter if he considered it safe to proceed. In the event of an aborted landing, he was required to reconfigure the aircraft for the go-around maneuver.

The simulated vortex encounters were made into the right or left vortex with a random selection of vortex strength, angle of the flight path relative to the vortex, and encounter altitude. In some instances, no encounter at all would be experienced. This procedure precluded the pilot from predicting when an encounter might occur, how severe it would be, and its precise nature.

For each encounter, the pilot was asked to assess if the encounter was hazardous. Hazard assessment was limited to concern for the safety of the aircraft with no consideration of passenger comfort. For the first simulation, a rating scale was developed to assess the encounter in terms of aircraft control, demands on the pilot, and aircraft excursions. This procedure was abandoned during the second simulation since it was found that the ratings in these areas bore no consistent relationship to the direct pilot assessment of hazard. A different pilot-rating scale was developed for the second simulation which dealt directly with hazard and permitted the establishment of each encounter as hazardous or non-hazardous.

5.2.3 Results and Discussion

The results of the first simulation were analyzed to determine which response parameter, or combination of parameters, would best correlate with pilot assessment of hazard. The data base from this simulation consists of more than 200 encounters for both IFR and VFR approaches. However, very few of the IFR encounters were rated as non-hazardous, so that the data correlation was restricted to VFR results.

It was anticipated that the hazard associated with a given encounter during the landing approach would be strongly correlated with the altitude at which it occurred. The procedure used in correlating the data, therefore, was to plot the various response parameters in roll, pitch, yaw, normal acceleration, etc., as a function of encounter altitude and seek the parameter which best accomplishes a separation of the data into hazardous and non-hazardous regions.

Of the various parameters considered, the roll responses were thought most likely to provide the desired criterion based on observation of the relative magnitudes of the responses and the fact that roll acceleration had been found in flight to correlate well with acceptable separation distance (ref. 70). In the present analysis, the parameter which yielded the best defined hazard boundary was maximum bank angle. This was chosen to be the maximum bank angle which occurred in response to the vortex and included any corrective action taken by the pilot to regain control. The correlation of the hazard assessment with roll parameters is shown in Fig. 5-1 and includes all encounters obtained under VFR conditions. Those encounters assessed as hazardous by the pilots are designated by the filled symbols. The tentative hazard boundary shown in the correlation in terms of maximum bank angle was drawn to separate the data into two regions: one containing no hazardous encounters; and the other in which an encounter is likely to be hazardous. It is not possible to extend this hazard boundary to altitudes less than about 60 meters because all of the encounters simulated at the lower altitudes were considered to be hazardous.

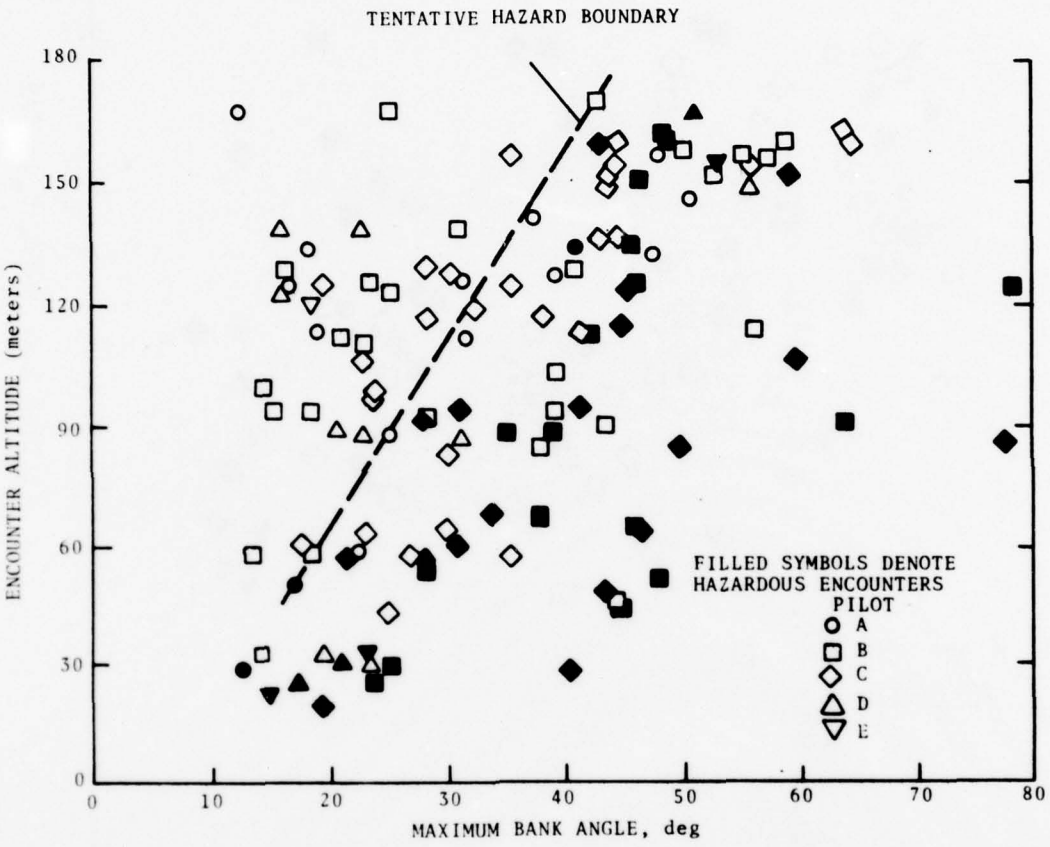


FIGURE 5-1. CORRELATION OF ASSESSMENT OF HAZARD WITH ROLL RESPONSE PARAMETERS

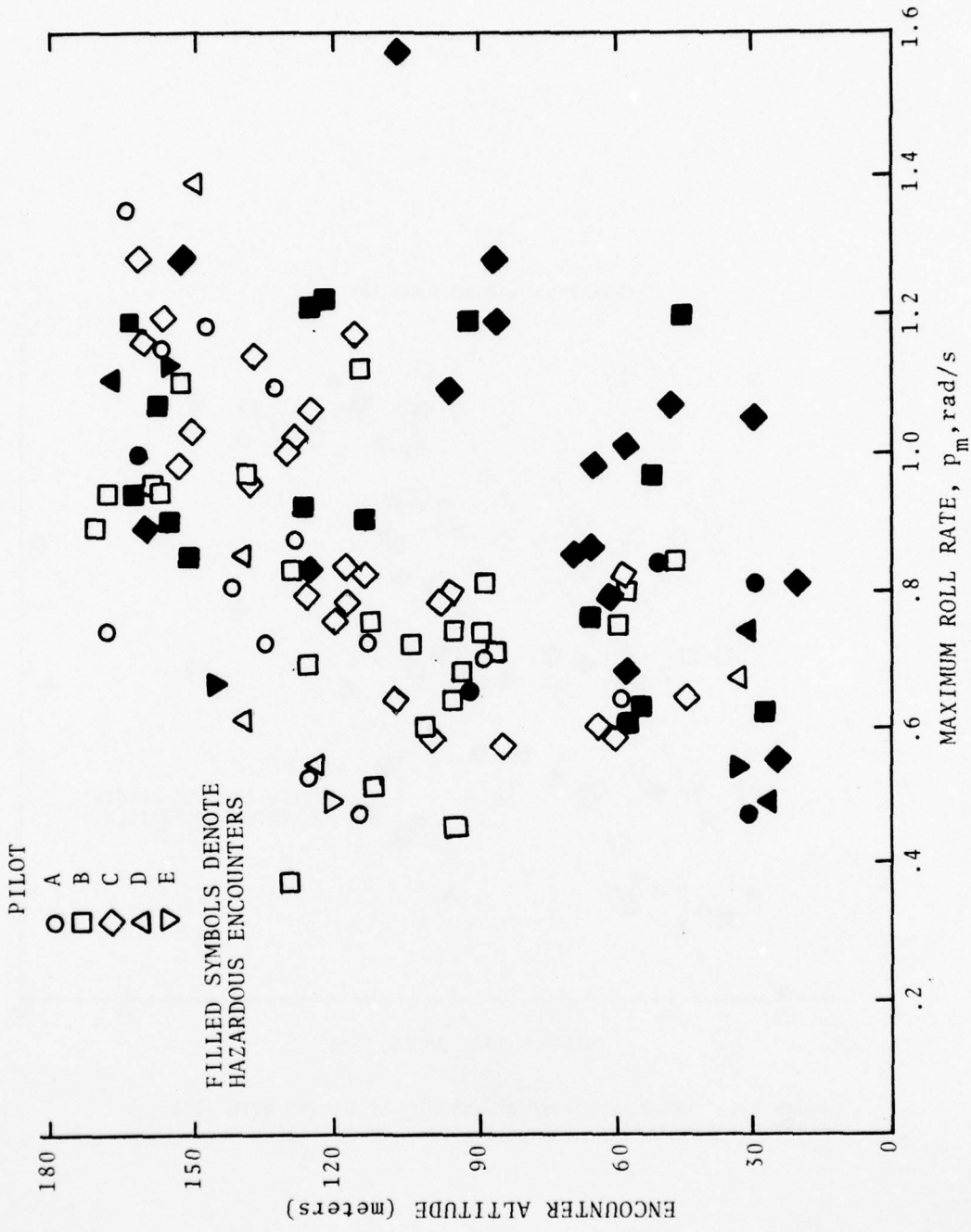


FIGURE 5-1. (CONTINUED)

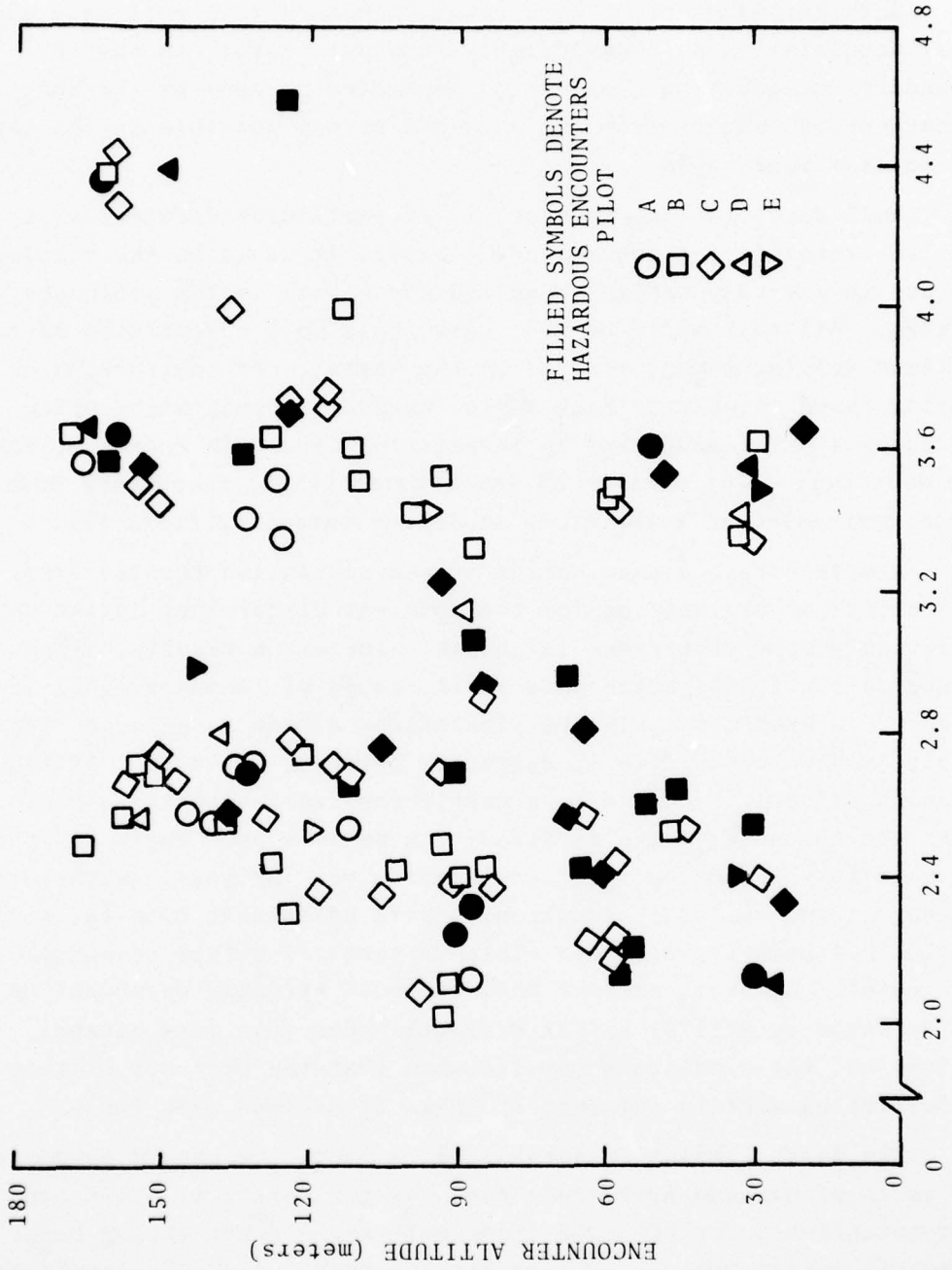


FIGURE 5-1. (CONTINUED)

Correlation of pilot assessment of hazard with roll rate and roll acceleration was considerably less successful, in that a boundary could not be drawn which separates as many of the non-hazardous encounters from the data set as was possible in the case of maximum bank angle.

Roll acceleration, however, is of particular interest as a hazard criterion for two reasons. First, it would be the simplest to use in any computations required for a wake vortex avoidance system. All that would be necessary would be a computation of the maximum rolling moment induced by the vortex. In contrast, a criterion based on maximum bank angle requires a computation which includes a pilot model and an integration to obtain a time history. In addition, pilot opinion of intentional flight encounters have been correlated in terms of an analogous parameter (ref. 70).

A more detailed examination of the simulation results (ref. 83) offers an explanation for the apparent discrepancy in the correlation parameter between flight and simulation results. The basic reason is the difference in the range of encounter angles covered in each case. In the simulation, a wide range of encounter angles was covered (7 to 15 degrees); however, the flight-test procedures probably resulted in a nearly constant encounter angle. When the encounter angle is fixed, the maximum bank angle and the maximum vortex-induced roll acceleration vary primarily with vortex strength, and for this situation, hazard assessment from the simulation has been shown to correlate in terms of either response parameter. However, maximum bank angle is strongly dependent on entry angle as well as vortex strength. For this more general situation, the simulation results show that the best correlation of hazard assessment is obtained in terms of maximum bank angle.

The first simulation established a tentative hazard boundary in terms of maximum bank angle for a single aircraft. This boundary was established for VFR conditions only and did not extend below about 60 meters because of insufficient data. A second simulation was conducted to complete definition of the boundary for the Learjet and to define a boundary for a much larger aircraft, the Boeing 707/720, having widely different response characteristics. The

Flight Simulator for Advanced Aircraft was chosen for the second simulation because of its better visual scene and lateral motion capability.

A comparison of results for three pilots participating in both simulations of the Learjet is shown in Fig. 5-2. In addition to the difference in simulators for the two data sets, there was some difference in the aircraft models in that the yaw damper was engaged only during the first simulation. The results indicate that a hazard boundary drawn to include all hazardous encounters for these pilots from the first simulation would exclude only four hazardous encounters from the second. However, drawing the boundary to include these points reduces the allowable maximum bank angle considerably.

A summary of the results of the second simulation from all participating pilots is shown in Fig. 5-3. At an altitude of 15 meters, it is indicated that maximum bank angle for the non-hazardous region is about 7 degrees for VFR conditions for either aircraft. The increase in allowable bank angle with altitude was somewhat greater for the lighter, more maneuverable aircraft. For instrument-flight conditions, there was no difference in the hazard boundary for IFR approaches between the two aircraft. This boundary is indicated to be only 7 degrees of bank at 60 meters and to never exceed 10 degrees over the altitude range of the simulation.

5.3 OTHER VORTEX ENCOUNTER SIMULATIONS

Flight-simulation programs such as the NASA/FAA effort at Ames Research Center, which used a piloted-flight simulator, require the use of expensive facilities and a significant quantity of pilot time. Although such flight simulation is well suited to the task of establishing hazard criteria, it is too expensive for defining hazard volume. A computer simulation of vortex encounters in which pilot response to aircraft perturbations is input mathematically offers a more acceptable method for mapping out the hazard volume.

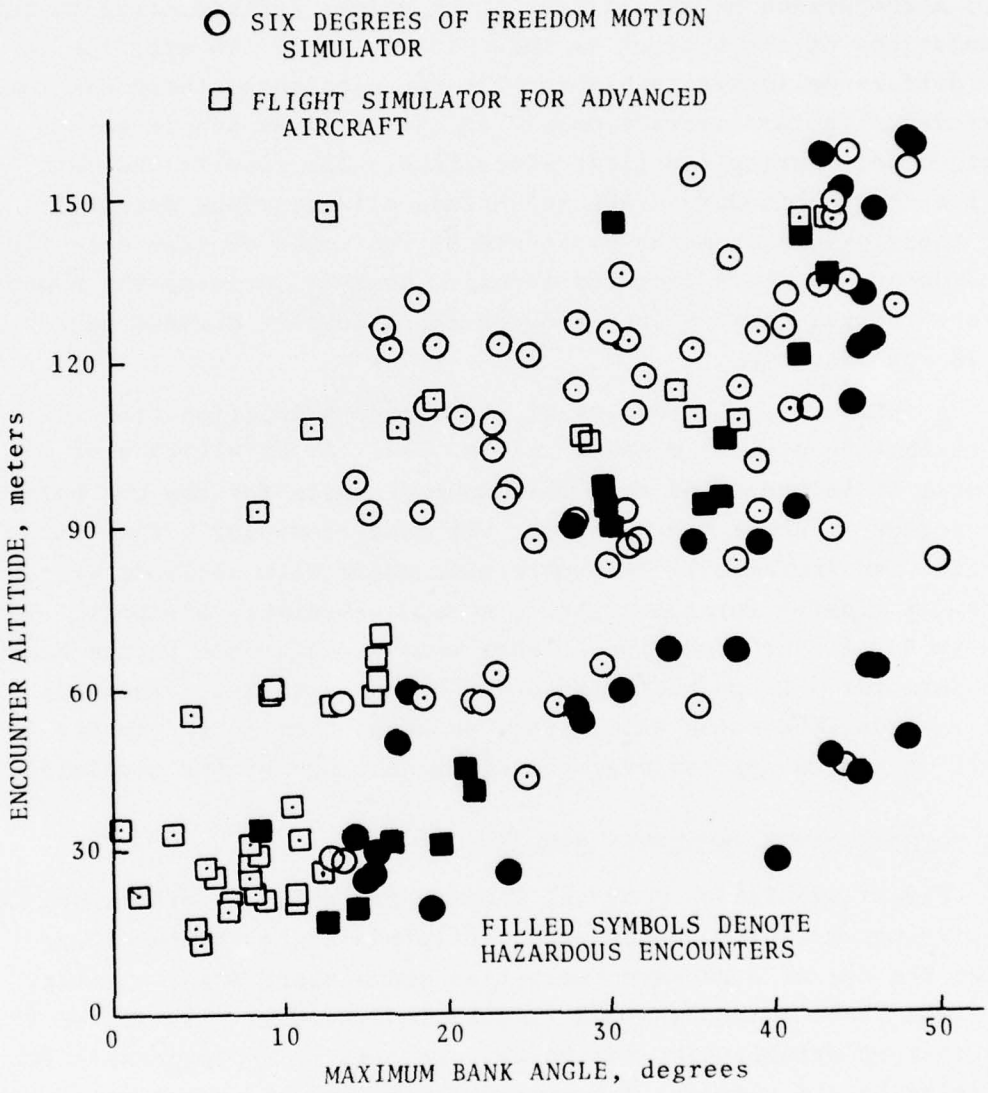


FIGURE 5-2. COMPARISON OF HAZARD ASSESSMENT FOR LEARJET VORTEX ENCOUNTERS BY PILOTS PARTICIPATING IN BOTH SIMULATIONS

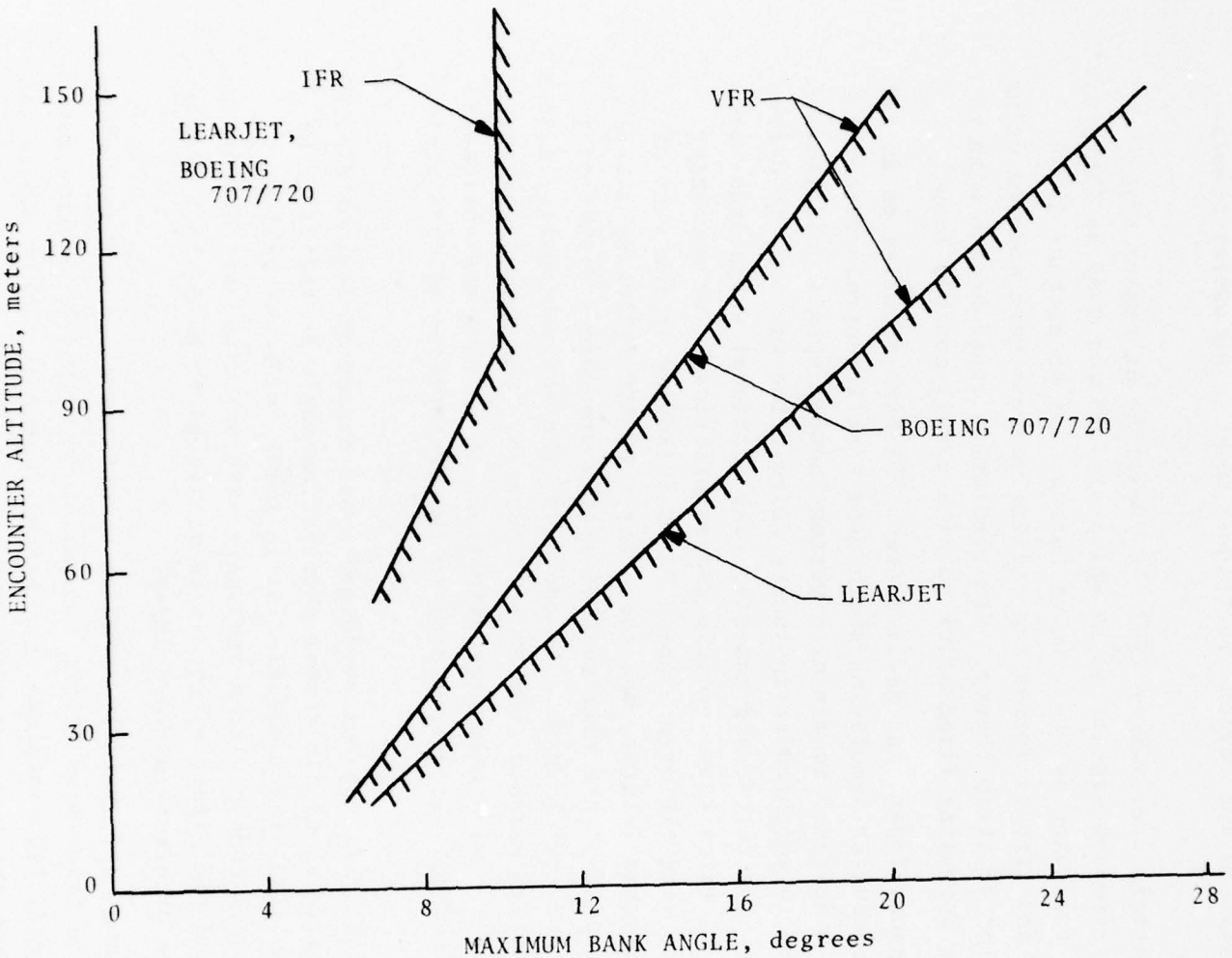


FIGURE 5-3. VORTEX HAZARD BOUNDARIES DETERMINED FROM SIMULATION

Several vortex-wake encounter simulations have been performed by various organizations. The following have been chosen to be illustrative of the various techniques used in encounter simulations.

Bernstein and Iversen (ref. 75) describe an analog three-degree-of-freedom simulation in which a C-130 was used as the probe aircraft following in the wake of both a C-5A or another C-130. Vertical and lateral forces and rolling moments were modeled using a variation of strip theory. The simulation could be run with the option of operating fixed-stick or with a roll-control loop.

Johnson, Teper, and Rediess (ref. 77) have reported on an all digital encounter simulation which uses a roll-control system especially designed to minimize vortex-induced upsets. In this simulation, a weighted strip-theory calculation was used to derive values for the forces and moments. The sectional weightings were adjusted to match known vehicle characteristics. Two encounter situations were explored: one a PA-30 following in the wake of a 13,600-kilogram Jetstar, and the other a CV-880 following a C-5A. It was found that the roll-control system provided a significant reduction in vortex upset. In one case, the maximum vortex-induced bank angle was reduced from 90 to 7 degrees. One surprising result was that there were encounter situations in which a conventional heading feedback was detrimental to the restoration of roll-angle control.

Nelson (ref. 78) has performed a six-degree-of-freedom digital simulation in which the vortex penetration angle is varied. The simulation also uses a modified strip-theory model as well as a pilot-control model. The vortex core size was also varied from run to run, and the effect of core size was found to be minimal over a wide range of practical core sizes.

Although not strictly speaking a self-contained computer simulation, the fixed-base flight simulation described by Jenkins and Hackett (ref. 79) contained interesting features. Their simulation differs from the previous simulations in that vortex-lattice theory was used in the aerodynamic model rather than some form of strip

theory. In this model, the vortex-induced velocities are superposed rather than superposing forces. The procedure takes into account binomial terms ignored by strip theory, an important feature in simulating violent encounters. Important forces in the plane of the wing were also taken into consideration by the use of the vortex-lattice method. The simulation was operated using pilots who were instructed to fly the glideslope, and encounters occurred at various points along the glideslope. The vortex circulation was varied as well as the penetration angle. It should be noted that the tracking function of the pilot tends to constrain the flight path, so that the encountering aircraft is not easily displaced from the vortex region.

5.4 THE TSC VORTEX-ENCOUNTER SIMULATION

To probe the spatial extent of vortex hazard relative to the vortex position, a computer simulation was developed at TSC. A strip-theory model of the aerodynamics was used to calculate the forces and moments caused by a non-uniform wind field which the vortex represents. Initial attempts at a fixed-stick simulation demonstrated that the probe aircraft was easily pushed away from the vortex center making a severe encounter difficult to recreate. An autopilot was added to constrain the probe to a given task such as completing an approach and letting the vortex act as a perturbation. The region around the vortex could thus be probed and a hazard volume mapped out.

The TSC Encounter Simulation is a hybrid program which uses a modified strip-theory calculation of forces and moments. The aerodynamic coefficients are calculated on a digital computer as are the various coordinate transformations (e.g., body axes to navigation axes). The equations of motion are solved on an analog computer, and the updated coordinates and their rates are fed back to the digital computer via analog-to-digital lines.

The general procedure in the simulation computation is to compute the vortex-induced moments in a body-fixed frame and to solve the equations of motion for the Euler angles. The resultant Euler

angles are then used in a transformation matrix to convert from the navigation frame to the body-fixed frame for another interaction. Similarly, the velocity vector is integrated to update the aircraft position.

Modified strip theory is used for the calculation of forces and moments. The wing section weighting functions were adjusted so that both the lift coefficient and the roll-damping coefficient fit published values. A sectional stall function was incorporated in the simulation to account for flow separation which could occur for large local angles of attack. Also, a ground effect routine was used to sense the altitude of the encounter, and thus, to calculate the ground effect corrections.

5.5 HAZARD VOLUME

The principal function of the TSC encounter simulation program was to define the area around a vortex pair in which the vortex could be considered to be a hazard to a following aircraft. For an aircraft following another aircraft on an ILS, the conditions under which the preceding aircraft's vortices will present a significant problem for the following aircraft are limited. The vortices generally descend below the flight path of the generating aircraft, and the vortices drift with the wind, so that any crosswind component will translate the wake laterally from the flight path. In the ground-effect region however, the following aircraft can encounter the trailing vortices of the preceding aircraft. To investigate this case, a series of encounters were programmed. The incoming aircraft was programmed to follow a 3-degree glideslope while the vortex, acting as a disturbance, was placed at various distances from the flight path, and a time history of all the significant aircraft variables was recorded for each flight.

An aircraft can only be affected by a vortex in a detectable manner under special conditions: (a) the vortex is strong enough when generated, (b) the encounter occurs soon enough after the vortex was generated that it has not decayed too much, and (c) the encountering aircraft passes close enough to the vortex. The TSC encounter simulation was used to determine the values of circulation

and lateral aircraft-vortex separation necessary to produce a hazardous encounter.

The results of the flight simulations described in Section 5.2 indicate the maximum-induced roll angle is the variable which best correlates with the pilot assessment of hazard. In Fig. 5-4, the maximum-induced roll angle is plotted as a function of the distance by which the flight path of a B-720 is displaced from the vortex axis. The curves are not symmetrical about the center of the vortex; the velocity fields cause differences in lift and side forces on each side of the vortex changing both the length of time the aircraft was exposed to the vortex and the distance of closest approach to the center of the vortex. For the cases considered here, a single vortex along with its ground image was used since vortices separate laterally in ground effect, and encounters will in general be with a single vortex. Applying the hazard criteria value developed by the flight simulation of 7-degrees maximum bank angle, it is seen (Fig. 5-4) that there are no significant upsets beyond 30 meters for any reasonable value of circulation. Thus, 30 meters is taken as a practical limit for the radius of a hazard volume surrounding the vortex axis. A horizontal line indicating a 10-degree roll-hazard criterion is also shown in Fig. 5-4. The hazard extent shows little sensitivity to the value of hazard criteria roll angle. Circulation values of 650, 460, 280 and 140 m^2/sec were used. For the B-720, 280 m^2/sec is seen as the minimum circulation of hazardous vortex; similar calculations for a DC-9 showed a larger upset for near encounters but exhibited the same hazard extent.

Harlan and Madden (ref. 76) analyzed the relationship between aircraft controlability (the ratio of maximum roll-control moment to vortex-induced roll moment) and vortex proximity as a function of the wing span of the encountering aircraft. For the cases where the induced roll-moment direction is opposite to the direction of rotation of the vortex; it was found that the smaller the wingspan, the greater the controlability. This is precisely the region where the hazard extent of a vortex is determined. For a given circulation, the hazard volume surrounding a vortex is smaller for aircraft

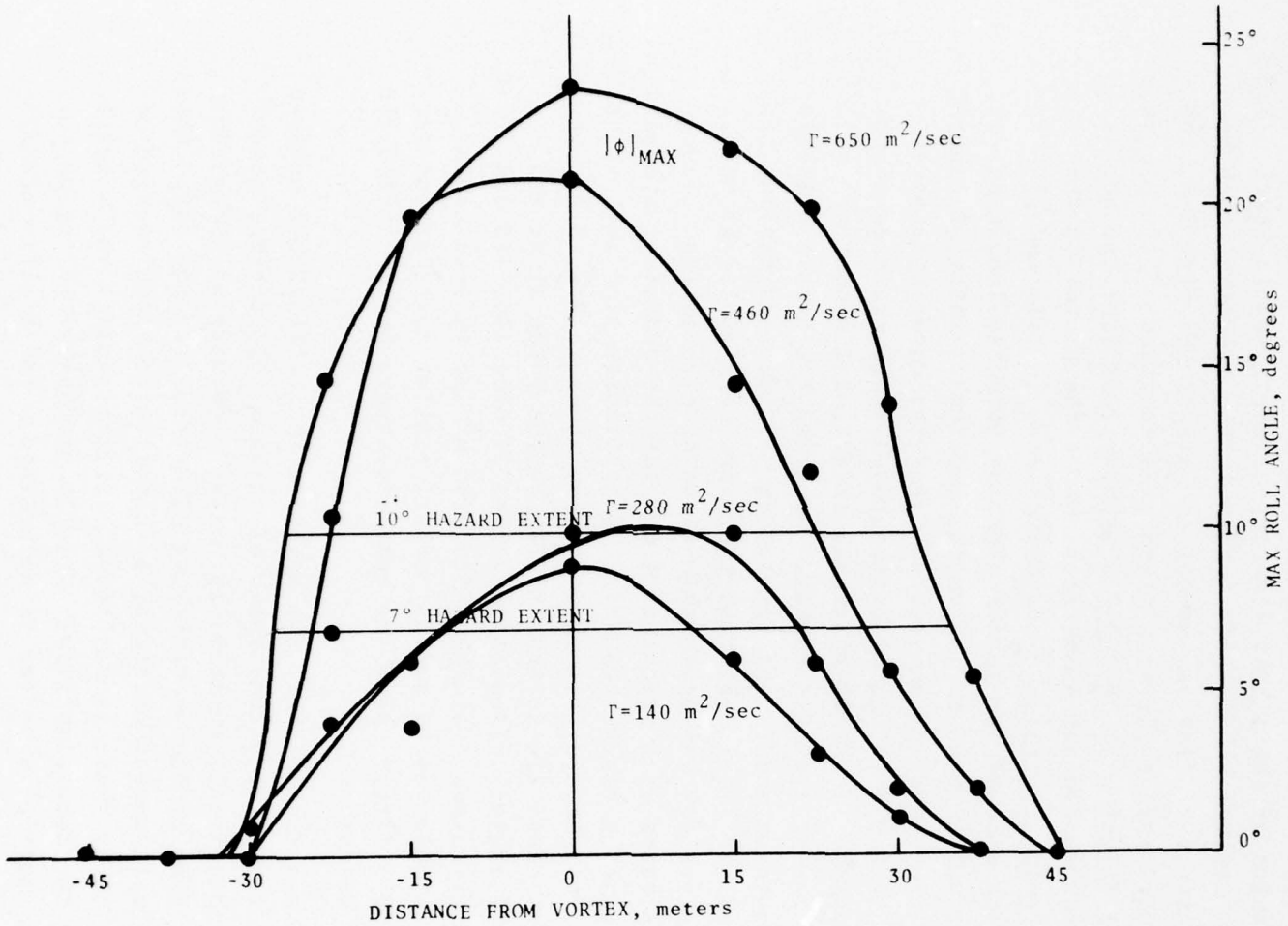


FIGURE 5-4. MAXIMUM INDUCED ROLL ANGLE AS A FUNCTION OF DISTANCE FROM THE VORTEX AXIS

with smaller wing spans even though the upset would be greater for a close encounter (see Fig. 5-5). For any wake vortex avoidance system based on just the motion of vortices (i.e., without knowledge of the strength of the vortices), the vortex hazard volume is determined by the B-720 class of aircraft and not the shorter wing span aircraft such as found in the general aviation class of aircraft.

For the landing case it is seen that an analytic approach to the definition of hazard can be accomplished. There are a number of steps in which simplifying assumptions have made the computational tasks manageable with a small computer. Because the hazard volume is defined in terms of the limit of minor upset, the results are not strongly dependent on the details of vortex structure or on the exact dynamics of an aircraft-vortex interaction. As seen in Fig. 5-4, the exact value of hazard criteria is not of appreciable significance.

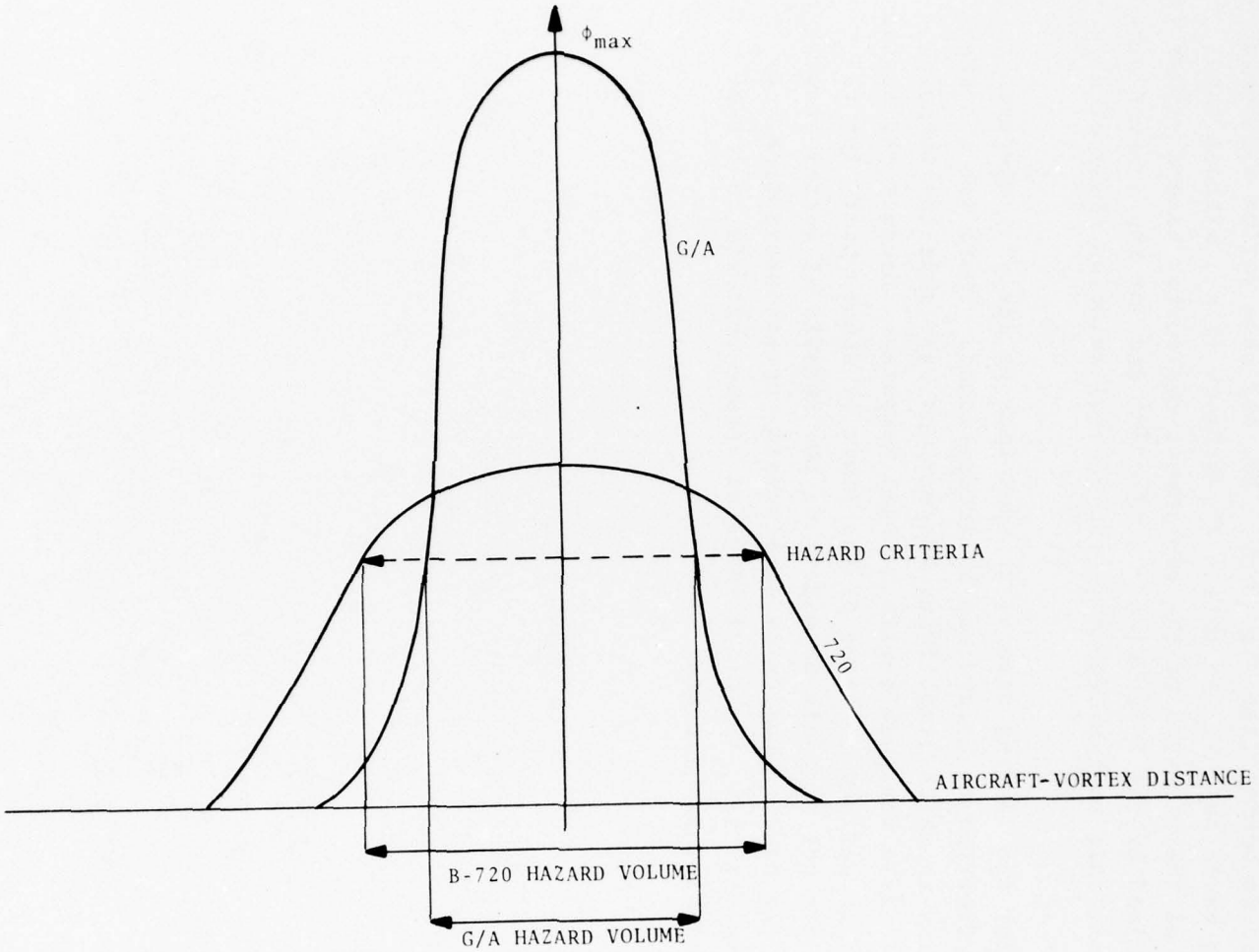


FIGURE 5-5. VORTEX HAZARD VOLUME FOR TWO CLASSES OF AIRCRAFT

6. VORTEX SENSORS

The quest to capture and subdue the hazardous wake vortex has taxed the capabilities of men and their instruments. A simple swirling mass of air has proved to be an elusive quarry. Conventional detection and measurement techniques have proved only partially effective; newly developed remote-sensing instruments have fared better. Almost every conceivable technology has been tapped in the quest to protect the airways from the wake vortex danger. This section is a chronicle of the last five years spent chasing the wake vortex.

6.1 GENERAL SENSOR REQUIREMENTS

A wake vortex sensor must interact with some physical property of the vortex. The usefulness of the sensor depends upon how closely the property sensed is related to the property which is to be determined. For example, smoke injected into the vortex by the generating aircraft is very useful for marking the vortex location, but it provides virtually no information on vortex strength. The question of the appropriateness of a sensor is particularly important for sensors which are intended to monitor the decay of wake vortex hazard. The property sensed may decay more quickly or more slowly than the actual hazard. The former case results in missed hazards while the latter leads to false alarms. These uncertainties have led to a strong emphasis in recent work on sensors which measure vortex strength.

6.2 SENSOR CHARACTERISTICS

In the following discussion of wake vortex sensors, five binary categories will be used to distinguish characteristics of the various sensors:

a) Remote/*in situ*: Can the sensor be located away from the point being sensed, or must it be located at the same point?

b) Active/Passive: Does the sensor project energy into the volume being sensed or does it simply extract energy already present?

c) Artificial Tracer/Natural Tracer: Does the sensor interact with something added to the vortex or with something occurring naturally within the vortex?

d) Operational/Research Only: Can the sensor be used during normal aircraft operations, or is it suitable only for special flight tests?

e) Airborne/Ground-based: Does the sensor have the potential for operation from an aircraft, or will it work only on the ground?

The first three categories are determined by the nature of the sensor's potential application. This section will concentrate on ground-based sensors. Apart from *in situ* sensors mounted on probe aircraft, very little work has been done on airborne wake vortex sensors.

The basic functions performed by wake vortex sensors are detection, tracking, and measurement. Each of these functions successively involves a higher order of complexity. Some sensors can detect and track but cannot measure. Normally, the most important vortex parameter to be measured is its strength. For those sensors which can measure strength, the detection and tracking functions were usually implemented first before strength measurement was attempted. Characterization of the detection function requires an understanding of miss and false-alarm rates as a function of detection threshold, vortex locations, and vortex properties. The tracking and measurement functions have the additional characteristic of accuracy. None of the wake vortex sensors have been completely characterized, but a number of them can be represented by simple models which give a reasonable indication of their utility. The operational usefulness of sensors depends upon their sensitivity to operational variables such as meteorological conditions, generating aircraft type, and the presence of interference in the environment.

6.3 DESCRIPTION OF WAKE VORTEX SENSORS

The potential usefulness of each type of physical interaction is examined in turn, and the particular sensors based on the interaction are described and classified according to the criteria discussed in Section 6.2. Table 6-1 lists the sensors discussed and their classification. Unless specified otherwise, the sensor development work was carried out at TSC.

6.3.1 Mechanical Techniques

Mechanical sensors provide *in situ* measurements of wind velocity or pressure. Some of the other physical interactions can also provide equivalent local measurements and are conceptually included here. For example, an acoustic anemometer provides data very similar to that from a hot-wire anemometer.

In situ sensors have a fundamental limitation for sensing aircraft wake vortices. If the sensors are located at altitudes high enough to probe the center of the vortex, they cannot be used in an operational environment because of the hazard posed to aircraft. Conversely if they are low enough to be installed at airports, they measure only the peripheral region of the vortex and cannot verify the location and persistence of the vortex core.

6.3.1.1 Wind Sensors - *In situ* wind sensors provide a direct measurement of the vortex-velocity field at the point where the sensor is located. Some of the earliest and most detailed vortex measurements were made with instrumented towers which were tall enough to measure the complete flow field of a vortex as it drifts through the tower (refs. 27,31-38). Although tall instrumented towers cannot be installed near airport runways, experience has shown that anemometers located near the ground can successfully detect and track wake vortices in runway-approach regions. Such a system, called the Ground Wind Vortex Sensing System (GWVSS), has produced the bulk of the currently available data on wake vortex transport in the airport environment. First tested in 1972, the system was subsequently installed at Kennedy, Stapleton, Heathrow,

TABLE 6-1. WAKE-VORTEX SENSOR CLASSIFICATION

Technology	Sensor	Status			Type						Capability				Function†			Limitations††		
		Proposed	Tested	Used for Airport Data Collection	Remote	*In Situ*	Active	Passive	Artificial Tracer	Natural Tracer	Operational	Research Only	Airborne Potential	Ground Based Only	Detection	Tracking	Measurement	Dependence	Interference	Meteorological Dependence
Mechanical	Instrumented Tower	*	*			*		*		*		*		*			*			S
	GWVSS	*	*	*		*		*		*	*			*	*		P			S
	Pressure Sensor (local)	*	*			*		*		*	*			*	*	*				S
	Pressure Sensor (spatial average)	*				*		*		*	*			*	*					S
Acoustic	DAVSS	*	*	*	*		*			*	*			*	*	*	*		S	S
	MAVSS	*	*	*	*		*			*	*			*	*	*	*		S	S
	PAVSS	*	*	*	*		*			*		*		*	*	*		M	S	S
	Passive	*	*		*			*		*		*		*	*	*		M	S	S
	Infrasonic				*			*		*				*	?	?		?	?	?
Optical	Flow Visualization	*	*		*			*	*			*		*	*	*				S
	Infrared	*			*			*		*			*		*	*		?	?	?
	Ultraviolet	*	*		*			*		*		*	?	?	*	*		?	?	?
	Lidar	*	*	*	*		*			*	*		*		*	*	*			
Electromagnetic	Radar	*	*		*		*			*		*	?	?	*	*	P			M
	Radar	*	*		*		*		*			*	?	?	*	*	P			
	Electrostatic	*			*			*	*		*		*		*	*			S	
Combination	GWVSS + PAVSS	*			*	*	*	*		*				*	*	*				
	GWVSS + MAVSS	*			*	*	*	*		*				*	*		*			

†P = potential function requiring development

††S = some

M = much

O'Hare, and Toronto International Airports for data collection (see Section 7).

The GWVSS consists of an array of single-axis anemometers installed on a baseline perpendicular to the aircraft path. Since the wake vortices induce winds near the ground which are perpendicular to the flight path, the anemometers are oriented to respond only to the perpendicular component of the wind (the crosswind). The theoretical crosswind at the ground produced by a pair of counter-rotating vortices is given by the expression

$$v_x = \frac{\Gamma_\infty}{\pi}\left[\frac{h_2}{h_2^2 + (x-x_2)^2} - \frac{h_1}{h_1^2 + (x-x_1)^2}\right], \qquad (6.1)$$

as a function of lateral position x, where x_1 and x_2 are the lateral positions of the two vortices, h_1 and h_2 are the altitudes of the two vortices, and Γ_∞ is the vortex circulation which is also designated as the vortex strength. Figure 6-1 shows the expected crosswind vortex signatures for three different vortex altitudes. It is assumed that the vortex-induced winds can be simply superimposed on the ambient crosswind.

The effects of the two vortices are easily distinguished since they are of opposite sign. When the vortices are at altitudes significantly less than their lateral separation, the peak vortex winds are located directly below the vortex centers. For altitudes greater than the vortex separation, the vortex signature deteriorates because the winds from the two vortices tend to cancel; the signal amplitude diminishes more rapidly than 1/h and the signature no longer clearly indicates the vortex locations. The success of the GWVSS is the result of the normal behavior of wake vortices near the ground. After creation, the vortices descend toward the ground at a rate of 1 to 2 m/sec. According to classical theory (ref. 84), when the vortices approach the ground they begin to separate and eventually reach an altitude of half of their initial spacing and a separation rate of twice their initial descent rate. Thus, the vortex motion produces the exact conditions needed to

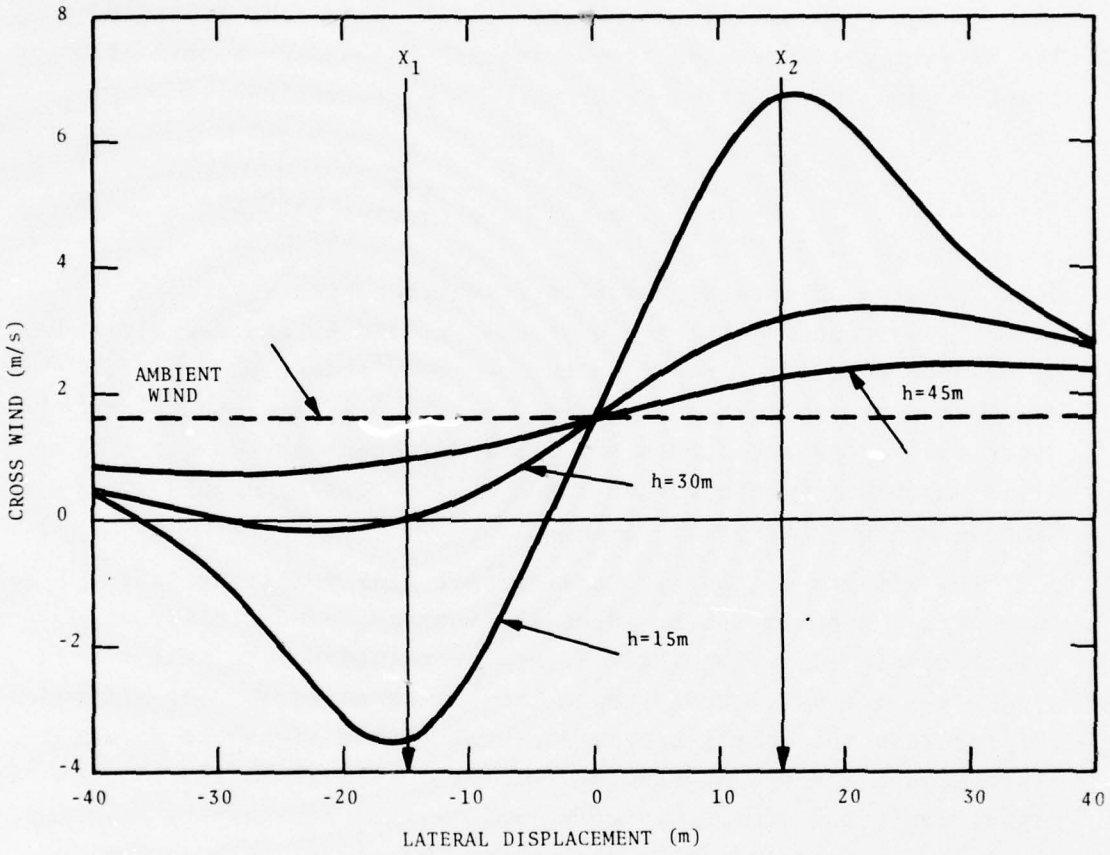


FIGURE 6-1. THEORETICAL GROUND LEVEL CROSSWIND VS. LATERAL POSITION. VORTEX STRENGTH = 300 m^2/sec, VORTEX SPACING = 30m, AMBIENT CROSS-WIND = +1.6 m/sec, AND VORTEX ALTITUDES = 15, 30, 45 m.

give good GWVSS signatures; namely, low altitudes and large lateral separations. The theory also predicts a maximum GWVSS crosswind of four times the initial descent rate; i.e., 4 to 8 m/sec.

Figure 6-2 shows some experimental data from the Heathrow GWVSS installation (ref. 85). The wind measured simultaneously at each anemometer is presented as a bar graph obtained by successively sampling each anemometer output in turn. The motion of the vortices to the left is evidenced by the displacement of the vortex peaks at different times. The algorithm used to obtain the vortex positions from GWVSS data simply designates the location of the anemometer reading the highest crosswind velocity as the lateral position of one vortex and the location of the anemometer reading the lowest velocity as the position of the other vortex. Figure 6-3 shows the stepped vortex tracks obtained from this algorithm. When the vortex signals decay to the level of ambient turbulence, the vortex locations given by the algorithm become random. The termination of the vortex tracks can be made automatic by means of consistency requirements.

The accuracy of the GWVSS vortex locations was evaluated in 1972 flight tests at NAFEC. Figure 6-4 shows some data from those tests plotted as time histories of the crosswind at each anemometer. Comparisons with photographic tracks of smoke entrained in the vortices showed that the peak in the anemometer response accurately measures the time when the vortex is directly above the anemometer. Because the vortex peak becomes asymmetrical as the vortex ages, the stepped track of Figure 6-3 tends to display a bias compared to the actual vortex tracks. The peak response representing the vortex arrival typically occurs considerally before the middle of the total time the vortex position is assigned to a particular anemometer location.

A typical GWVSS installation is shown in Fig. 6-5. Fixed-axis propeller anemometers using dc generators are mounted on posts about 3 m high with lateral spacing of about 15 m. The spacing between anemometers should be roughly equal to the expected minimum vortex altitude (about 3/8 of the wing span), so that vortices are

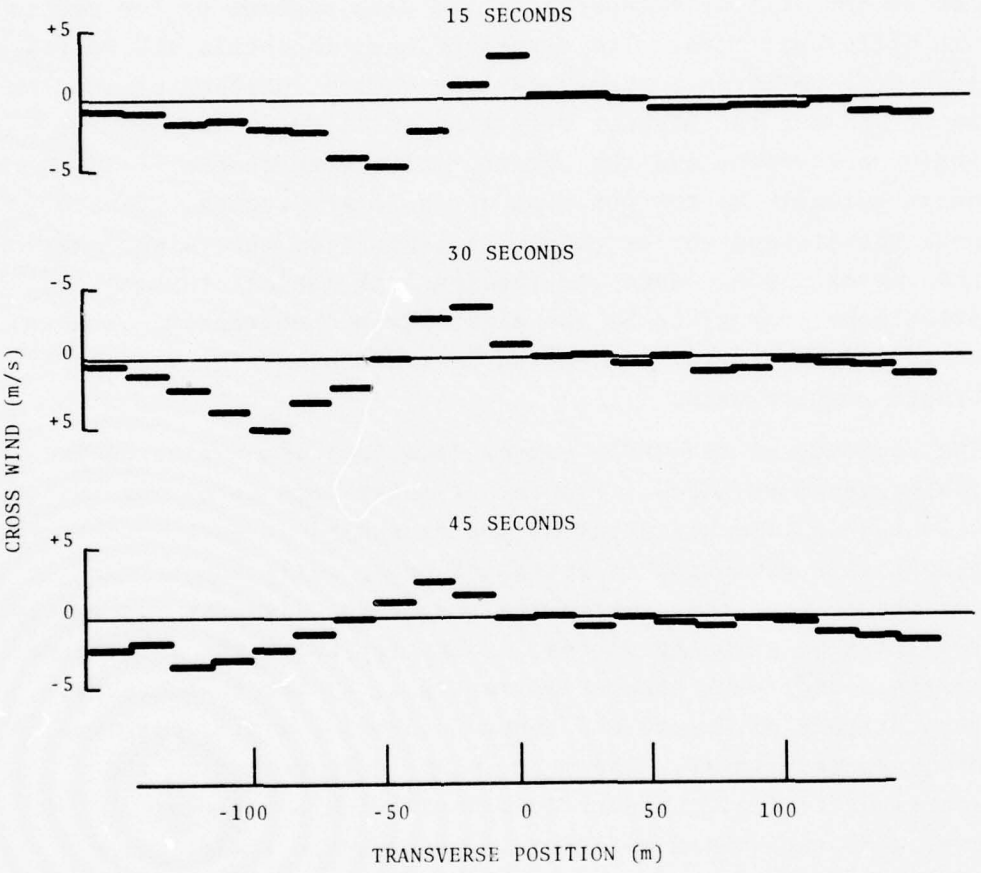


FIGURE 6-2. GWVSS DATA FOR A BOEING 707 AIRCRAFT. CROSSWIND PROFILES FROM THE INNER GWVSS BASELINE AT HEATHROW AIRPORT RUNWAY 28R ARE SHOWN FOR THREE ELAPSED TIMES AFTER AIRCRAFT PASSAGE AT 1123 HOURS ON 29 APRIL 1974.

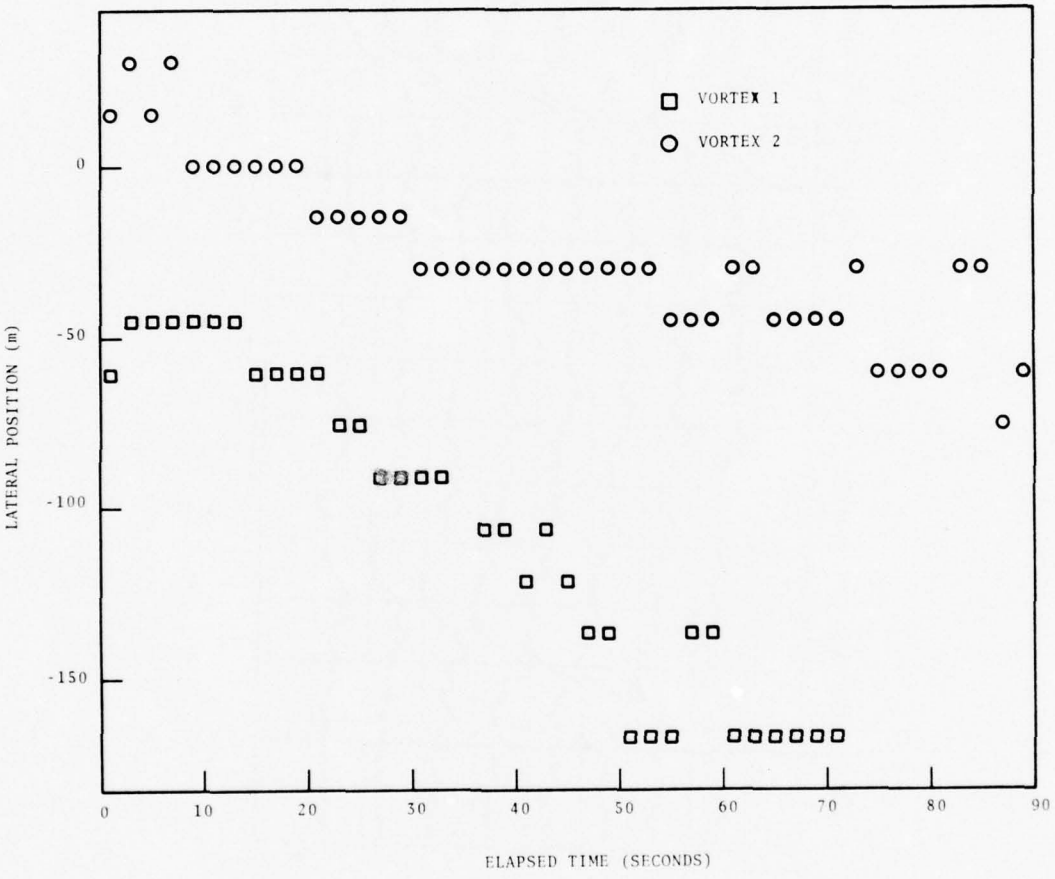


FIGURE 6-3. VORTEX TRACKS FROM THE INNER GWVSS BASELINE AT HEATHROW AIRPORT. THE DATA ARE FROM THE SAME RUN SHOWN IN FIG. 6-2.

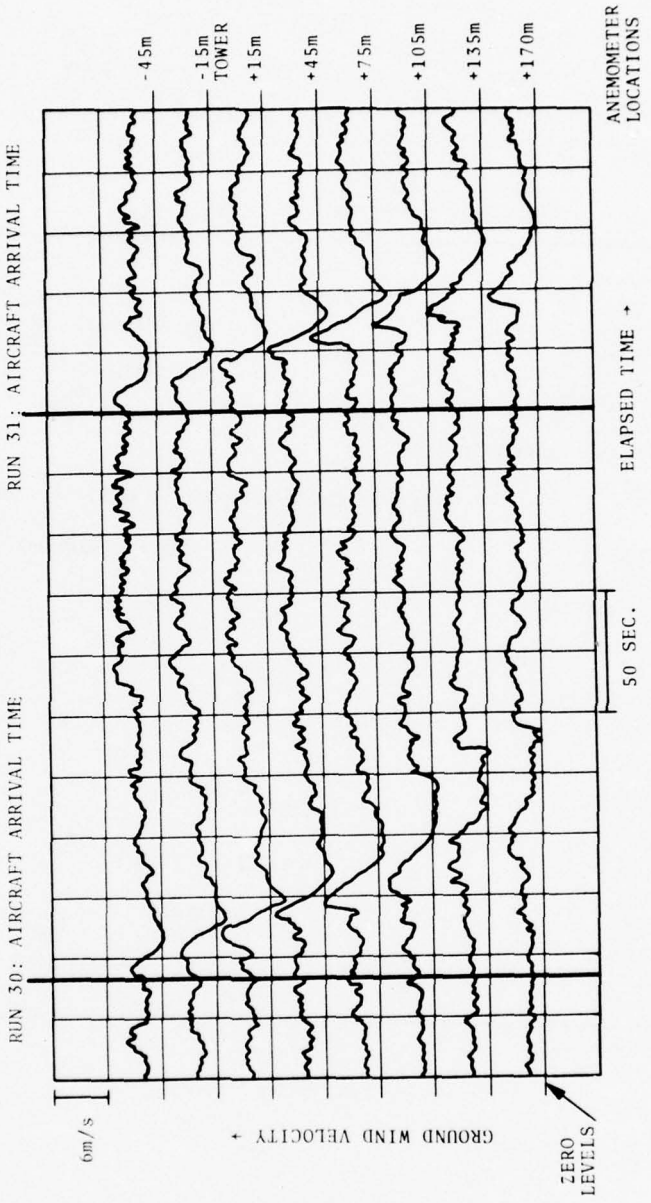


FIGURE 6-4. GWVSS TIME HISTORY DATA FROM A BOEING 747 AIRCRAFT IN HOLDING CONFIGURATION. TWO PASSES FROM THE 17 SEPTEMBER 1972 NAFEC CALIBRATION TESTS ARE SHOWN. DISTANCES ARE WITH RESPECT TO THE INSTRUMENTED TOWER. NOMINAL AIRCRAFT ALTITUDE WAS 60 m, AND LATERAL POSITION WAS - 45m.

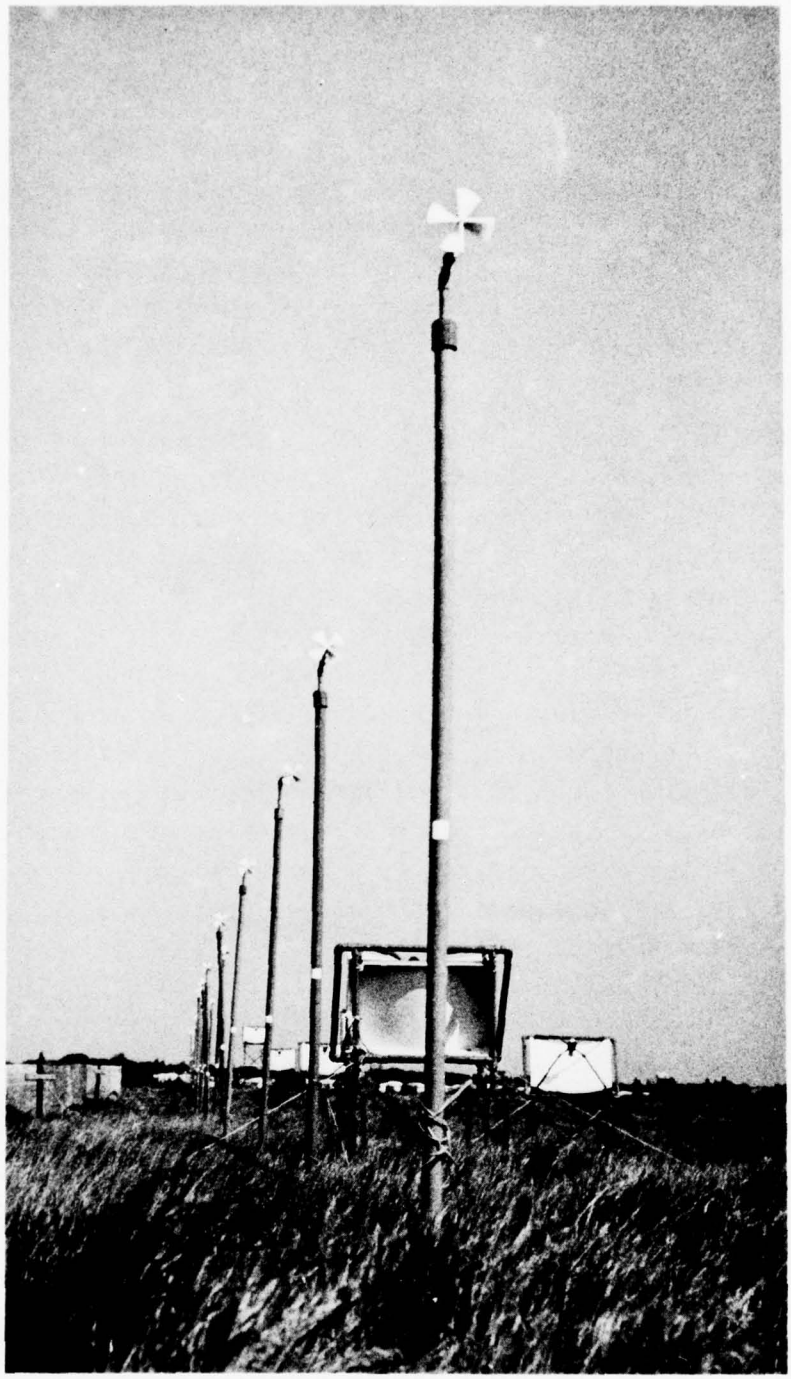


FIGURE 6-5. GWVSS INSTALLATION AT KENNEDY INTERNATIONAL AIRPORT

not lost between sensors. The altitude of the anemometers is not critical but they should be well above any obstructions which could disrupt the wind flow. The 3 m height was selected to discourage unauthorized removal of the anemometers as much as for clearance to eliminate ground effects from the data. Proper orientation of the anemometers is important for reliable vortex tracking. A single anemometer skewed into the wind can falsely indicate the presence of a vortex at its location.

The GWVSS is well established as a reliable technique for obtaining the transverse positions of wake vortices located near the ground. However, the current tracking algorithm makes no use of the magnitude of the vortex signal which could perhaps give some indication of vortex height h or strength Γ_∞. The peak vortex signal from equation (6.1) is $\Gamma_\infty/\pi h$ for $h << (x_2-x_1)$. A basic limitation of the GWVSS is that the decrease or disappearance of a vortex signal could be caused by the decay of Γ_∞, and hence a decay in hazard, or to an increase in h which could even increase the hazard to a following aircraft. The data-collection efforts using the GWVSS have usually included another vortex sensor sensitive to height to verify the disappearance of a vortex signal. At present, the boundary-layer effects on GWVSS vortex signatures are not well enough understood to allow the influence of Γ_∞ and h to be disentangled from GWVSS data alone.

6.3.1.2 Pressure Sensors - For the purposes of the discussion, the pressure signature associated with a wake can be represented by the Bernoulli equation (see ref. 84 for a more complete description):

$$\Delta p \approx - \frac{1}{2} \rho v^2 \quad , \tag{6.2}$$

where Δp is the pressure change, ρ is the air density, and v is the magnitude of the air velocity. In 1971, data were first collected (refs. 86 and 87) on the ground-level pressure and velocity signatures of wake vortices. Since the velocity was measured with a hot-wire anemometer which was not sensitive to direction, the vortex signatures were similar for both sensors. Subsequent work (ref. 88)

concentrated on the pressure sensor because of its superior reliability. The first basic difficulty encountered with the simple pressure sensor was its inability to distinguish which vortex was being sensed. Under the conditions of the tests, both vortices gave negative signals, as expected from equation (6.2). The desire to discriminate between the two vortices led to a more complex configuration consisting of a differential pressure sensor connected to two oppositely directed pitot tubes. This arrangement succeeded in providing opposite polarity signals for the two vortices, but it also uncovered the fundamental problem of nonlinear response to the vortex winds. Because the air velocity $\vec{v}$ is a superposition of the vortex and ambient winds, the pressure signature given by equation (6.2) depends strongly on the ambient wind. This dependence was particularly troublesome under conditions where the ambient wind was predominantly perpendicular to the flight path; the vortex which added to the ambient wind usually gave much larger signals than the vortex which subtracted from the ambient wind. At this point in the development, it was concluded that a linear sensor should be used to measure the vortex crosswind signatures, so that the two vortices could be distinguished, and so that the ambient wind would not influence the measurements. The Gill propeller anemometer was found to have the required linear single-axis response and has been used in all GWVSS installations to date.

A vortex-warning detector using a pressure sensor has been proposed by Bedard (unpublished) of the NOAA Wave Propagation Laboratory. The basic concept is to average spatially the ground-level pressure along the direction of flight to reduce random noise while maintaining the response to the spatially coherent vortex. The pressure averaged over a 300-m distance is to be obtained by means of a pipe with periodically spaced leaks to the atmosphere. A complete vortex detector might consist of three such pipes placed on the approach-path centerline and 100 m to either side. Two differential pressure sensors would compare the average pressure in the center pipe to that in the two side pipes. In the absence of a vortex, all three pipes should measure the same pressure with a low noise level since they are exposed to the same averaged ambient

wind. However, if a vortex is located near the centerline, both differential sensors will show a non-zero response apart from a few special null conditions which should last for only short periods of time. If both differential responses exceed a threshold, a vortex warning could be issued. The sensor will show a reduced response from a vortex which is skewed with respect to the runway centerline because the vortex is no longer coherent over the full length of the pipe. This feature may actually be desirable for protection against hazardous vortices since a strongly skewed vortex will also not interact coherently with an incoming aircraft. The noise level to be expected from the sensor is uncertain, but it is expected to increase with the square of the ambient wind, and also, to be very sensitive to obstructions such as large buildings or woods which could induce large-scale gradients in the surface wind.

6.3.2 Acoustic Sensors

A variety of acoustic sensors have been developed for the remote sensing of aircraft wake vortices. They all suffer from sensitivity to ambient noise. The major noise sources which limit the performance of acoustic sensors in the airport environment are aircraft operations and meteorological effects such as rain hitting the antenna and wind whistling around the antenna. At the current state of development, no acoustic sensor can be designated as an "all-weather" system.

The capabilities of an acoustic-sensing system are normally limited by the tradeoffs involved in antenna design. Since most sources of ambient noise and spurious reflections are located on the ground, antennas are designed to have low side response. The standard acoustic antenna consists of a transducer and horn at the focus of a parabolic dish. Low side response is achieved by surrounding the antenna with a shield which is covered on the inside with sound-absorbing material to eliminate internal reflections. One should note that mechanically scanned antennas such as used in radars are generally impracticable for acoustic antennas because of limitations posed by the slow speed of sound. Consequently, multiple beam antennas are often used to span an area, and can be

constructed simply by using an array of transducers in the same dish. One of the limitations of the horn-dish-shield antenna configuration is that the feasible angular coverage of a single antenna is probably less than 50 degrees. Moreover, as the angular coverage increases, the side response also tends to increase, thus leading to lower signal-to-noise ratios.

One of the critical parameters for acoustic sensors is the frequency of operation. The acoustic absorption of air increases rapidly with frequency, and has a strongly peaked dependence on the absolute humidity (ref. 89). Acoustic absorption serves both to attenuate the desired vortex signals, and also, to reduce the ambient noise from distant sources. Proper selection of the frequency requires a balancing of the relative advantages of high frequency: smaller antennas and less ambient noise; and those of low frequency: longer range for a given signal loss and greater transducer efficiency. One pitfall in frequency selection should be noted. If the frequency chosen for a particular range is just satisfactory under normal meteorological condidions, the humidity-absorption peak can severely degrade the range capabilities under conditions of low absolute humidity.

6.3.2.1 Active Acoustic Sensors

Sound waves interact with wake vortices via a number of scattering mechanisms. Turbulent fluctuations in the air cause some of the sound to be scattered in all directions. The scattered signals are Doppler-shifted by the mean wind in which the turbulence is imbedded. The change in frequency Δf is given by

$$\Delta f = 2f_o(w/c_s) \sin \frac{1}{2} \theta \quad , \tag{6.3}$$

where f_o is the transmitted frequency, θ is the scattering angle, w is the mean velocity component of the wind in the direction bisecting the angle between the transmitted and received beams, and c_s is the speed of sound.

The angular distribution of the acoustic energy scattered from turbulence depends upon the nature of the associated fluctuations

(ref. 90). Figure 6-6 compares the expected scattering cross section for velocity and temperature (density) fluctuations with a Kolmogorov spectral distribution. The cross section decreases rapidly with angle and reaches a null at 90 degrees. An additional null occurs at 180 degrees scattering for velocity fluctuations. The positions of these nulls have influenced the design of Doppler Acoustic Vortex-Sensing Systems (DAVSS). Although a bistatic (separated transmitter and receiver) acoustic sensor can respond to both velocity and temperature fluctuations, a monostatic (single-location) sensor views 180 degrees scattering which can be produced only by temperature fluctuations. The characteristics of a monostatic acoustic sensor are, therefore, strongly dependent upon the distribution of thermal fluctuations in the wake, which may vary considerably with aircraft engine placement. Because of this uncertainty, the first DAVSS experiments (refs. 91 and 92) employed bistatic configurations rather than the simpler monostatic configuration which would also provide greater velocity resolution according to equation (6.3).

Another mechanism for acoustic scattering is the modification of acoustic propagation by the non-fluctuating properties of the vortex. The dominant effect is a deflection or refraction of the sound propagating through the vortex core. The direction of propagation $\bar{n}$ is bent in the direction of vortex rotation according to the vector equation (ref. 93)

$$\frac{d\bar{n}}{ds} = - \bar{n} \times (\bar{\nabla} \times \bar{v}/c_s) \quad , \tag{6.4}$$

where s is the distance along the direction of propagation, and $\bar{\nabla} \times \bar{v}$, the curl of the vortex flow field, is the vorticity which is large only near the vortex core. One can integrate equation (6.4) to obtain the maximum scattering angle

$$\theta_m = \Gamma_\infty / \pi c \bar{r} \quad , \tag{6.5}$$

where $\bar{r}$ is mean vortex radius weighted according to the radial variation in vorticity. The approximations leading to equation (6.5) become inaccurate as θ_m approaches 1.0 radian. The aircraft

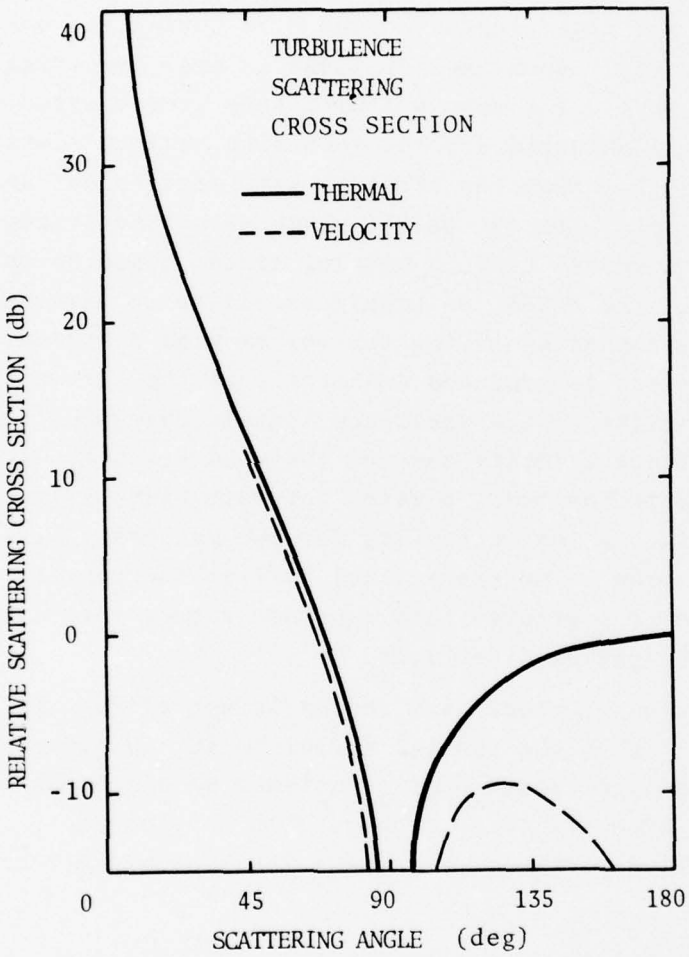


FIGURE 6-6. TURBULENCE-SCATTERING CROSS-SECTION VERSUS SCATTERING ANGLE.

dependence of equation (6.5) lies in the two parameters Γ_∞ and $\bar{r}$. For aircraft operating with the same coefficient of lift and wing shape (a reasonable approximation for a commercial jet transport), Γ_∞ is proportional to the wing span b. The maximum scattering angle is then inversely proportional to $\bar{r}/b$, the relative size of the core with respect to the wing span. A factor-of-three variation in θ_m has been observed (ref. 54) for different types of landing aircraft. The observed variation can be related to the proximity of engine-jet blast to the vortex core during the wake roll-up process (ref. 95). When the jet blast is near the origin of the vortex core (i.e., for aircraft with four wing-mounted engines), the vortex core is enlarged and the resulting maximum scattering angle is smaller than that for aircraft with engines far away from the vortex core (e.g., on the tail). Because of the strong variation in θ_m with aircraft type, a sensing system based on refractive scattering; e.g., the PAVSS, is highly sensitive to aircraft type. It is also incapable of measuring the vortex-wind distribution. Since the scattering is produced coherently by the vortex as a whole, Doppler shifts in the scattered signals characterize only the vortex-transport velocity and not the wind velocity within the vortex. The scattering cross section for refraction is much larger than that for fluctuation scattering for two reasons. First, the entire incident beam is scattered, not just a fraction of it. Second, the beam is scattered into a plane, rather than a sphere of resultant propagation directions.

The refraction of sound in a vortex is not adequately described by equation (6.4) when the spatial variation in the acoustic propagation medium is significant over a distance of one acoustic wavelength λ. When a vortex core is comparable in size to λ, it scatters sound in all directions, even at a 180-degree scattering angle.

Spatial resolution in active acoustic sensors is achieved by using narrow angular beams and/or short transmitted pulses. Since two dimensions must be specified to define a point in a plane, three basic configurations are available for resolving vortex location:

a) Two beam angles

b) One beam angle plus one pulse arrival time

c) Two pulse arrival times.

Figure 6-7 illustrates how each of these three configurations can be used to provide bistatic coverage of a plane perpendicular to the aircraft flight path. Each beam angle to be resolved requires a fan of narrow antenna beams. Each time to be resolved requires a wide beam antenna. The roles of transmitting and receiving antennas are interchangeable as far as spatial resolution is concerned. For the monostatic configuration, illustrated in Fig. 6-8, spatial resolution is achieved by range and beam-angle measurements.

From the viewpoint of operational use, the monostatic configuration is superior to the bistatic configurations because it can be installed directly under the flight corridor to be monitored where the real estate is normally already available at airport sites. Moreover, the monostatic configuration minimizes the range to the vortex (and hence, the acoustic attenuation), and maximizes the spatial resolution for a given antenna beam width. The specific configuration of Fig. 6-8 is designed for monitoring wake vortices at the middle marker location of the approach corridor (1100 m from the runway threshold) using a maximum range of 100 m.

6.3.2.2 DAVSS - The term Doppler Acoustic Vortex-Sensing System (DAVSS) does not refer to a particular sensor configuration, but rather to a host of sensor configurations sharing the common feature that the acoustic returns from turbulence within a vortex are spectrally analyzed to yield information on the velocity profile of the vortex. Doppler processing of the turbulence-scattering signals is necessary for reliable vortex-tracking even if the velocity information is not required. Since the turbulence is distributed throughout the vortex, the vortex center cannot be consistently identified by a maximum in the scattered signal. In fact under some atmospheric conditions, the scattering from ambient turbulence is so large that even the presence of a vortex cannot be detected by the magnitude of the scattered signals.

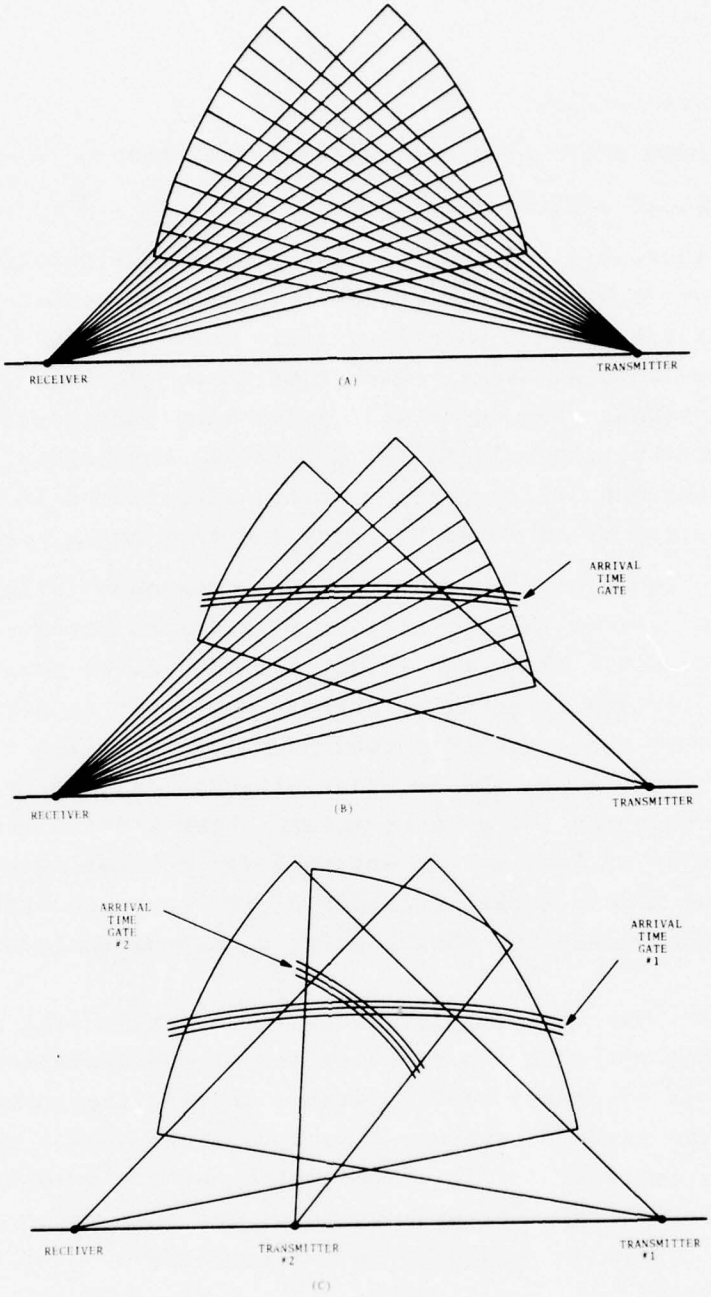


FIGURE 6-7. BISTATIC ACOUTIC SCATTERING CONFIGURATIONS. SPATIAL RESOLUTION IS OBTAINED BY: (A) TWO BEAM ANGLES, (B) ONE BEAM ANGLE AND ONE ARRIVAL TIME, AND (C) TWO ARRIVAL TIMES.

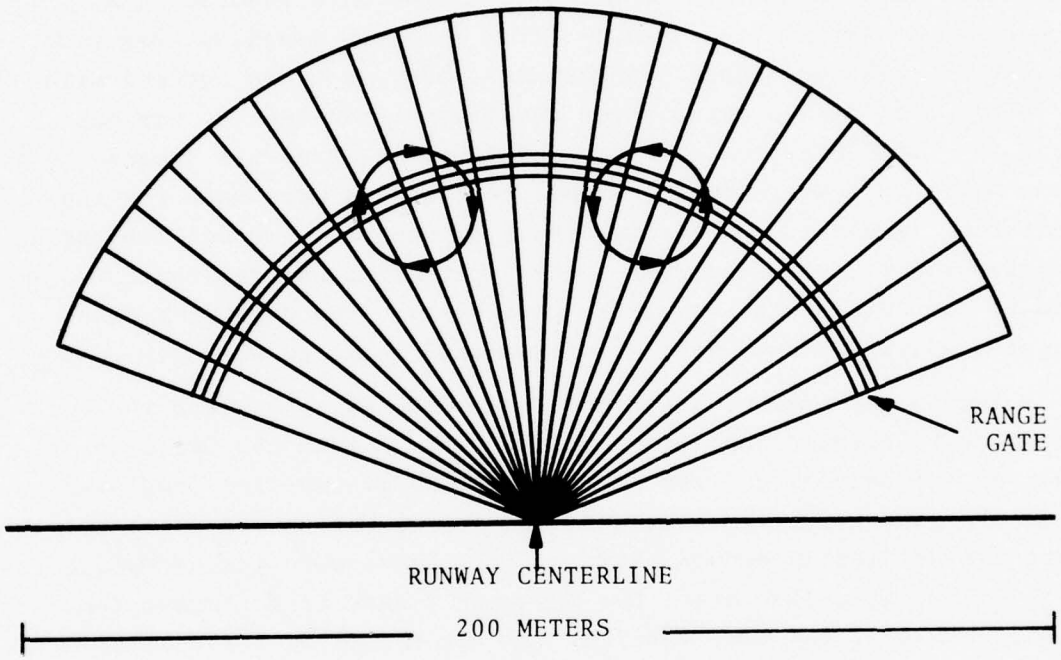


FIGURE 6-8. MONOSTATIC ACOUSTIC SCATTERING CONFIGURATION; VIEW ALONG THE FLIGHT PATH. THE VORTICES ARE SHOWN AT A TYPICAL AIRCRAFT ALTITUDE OVER THE MIDDLE MARKER.

The first DAVSS development work was done by the Xonics Corporation. In late 1970 and early 1971, they experimented with Doppler scattering from aircraft vortices at airport test sites. They then carried out two series of flight tests under FAA sponsorship at NAFEC in the fall of 1971 (ref. 91) and the spring of 1972 (ref. 92). Two types of experiments using bistatic configurations were carried out during these tests:

The first involved a detailed comparison of acoustic velocity measurements with those from hot-wire anemometers mounted on a 43-m tower. A cw transmitter radiated into a narrow vertical beam near the tower. The scattered signals were received by an antenna with multiple beams which intersected the transmitted beam at various heights. The DAVSS and instrumented tower measurements showed reasonable agreement after suitable corrections were made for the different resolution of the two types of sensor. A model for the Doppler spectra expected from vortex scattering was developed to aid in the interpretation of the DAVSS data. The data from the tower comparison tests were also processed to yield vortex strength.

The second type of experiment was designed to explore the high-altitude tracking capabilities of the DAVSS. Both configurations (a) and (b) in Fig. 6-7 were explored. The transmitter consisted of a phased array of transducers. In configuration (a) eight beams were synthesized by proper phasing. The beams were scanned sequentially, two at a time using two distinct transmitted frequencies. The location of the wake vortices was determined by the beam(s) showing the greatest Doppler spread. Vortices were detected at altitudes as high as 400 m with configuration (a).

Late in 1972, work began on DAVSS monostatic configurations. Work at Xonics led to a demonstration of a monostatic DAVSS designed to track wake vortices in real time (ref. 96). TSC collected some monostatic acoustic wake vortex scattering data during the fall 1972 sensor-calibration tests at NAFEC. The success of this simple data-collection effort led to the development of the Monostatic Acoustic Vortex-Sensing System (MAVSS) for studying the decay of wake vortex strength. The MAVSS is simply a particular DAVSS

configuration, but it is discussed as a separate sensor because of its important role in data collection at airports.

In 1973, Avco Corporation built an engineered DAVSS with real-time vortex-tracking capability and the versatility to operate in any DAVSS configuration. The Avco DAVSS was installed in 1974 at Kennedy International Airport. Four antennas were placed in a bistatic configuration, and four in an incomplete monostatic configuration. Figure 6-9 shows the bistatic Avco DAVSS' configuration designed to monitor the landing glide-slope window with two transmitting and two receiving antennas. Depending upon transmitter and frequency selections, it can be operated in the cw or pulsed mode and in the forward- or back-scatter modes. A comparison between the monostatic and bistatic vortex data showed the former to be much more useful because of larger Doppler shifts (equation (6.3)), higher spatial resolution, and lower noise levels (because the receiving antennas were elevated farther above the horizon). As a result of these observations, the bistatic baseline was abandoned and the eight antennas were installed together to give the full 24-beam monostatic DAVSS coverage shown in Fig. 6-8. Figure 6-10 shows a photograph of this installation. The need for four 36-degree receiving antennas to sense a plane through the approach corridor is a cumbersome consequence of the previously mentioned angle limitations of horn-dish antennas. It is unlikely that fewer than three antennas could span the corridor without a radical change in antenna design. One attempt to simplify the antenna configuration used three 50-degree fan-beam antennas (one vertical and one tilted to each side) to span the whole corridor. It was found that the tilted antennas had too much response to surface-noise sources to give satisfactory performance.

In the Avco DAVSS, the received signals go to a computerized processor which produces real-time displays and digital records of vortex locations. The processor simultaneously analyzes the signals from 24 receiver beams using a 6-frequency comb filter to characterize the Doppler spectrum of each signal. The spectral characteristics feed into a search algorithm which locates any vortices in the field of the antennas and determines their sense

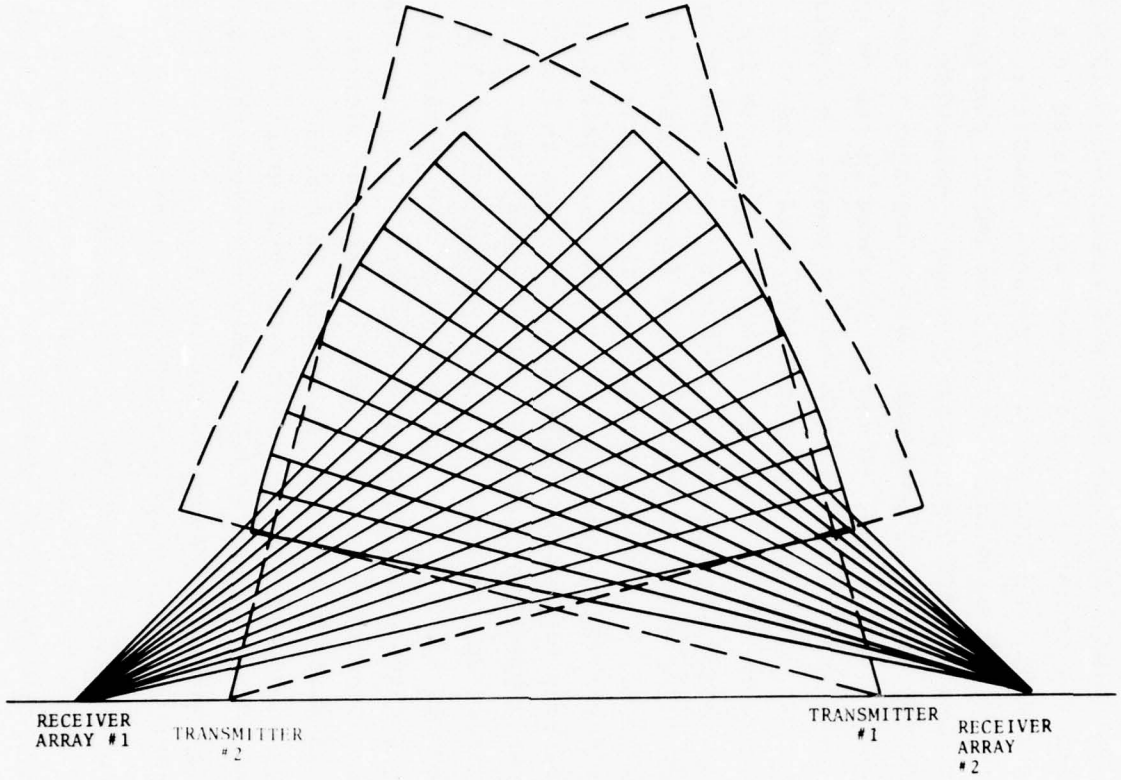


FIGURE 6-9. AVOCO DAVSS BISTATIC CONFIGURATION

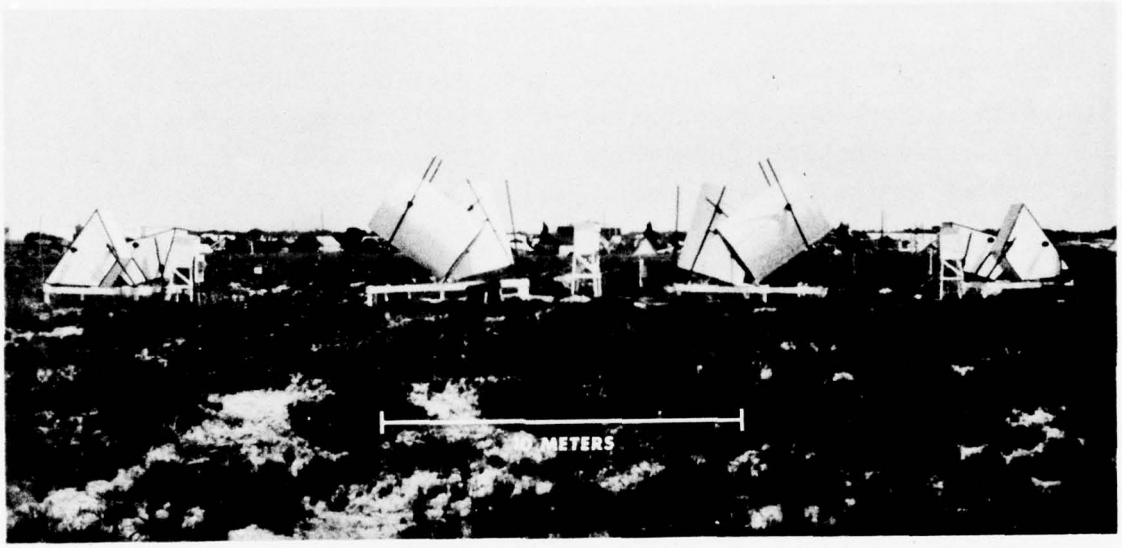


FIGURE 6-10. AVCO DAVSS MONOSTATIC INSTALLATION: VIEW ALONG THE FLIGHT PATH. THE CYLINDRICAL ANTENNAS ARE RECEIVERS WHICH RESOLVE 6 NARROW BEAMS WITH 6 DEGREES SPACING. THE TRAPEZOIDAL ANTENNAS ARE TRANSMITTERS WHICH PRODUCE FAN BEAMS.

of rotation. The current algorithm also provides a crude estimate of vortex strength. Figure 6-11 shows some vortex tracks produced by the Avco DAVSS. The lateral position and altitude of the port and starboard vortices are plotted as a function of time after aircraft passage. In this run, the vortices are seen to drop toward the ground and separate as predicted by the classical theory in the case of a small crosswind. The port vortex drifts out of the sensor view, but the starboard vortex remains within the sensitive area until it dissipates.

6.3.2.3 MAVSS - The MAVSS antenna configuration illustrated in Fig. 6-12 was originally conceived as a simple test for studying the 180-degree acoustic-scattering properties of wake vortices. The Doppler shifts in this configuration depend only upon the vertical component of the wind in the sensitive volume. The test data showed scattered signals large enough to allow accurate measurement of the vertical wind profile of the aircraft wake (see Fig. 6-13). In fact, the analysis of the test data proved the simple MAVSS configuration to be a promising technique for studying vortex strength.

The MAVSS configuration is superior to the more complex DAVSS configurations for vortex-measurement studies because the vortex measurements are not contaminated by the ambient wind which has little vertical component. Moreover, the simplicity of the MAVSS configuration allows a whole array of MAVSS antennas to be processed with the same effort required for a single DAVSS configuration. For example, the DAVSS NAFEC tower comparison tests gave vortex-strength information similar to that from the MAVSS but required Doppler processing of twelve signals instead of one.

The choice between the MAVSS and DAVSS configurations for data collection on vortex decay poses a dilemma. Since vortices are likely to drift laterally under most meteorological conditions, a MAVSS array laid out perpendicular to the flight path will usually give a more complete history of vortex decay than a single DAVSS located under the flight path. Unfortunately, a MAVSS array cannot measure the decay of vortices which do not drift at a significant

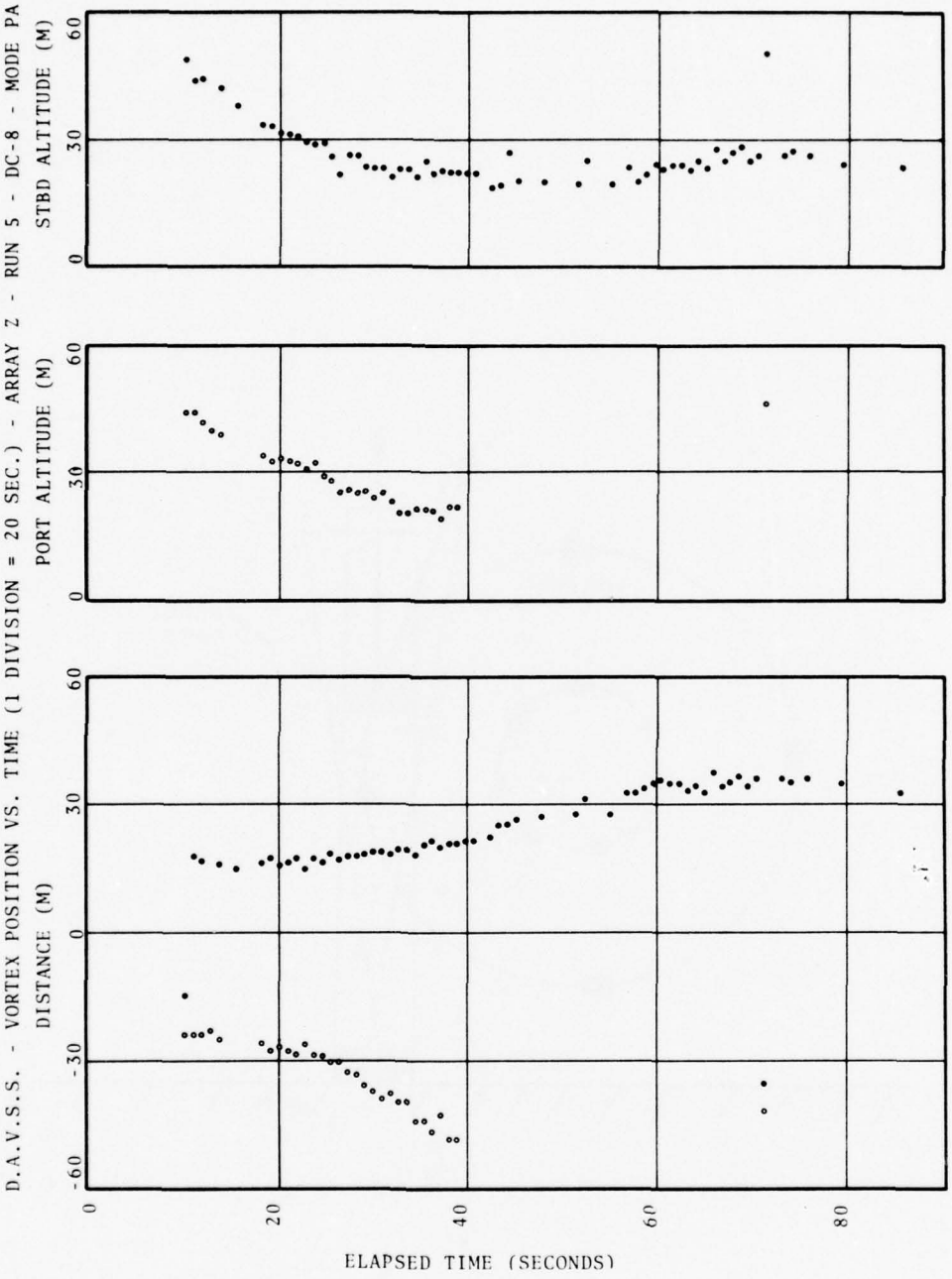


FIGURE 6-11. MONOSTATIC DAVSS VORTEX TRACKS, KENNEDY AIRPORT, RUNWAY 31R, DC-8 AIRCRAFT.

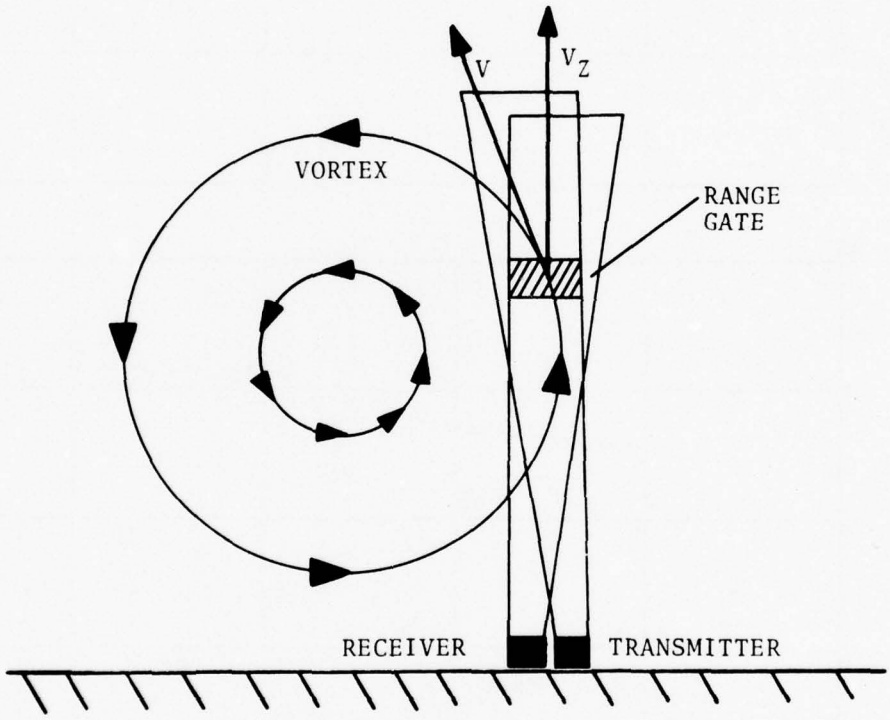


FIGURE 6-12. NARROW BEAM MONOSTATIC ACOUSTIC SENSOR.

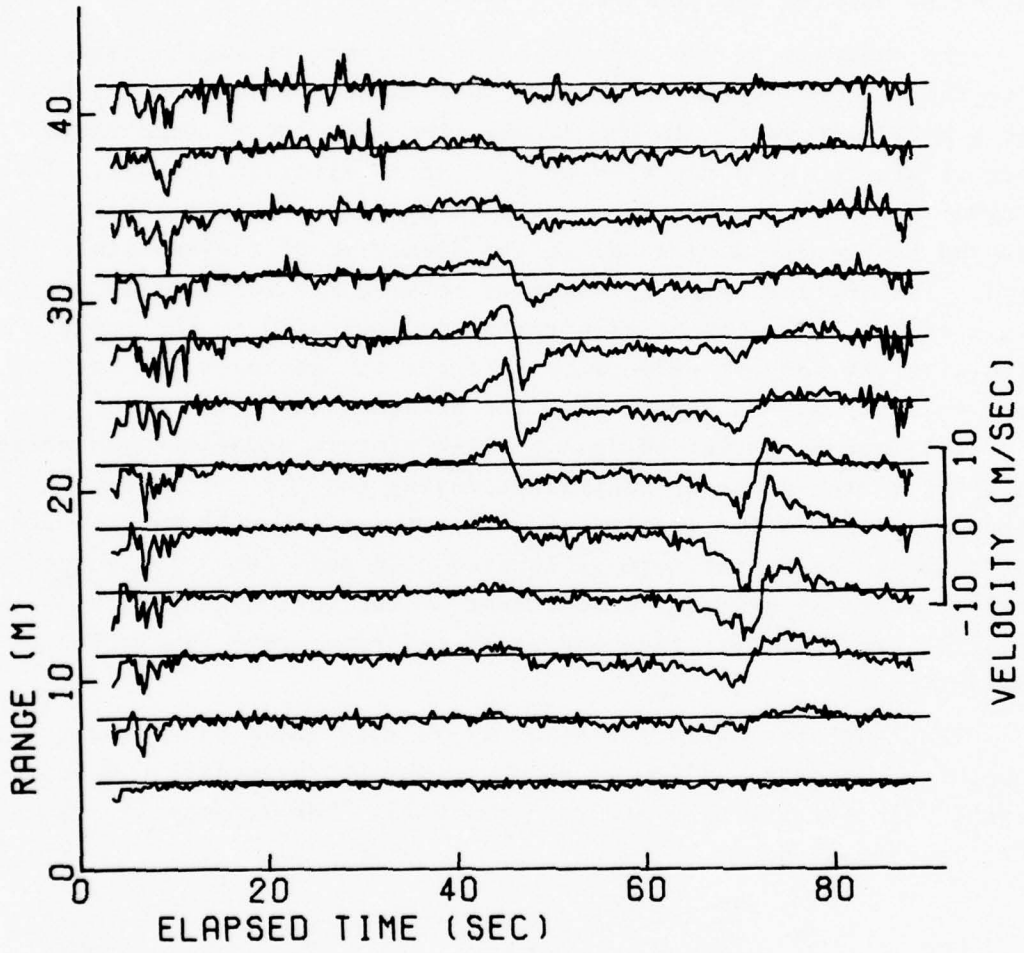


FIGURE 6-13. MAVSS WAKE VELOCITY PROFILE. B707 AIRCRAFT LANDING ON RUNWAY 31 R, KENNEDY AIRPORT, AT 1508 HOURS ON 13 NOVEMBER 1973. NOTE THE VORTEX ARRIVALS AT 46 AND 72 SECONDS. THE MAVSS ANTENNA WAS LOCATED 183 m FROM THE RUNWAY CENTERLINE.

speed. Since the primary wake vortex hazard is produced by the infrequent vortices which stall near the flight path, one is left with the difficult data-collection question of collecting much data on vortices which are not in dangerous locations, or collecting skimpy data on vortices which remain in dangerous locations. An understanding of the influence of vortex motion on vortex decay is needed to resolve the dilemma.

The analysis of MAVSS data to yield vortex strength starts with the vertical velocity profile such as that shown in Fig. 6-13 for a B-707 aircraft. In the figure, the velocity at each range gate is plotted as a function of time after aircraft passage. The arrival times of the two wake vortices over the antenna can be located by the rapid reversal in the direction of the vertical wind. The vertical wind is negative between the vortices as one would expect. The height of a vortex is indicated by the range gate with the largest velocities. If one can estimate the transport velocity of the vortex past the antenna, the time data of Fig. 6-13 can be converted to a spatial picture under the assumption that the vortex decay is negligible during the time of passage. Figure 6-14 shows the results of such a transformation for the range gates where the vortex core is located. In this case, the range gate velocity is a direct measurement of the vortex tangential velocity averaged over the beam angle and range-gate resolution of the system.

The tangential velocity $v(r)$, where r is the vortex radius, completely describes a vortex which is axially symmetric. Other useful parameters can be derived from $v(r)$. The vortex circulation $\Gamma(r)$ is defined by

$$\Gamma(r) = 2 \pi r v(r) . \qquad (6.6)$$

Figure 6-15 shows the radial dependence of the circulation for the velocity data in Fig. 6-14. The circulation values for positive and negative radius are averaged to eliminate some sources of bias. The solid lines in Fig. 6-15 are a weighted least-squares fit to the data of the two parameter form:

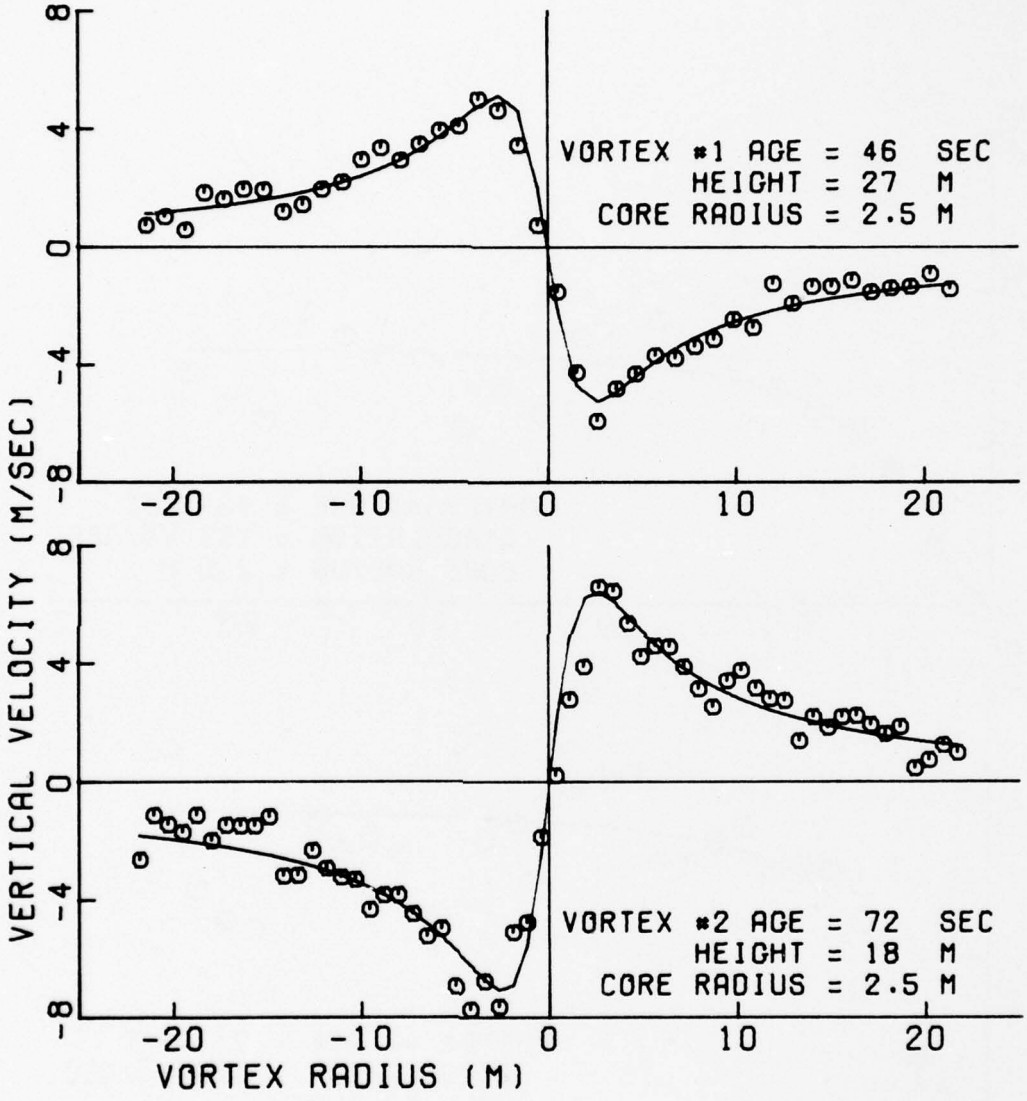


FIGURE 6-14. EXPANDED SCALE PLOTS OF THE DATA IN FIG. 6-13. THE VELOCITY IN THE RANGE GATE CONTAINING THE VORTEX CORE IS PLOTTED AGAINST DISTANCE FROM THE VORTEX CENTER FOR EACH VORTEX. THE SOLID LINES ARE THE RESULT OF A TWO-PARAMETER FIT TO THE CIRCULATION DATA IN FIG. 6-15.

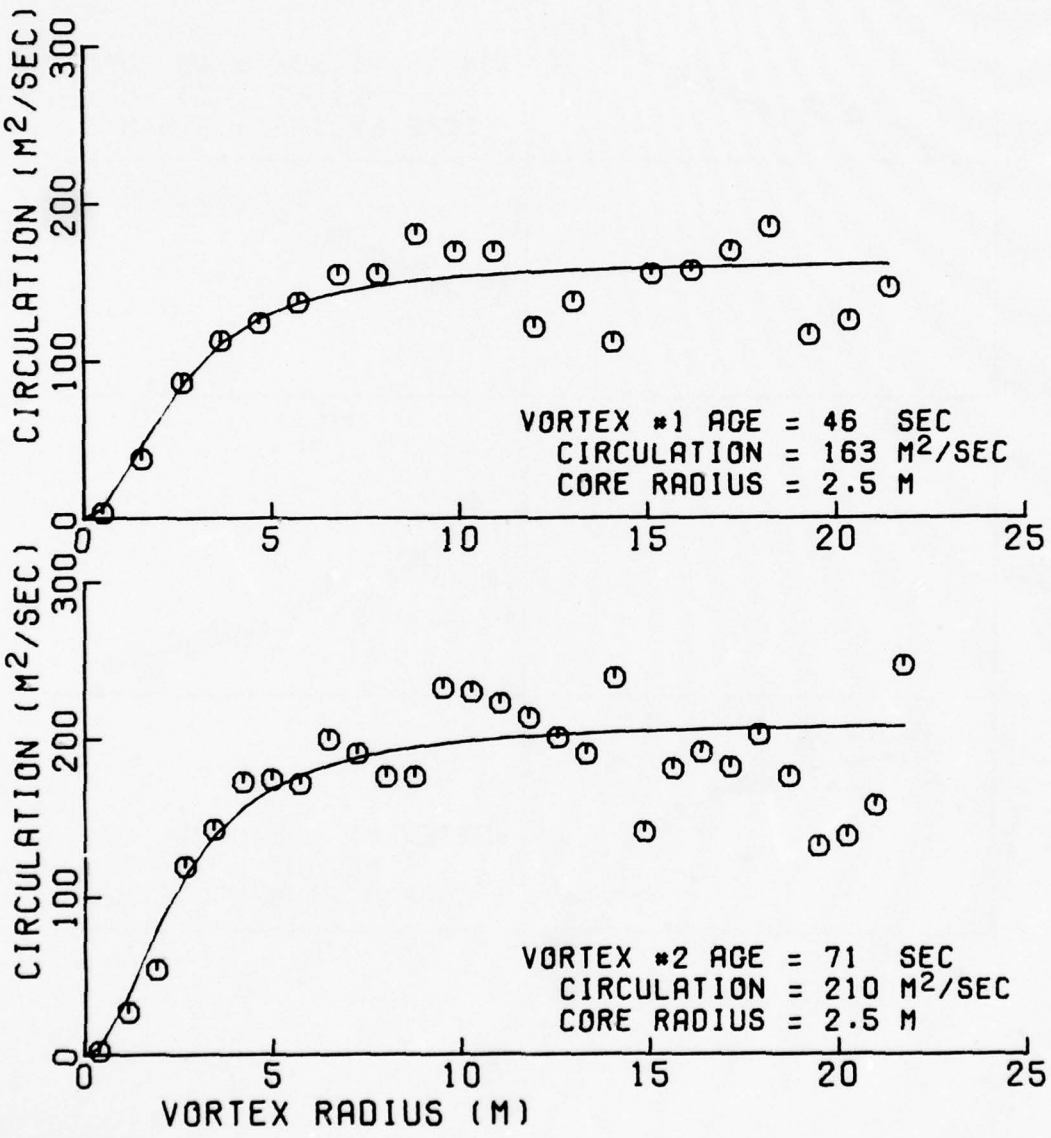


FIGURE 6-15. CIRCULATION VERSUS RADIUS FOR THE DATA IN FIG. 6-14.

$$\Gamma(r) = \frac{\Gamma_\infty}{1 + (r/r_c)^2} , \qquad (6.7)$$

where Γ_∞ is the circulation for infinite radius (also defined as the vortex strength), and r_c is the vortex core radius. This simple vortex model generally fits the MAVSS data reasonably well, and it has the virtue that r_c is both the radius of maximum velocity (equation 6.6)) and of half-circulation ($\Gamma(r_c) = \Gamma_\infty/2$). The value of r_c obtained in the data-fitting is not necessarily related to the actual core radius. Only if the core radius is larger than the antenna beamwidth can one assign a physical significance to r_c. The vortex tangential velocity data can also be used to calculate the maximum rolling moment on a wing of span b centered in the vortex. The rolling moment can be shown to be proportional to

$$\Gamma'(b) = \frac{2}{b}\int_0^{b/2} dr\ \Gamma(r), \qquad (6.8)$$

the average circulation up to radius 1/2 b. The value of $\Gamma'(b)$ approaches Γ_∞ as the span increases. The techniques of vortex parameterization discussed here assume that the vortex is isolated. The assumption is reasonable for old vortices which have had time to separate, but it leads to errors for fresh vortices which are still close together. (See Section 8.2.2.)

The measurement of wake vortex decay with the MAVSS uses an array of antennas which sequentially probe the vortices as they drift past. Figures 6-16 and 6-17 show some MAVSS data obtained from a four-antenna array. The vortex tracks in Fig. 6-16 are determined by the arrival time and altitude at each antenna. The time variations in the vortex parameters strength Γ_∞, core radius r_c and rolling moment Γ'(b=60 m) are shown in Fig. 6-17. The values of Γ' and Γ_∞ tend to agree for the large span b = 60 m. It should be noted, that the measurements for short times are less accurate because of interference from the other vortex, aircraft noise, and poorer estimates of the transport velocity.

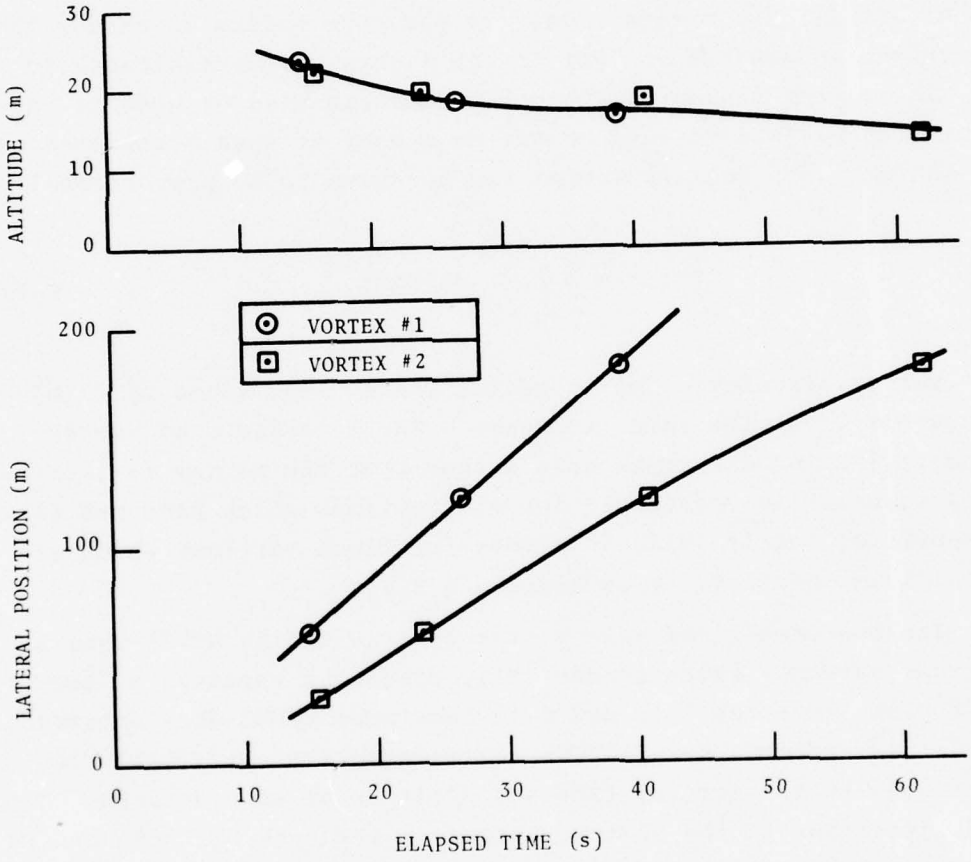


FIGURE 6-16. MAVSS VORTEX TRACKS: DC-8 AIRCRAFT, KENNEDY AIRPORT RUNWAY 31R, 1 JULY 1974 AT 1153 HOURS.

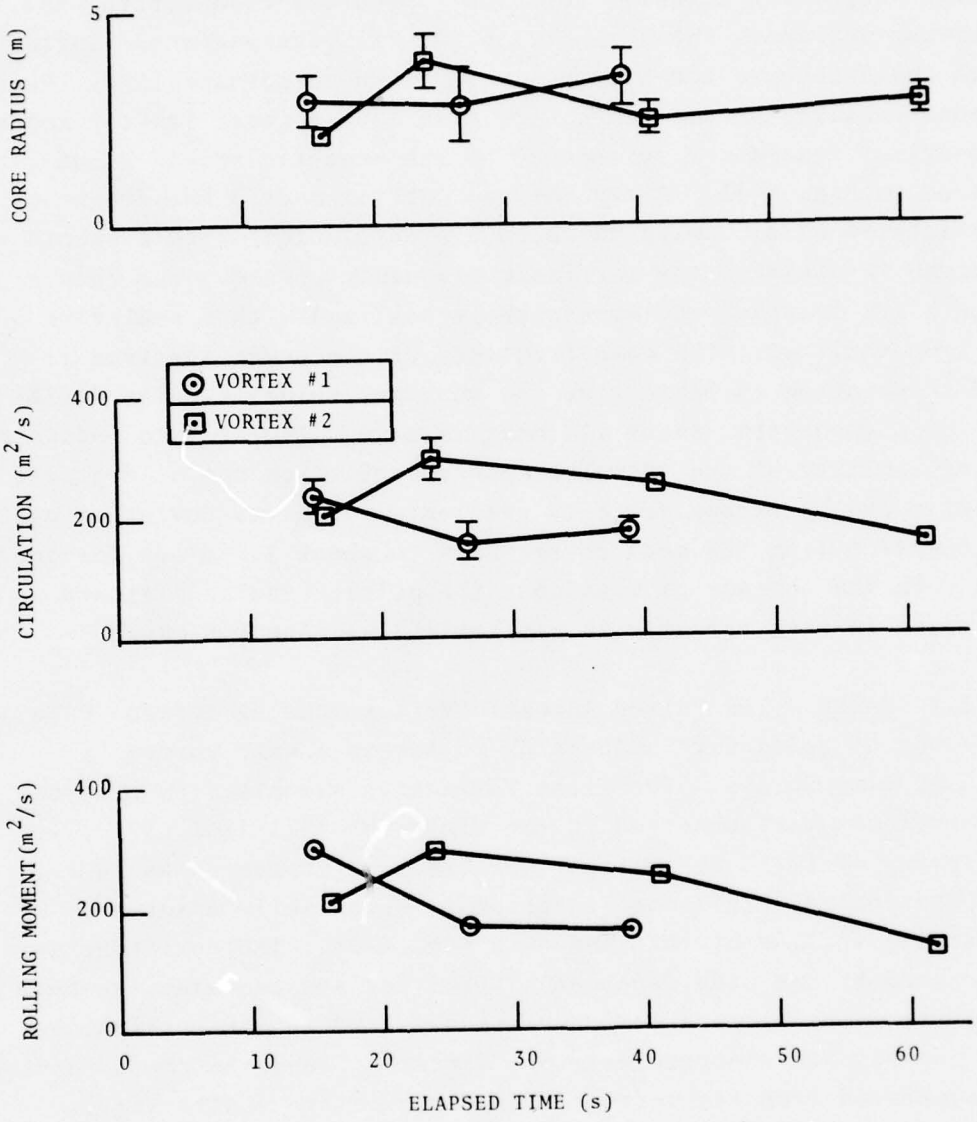


FIGURE 6-17. MAVSS VORTEX PARAMETERS VERSUS TIME FOR THE SAME RUN AS FIGURE 6-16. THE CORE RADIUS AND CIRCULATION ARE THE RESULT OF A WEIGHTED LEAST-SQUARES FIT; THE ERROR BARS INDICATE THE GOODNESS OF THE FIT. THE ROLLING MOMENT PLOTTED IS THE AVERAGE CIRCULATION Γ' FOR A WING SPAN OF 60 m.

The MAVSS configuration is essentially a meteorological acoustic sounder modified for wake vortex studies which require shorter ranges and higher resolution. Separate transmitting and receiving antennas, shown in Fig. 6-18, eliminate antenna-ringing which could obscure low-altitude returns up to perhaps 15 m. Each antenna consists of a 1.2-m square dish (0.8-m focal length) and a horn-driver transducer surrounded by the acoustic shield which can be seen in Fig. 6-18. A transmitted carrier near 3-kHz frequency is modulated by a 20-msec pulse (3.5-m resolution) with a smooth envelope to minimize the intrinsic frequency spread. The return signals are recorded and subsequently analyzed with a real-time spectrum analyzer. The mean frequency of the power spectrum is used in equation (6.3) to give the vertical velocity. The deviation of the spectrum about the mean is also calculated to indicate the reliability of the velocity measurement which can be degraded by noise and by strong velocity gradients. The rms deviation of the spectrum from the mean corresponds to about 1.2 m/sec for good data. In the absence of vortices, the pulse-to-pulse standard deviation in mean velocity is typically less than 0.6 m/sec.

6.3.2.4 PAVSS - The Pulsed Acoustic Vortex-Sensing System (PAVSS) makes use of refractive scattering to locate a wake vortex by means of time delays. The first refractive signals from aircraft wake vortices were observed in the winter of 1971 (ref. 97). In the spring of 1971, the basic PAVSS tracking system shown in Fig. 6-19 was tested. This configuration is essentially a forward-scattering version of that shown in Fig. 6-7c. The sensitive area is scanned by one wide fan-beam transmitter and two wide fan-beam receivers. The antenna response extends down to the horizon, so that two signals are received, one directly along the ground and one scattered from the vortex. Since refractive scattering is produced by a bending of the propagation path in the direction of vortex rotation, only one of the two vortices will be seen by a particular transmitter-receiver pair (see Fig. 6-19).

Figure 6-20 shows a picture of PAVSS signals received from one receiver in Fig. 6-19. The CRT intensity indicates the received

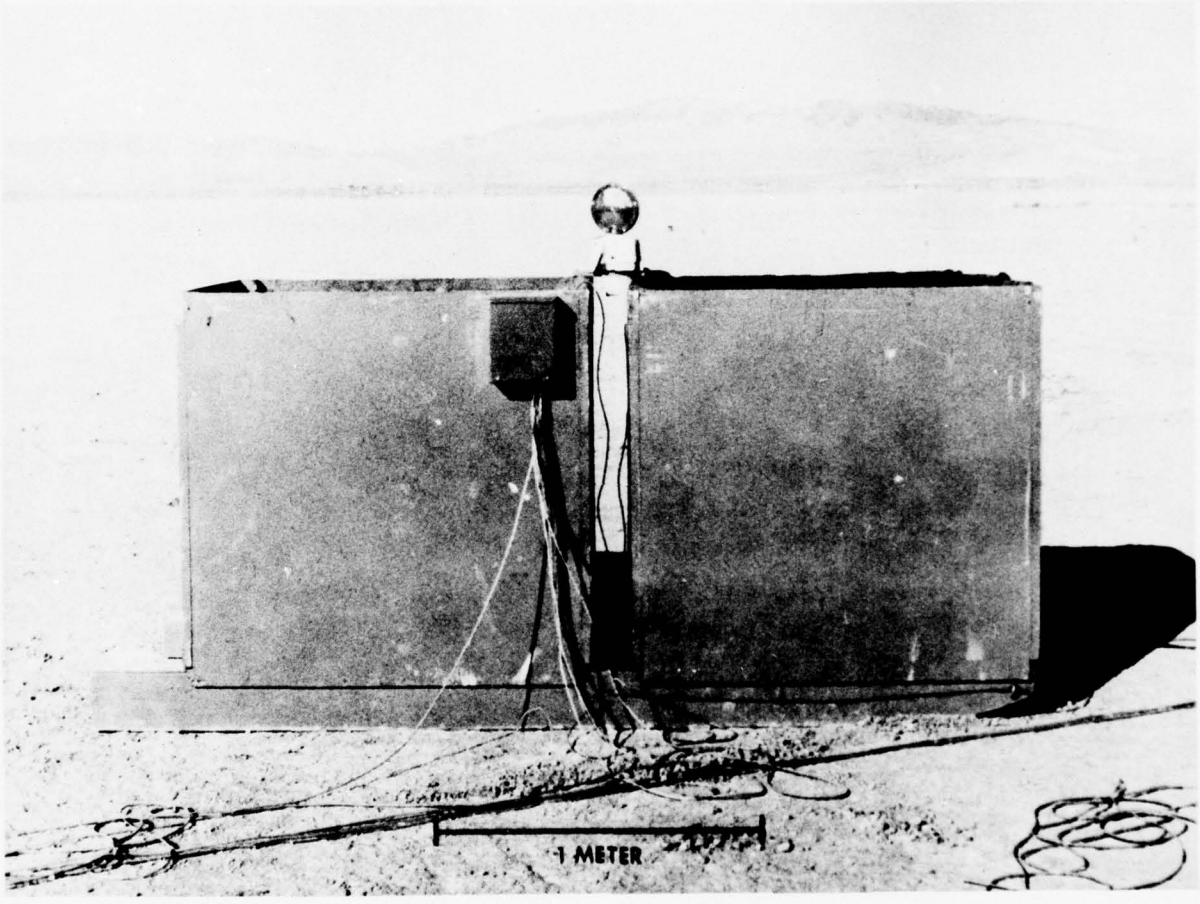


FIGURE 6-18. MAVSS ANTENNA

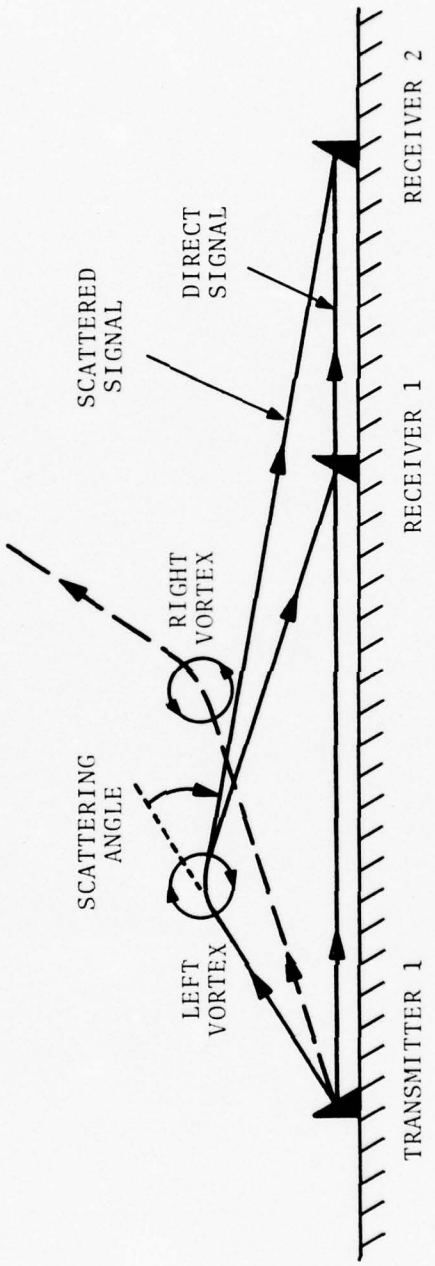


FIGURE 6-19. SIMPLE PAVSS CONFIGURATION. NOTE: THE RIGHT VORTEX SCATTERS SOUND AWAY FROM THE GROUND AND WILL NOT BE DETECTED.

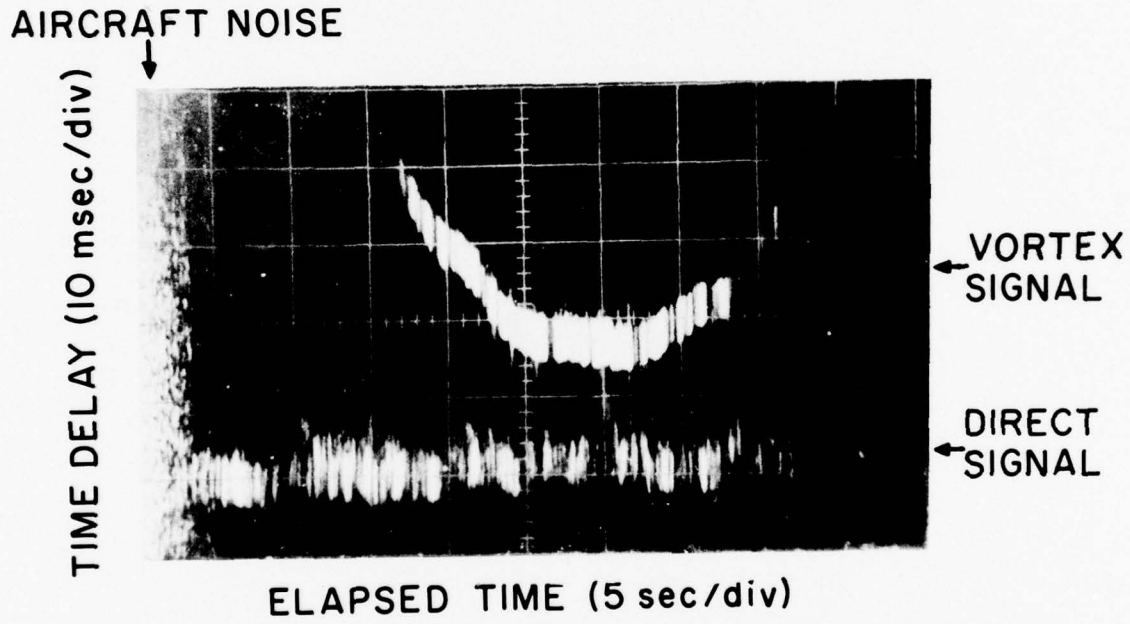


FIGURE 6-20. PAVSS SIGNALS FOR A B-747 AIRCRAFT LANDING ON RUNWAY 22L, LOGAN AIRPORT, 3 JUNE 1971. TRANSMITTER-RECEIVER SEPARATION = 138 m.

acoustic intensity. The picture is scanned rapidly in the vertical direction in synchronization with the transmitter pulses (5 msec long with a 60 msec period). A slow horizontal scan gives the dependence of the signals as a function of the time after aircraft passage. The direct signal appears as a horizontal band near the bottom of the picture. The vortex signal is vertically displaced (delayed) with respect to the direct signal by an amount which depends upon the vortex location, and hence, varies with time. The time delay in arrival of the scattered signal determines that the vortex lies on an ellipse with foci at the transmitter and receiver. The exact vortex location can then be determined by the intersection of ellipses from two different transmitter-receiver pairs (see Fig. 6-21).

Comparisons with the NAFEC tower in the summer of 1971 (ref. 86) showed that the PAVSS gave reasonably accurate vortex locations. The PAVSS was then developed to its final configuration by the winter of 1972 (ref. 88). Frequencies in the 2 to 3 kHz range and pulse widths of 2 to 3 msec are used. Three antennas are placed on either side of the runway centerline. Each alternately transmits and receives, so that both vortices can be detected. The multiplicity of antennas is needed to give the desired spatial coverage while maintaining reasonable location accuracy. The tracking limitations of the PAVSS are discussed below.

PAVSS development continued with calibration tests at NAFEC during the fall of 1972, studies of take-off vortices at Logan Airport during the winter of 1973, and the demonstration of real-time tracking using a minicomputer during the spring of 1973. The calibration tests further verified that the PAVSS gives accurate vortex locations when properly configured for the altitudes of interest. Increasing the antenna separation to 800 m was found to increase the PAVSS altitude range to 200 m.

Avco Corporation built an engineered version of the PAVSS which could measure vortex locations in real-time simultaneously at two different distances from the runway threshold. The system was installed at Kennedy Airport during the spring of 1974. Figure 6-22 shows the wide-beam antenna used in the Avco PAVSS. (The

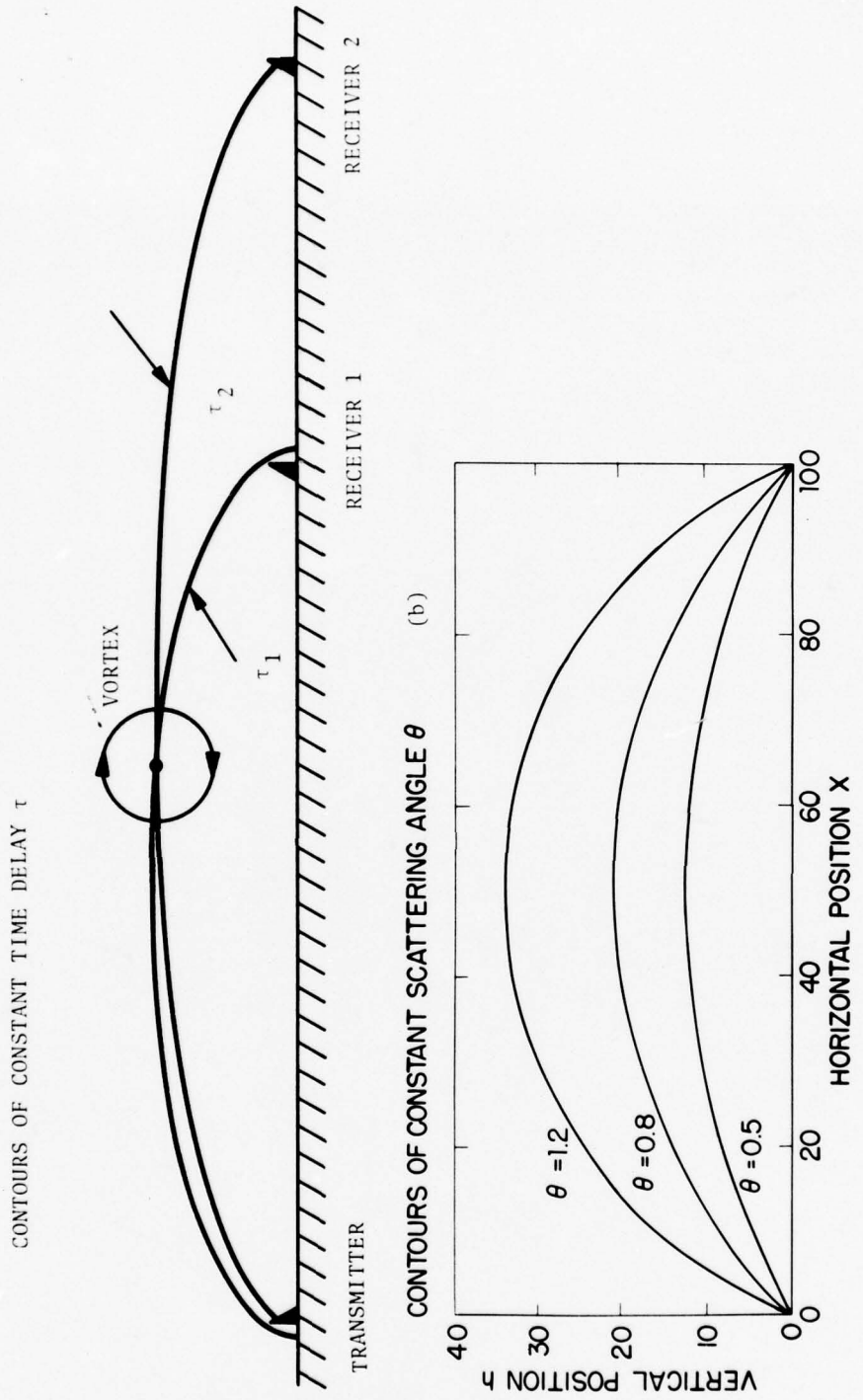


FIGURE 6-21. (A) VORTEX LOCATION BY THE INTERSECTION OF CONSTANT TIME-DELAY ELLIPSES FOR TWO TRANSMITTER-RECEIVER PAIRS. (B) CONTOURS OF CONSTANT SCATTERING ANGLE (RADIANS) FOR THE TRANSMITTER-RECEIVER ONE PAIR. THE DISTANCE UNITS ARE ARBITRARY.

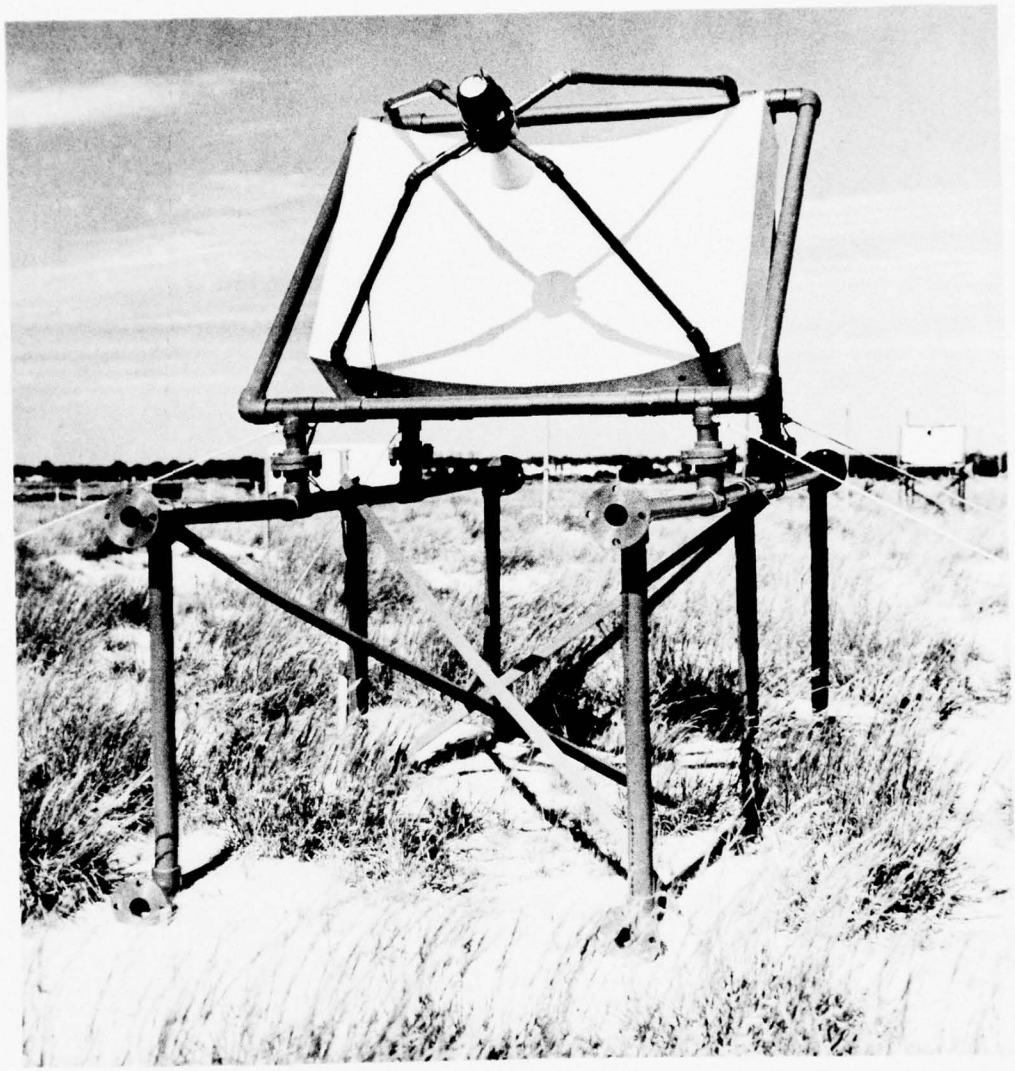


FIGURE 6-22. AVCO PAVSS ANTENNA. DISH PARAMETERS: FOCAL LENGTH = 0.51 M, WIDTH = 1.32 M, AND HEIGHT = 0.91 M.

antenna array can also be seen in Fig. 6-5.) Figure 6-23 shows some vortex tracks obtained from the AVCO PAVSS.

The ability of the PAVSS to detect and track wake vortices is strongly dependent upon the scattering angle θ defined in Fig. 6-19. Because the refractive scattering angles are small, the two ellipses in Fig. 6-21a are very flat. Consequently, the horizontal position determined by their intersection can have large errors for small errors in the time-delay measurements. The vortex height is much less influenced by timing errors, and therefore, is given more accurately by the PAVSS. The timing errors in the signal delay measurements are typically several msec. Errors of this size lead to a horizontal position accuracy which is useless unless one of the scattering angles is greater than 0.5 radian. Smaller values of θ also lead to difficulty in separating the direct and scattered signals since the time delays are proportional to θ^2 for small θ. The difficulty is illustrated in Fig. 6-23 where the vortex signals are lost for a time when the port-vortex altitude is so low that the resultant scattering angles and time delays are too small.

The maximum vortex-scattering angle θ_m (equation (6.5)) determines the area where a vortex can be detected. Figure 6-21b shows the detection limits for three values of scattering angle. The useful tracking area is roughly the region between the 0.5-radian contour and the θ_m contour. As discussed previously, the values of θ_m range from 0.5 to 1.2 radians for different types of aircraft (ref. 94). The PAVSS is thus very useful for B-727 vortices (θ_m=1.2 radians) and is worthless for B-707 vortices (θ_m=0.5).

6.3.2.5 Passive Acoustic Sensors - Some wake vortices generate a swishing sound with energy in the spectral range of 1 to 5 kHz. The sound is heard from vortices with very tight cores such as those from landing B-727 and DC-10 aircraft. Because the sound is extremely variable in time and does not occur consistently even for the most likely aircraft, no development work has been done to exploit this signal. One should note that the vortex-generated

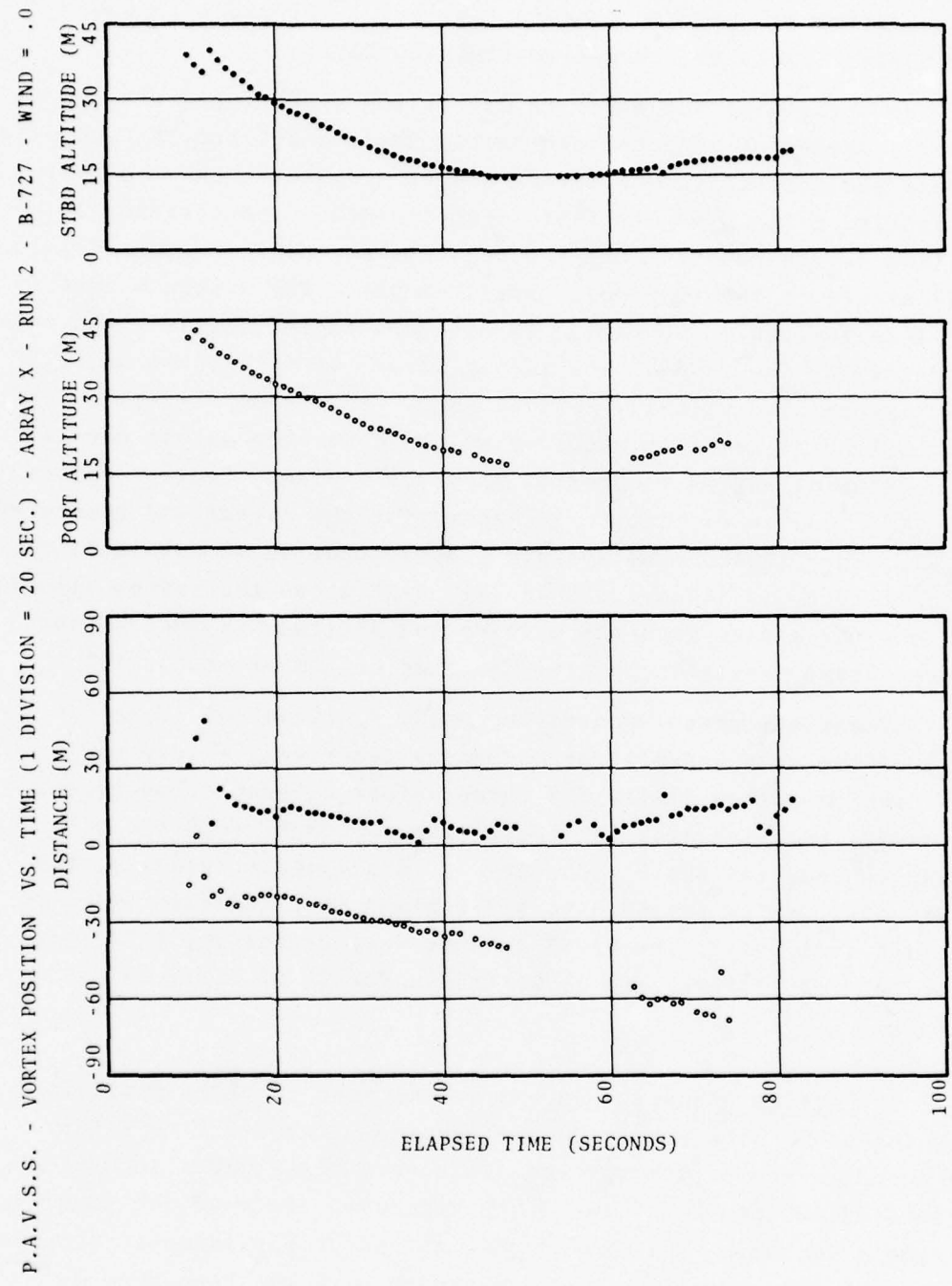


FIGURE 6-23. VORTEX TRACKS OBTAINED WITH THE AVCO PAVSS: B-727 AIRCRAFT LANDING ON KENNEDY AIRPORT RUNWAY 31R AT 0810 HOURS ON 2 JUNE 1975.

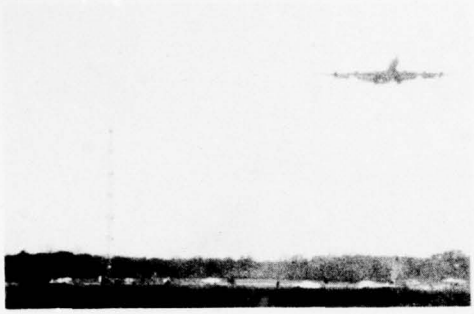
noise can interfere with the proper operation of the DAVSS and MAVSS sensors. MAVSS data show that the sound is generated in the vortex core.

Bedard at NOAA (unpublished) has proposed the possibility of detecting a wake vortex by the infrasonic radiation it generates. The concept has not been explored; however, infrasonic microphones have been used to explore the near-field pressure signature of vortices near the ground. The technique is identical to the pressure measurements of Section 6.3.1.2 except that the dc component of the signal is lost, thus producing less easily interpreted signatures.

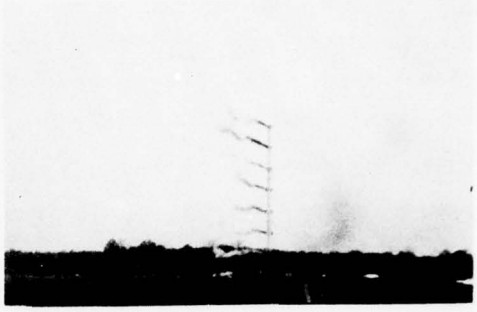
6.3.3 Optical Techniques

Optical techniques have the general advantages of high resolution and long range. They are degraded by conditions of low visibility. Infrared sensors are less affected than those using visible light.

6.3.3.1 Passive Optical Techniques - Wake vortices can become visible if they contain a sufficient density of light-scattering particles. Under certain natural conditions (high-altitude flight or high humidity), water vapor condenses in the wake vortices and remains trapped until the vortices dissipate. The effect is familiar to anyone who observes contrails. Under normal atmospheric conditions, particles must be added to make vortices visible. Two techniques have been developed for dedicated flight tests. In the first, smoke grenades or smoke generators are mounted on an aircraft in an appropriate spot to mark the core of the wake vortex. In the second, smoke grenades are mounted on a tower through which the wake drifts after the aircraft has passed. Figure 6-24 shows some photographs of the second technique, which was used to provide an absolute reference for the other sensors in the 1972 NAFEC calibration tests. The proper interpretation of the photographs in Fig. 6-24 requires careful corrections for the effects of the ambient wind.



t = 0 sec.



t = 21 sec.



t = 39 sec.



t = 48 sec.



t = 57 sec.



t = 66 sec.

FIGURE 6-24. FLOW VISUALIZATION OF WAKE VORTICES FROM A B-707 AIRCRAFT. TOWER HEIGHT = 43 m, CAMERA DISTANCE = 600 m.

A number of proposals have been made to detect wake vortices by passive infrared scanners. The technique is based on the excess radiation from the aircraft wake which contains heat, H_2O, and CO_2 from the engine exhaust. Appropriate wavelength filtering could allow an infrared sensor to be very sensitive to this excess radiation. The infrared signature of the wake is likely to give the general vortex locations, but it is uncertain how easily it can indicate vortex decay. Some experimental data will be needed to allow a definitive assessment of infrared vortex-sensing feasibility.

During the 1972 NAFEC calibration tests, a UV photographic sensor was tested (ref. 98). The sensor apparently makes use of sunlight scattered from nitrogen compounds in the wake. No feasibility information is available.

6.3.3.2 SLDVS - The Scanning Laser Doppler Vortex Sensor (SLDVS) operates in the far infrared at the CO_2 laser wavelength λ of 10.6 microns. This wavelength selection offers the advantages of high available power, low personnel hazard, long range in fog, and feasible heterodyne detection. The SLDVS operates in the cw backscatter mode, making use of naturally occurring aerosols as scattering targets. The Doppler shifts in the return signals measure the component of the wind along the laser beam line-of-sight. The Doppler shifts (equation (6.3) with θ = 180 degrees and c_s = the speed of light) are much larger than those observed in acoustic scattering in the MHz region (1.9 MHz for 10 m/sec velocity). The laser frequencies are reduced to the MHz region by means of heterodyne detection which also serves to give a good signal-to-noise ratio at the detector. If the scattered light is simply mixed with the transmitted signal, the resultant velocity measurement has a sign ambiguity which can be confusing in many cases. The ambiguity can be removed if the mixing signal is offset or translated with respect to the transmitted signal.

The spatial resolution of the SLDVS is achieved by focusing the cw laser beam at the desired range D. For ranges much larger than the optics diameter d, the focal spot diameter is approximately

λF where $F = D/d$ is the f-number of focus distance. The length of the focal spot is approximately equal to $F^2 \lambda$, and therefore, is much larger than the focal width for the usual values of F. Since the length of the focal region increases as the square of the range, there is a limiting range beyond which the SLDVS gives no range resolution. For a 30-cm diameter Gaussian beam, the half-power focus length is about 4.5 m at range of 100 m.

The maximum useful range for such a beam diameter is roughly 500 m. The focusing technique for achieving spatial resolution also suffers from the fact that the response does not fall off rapidly outside the focal region (ref. 99). This limitation can cause some difficulty in signal processing, especially if the concentration of scatterers varies along the beam. The SLDVS can map the line-of-sight velocity field in a region by scanning its beam direction and the focal distance. The allowed scan rate is limited by the requirement that the same focal region must be observed for a time approximately equal to the inverse of the desired Doppler frequency resolution. This requirement is normally more restrictive for angle rather than range scans. The maximum rate of angle change is roughly 200 degrees/second for a beam diameter of 30 cm and a frequency resolution of 100 kHz.

The question may be asked: Why not use a pulsed laser to achieve range resolution, as in Doppler radar and Doppler acoustic sensors, instead of using the complicated focusing system of the SLDVS? The answer is that, for a specific desired spatial resolution, the single pulse-velocity resolution at $\lambda = 10.6$ microns is a factor of 100 worse than for a 3 kHz Doppler acoustic sensor. Moreover, it may not be possible to integrate over many pulses, as in a Doppler radar, because the coherent times of the scattered signal is limited by diffusion of the aerosol scatterers.

6.3.3.2.1 SLDVS historical development - The basic research in the development of laser Doppler systems was initiated during the early 1960s at the NASA Marshall Space Flight Center (MSFC). The initial emphasis was to find an acceptable technique for measuring wind-tunnel flow fields about models without obstructing the flow. The

resulting success with the technique led researchers to investigate the feasibility of applying the technology to measure atmospheric flow fields and turbulence, particularly the turbulence which was known to be hazardous to aviation. Initial feasibility was demonstrated in 1969 when successful measurements were made of the vortices from a DC-3 aircraft. This success led to continued systems studies and testing which showed the feasibility of practically applying the technique in detecting, tracking, and measuring aircraft vortices. In 1972, the FAA requested NASA to accelerate this applied research activity to provide assistance in understanding the aircraft wake-turbulence problems. The result of the extensive research into the application of the laser Doppler principle to atmospheric flow-field problems led to the design and development of the SLDVS (ref. 100). The SLDVS was used at the JFK Airport to detect, track, and measure the vortices generated by aircraft in the approach corridor of runway 31R between September 1974 and May 1975.

Subsequent to the JFK work, a mobile SLDVS was developed by Lockheed. This system has more limited real-time processing capability than the NASA SLDVS, but it is easily moved and has a more versatile beam scanner. It has been used to collect wake vortex data at a variety of airports (ref. 101) and at some special B-747 vortex tests conducted at a California dry lake (see Section 10).

6.3.3.2.2 JFK installation - The JFK installation consisted of two SLDVS units each scanning in range and elevation perpendicular to the landing corridor (ref. 102). They were positioned near the middle marker, 762 m from the end of runway 31R, approximately 122 m on either side of the extended runway centerline. A vertical plane across the approach corridor is scanned to determine the tracks of the aircraft vortices. The detected vortices are then monitored and displayed as they move across the scan plane. The tangential velocity profile of the vortex is also measured and recorded for later data evaluation.

SLDVS testing was performed at JFK in two separate test periods. The first series of tests was carried out during the time between September 7, 1974, when the equipment was installed, and December 13, 1974, when the system was placed in a standby condition. The second series of tests was performed from March 3, 1975, when the systems were returned to an operational status, through June 2, 1975, when the systems were returned to MSFC. At the conclusion of the second test period, vortex data had been recorded on 1619 aircraft landings.

6.3.3.2.3 SLDVS hardware description - The basic SLDVS consists of a very stable single-frequency CO_2 laser, Mach-Zehnder interferometer, transmit-receive optics, infrared detector, range-angle scanner, velocity-frequency analyzer, data-algorithm processor/display, and recorders. The laser beam is directed optically and focused at the point of interest in the atmosphere. Aerosol particles, always present in the atmosphere, scatter some of the transmitted radiation in all directions, and since the particles move with the atmosphere, the frequency of the scattered light is Doppler-shifted from the frequency of the directed beam. Receiving optics collect the backscattered radiation and direct it onto an infrared detector, where it is mixed with a small portion of the original beam. The total radiation seen by the detector fluctuates at a beat frequency which is a measure of the wind velocity at the point of interest. The SLDVS measures the wind velocity component which is in the direction of the sensor line-of-sight (along the laser beam).

Figure 6-25 shows a block diagram of a single SLDVS unit. Two were actually used in the JFK tests. The optical assembly and associated electromechanical scanning components are at the left side of the diagram, and the remainder consists of electronic circuitry for scan control and for processing the signal from the detector.

Each SLDVS unit contains an interferometer to couple the laser beam into the transmitter and detector and to recombine the signal and local oscillator beam. The interferometer was designed to

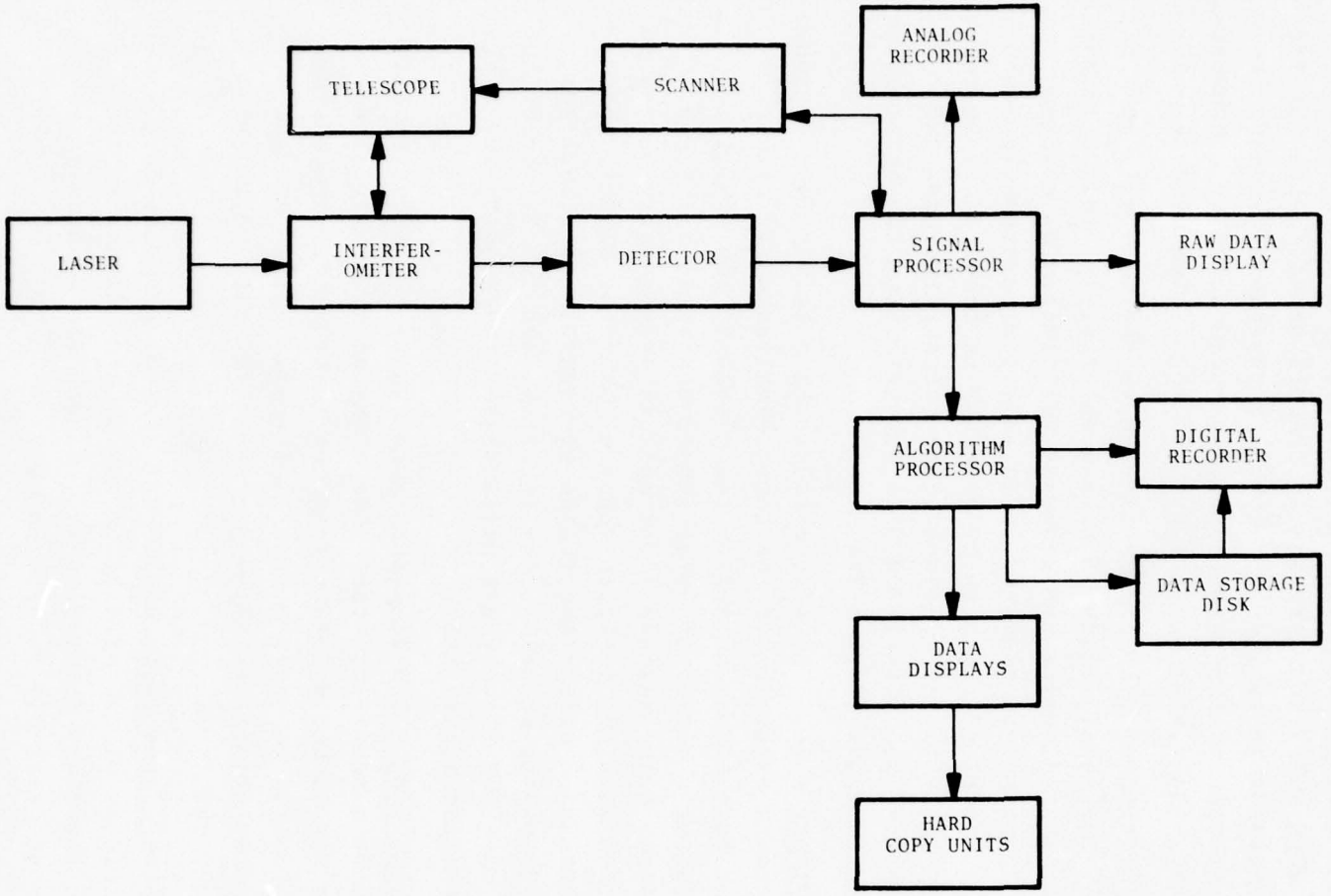


FIGURE 6-25. SLDVS OVERALL BLOCK DIAGRAM

provide the local oscillator powers suitable to a wide variety of detectors with a nominal laser power of 17 watts. The interferometer is also configured so that a frequency translator can be installed with only minor changes in the alinement. With the frequency translator installed, the SLDVS is capable of sensing the direction as well as the magnitude of detected velocity components. The frequency translator was not part of the system used at JFK.

The function of the scanner is to move the beam axis and the location of the focal region in such a way that (a) the coordinates of the illuminated region are known at all times; (b) a given region of space may be examined in an efficient systematic manner; and (c) the nature of the scan program may be conveniently altered to suit a variety of applications. The scanner includes two servomechanisms (and associated data output) which can be programmed in three basic modes (Fig. 6-26):

1) Finger scan. The figure-scan uses a fairly fast periodic linear sawtooth excursion of the focus simultaneously with a similar but much slower motion of the elevation angle of the optical axis, producing a series of petal-shaped contours, or "fingers" in the x, y space being scanned. The mode is particularly suited to detecting and locating vortices since a number of closely spaced traverses are made across the region of significant velocities, irrespective of the actual vortex location, and the filter-output sequences obtained thereby are particularly amenable to the application of location algorithms.

2) Line scan. The line-scan mode causes the focus to move vertically at a nearly constant rate along an imaginary line located at any chosen distance from the instrument. By causing three instruments to use the same line and grouping the data, it is possible to obtain the three-component velocity vector at all points along the line.

3) Single axis (Arc scan). For special purposes (e.g., calibration), either degree of freedom may be arc-scanned in the normal mode while the other is stationary, or both may be made to remain stationary at precisely located values.

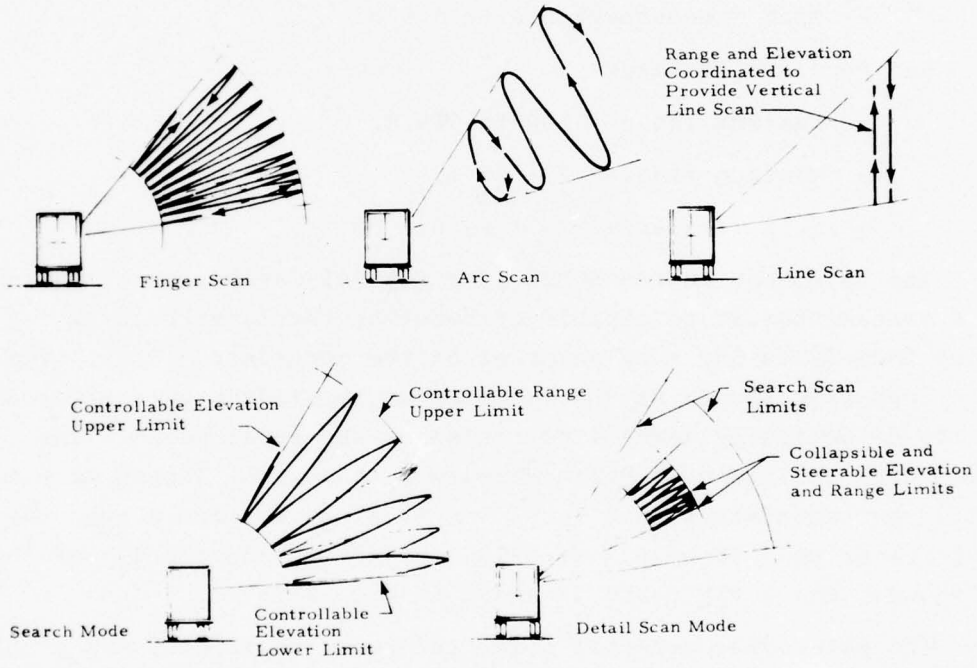


FIGURE 6-26. SCHEMATIC REPRESENTATION OF THE BASIC SCANNING MODES

In addition to the main modes, provision has been made for a search and detail scan, which is basically mode (1), but in which the boundaries of the scan pattern can be rapidly enlarged or contracted and the center of the pattern rapidly translated to any other point in space. This was done to facilitate vortex-tracking; i.e., keeping a moving vortex enclosed in the scan pattern. (Normally, fixed-scan boundaries are used.) The scanner system permits the following range and angular scan coverage and rates:

a) Elevation

- Upper angle-- 10 to 59 deg.
- Lower angle-- 3 to 59 deg.
- Scan frequency-- 0.1 to 1.0 Hz.

b) Focal Point Range

- Maximum range-- 100 to 599 m.
- Minimum range-- 32-599 m.
- Scan frequency-- 0.1 to 6.9 Hz.

The telescope in the SLDVS is a coaxial Cassegrainian system. As a transmitter it is capable of focusing the laser beam at any point from 32 to 599 m by movement of the secondary mirror. The telescope also serves as the receiver of the radiation scattered in its direction by aerosol particles at the focal point. The telescope consists of a 0.3-m primary with a focal length of 0.6 m, a 12.7-mm secondary with a focal length of 24 mm, and a scanning flat measuring 0.46 by 0.3 m. Figure 6-27 is a photograph of the telescope, and a ray trace is shown in Fig. 6-28.

The heterodyne detector mixes the local oscillator and signal beams to generate an electrical signal at the difference frequency. For efficient use, the detector must be capable of operating at a level where the shot noise generated by the local oscillator beam exceeds all other noise sources. The detectors are mercury-cadmium-telluride photodiodes which are square chips with sides of approximately 250 μm and are mounted in stainless-steel dewars for operation at the liquid-nitrogen temperature of -196°C.

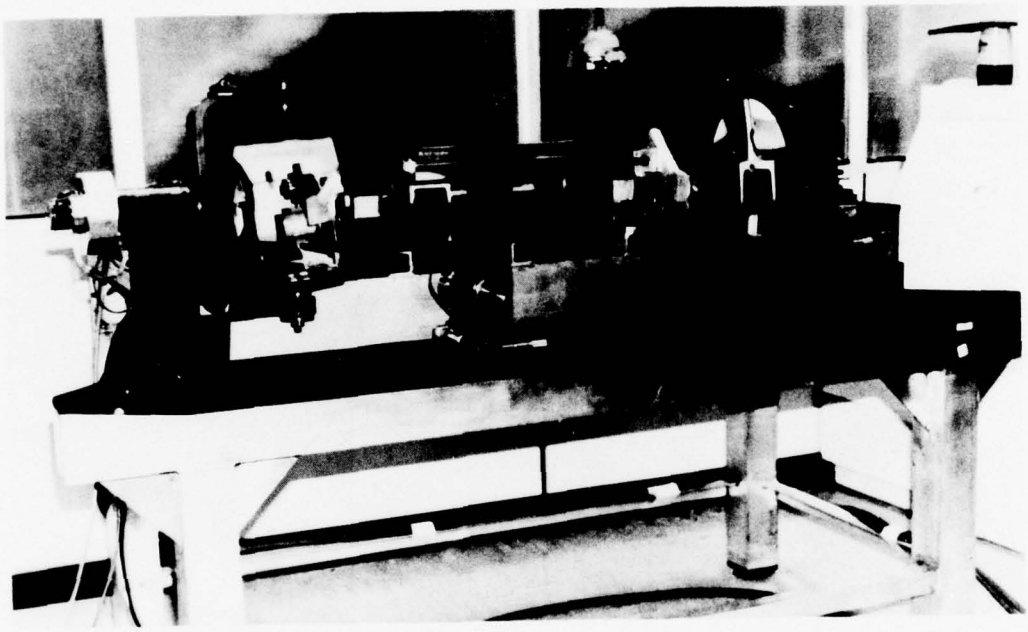


FIGURE 6-27. SLDVS TELESCOPE

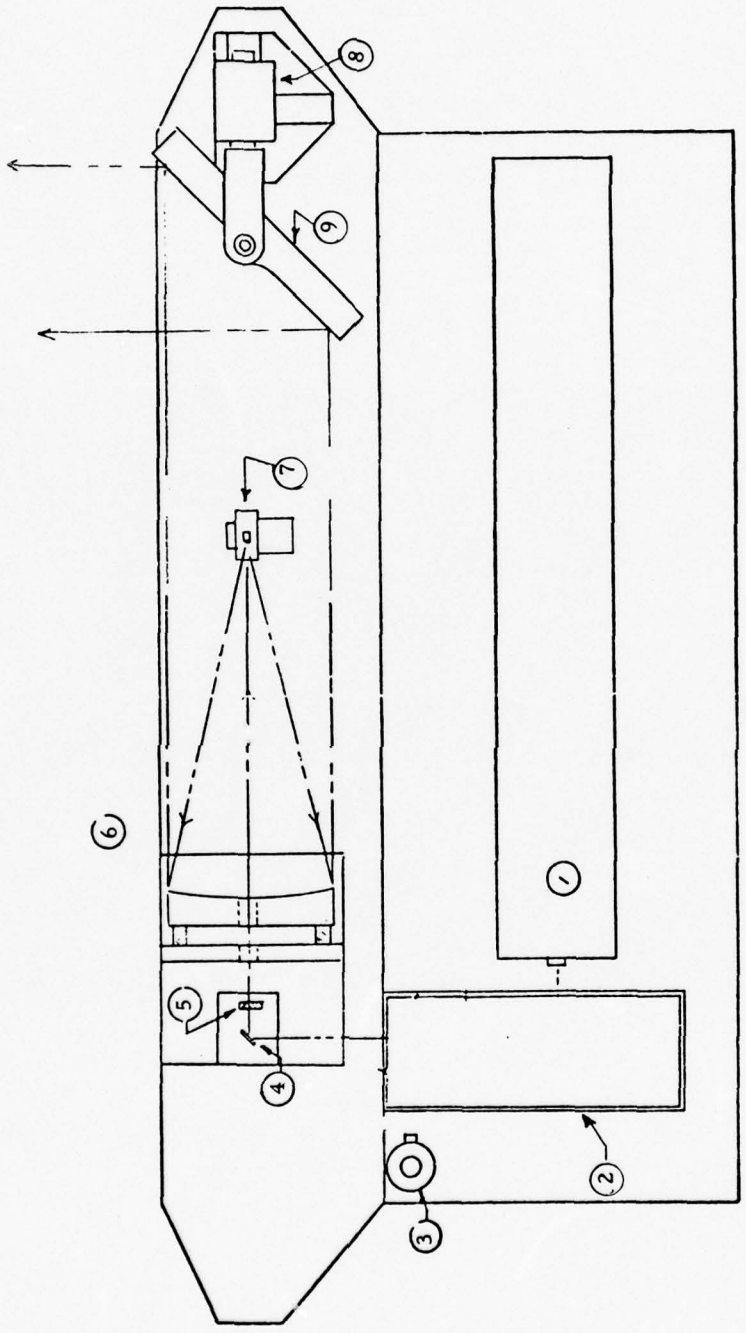


FIGURE 6-28. TELESCOPE AND SCANNING MECHANISMS

In the daily operation of the SLDVS system hardware, performance data were obtained from a hard target which consisted of a sandpaper disk mounted at an angle to the beam and rotating to produce a Doppler signal. These data were used to evaluate system performance in terms of signal-to-noise ratio, range resolution, and calibration.

6.3.3.2.4 SLDVS data processing - A block diagram of the signal-processing equipment is shown in Fig. 6-29. The signal processor accepts video detector signals and outputs velocity and intensity information. There are five subdivisions in the overall circuitry provided: (a) the spectrum analyzer, (b) the spectrum integrator, (c) the velocity discriminator, (d) the display interface, and (e) the formatter. They function in series, first in analog form to provide frequency resolution, then in digital form to achieve signal-to-noise improvement (video integration) and frequency discrimination, and finally in analog form again for the purpose of real-time display of the significant velocity data. The formatter collects binary data from various points in the processor and provides a serial output for biphase recording. The signal processor accepts signals from the laser assembly with or without the use of a laser output-frequency translator. Without the translator, the velocity coverage is either 0 to 30 m/sec or 0 to 52 m/sec; with

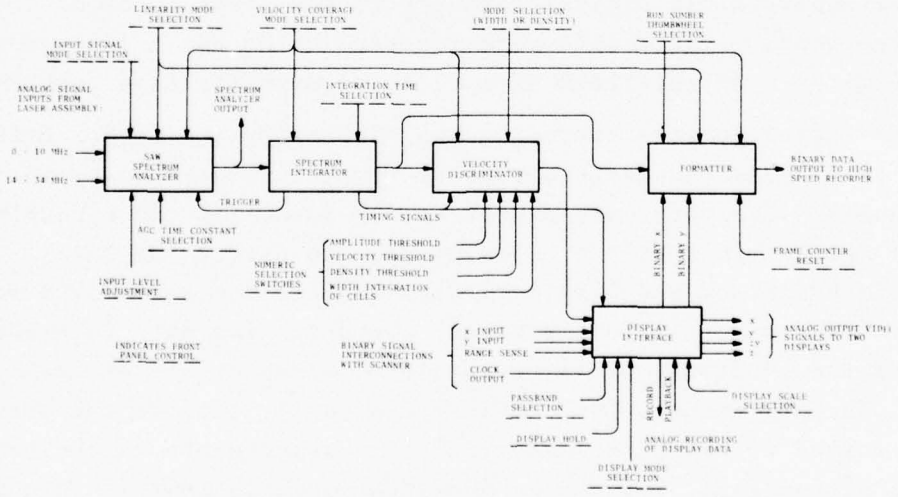


FIGURE 6-29. OVERALL BLOCK DIAGRAM OF SIGNAL PROCESSOR FOR SLDVS.

the translator the velocity coverage is either 0 to ± 52 m/sec, -36 to 36 m/sec, or 30 to 61 m/sec. Outputs provided for display and recording are range, altitude, and velocity information. The input to the signal processor from the laser assembly is in the frequency range of 0 to 10 MHz for operation without the translator and in a band centered at 25 MHz for operation with the translator. With the translator, the spectrum analyzer is capable of accepting a band up to 20-MHz wide. The performance of the spectrum analyzer is highest in the center of the band, providing 100-kHz resolution over a 6-MHz range. Beyond this central range, the resolution and sensitivity decrease, depending on the bandpass characteristic of the surface-acoustic-wave (SAW) dispersive delay line used in the spectrum analyzer.

Tape recording was used in the SLDVS field-test operations for two purposes. The first, requiring a high data rate, was to record the raw Doppler signal and the SAW spectrum signal for later analysis. The second, requiring a lower data rate, was to record the display data. The recording of the raw Doppler signal allowed a particular flyby effectively to be repeated on site as many times as desired for optimizing the detection criteria. This was normally recorded on a direct track of a wideband tape recorder. The recording of the SAW spectrum signal (i.e., the processor signal after integration but before any detection logic) allowed a comprehensive off-line analysis via digital computer in the development of detection algorithms. These data were recorded using pulse code modulation (PCM) on a direct track of a wideband magnetic-tape recorder.

The Data-Algorithm Processor and Display System serves effectively to display the large amount of raw data generated by the two SLDVS units. The operators cannot easily determine the effectiveness of the entire system by viewing the raw data. The Data-Algorithm Processor and Display System accepts these raw data from the two SLDVS units in real time and processes the data to produce plots of the positions of the aircraft vortices on a scan-frame basis. In this manner, the operator can easily observe the success of the vortex tracking and make real-time adjustments in the processing parameters. The system provides flexible control through

system-user interaction for collecting vortex data, processing these data in real time, displaying the processed data, storing raw data on magnetic tape, and post-processing raw data. The Data-Algorithm Processor and Display System consists of a PDP-11/35 CPU with 32K words of memory and floating point arithmetic, a 1.2-million word disk, an industry-compatible 9-track tape unit, a display terminal, a storage-display monitor with a hard-copy unit, and a data tablet. Also included are interfaces to the signal processor and a start of run/aircraft identification unit.

The data available to the computer from the signal processor include position coordinates (x and y), N, I_{pk}, V_{max}, and V_{pk}. Definitions of the data parameters are given in Fig. 6-30 which shows a typical velocity-amplitude spectrum output. The data-processing algorithm used in on-site processing used combinations of these parameters to determine vortex location. Examples of the display data showing vortex tracks are given in Figs. 6-31 and 6-32.

During the JFK Airport operations, information was collected on more than 1600 aircraft landings. The information was stored on magnetic tape from three different data-processing points in the system for analysis. This included velocity and position of the flow field of the entire scan plane, the flow field of the vortex, and the track of the vortex centers.

Analysis of the JFK Airport data indicates that vortex location to within 3 m were achieved, and that vortices were tracked to a range of 450 m and for a duration in excess of 80 seconds. Vertical and horizontal transport of the vortices as well as vortex-circulation information were also obtained.

6.3.4 Electromagnetic Techniques

Although the radar cross sections of wake vortices are too small for the use of conventional radar systems (ref. 97), some observations (ref. 103) of Doppler shifts caused by wake vortices have been made using chaff and snow as scatterers. It has been proposed that wake vortices could be detected by means of electrostatic charge injected by an aircraft into the wake. Such charge may

V_{pk} = VELOCITY OF HIGHEST CHANNEL ABOVE AMPLITUDE THRESHOLD

V_{max} = VELOCITY OF THE CHANNEL HAVING THE PEAK SIGNAL

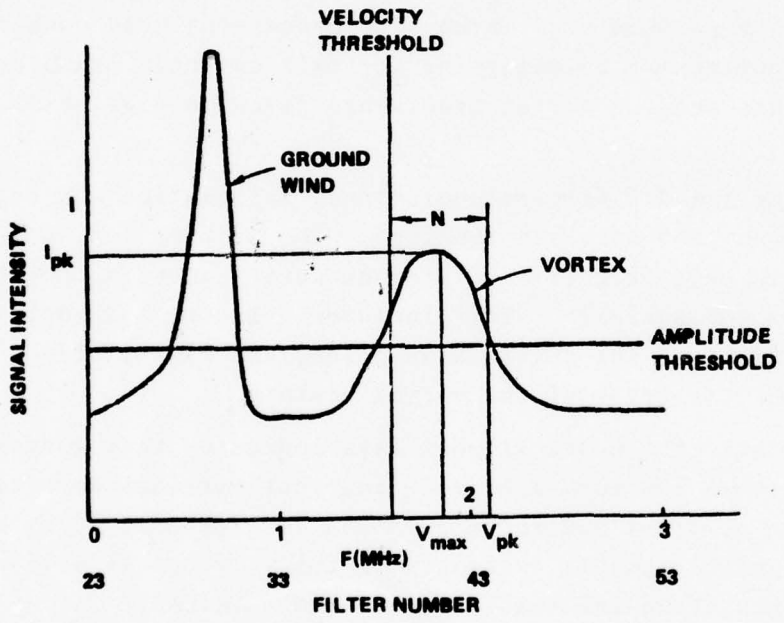


FIGURE 6-30. SAMPLE SPECTRUM OUTPUT

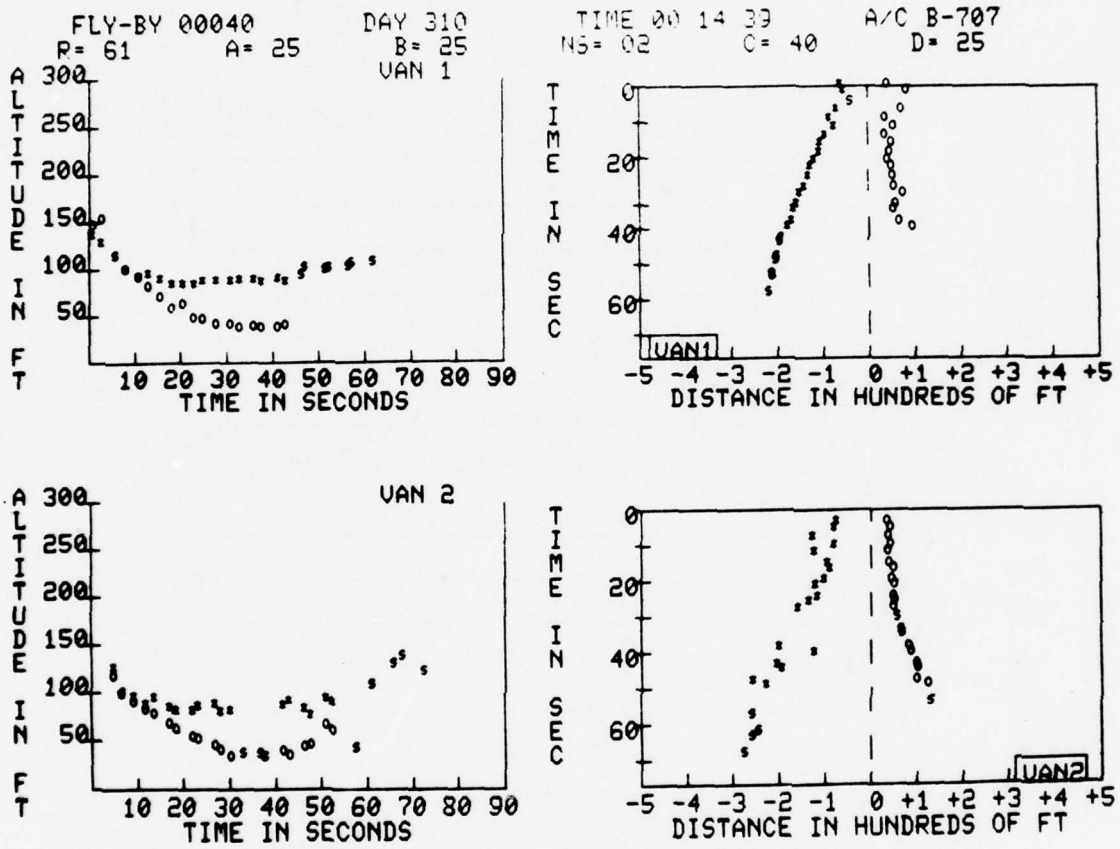


FIGURE 6-31. SAMPLE TIME-POSITION DATA PLOT

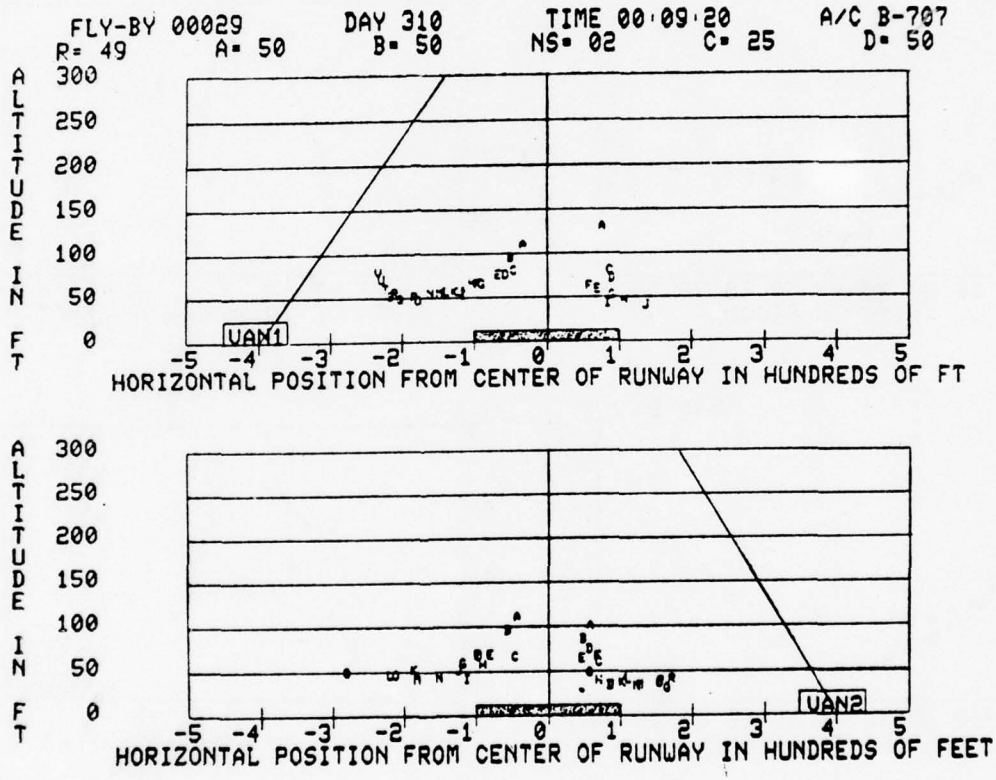


FIGURE 6-32. SAMPLE X, Y DATA PLOT

occur naturally via the discharge electrodes on aircraft wings, but it could also be intentionally injected, perhaps putting opposite polarity on the two vortices. No experimental data are available on the electric potentials near wake vortices. An airborne electrostatic sensor might be capable of detecting electrostatically marked vortices from a preceding aircraft.

6.3.5 Combination Techniques

A combination of techniques may be more useful than a single one if the strengths and weaknesses are complementary. Two combination techniques have been suggested during the wake vortex sensor development

The first combines the PAVSS and the GWVSS. If the lateral position of a vortex is known from the GWVSS, the vortex height could be accurately determined by a pair of PAVSS antennas. Such a system would still be subject to the aircraft-type limitations of the PAVSS.

The second combines the MAVSS and the GWVSS to yield a direct measurement of circulation for vortices stalled near the runway centerline. The circulation within an area is computed directly as a line integral around the area. The MAVSS is ideally suited for measuring the velocity line integral along a vertical line. The measured line integrals are in reasonable agreement with the theoretical values based on the vortex-strength measurement. Two MAVSS antennas would measure the vortex line integrals along the sides of the area. The GWVSS sensors would complete the integral between the two MAVSS antennas. For low-altitude vortices, the top of the area makes no significant contribution to the line integral.

6.3.6 Future Sensor Development

Perhaps, the most important goal in future sensor development is to establish a satisfactory method of measuring the strength of stalled vortices. To that end, a DAVSS strength algorithm could be implemented, and the MAVSS-GWVSS combination could be tested.

Improved SLDVS strength algorithms could also be developed. Another goal is to gain an understanding of the boundary-layer processes influencing GWVSS signatures. A better understanding of the GWVSS is needed because it is currently the most likely sensor candidate for incorporation into any vortex-avoidance system. Improved processing for GWVSS data and careful comparisons with data from the MAVSS sensor may lead to valid measurements of vortex decay using GWVSS data alone. Such a development would substantially increase the usefulness of the large GWVSS data base already collected.

6.4 AIRBORNE WAKE-VORTEX DETECTION

Active and passive remote-sensing systems have been assessed (ref. 104) to determine the feasibility of detecting aircraft-trailing vortices using instrumentation on-board an aircraft. It was found that a modification of the front-end receiver of a 10-GHz weather radar system or a change of frequency to 35 GHz may allow vortex identification over a range of several kilometers. A 10.6-micron coherent Doppler optical radar and passive radiometric techniques in the 8-14 micron region indicate promise. Incoherent lidar, Raman shift techniques, fluorescence-scattering, acoustic radar, and ultraviolet emissions were shown not to possess sufficient sensitivity.

7. DATA-COLLECTION SITES

To learn more about how vortices move and die in the terminal environment, four test sites were instrumented to track vortices shed by landing aircraft and one site for departing aircraft. Vortex behavior is then correlated with the recorded meteorological conditions. The landing zone was monitored as this is potentially the most dangerous region (Section 2) as all aircraft must pass through essentially the same airspace to execute a landing. The takeoff zone was monitored to determine if procedures are unduly restrictive because of wake vortices, and thus may be modified to speed up traffic flow.

The emphasis of the test program activities are therefore directed toward the acquisition of the data required in the development of a vortex behavior model. The method of approach followed at the test sites generally consists of:

a. Deployment of vortex sensors and their use in tracking actual vortex motion.

b. Deployment of a meteorological sensor network.

c. Recording of vortex-position data from the various vortex sensors and of the concurrent meteorological conditions.

d. Reduction of the acquired data to evaluate the performance of vortex sensors, verification and refinement of the predictive models of vortex motion and decay, and the establishment of a large data base for use in the design of vortex-avoidance systems.

This chapter describes each of the data collection sites. The following chapter reviews the analyses of the data from the Denver, Kennedy, and Heathrow sites. The use of the Chicago site is discussed in Section 9 and the use of the Toronto site in Section 10.

7.1 JFK VORTEX TEST SITE

The approach region to runway 31R at JFK was selected as the primary vortex test site (Ref. 105) because of the availability of the real estate necessary for the deployment of a large number of vortex-sensing systems and a meteorological tower network, as well as the availability of a large and representative sample of aircraft. As shown in Figure 7-1, the region between the runway threshold and 1050 meters from the threshold (the critical region for landings) was instrumented with six vortex-sensing systems whose sensor planes are perpendicular to the extended runway centerline, thereby providing a detailed track of vortex position over the length of the vortex filament. The meteorological sensors are placed on an L-shaped tower array with a 42-meter tower located 990 meters from the runway centerline, two 12-meter towers at 120 meters from the centerline, and a 9-meter tower located closer to the threshold.

Two of the GWVSS lines are extended 900 meters perpendicular to the runway centerline; their purpose is to measure and verify the predicted distances vortices travel in ground effect. This information is required for the assessment of the vortex hazard, if any, associated with closely spaced parallel runway operations (Section 10).

Spaced along the extended GWVSS lines were six MAVSS. These are abbreviated versions of the DAVSS operating in the backscatter mode. Each unit consists of a single, narrow-beam transmitter and receiver. As a vortex passes through the beams, the backscattered signal is received, recorded, and analyzed to determine the vortex velocity distribution, and hence, its strength and potential hazard to an encountering aircraft. The string of MAVSS thus provides a means to measure vortex circulation as a function of time, required in the verification of the vortex-decay models (Section 8).

A monostatic acoustic sounder is used to probe the lower atmosphere yielding information on the heights of atmospheric structure fluctuations, continuous information on inversion heights, and the depth of the mixing region which influences

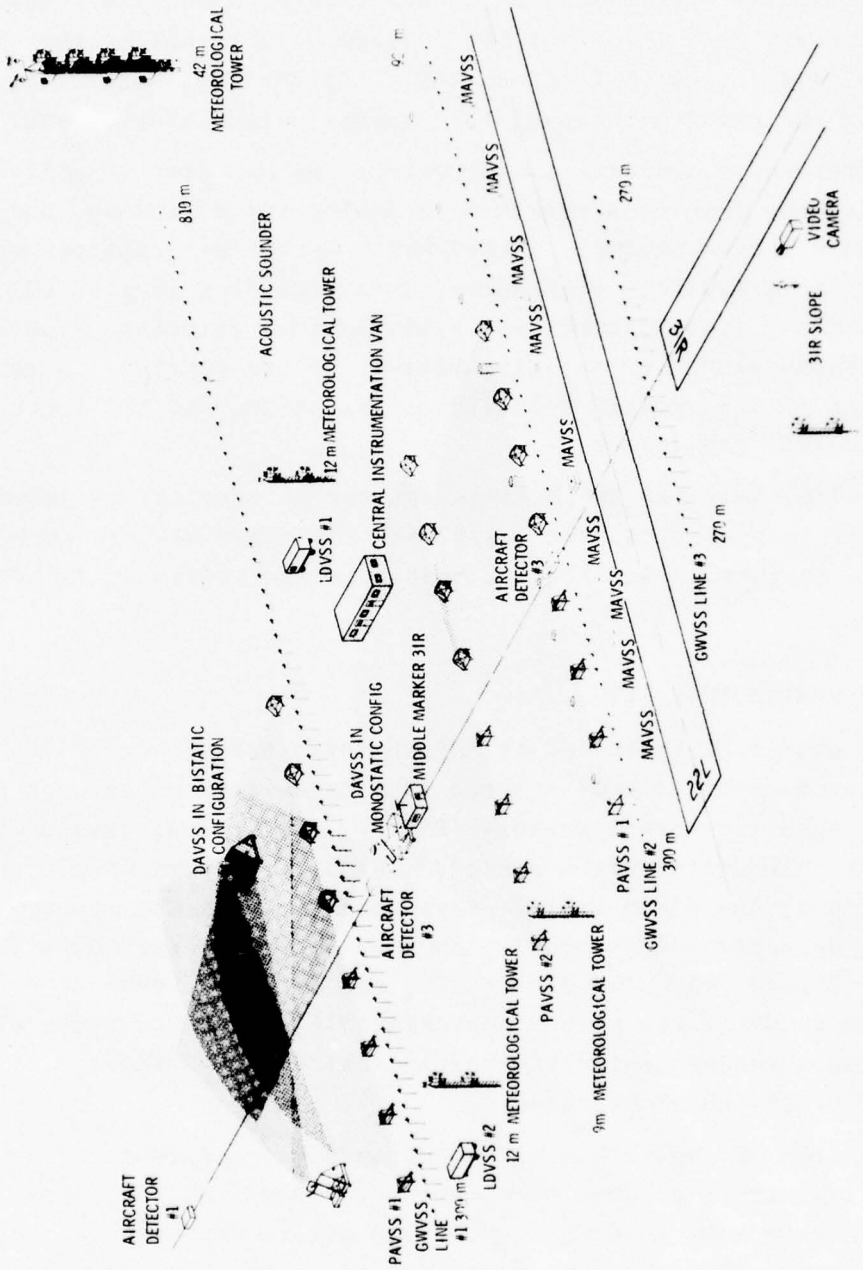


FIGURE 7-1. JFK TEST SITE

vortex behavior. Pressure transducers located along the runway centerline are used to detect the passage of aircraft by the pressure wave the aircraft generates. All control, monitoring and recording equipment are housed in a large instrumentation van.

Operation of the site is automatic. An operator visually identifies the type of aircraft approaching for a landing, and depresses a correspondingly marked key. As the aircraft passes over the first pressure transducer, data recording is started and includes: type of aircraft, arrival time, velocity, separation from previous aircraft, the time history of its vortices in each of the sensor planes, vortex-velocity distribution, and the concurrent meteorological conditions.

In 1976, only the GWVSS lines and the meteorological network were still in operation; the tests with the other sensors were concluded in late 1975. The JFK test site was closed in January 1977.

7.2 DEN VORTEX TEST SITE

The equipment installed at the approach end of runway 26L at Stapleton International Airport (DEN) consisted of one set of bistatic acoustic vortex sensors (PAVSS), two sets of ground-wind propeller anemometer vortex sensors (GWVSS), two sets of ambient wind sensors, one 35-mm still camera, and one pressure-sensor aircraft detector. An overall plan view of the sensor locations is given in Figure 7-2. The electronics and data recorders were housed in a Cortez van parked approximately 100 meters south of the extended runway centerline and approximately 45 meters to the east of the outer baseline.

The area of the test site where the sensors were located was fairly flat with a gradual rise (approximately 1 percent) in elevation from west to east. About 100 meters north of the sensor location there is a sharp drop off (12 meters). The area to the south of the airport boundary consists of residential houses, mostly single-story ranch type, and a few trees (heights between 6 and 9 meters).

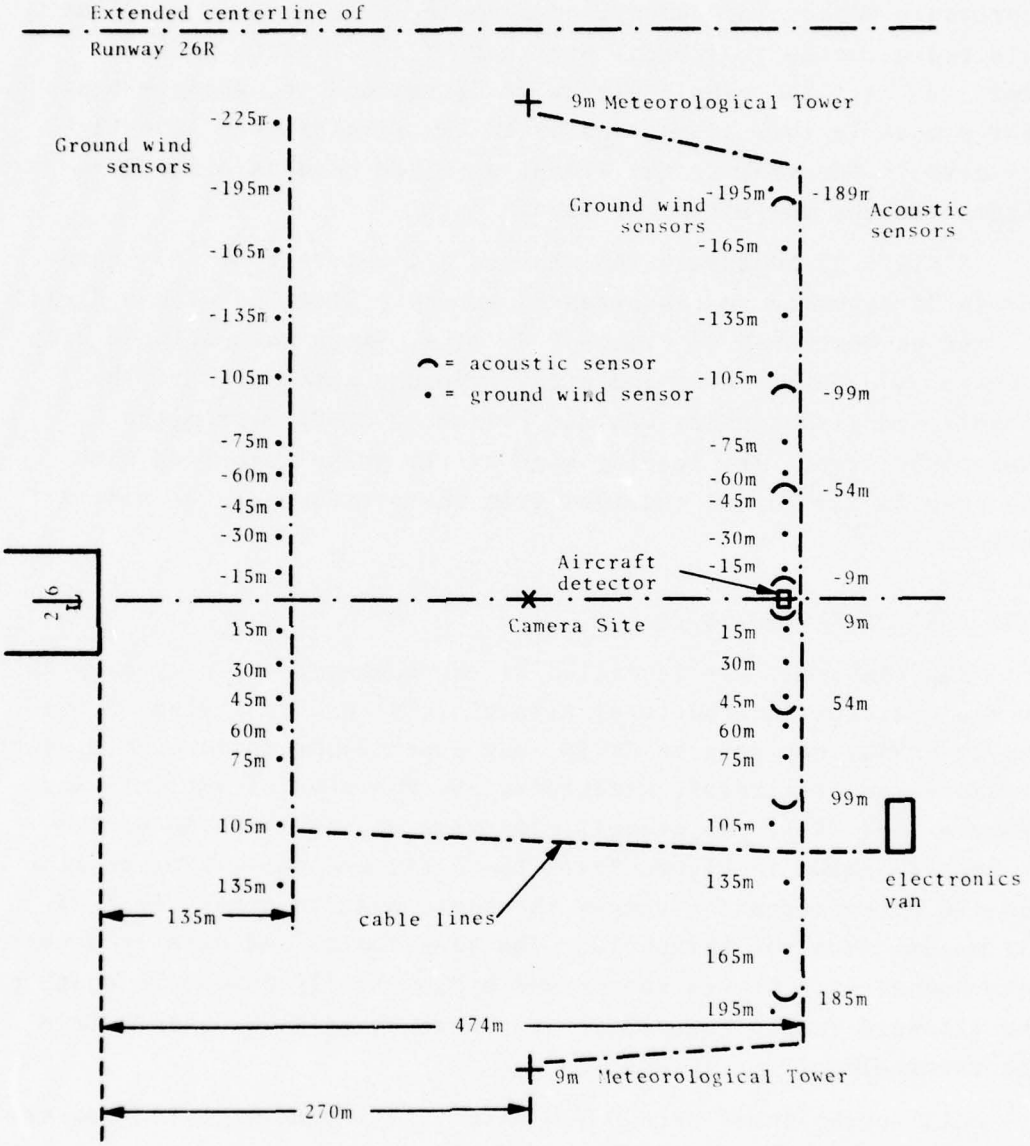


FIGURE 7-2. OVERALL PLAN VIEW OF SENSOR LOCATIONS AT STAPLETON AIRPORT.

A U-V-W propeller anemometer ambient wind sensor was mounted at 9-meter elevation at each of two sites, 270 meters from the runway threshold, and +225 and -235 meters as shown in Figure 7-2. A pressure sensor located at the midpoint of the outer baseline detected a change in ambient pressure as an aircraft passed overhead. (It has been empirically determined in previous tests that a peak in this signal indicated the aircraft was directly overhead.) The peak in the signal was then used as a start-of-run signal for the collection of data.

A Nikon 35-mm camera was mounted 270 meters from the runway threshold directly on the extended runway centerline with a field of view as described in Figure 7-3. The camera was equipped with a medium wide-angle lens and a 250-exposure motor drive. The shutter and film advance was controlled by a pulse from the electronics van. The leading edge of the pulse coincided with the peak in the signal received from the pressure-sensor aircraft detector.

7.3 LHR VORTEX TEST SITE

The equipment was installed at the approach end of runway 28R at the Heathrow International Airport (LHR) and consisted of one set of PAVSS, two sets of GWVSS, one Super-Eight movie camera, two pressure sensor aircraft detectors, and two sets of ambient wind sensors (Ref. 85). An overall plan view of the location of the sensors is shown in Figure 7-4. The PAVSS and one GWVSS baseline was 450 meters from the runway threshold and the other GWVSS was 732 meters from the threshold. The electronics and data recorders were housed in a Cortez van parked approximately 30 meters south of the extended runway centerline and approximately 550 meters from the threshold of runway 28R.

Gill-type, three-axis U-V-W propeller anemometer wind sensors were mounted at two heights on each of two support towers to measure the local ambient wind. One tower was 15 meters in height with one U-V-W sensor mounted at the 6.1-meter level and another at the 15-meter level. The largest obstructions in the vicinity

FIGURE 7-3. CAMERA FIELD OF VIEW

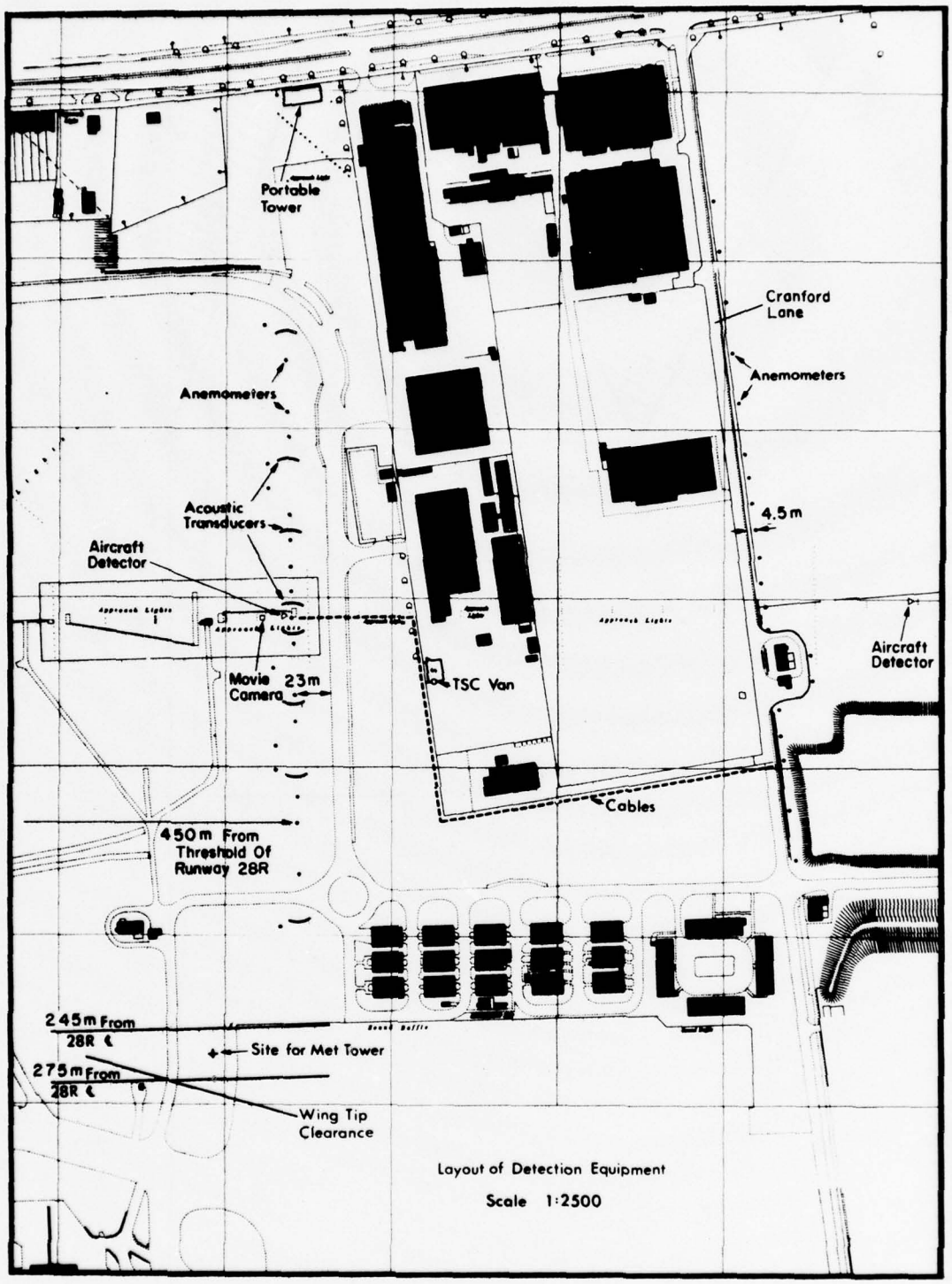


FIGURE 7-4. THE SITE LAYOUT OF THE EQUIPMENT ON THE APPROACH TO RUNWAY 28R AT HEATHROW.

of this tower were the B-747 hangar, approximately 200 meters to the southeast with a height of 34 meters and the British Airways stores approximately 115 meters to the southwest with a height of 15 meters. The other tower was 10 meters in height with one U-V-W sensor mounted at the 6.1-meter level and another at the 10-meter level. The largest obstructions in the vicinity of this tower were a tree approximately 18 meters to the northwest with a height of 8.5 meters, a second tree approximately 18 meters to the northeast with a height of 7 meters, and a building approximately 35 meters to the southeast.

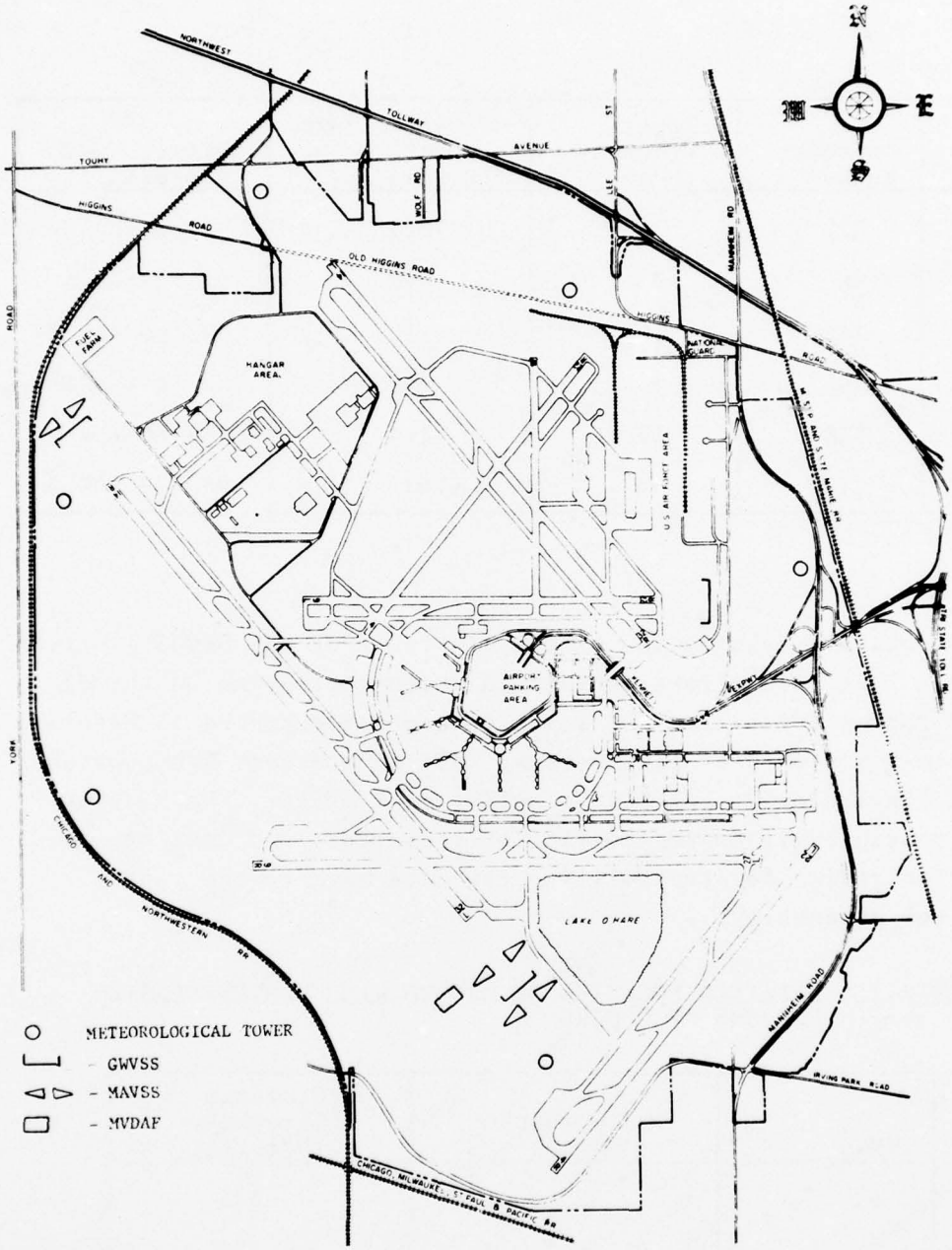
A Super-Eight movie camera was located 430 meters from the runway threshold directly on the extended runway centerline. It was mounted on a wood fence, approximately 1.2 meters high, and pointed slightly upward with a field of view as shown in Figure 7-5. The movie camera selected was designed for remote surveillance and came equipped with automatic exposure, remote control capability, and a protective housing. It had a zoom lens (13 to 28 mm) which was operated in the wide-angle (13 mm) position.

7.4 ORD VORTEX TEST SITE

Equipment was installed at the approach end of the six major landing runways at Chicago's O'Hare International Airport (ORD). The total installation consisted of six meteorological towers, three GWVSS, three aircraft detectors, three sets of MAVSS, and a Mobile Vortex Data Acquisition Facility (MVDAF). A layout map showing the location of the equipment is given in Figure 7-6.

A detailed description of the location of the meteorological towers is given in Table 7-1. All towers are 15 meters high with the exception of tower 4 at 14L which is only 12 meters high (to satisfy FAR Part 77 height restrictions). Each tower has three sets of wind sensors, one mounted at the top and two mounted 3 meters lower which allows for redundant wind readings, and hence, a check on sensor performance and reliability. The sensors are of the cup-and-vane type. Each tower has a multiplexer, analog-to-digital converter, and data-transmission electronics for transmitting the raw data back to the control tower for processing.

FIGURE 7-5. FIELD-OF-VIEW OF THE MOVIE CAMERA



Layout map of Chicago O'Hare International Airport

FIGURE 7-6. LAYOUT MAP OF CHICAGO O'HARE INTERNATIONAL AIRPORT

TABLE 7-1. DETAILED LOCATION OF THE METEOROLOGICAL TOWERS

Tower	Approach Runway	Tower Height (Meters)	Distance from Threshold (Meters)	Offset (Meters)
1	32L	15	1021	92 to the SW
2	9R	15	945	92 to the N
3	14R	15	12	305 to the SW
4	14L	12	762	92 to the SE
5	22R	15	274	244 to the NW
6	27R	15	915	92 to the N

A detailed description of the locations of the GWVSS is given in Table 7-2. All arrays contain 15 anemometers, one on the extended runway centerline and seven on each side spaced 15 meters apart to a distance of ±105 meters. All anemometers are mounted on Polyvinylchloride poles at a height of 3 meters. Each array has a multiplexer, analog-to-digital converter, and data-transmission electronics for transmitting raw data back to the control tower for processing.

TABLE 7-2. DETAILED LOCATION OF GROUND-WIND VORTEX-SENSING SYSTEMS AT O'HARE

GWVSS	Approach Runway	Distance from Threshold (Meters)
1	32L	472
2	14R	472
3	27R	381

Each of three aircraft detectors is housed in the ground-wind electronics box which is located in the center of the propeller anemometer array. The sensor consists of a general-purpose tweeter-type speaker mounted on a circuit board in the electronics housing with associated electronics to provide a voltage output proportional to the magnitude of the aircraft noise (whose peak indicates that the aircraft is directly overhead of the speaker).

Three MAVSS were installed at the location described in Table 7-3. MAVSS lines 1 and 2 have two sensors on the positive side spaced 60 meters apart to a distance of 120 meters, and five sensors on the negative side spaced 60 meters apart to a distance of 300 meters. Physical limitation (taxiway and airport boundary) made it necessary for the lines to be unsymmetrical. The sensors provide information as to vortex strength and location as a function of time. MAVSS line 3 has three sensors, one in the center, one at +30 meters, and one at -30 meters, and are to be used in a special experiment to test an algorithm for determining characteristics of vortices stalled in the region near the runway centerline.

TABLE 7-3. DETAILED LOCATION OF MONOSTATIC ACOUSTIC VORTEX-SENSING SYSTEMS AT O'HARE

MAVSS	Approach Runway	Distance from Threshold (Meters)	Antenna Locations (Meters)
1	32L	655	60, 120, -60 -120, -180, -240, and -300
2	14R	503	60, 120, -60 -120, -180, -240, and -300
3	32L	472	30, 0, and -30

7.5 YYZ VORTEX TEST SITE

The major effort to date in the vortex program has centered on the approach and landing region as the accident statistics indicated that this is the major problem area. However, concern has been expressed for vortex encounters on the takeoff and departure phase of airport operations. This phase becomes particularly significant at airports where landings and takeoffs are made in opposite directions on the same or neighboring runways to alleviate the noise-abatement problem.

A joint United States Department of Transportation and Canadian Ministry of Transport effort is now underway at the Toronto International Airport (YYZ) to detect, track, and measure the strength of vortices from departing aircraft and to correlate these with associated meteorological measurements. The system includes narrow-beam acoustic sensors for vortex-strength measurements (MAVSS), a laser-Doppler sensor for detection and tracking of higher altitude vortices as well as wind and wind shear measurements, and ground-wind sensors (GWVSS) for tracking vortices in ground effect.

The equipment was installed at the southwest end of runway 23L at the Toronto International Airport in the general area where most aircraft will be airborne in the process of taking off. Three GWVSS, one set of MAVSS, three aircraft detectors, and one photographic system were installed. A laser vortex sensor was also installed for brief periods during the tests. An overall plan view of the location of the sensors is given in Fig. 7-7.

The electronics and data recorder are housed in an equipment shelter near the approach end of runway 5R. In general, the terrain is fairly flat with no large obstacles to perturb the winds.

Three acoustic aircraft detectors were installed at the location shown in Fig. 7-7. The detectors consist of an acoustic horn and driver mounted at the focal point of an antenna with a very narrow (approximately 5 degrees at 3 kHz) azimuth beamwidth and a broad (approximately 60 degrees) vertical beamwidth. The

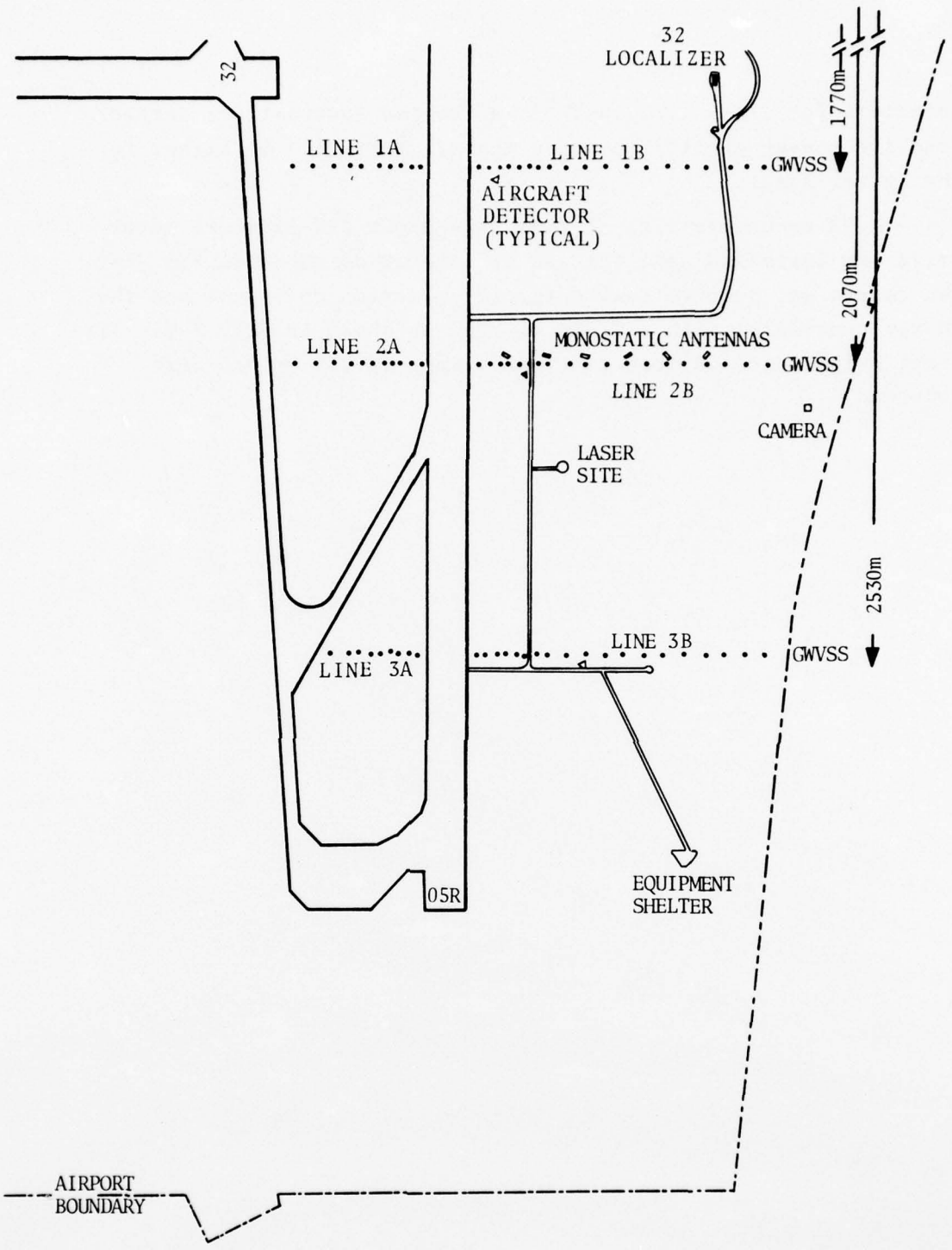


FIGURE 7-7. OVERALL PLAN VIEW OF TORONTO VORTEX TEST SITE

detectors for lines 1, 2, and 3 are located successively farther from the runway centerline since the aircraft will be higher for the latter lines.

A 35-mm camera with a 28-mm lens and a 250-exposure motor drive was installed near the end of line 2B as shown in Fig. 7-7. The camera was pointed toward the intersection of line 1 and the runway centerline with a field of view as shown in Fig. 7-8. Aircraft heights to a distance of approximately 230 meters were recorded.

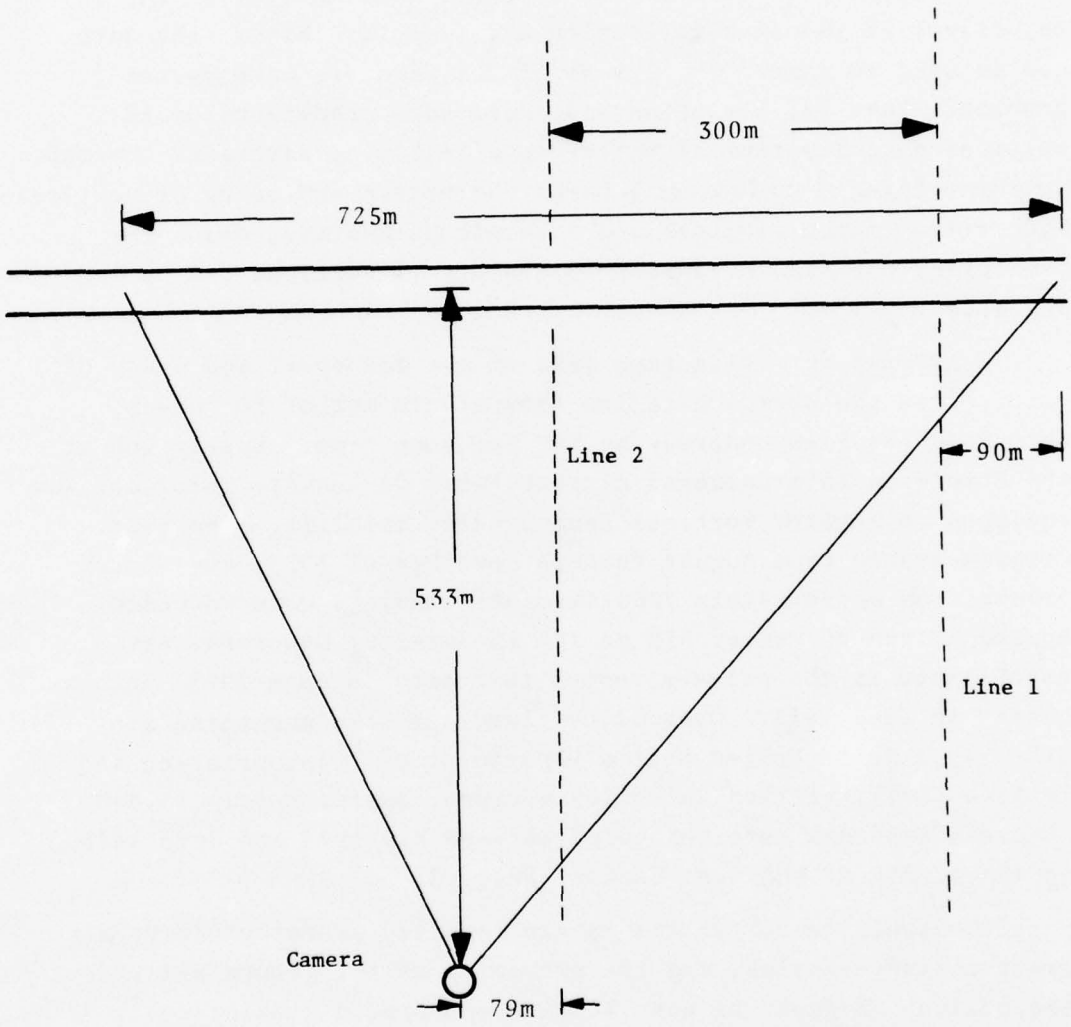


FIGURE 7-8. CAMERA FIELD OF VIEW.

8. ANALYSIS OF LHR, JFK, AND DEN DATA

Under the aegis of the FAA, TSC has been collecting extensive data on the motion and decay of aircraft wake vortices. The objectives of the data collection are twofold: First, the data can be used to assess the extent of the aircraft wake vortex problem. That is, how often and under what conditions could vortices pose a potential threat to a following aircraft? Second, by identifying correlations between the motion and decay of vortices and various meteorological and aircraft parameters, means for predicting the time evolution or history of vortices can be developed.

A program for collecting data on the transport and decay of vortices in the approach region from middle marker to runway threshold has been underway by TSC for some time. Runway 26L at the Stapleton International Airport (DEN) in Denver, Colorado, was equipped to monitor vortices from landing aircraft. The test program lasted from August through November of 1973, and vortex tracks from approximately 7000 aircraft landings were recorded. The approach zone of runway 31R at JFK in Jamaica, New York, was established as the primary vortex test site in June 1973, and was closed in Jan. 1977. Over 14,000 landings were monitored at JFK. In a joint United States Department of Transportation and British Civil Aviation Authority venture, approximately 13,000 aircraft landings were monitored between May 1974 and June 1975 on runway 28R at LHR near London, England.

Thousands of vortex tracks are required as meteorology, aircraft characteristics, and the proximity of the ground all affect the motion and decay of wake vortices; hence, a statistically significant data base is necessary. The characteristics of the wake vortices generated by an aircraft in flight are established initially (see Section 3) by factors related to the aircraft such as gross weight, flight speed, configuration (flap settings), and wing span. Subsequently, the vortex characteristics are altered

and eventually dominated by interactions between the vortices and the ambient atmosphere. The wind, wind shear, turbulence, atmospheric stability, and the proximity of the ground affect the motion and decay of a vortex system.

The extensive data-collection program began with the objective of confirming the adequacy of the current separation standards. The JFK and DEN data demonstrated that the standards were indeed safe vortexwise for commercial airliners; in fact, the data indicated that the separations were almost always too conservative. A subsidiary program (Section 8.2.2) examined the separation standards for light aircraft (less than 5670 kilograms), and led to a recommendation, since adopted, for increasing their separations behind larger aircraft. The LHR effort was initiated as the British were reporting a number of vortex incidents (vortex encounters of varying degree of concern -- but not accidents). An objective of the joint program was to correlate the reported incidents with measured vortex behavior inside the middle marker. Analysis of the data from the three sites contributed significantly to furthering the knowledge about vortex behavior, and suggested possible avenues for systems which could specify when the separation standards might be relaxed.

8.1 VORTEX TRANSPORT AND DEMISE

All the data discussed in this section were collected using baselines of propeller anemometers (see Section 6.3.1.1). The location of the sensor baselines varied from 140 to 1160 meters from the runway threshold (see Section 7 for the locations of the sensor baselines at the various test sites). Different locations were chosen to determine if discernible differences occur in the vortex motion and lifecycle as a function of the distance from the runway threshold or, equivalently, as a function of the mean altitude of the vortex-generating aircraft above the ground. The results discussed herein are based on the analysis of the vortex-tracking data from over 35,000 aircraft. Data reduction and analyses are still continuing.

8.1.1 Safety Region

Since it was anticipated that vortices from a landing aircraft usually move away or dissipate before a following aircraft arrives, it was decided to analyze the extensive amount of vortex track data in terms of how soon the vortices exit a "safety region." The safety region is centered on the extended runway centerline. The width of the safety region was determined by considering two points: First, a measurement program by TSC at DEN showed that 3σ or 99.74 percent of all landing aircraft were within 15 meters of the extended runway centerline near the middle marker. Second, 6-degree-of-freedom aircraft-vortex encounter simulations (see Section 5.5) indicated that if the fuselage of any aircraft were at least 30 meters from the center of any vortex, the encountering aircraft would not experience an unacceptable disturbance. The figure is conservative, and represents the worst case of a light general aviation aircraft approaching a vortex formed by a wide-body jet; the exact figure depends upon the individual characteristics of the vortex-generating aircraft and the encountering aircraft. Thus, the safety region was selected to have a width of 15 + 30 or 45 meters on both sides of the extended runway centerline. If both vortices are clear of the safety region, they cannot pose any threat to a following descending aircraft landing on the same runway. The size of the safety region is very conservative; even if both the following aircraft and a vortex from a preceding aircraft are observed to be in the safety region at the same time, the vortex may have decayed sufficiently that it could not affect the following aircraft. Additionally, the aircraft and vortex can be separated by as much as 60 meters and yet both be within the safety region.

8.1.2 Residence-Time Data

In the ensuing discussion of the data, the term "residence time" refers to the time it takes for both vortices to exit the safety region. Each vortex may either be blown out of the safety region or be eliminated by a decay process while the vortex is still within the safety region. Note that the existence of a vortex

within the safety region at a given time does not necessarily imply that it could constitute a hazard to a following aircraft: The vortex could have decayed to a strength sufficiently below the hazard threshold of the encountering aircraft, the vortex being tracked may have been generated by an aircraft whose vortices will not affect the following aircraft (e.g., a Twin Otter followed by a B-747), or the vortex of the oncoming aircraft might be separated by sufficent lateral distance such that the aircraft will barely detect the presence of the vortex in the safety region.

Figure 8-1 shows the probability of finding a vortex in the safety region as a function of the time after an aircraft passed over the vortex-tracking equipment. For example, 16 percent of the data yielded a vortex in the safety region after one minute; in the remaining 84 percent of the cases, the vortices either exited the safety region or decayed within it. The figure is a composite of data recorded at Denver, Kennedy, and Heathrow Airports and represents the results of 35,303 aircraft.

In the following subsections, the information in Fig. 8-1 is re-examined to ascertain the dependence on aircraft type, the winds, the mode of exiting the safety region (drifting out or decaying), the different vortex behavior at various sensor baseline locations, the time between the first and second vortex exiting the safety region, and the conditions which lead to residence times in excess of 80 seconds.

8.1.3 Residence Times by Aircraft Type

In Fig. 8-2, the data of Fig. 8-1 is reproduced along with curves for the wide-body jets (B-747, DC-10, and L-1011) and for small commercial jets (DC-9 and BAC-111). The type of aircraft generating the vortices plays an important role on the longevity of a vortex within the safety region. The wide-body jets constitute a significant portion of the older residence-time cases. If a vortex is found inside the safety region after 80 seconds, the probability is very high that the vortex was shed by a wide-body aircraft.

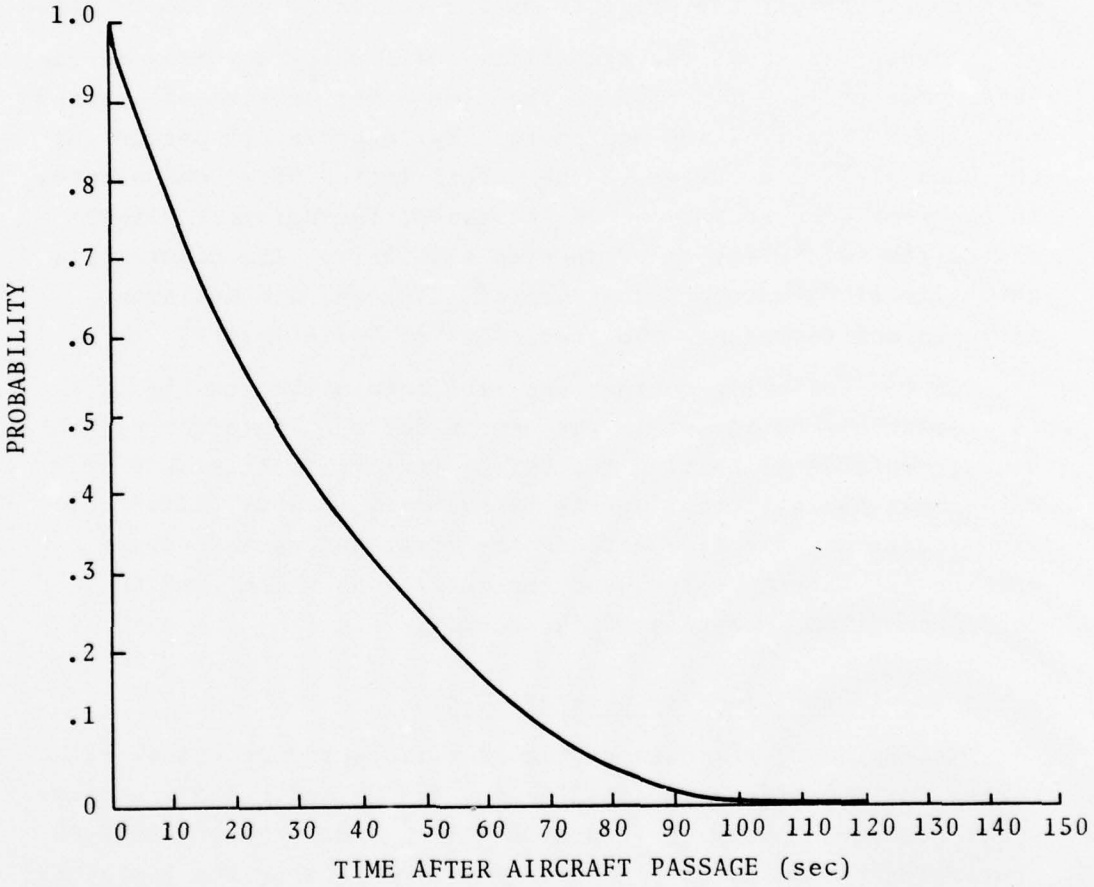


FIGURE 8-1. PROBABILITY OF FINDING A VORTEX IN THE SAFETY REGION.

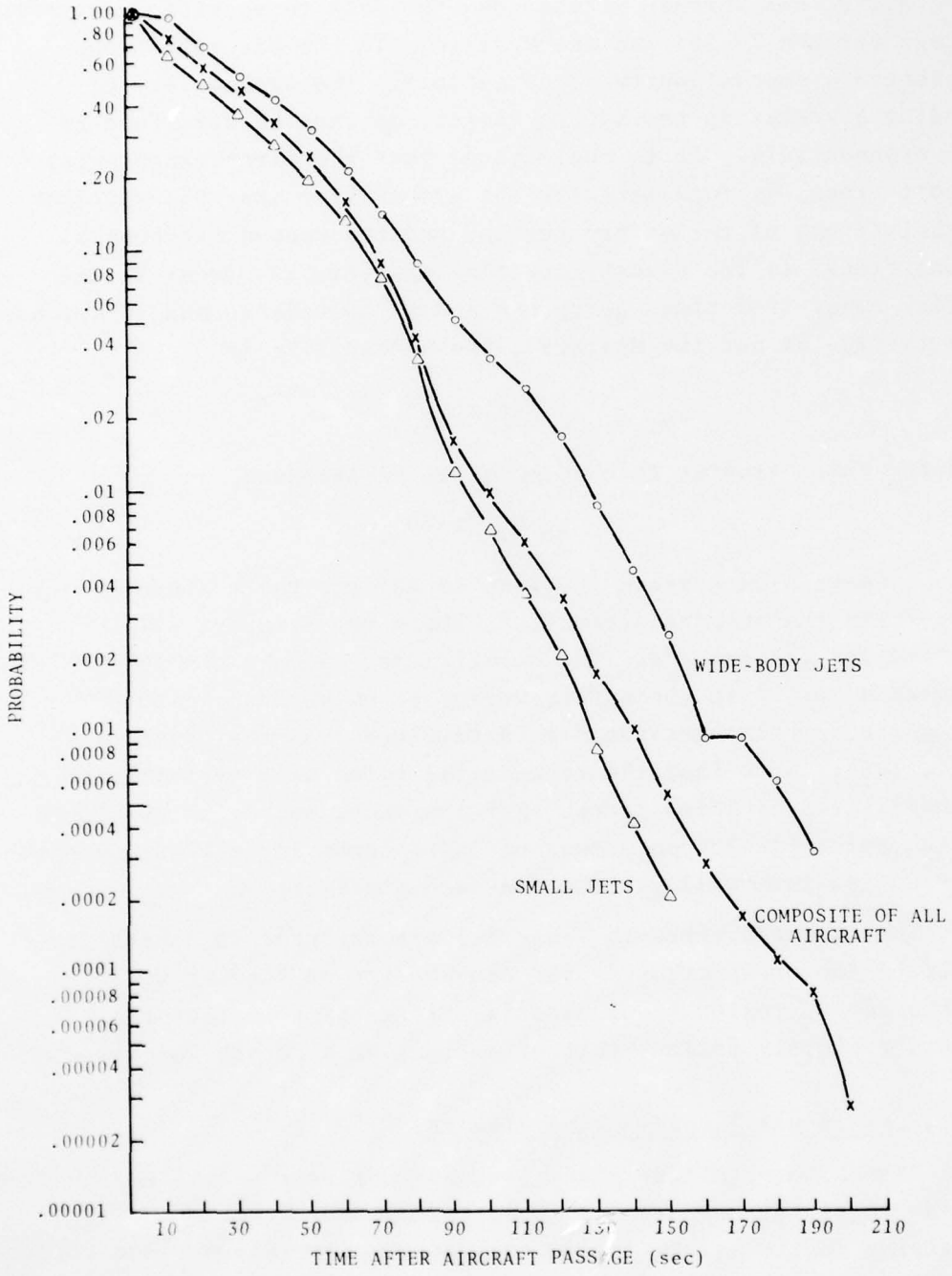


FIGURE 8-2. PROBABILITY OF FINDING A VORTEX IN THE SAFETY ZONE

Figure 8-3 further breaks down the data to specific aircraft. Except for the TU-134 and the Mystere, all the aircraft types exhibited a discontinuity at 60 seconds. The probability of finding a vortex in the safety region can thus be described by two exponentials. It is conjectured that the first exponential (short times) is fundamentally the probability that the vortices translate out of the safety region, and the second exponential (long times) is the probability that the vortices decay in the safety zone. For times between 0 and 60 seconds (0 and 40 seconds for the TU-134 and the Mystere), the probability is

$$e^{-\alpha_1 t} \quad ,$$

and for times greater than or equal to 60 seconds,

$$Ae^{-\alpha_2 (t-60)} .$$

The exponent will contain the term (t-40) for the Mystere and the TU-144; in the ensuing discussion, these two aircraft will be omitted for convenience. The coefficient A is the probability of finding a vortex in the safety region at 60 seconds. Table 8-1 gives the relevant constants as determined from the Heathrow data (Ref. 106). Note that the exponential forms will overestimate the probabilities at large times. For instance, no vortex was found in the safety region in excess of 120 seconds for a B-727, yet the exponential form will yield a non-zero probability.

The aircraft types in Table 8-1 are arranged in decreasing order of the coefficient A, the probability of finding a vortex in the safety region at 60 seconds. It is of note that the ordering closely follows that of decreasing aircraft weight.

8.1.4 Residence Times -- Wind Effects

Crosswind magnitude plays an important role in the motion of the vortices. Figure 8-4 shows the probability of a vortex remaining in the safety region for various crosswinds. The figure is a composite of all aircraft types; the data for specific aircraft types are similar; the lighter the vortex-generating aircraft, the

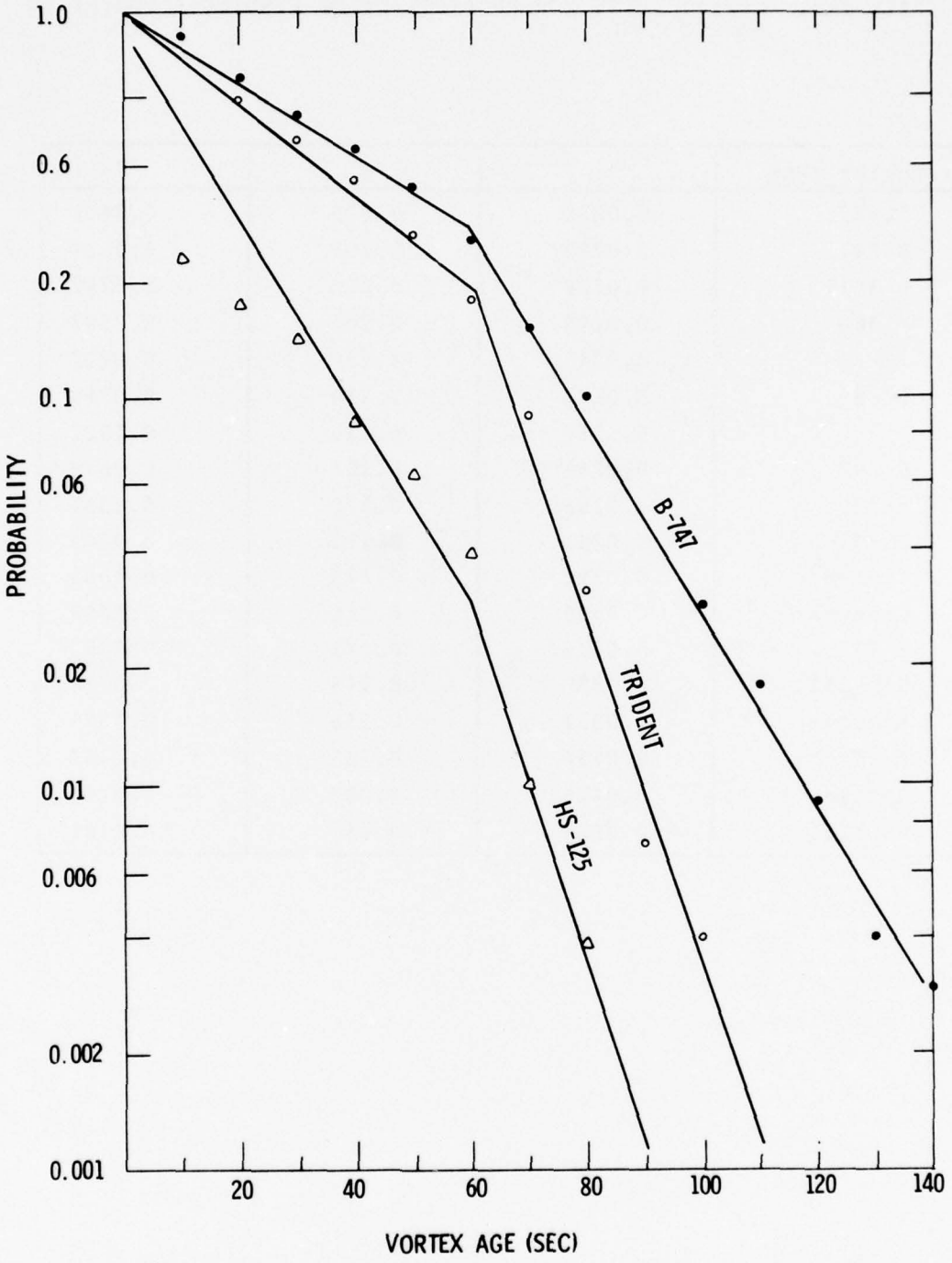


FIGURE 8-3. PROBABILITY OF FINDING A VORTEX IN THE SAFETY ZONE FOR SPECIFIC AIRCRAFT

TABLE 8-1. COEFFICIENTS FOR PROBABILITY OF FINDING A VORTEX IN SAFETY ZONE

AIRCRAFT TYPE	α_1	A	α_2
IL-62	0.0215	0.275	0.0552
B-747	0.0230	0.252	0.0554
L-1011	0.0229	0.252	0.0742
A-300	0.0245	0.230	0.0583
VC-10	0.0245	0.230	0.0777
DC-8	0.0245	0.230	0.0784
B-727	0.0256	0.219	0.1027
B-707	0.0262	0.207	0.0649
B-720	0.0288	0.178	0.0353
DC-9	0.0291	0.175	0.0763
Trident	0.0292	0.173	0.1031
Caravelle	0.0300	0.165	0.0758
B-737	0.0316	0.148	0.0702
BAC-111	0.0335	0.143	0.0715
Viscount	0.0332	0.136	0.1070
F-27	0.0334	0.135	0.2453
Herald	0.0415	0.083	0.2209
HS-125	0.0541	0.038	0.1181

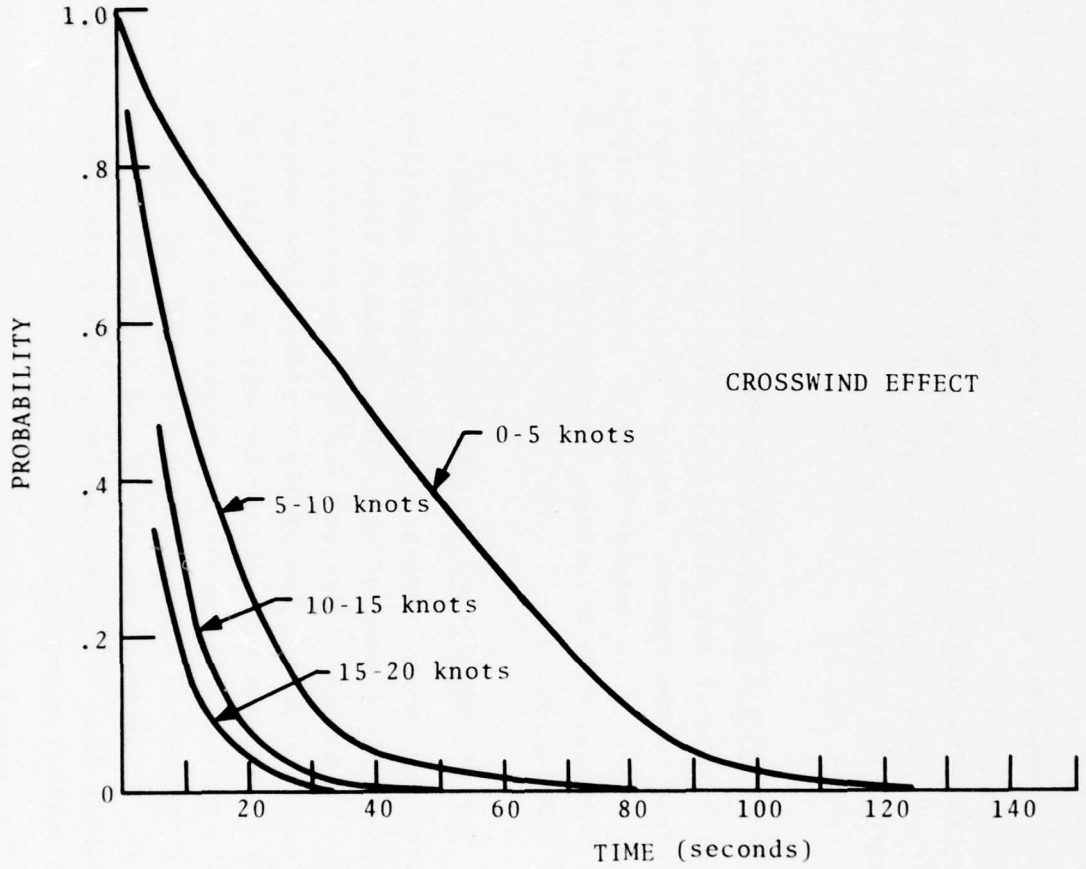


FIGURE 8-4. PROBABILITY OF FINDING A VORTEX IN THE SAFETY ZONE FOR VARIOUS CROSSWINDS.

closer the curves approach the origin of the graph. Eighty seconds represents an aircraft-to-aircraft spacing of less than three nautical miles for the approach speeds of most aircraft. On the basis of Fig. 8-4, it is reasonable to predict that wake vortices are unlikely to be troublesome when there are crosswinds greater than 5 knots.

For a specific crosswind, the average residence time increases with aircraft size. The largest average residence times occur at a higher crosswind magnitude for the jumbo jets than for all other aircraft. These trends are related to the fact that the stronger the vortex, the higher the crosswind required to stall the vortex in the safety region.

8.1.5 Residence Times -- How Vortices Exit Safety Region

Vortices exit the safety region by either transporting out or by decaying in the region. Most of the vortices with a residence time in excess of 40 seconds decay in the safety region while most of the vortices with a residence time of 40 seconds or less move out of the region.

8.1.6 Vortex Behavior at Various Sensor Baselines

Near the runway threshold, the aircraft generating the vortices are well within ground effect. The downwash field causes the vortices initially to descend and to interact very strongly with the ground. Usually, one of the vortices (the upwind vortex) very quickly disappears most likely because of a catastrophic interaction with the ground. The remaining vortex then moves away very quickly. It is a rare event when a vortex shed near the runway threshold persists for 80 seconds; because of the strong ground interaction, it is unlikely that such a vortex could have sufficient strength to affect another aircraft.

At or beyond the middle marker location (1070 meters from the runway threshold), the aircraft are over 60 meters above the ground, so that the vortices are barely within ground effect. For the first 10 to 20 seconds, the vortices move with the wind, and usually,

do not remain in the safety region for any significant amount of time. When a vortex stalls, it usually is outside the region or at least is low enough below the typical aircraft glide path that it is unlikely that the vortex could cause an unacceptable disturbance to a following aircraft. Most of the cases in this location where a vortex is found in the safety region after 80 seconds are those in which the vortex either exited the region and reentered or stalled near the extreme edge of the region.

The sensor baselines positioned about 600 meters from a runway threshold are the important baselines. Here, when a vortex lingers, the vortex is at about the same altitude as a following aircraft would be, and these vortices, in a probabilistic sense, are the ones which can linger longer than those near the runway threshold or the middle marker. Each test site always was provided with a sensor baseline in this region. All the data presented in the figures refer to the 600-meter location.

The residence times for two sensor lines which were both in the intermediate regime (400 and 732 meters from the runway threshold) were compared (Heathrow). Since the aircraft altitude is about the same over both baselines, the residence times should be about the same. The wind at the two sensor lines need not be the same, particularly with low winds, and should be reflected in a random variation between the residence times and lead to a nonnegligible standard deviation. For the Heathrow data, the residence times differed by only 1.6 seconds on the average with a standard deviation of 23.7 seconds; the lower the winds (and hence, the larger the variation in the winds between the two baselines), the higher the standard deviation (a maximum of 36.1 seconds). With high winds, particularly high crosswinds, the standard deviation decreased to a minimum of 7.9 seconds.

8.1.7 First and Second Vortex Crossings

Residence time was defined as the time required for both vortices to exit the safety region; in other words, the time the

second vortex leaves the safety region. Suppose the time of the exiting of the first vortex is known, can the time that the second vortex exits be predicted?

Figure 8-5 shows the distributions of the crossing times as a function of the crosswind (data from the Heathrow tests, ref. 106). The broken lines indicate the distributions of the first crossing, and the solid lines indicate the second crossing. As the crosswind magnitude increases, the first vortex exits sooner (the peak of the distribution), and the distribution becomes narrower. The second vortex seems to exit the safety region almost randomly for crosswinds up to 4 knots, but the distribution becomes more peaked, and the vortex exits sooner as the crosswind increases. Similar distributions exist for specific aircraft types, only the location of the peaks of the distributions differ (earlier times for the lighter aircraft, and later times for the heavier aircraft). The crosswind magnitude, however, appears to be the most important quantity for estimating when the safety region will be clear of vortices. If a high confidence level is necessary (as indeed it would be for any predictive system), knowing the time at which the first vortex exits does not significantly improve a prediction of the residence time.

8.1.8 Residence Times -- Cases Which Exceed 80 Seconds

One method for regaining or increasing the capacity of an airport would be to determine those times during which all aircraft separations on final approach could be safely decreased to 3 nautical miles (instead of the current 3,4,5, or 6 nautical miles depending on the type of lead and following aircraft). It would be expected that such times are dependent on the wind velocity; crosswinds in excess of 5 knots were shown in Section 8.1.4 to appear to alleviate the wake vortex problem.

To pursue the appropriate wind conditions, data on the heavy aircraft (B-747, DC-10, L-1011, stretched versions of DC-8 and B-707, Super VC-10, IL-62, and A-300) whose vortices had a residence time of 80 seconds or more were segregated from the data base. A ground speed of 135 knots means that 3 nautical miles is equivalent

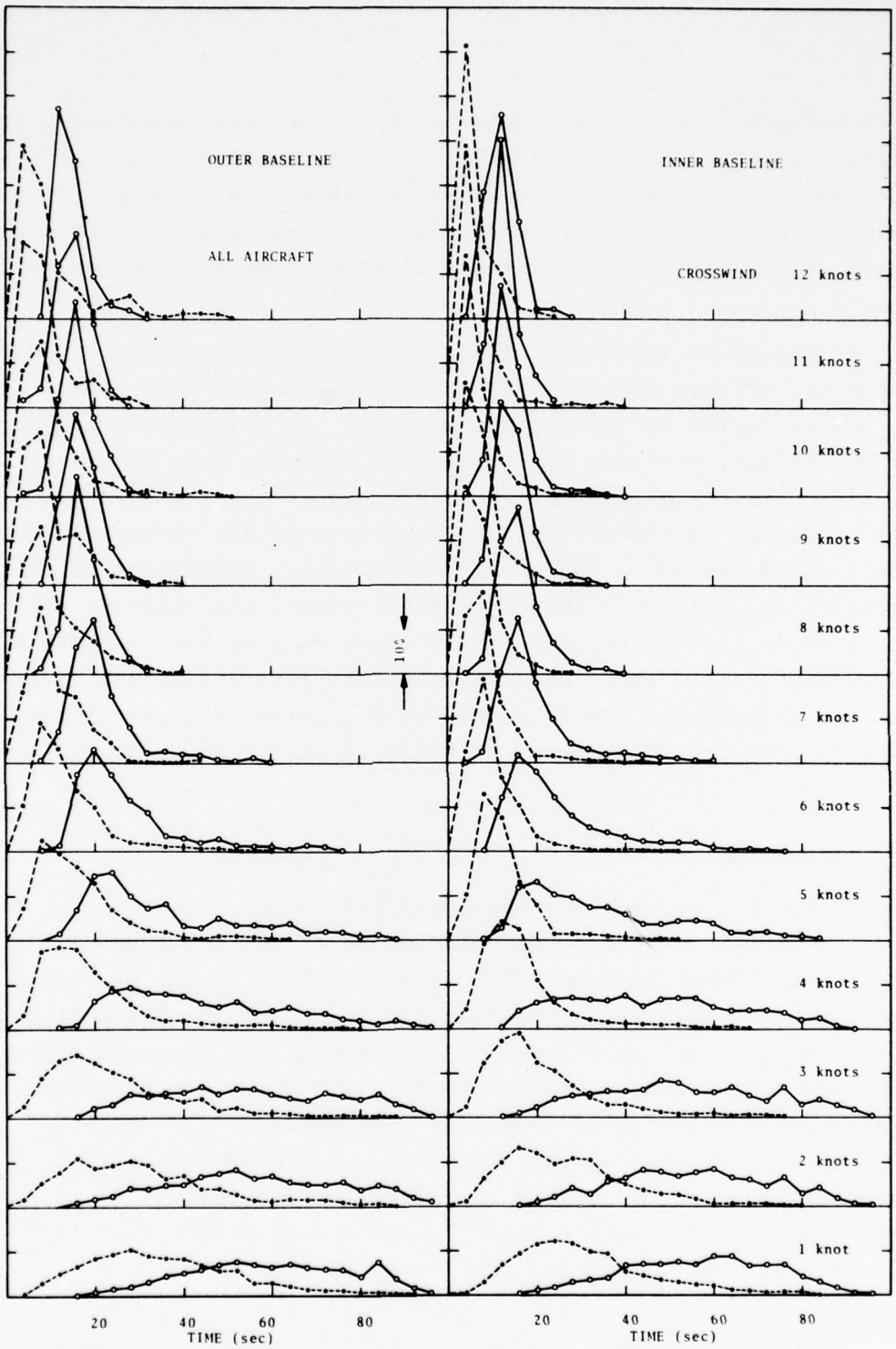


FIGURE 8-5. CROSSING TIMES FOR THE FIRST AND SECOND VORTEX

to 80 seconds. All the 80-second or more data are contained within an ellipse with a semi-major axis (headwind/tailwind axis) of 12 knots and a semi-minor axis (crosswind axis) of 5.5 knots. Any number of geometrical patterns could have been used to enclose the data, but the ellipse is a convenient pattern with a low enclosed area.

It should be noted that just because winds are measured to be within the ellipse does not mean that every vortex will remain in the safety region for 80 seconds or more. If a vortex does linger within the safety region for 80 seconds or more, then the winds will be within the ellipse. When the winds are within the ellipse, less than 5 percent of the vortices will persist in the safety region in excess of 80 seconds. The overly conservative dimensions of the safety region, the ignoring of aircraft types, the ignoring of vortex decay because of atmospheric turbulence or the non-stability of the atmosphere, etc., all contribute to restricting the times when the separations could be decreased. Additional research now underway should provide other criteria to shrink the size of the ellipse.

8.2 VORTEX DECAY

Although vortices have been detected in the safety region for times in excess of 80 seconds, nothing is as yet known about the strength of these vortices. The data discussed in the previous sections were collected using baselines of propeller anemometers. It is possible that only remnants of the vortices are being tracked which would be unable to affect an aircraft which inadvertantly penetrated or encountered them. In this section, the demise of vortices as indicated by the wealth of anemometer data will be discussed first. The section will close with a discussion of an ongoing program to measure directly the strength or circulation decay of vortices in the terminal environment.

8.2.1 Anemometer Data

Various studies have shown that the magnitude of the total wind correlates best with the demise of vortices. The lower the wind

magnitude, the longer a vortex will survive on the average. McGowan (ref. 60) devised a curve to indicate the maximum lifetime of a vortex as a function of the total wind. He obtained the relationship by fairing a curve to all the known (in 1970) vortex lifetime data in such a manner that all the data were included under this curve (see Figure 8-6). McGowan's curve has been widely used. The Heathrow data (ref. 106) includes conditions omitted from the McGowan curve. Most of the data that McGowan had available came from tower tests. Smoke from canisters on a tower became inbedded in the vortices shed by aircraft making low passes upwind of the tower. Decay was assessed visually. By necessity, this type of data involved mainly a crosswind component since a crosswind was required to translate the vortices to and past the tower. At Heathrow, the winds were from all directions, and a particular component of the wind was not required to move the vortex, so that it could be tracked. What McGowan's curve neglects is the effect of winds along the direction of the vortex. Winds along the vortex axis seem to suppress meanderings of the vortex and thus delays at least one of the known decay modes (sinuous or Crow instability). When the wind is orthogonal to the vortex axis, the shearing action of the wind across the vortex can aid in the dissipation process. Thus, the Heathrow data alter the McGowan curve for the high winds as shown in Figure 8-7.

Figures 8-8 and 8-9 present the probability of finding a vortex still active at a given age for various total wind magnitudes. The vortex lifetime for each increment of the horizontal wind can be fitted with the form

$$T_{life}(t) = 1.0, \qquad t \leq t_A,$$

$$= e^{-B(t-T_A)}, \qquad t \geq T_A.$$

For the two cases shown, the B-747 and the Trident, T_A was found to be dependent on the horizontal wind. An increasing wind causes the vortices to dissipate sooner. The death rate B does not exhibit a strong dependence on the total wind. The natural turbulence in the wind appears to dissipate the vortices in high winds. When the

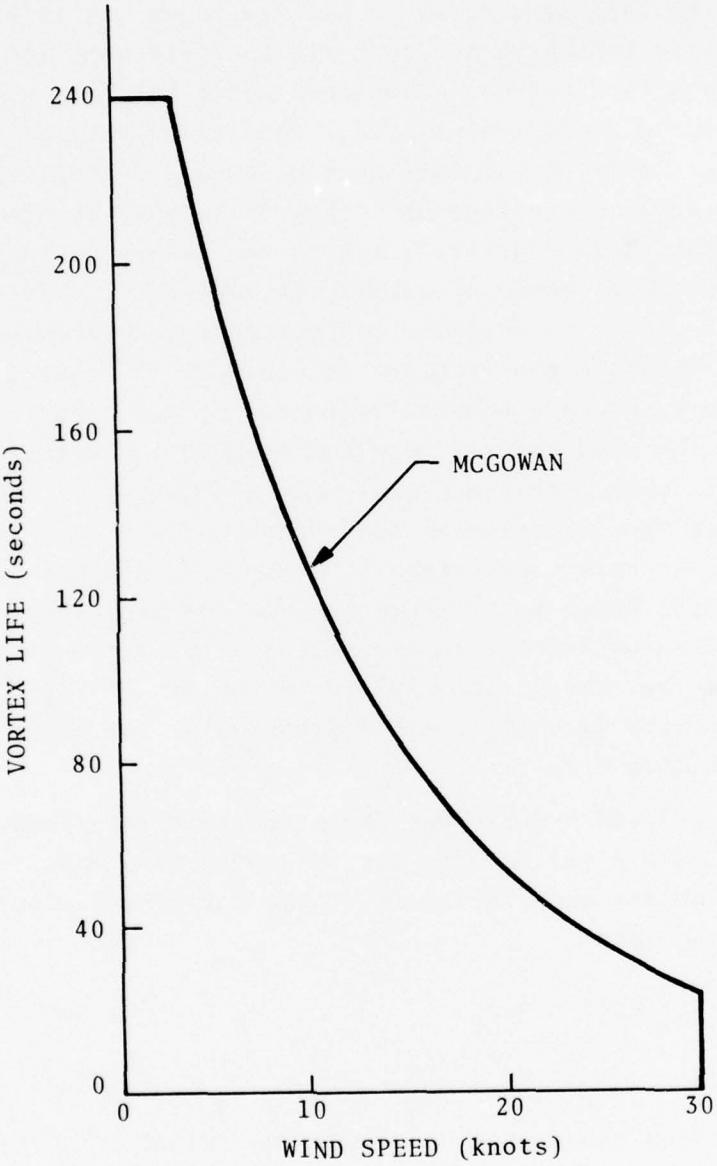


FIGURE 8-6. MCGOWAN VORTEX LIFETIME CURVE

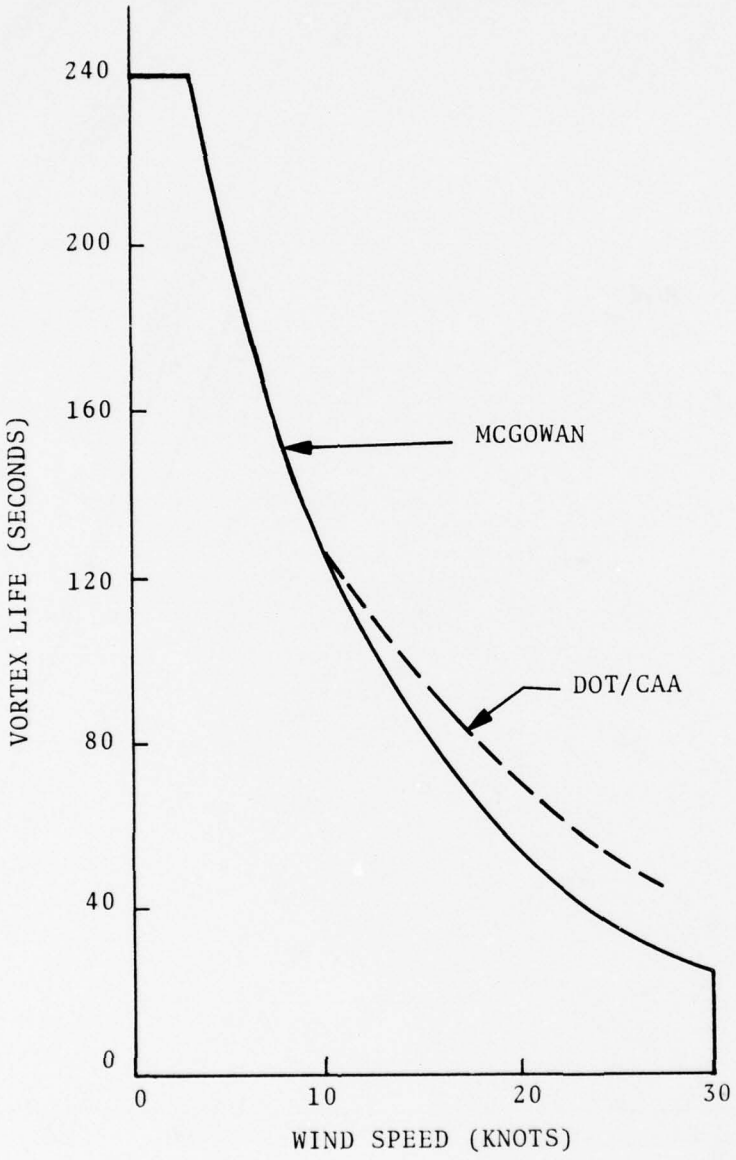


FIGURE 8-7. REVISED MCGOWAN VORTEX LIFETIME CURVE.

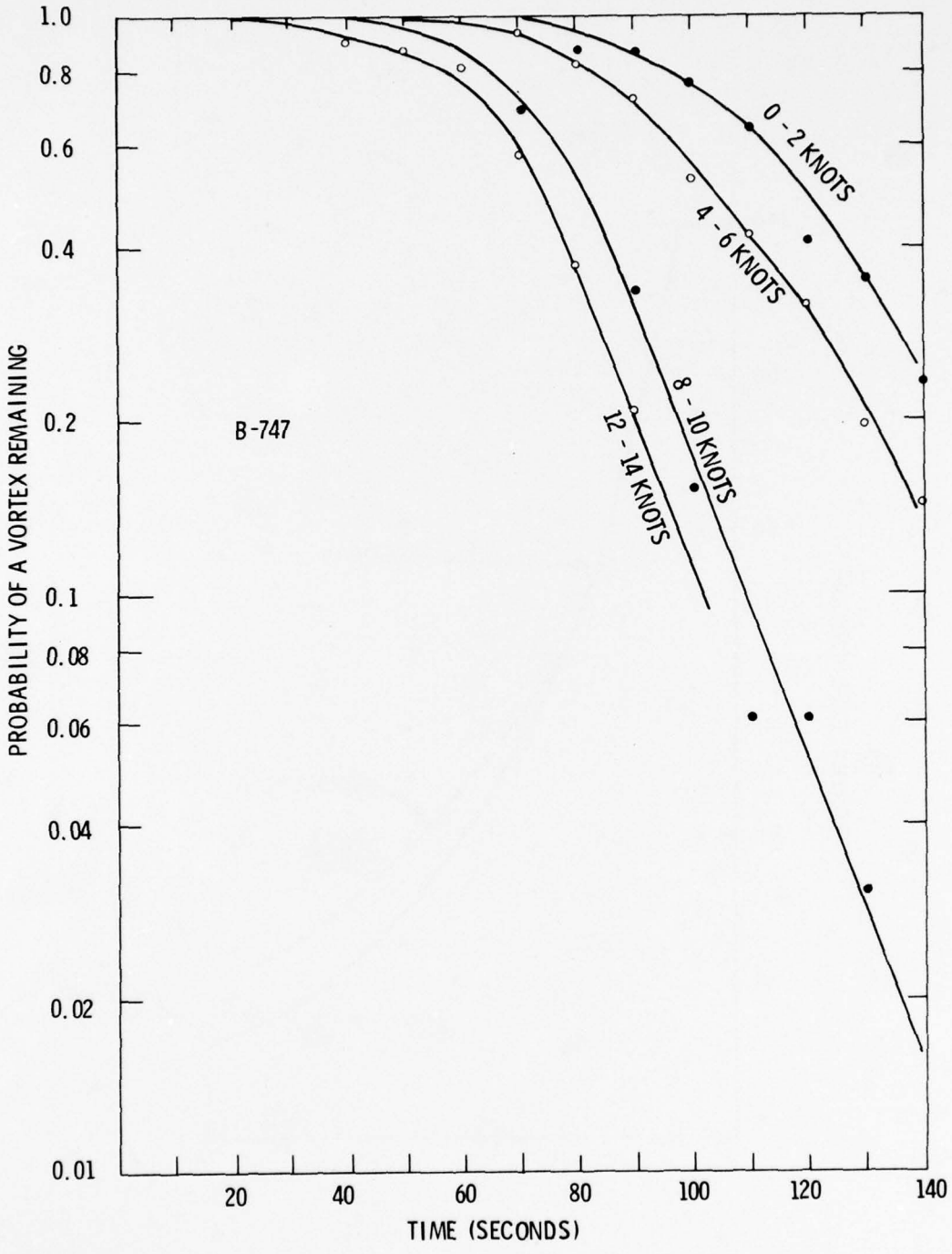


FIGURE 8-8. PROBABILITY OF A B-747 VORTEX EXISTING UNDER VARIOUS WIND CONDITIONS.

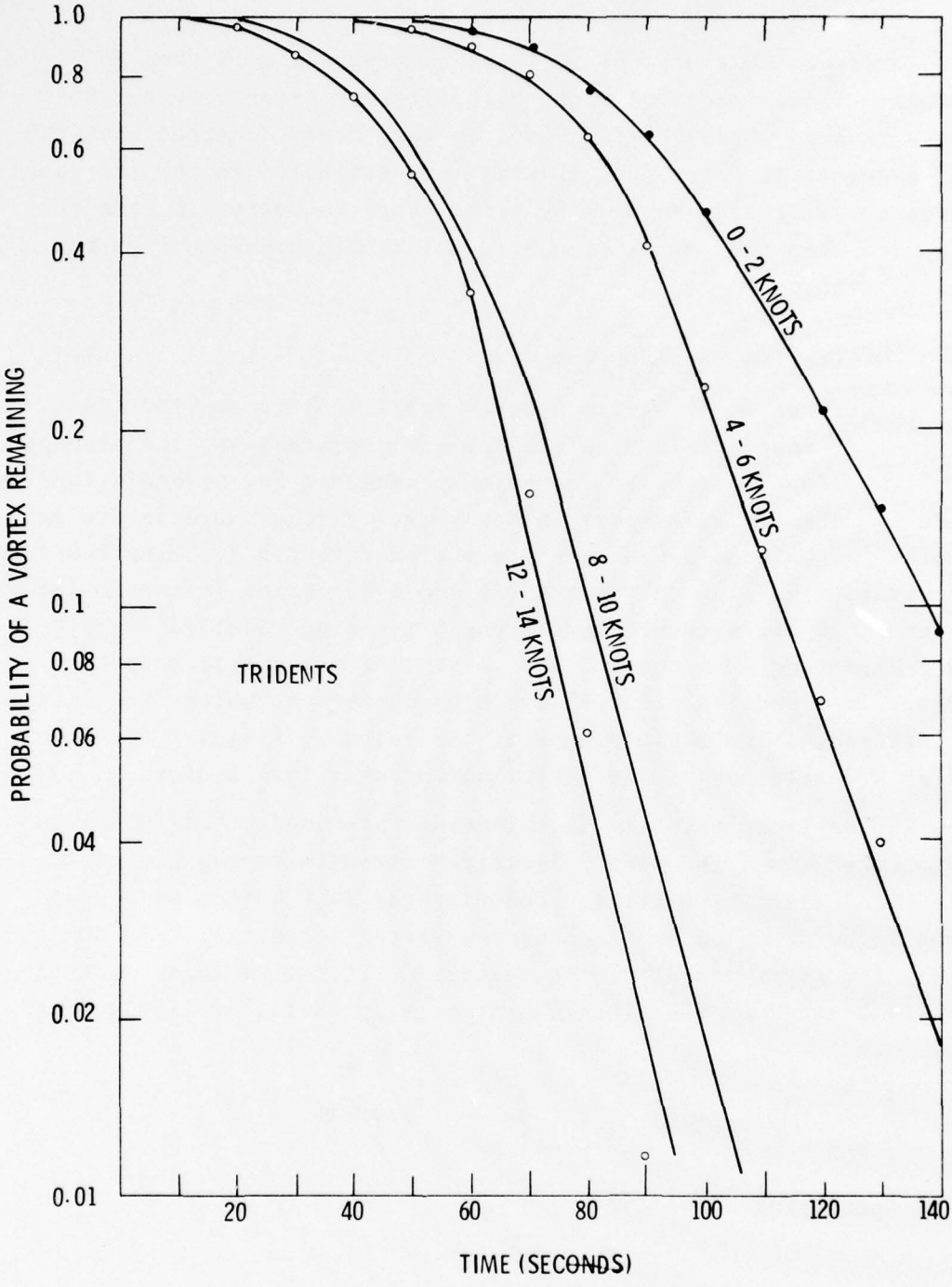


FIGURE 8-9. PROBABILITY OF A TRIDENT VORTEX EXISTING UNDER VARIOUS WIND CONDITIONS.

winds exceeded 20 knots, no vortices existed for more than 60 seconds. The vortices of light aircraft very often were not detected in high winds; HS-125 vortices were never detected when the wind exceeded 15 knots, but this may be attributed to the increased sensor noise level. When using anemometers, a vortex is said to have died when the vortex signal is not distinguishable from the ambient wind.

8.2.2 Monitoring Vortex Decay

As part of an extensive program (ref. 105) to monitor the behavior of wake vortices in the terminal environment, the strength or circulation of vortices was briefly measured for aircraft landing on runway 31R at JFK Airport in New York. Further work is now in progress at Chicago's O'Hare where vortex strength is being recorded for aircraft landing on runways 32L and 14R, and at Toronto's International Airport where vortex strength is being recorded for aircraft departing from runway 23L. Arrays of monostatic acoustic sensors (see section 6.3.2.3) are used to measure vortex-velocity fields; successive measurements of the velocity field of the same vortex are obtained as the vortex passes over each sensor.

The vertical velocity distributions are used to calculate an "effective" strength. The "effective" strength is the circulation of an equivalent line vortex producing the same torque on a wing as would be produced by the measured vortex velocities. In other words, the first moment of the measured vertical velocity distribution is equated to the first moment of a potential or line vortex:

$$\int_{-b/2}^{b/2} V_{potential}\, r\, dr = \int_{-b/2}^{b/2} V_{measured}\, r\, dr.$$

Since $V_{potential} = \Gamma/(2\pi r)$,

$$\Gamma = \frac{2\pi}{b} \int_{-b/2}^{b/2} V_{measured}\, r\, dr,$$

where Γ is the "effective" strength, b is the wing span of a hypothetical vortex-encountering aircraft, and $V_{measured}$ are the vertical velocities measured by the monostatic acoustic sensors. To perform the integration, the radial parameter is transformed to time as the measured velocities are recorded as time histories. Thus, $r = V_T t$, where V_T is the horizontal transport velocity of a vortex over each sensor (obtained by noting the times at which the vortex is directly over each sensor and assuming a constant transport velocity between sensors).

Figures 8-10, 8-11, and 8-12 show examples of the data from the brief trials at Kennedy Airport; each figure exhibits an apparently different but equally probable mode of decay. Up to four independent measurements of effective vortex strength can be made for each vortex (noisy channels often precluded obtaining all four measurements). Solid lines in the figures connect the data for the same vortex. In Fig. 8-10, four of the cases have been extended with broken lines; here, the vortex was not seen in the next sensor as the strength decayed below the instrumental threshold.

Figure 8-10 displays cases where the strength very rapidly decays. Once the rapid decay commences, the strength is seen to decrease by a factor of 2 in approximately 15 seconds. Two trends have been observed: (a) the rapid decay begins sooner and it occurs more often when the ambient turbulence is high, and (b) for a given turbulence level, the vortices from larger aircraft begin the rapid decay later than those from smaller aircraft. It is suggested that the rapid decay is caused by a sinusoidal instability in which the vortex has linked with its image vortex.

Gradual decay is depicted in Fig. 8-11. The strength appears to erode slowly to a negligible value (at least below the instrumental threshold) with a halving of strength every 30 to 60 seconds. The dissipation of the vortex varies as $(\text{time})^{-1}$, and is probably a turbulent diffusion process.

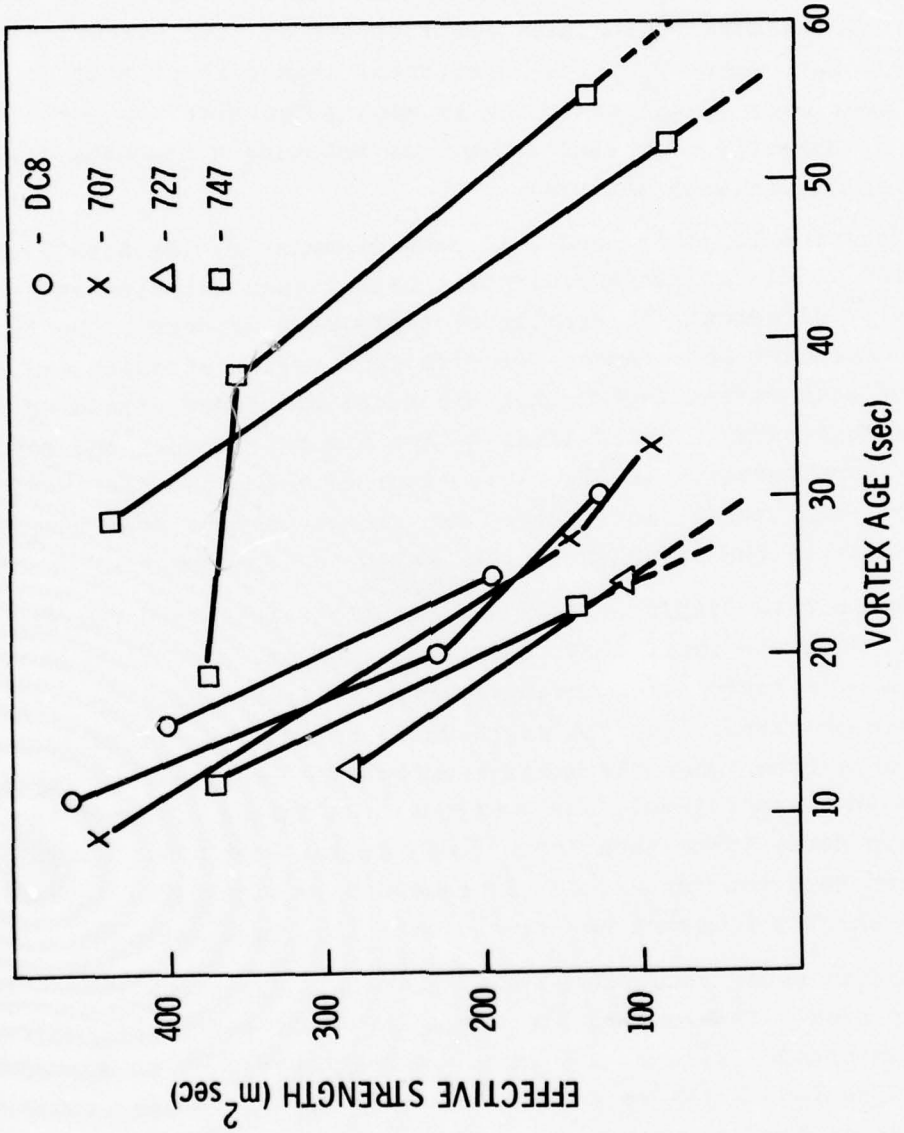


FIGURE 8-10. VORTEX DECAY VIA LINKING WITH THE GROUND.

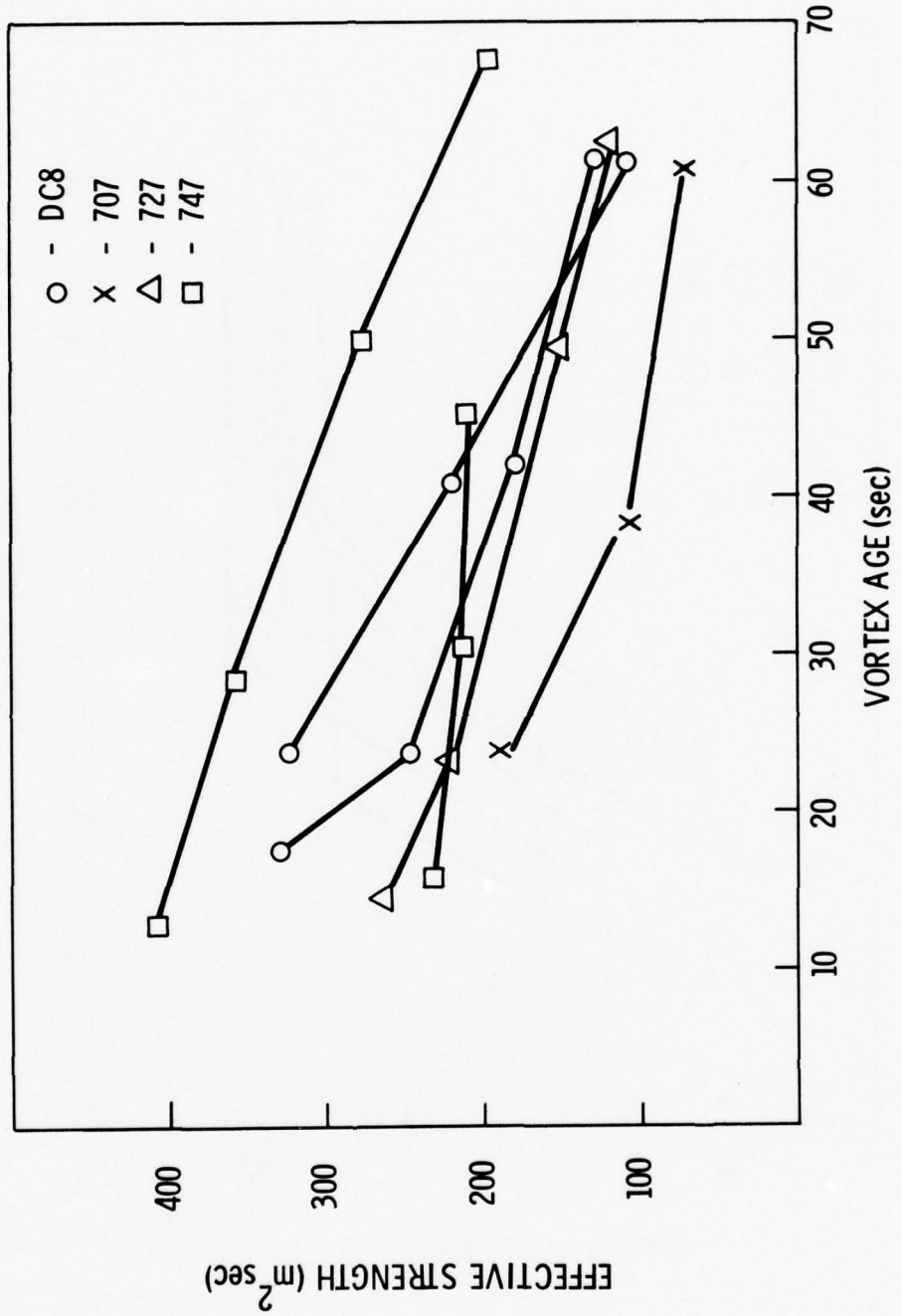


FIGURE 8-11. VORTEX DECAY VIA TURBULENT DIFFUSION.

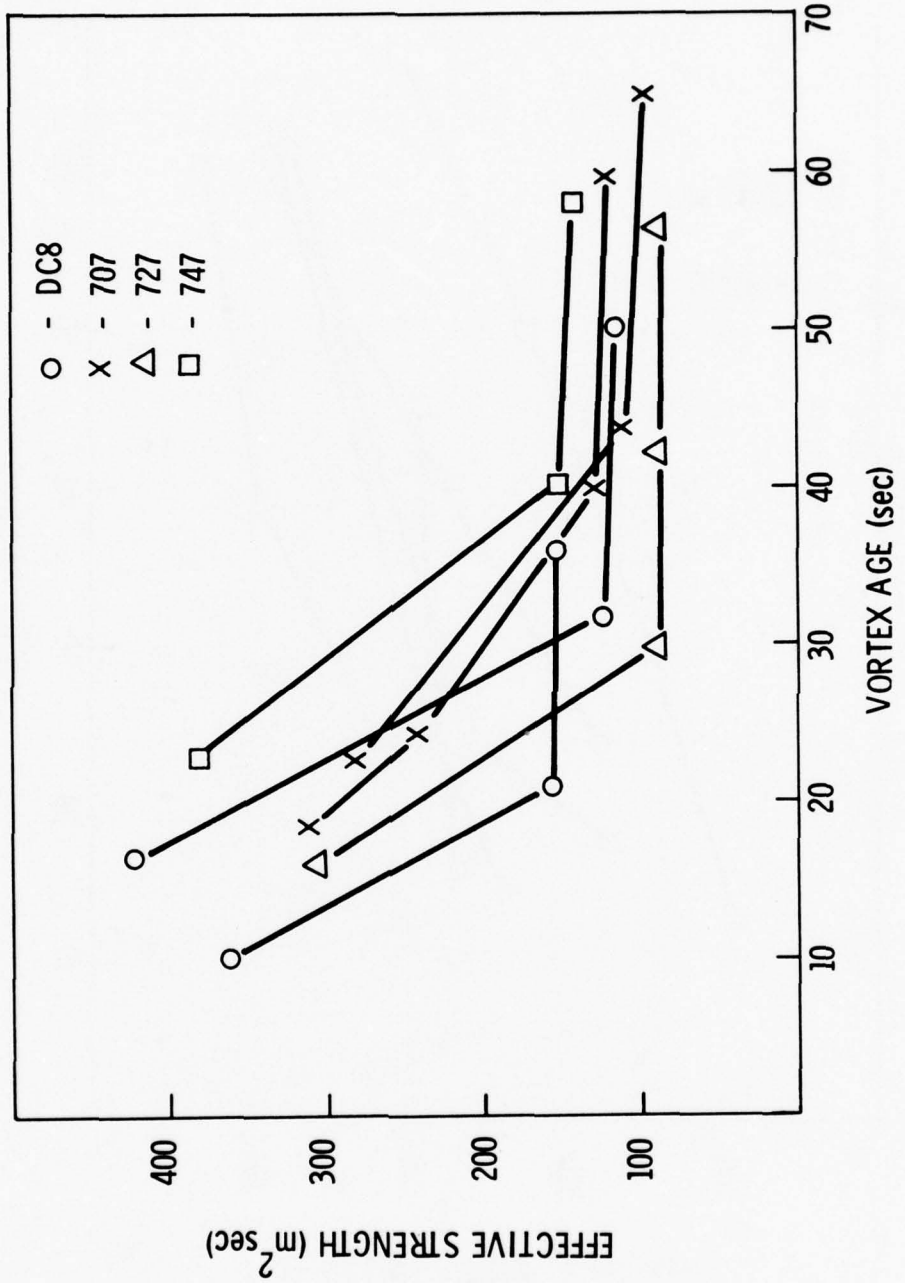


FIGURE 8-12. VORTEX DECAY VIA CORE-BURSTING.

Figure 8-12 exhibits a third mechanism: the vortex experiences a rapid decay which ultimately is curtailed leaving behind a relatively constant but weaker vortex or remnant in its stead. It is suggested that vortex breakdown or core-bursting has occurred leaving behind a remnant which mixes little with the atmosphere. The strength of the remnant correlates with the size of the vortex-generating aircraft: B-727 vortex remnants are weaker than B-707 or DC-8 remnants which in turn are weaker than B-747 remnants. In flight tests where smoke has been injected into the cores of the vortices, often after a vortex has "burst," a smaller core becomes discernible as smoke is transported by the axial flow in the vortex from an unburst portion to the remnant.

9. VORTEX AVOIDANCE SYSTEMS

A straightforward approach was taken in the formulation of system concepts for wake vortex avoidance and began with defining the systems users, the user requirements, and the operational requirements. A block diagram of the approach is shown in Fig. 9-1.

In general, the users can be divided into three main groups: airports, aircraft, and air traffic control (ATC). The user interests and needs are diverse. Airports require:

1. An increase in runway capacity,
2. Maintenance of safety of operations,
3. The minimization of system acquisition-and-ownership costs, and
4. Site-independent-system performance.

For aircraft the needs are to:

1. Improve the safety of operations,
2. Be operational under all weather and visibility conditions,
3. Have coverage for all aircraft,
4. Have a low/no cost to acquire use of system, and
5. Improve economics of operation.

The ATC must:

1. Maintain safety of operations,
2. Optimize use of airspace and runways, and
3. Have no interference or degradation on other ATC functions.

Based on this list of user needs one can arrive at the following set of requirements a wake vortex avoidance system must meet:

1. Replace fixed separation standards with adaptive separation standards, thus maximizing traffic flow.

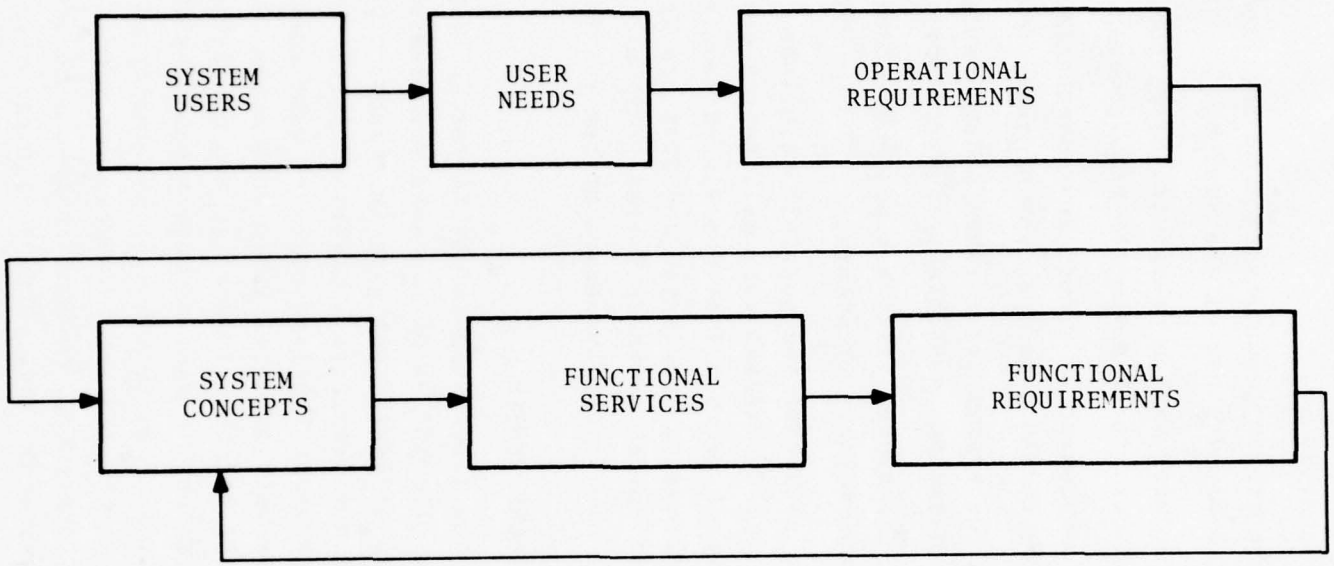


FIGURE 9-1. APPROACH USED IN THE DESIGN OF WAKE VORTEX AVOIDANCE SYSTEMS

2. Detect presence of a vortex hazard and generate information necessary to avoid it.

3. Make the system ground-based. No additional avionics are to be required to acquire use of the system.

4. Use a modular system design tailoring the system capabilities and cost to an airport's requirements.

5. Use a complement of ground instrumentation to insure uniform system performance independent of site constraints.

6. Design the system for maximum independence from other ATC systems to insure maximum possible system reliability.

7. Use of the system shall not place any additional burden on air traffic controllers or pilots.

Fortunately, the nature of the possible solutions to the wake vortex problem lend themselves very well to the development of a modular system which meets all of the listed requirements. A series of systems of increasing complexity and cost are feasible starting with the simplest Vortex Advisory System (VAS) and ending in the fully automated Wake Vortex Avoidance System (WVAS).

9.1 VORTEX ADVISORY SYSTEM

The VAS is the first step in the hierarchy of systems to be designed for the alleviation of the wake vortex problem. The use of a VAS promises a significant gain in airport capacity through reduced approach and departure separation times. Until recently the lack of knowledge about the life-cycle of wake vortices generated by today's large aircraft mandated large separation distances for following aircraft and thus limited approach-and-landing capacities. Analysis of the extensive data on vortex behavior as a function of meteorological conditions (Section 8) has indicated that there are wind conditions which predictably remove vortices. A wind rose criterion could, therefore, be used to determine when the separations could be uniformly reduced to 3 nautical miles for all aircraft types rather than using the 3-, 4-, 5-, and 6-mile separations currently required.

The VAS was designed to take advantage of the wind rose criterion. The system is based on comparing the measured wind magnitude and direction (with respect to each runway heading) with the wind criterion. The comparison indicates via a simple display when separations could be safely reduced to three nautical miles for all aircraft.

A decision was made to test the VAS concept at an airport under actual operating conditions. Since the main objective of the VAS is to allow increases in capacity, the major high-density terminals with a significant percentage of jumbo-jet operations and with capacity at or near saturation were considered for the feasibility tests. Those airports considered included the Chicago O'Hare, Los Angeles, Miami, Philadelphia, Seattle-Tacoma, Kennedy, and Hartsfield Atlanta International Airports, and the Detroit Metropolitan Wayne County Airport. Chicago was selected on the following criteria: adequate available real estate for the VAS equipment; operations near saturation during VFR conditions, and beyond saturation during IFR conditions; and a significant percentage (17 percent) of jumbo-jet operations in the traffic mix.

The main purpose of the VAS system deployed at Chicago O'Hare is to determine the feasibility of reducing longitudinal separations when either the wake vortices have been blown out of the approach corridor, or the vortices have decayed and no longer present a hazard to the following aircraft. VAS testing was implemented by using an instrumentation system to measure the vortex positions as a function of time and the ambient meteorological conditions and correlating the vortex tracks with the VAS displayed output. The amount of time that the VAS indicates reduced separations could be used will be evaluated to determine how many additional operations could be accommodated if reduced separations were in effect. The evaluation must be performed under all combinations of approach and landing runway scenarios as well as under VFR and IFR weather conditions. It is anticipated that the system will allow reduced separations up to 60 percent of the time, and that significant increases in capacity will be possible, especially during IFR conditions when current capacity is oversaturated.

9.1.1 VAS Design Details

The VAS design details given below represent the present state of the VAS. It is anticipated that some hardware and software changes will be required during the feasibility evaluation phase (June 1976 to March 1977). The intent of the VAS feasibility demonstration at O'Hare is to test the validity of the concept and is not intended as a final hardware design. Should, as the initial indications show, the VAS prove itself capable of improving operations, the final product of the effort will be a detailed system specification.

9.1.1.1 Meteorological Towers - The VAS consists of a network of instrumented meteorological towers whose signals are transmitted to a centrally located processor which uses a simple algorithm to determine the vortex conditions, and displays them to the controllers. As shown in Fig. 9-2, the tower network consists of seven 15-meter meteorological towers positioned to measure the wind close to each operating corridor. A network of towers is required as tests at O'Hare and JFK Airports have proved that the inhomogeneity of the atmosphere precludes the use of a single centrally located sensor for the measurement of wind. The towers are free-standing on a cement base and are marked and lighted per FAA Advisory Circular 70/7460-1.

9.1.1.2 Meteorological Sensors - Each tower is instrumented with three wind magnitude-and-direction sensors, one at the 15-meter level and the other two at the 12-meter level. The 12-meter sensors are mounted on opposite sides of the tower to provide a measurement undisturbed by tower-shadowing. The sensors are manufactured by the Climatronics Corporation and were modified to withstand the airport environment. The wind-speed sensor (cup anemometer) has the following salient characteristics: range of 0 to 90 knots, accuracy of $\pm$0.5 knots or 2 percent, threshold of 0.75 knot maximum, and a distance constant of 2.5 meters. The wind-direction sensor (vane) has a range of 0 to 540 degrees, accuracy of $\pm$2 percent, threshold of 0.75 knot maximum, distance constant of 9 meters, and a damping ratio of 0.4 to 0.6. All sensor and communication

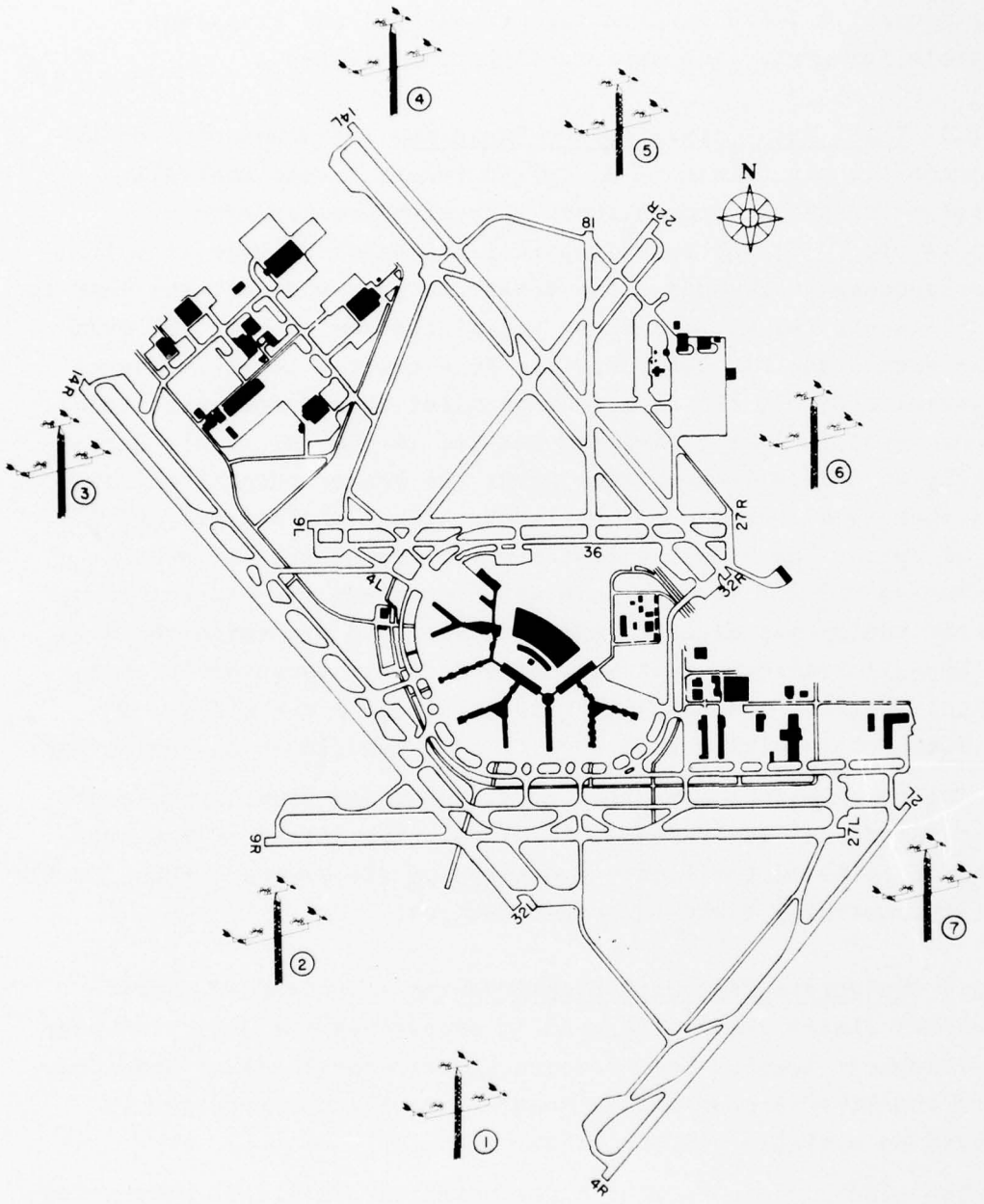


FIGURE 9-2. LOCATIONS OF THE VAS METEOROLOGICAL TOWERS AT CHICAGO O'HARE.

electronics at each tower are housed in an environmental enclosure. Each tower is supplied with a 220/110-volt 60-Hz power source, a 2-KVA line-voltage regulator, and transient arrestors for protection against lightning strikes.

9.1.1.3 Tower Data-Communication Subsystem - Transmission of the data from the set of widely dispersed towers to the centrally located processor is accomplished with standard hardware. As shown in Fig. 9-3, the meteorological VAS block diagram, a multiplexer successively samples the sensor outputs and converts them to a parallel digital word which is serialized and transmitted over standard existing FAA control lines to a central facility where receivers reconvert the data to a parallel format for input to a microprocessor. A Datel Systems DAS-16, 16-channel 12-bit data-acquisition system sequentially scans the sensor outputs and converts them to a 16-bit word consisting of a 4-bit address and 12 bits of data. The DAS-16 operates under the control of a Larse Corporation LSC-111 sending unit which commands the channel scan, converts the output data to serial format, and transmits the data to a LCR-211 receiving unit where the data are reconverted to a parallel format. The sampling rate is fixed by the LSC-111 at 5600 bits/sec resulting in a word rate of 5600/16 or 350 words/sec.

The high channel capacity, resolution, and sampling rate are in excess of what is presently required. The intent of the overdesign is to allow for future expansion of the system without costly and time-consuming field-equipment changes.

9.1.1.4 Meteorological Data-preprocessing - Individual microprocessors (Intel 8080A) are used to preprocess the data from each meteorological tower. The microprocessors contain 8K of Read-Only-Memory and 8K of Random-Access-Memory. Each microprocessor is packaged on a single plug-in board.

The microprocessors sample the meteorological data output from each LCR-211 receiver at a rate of 2 samples/sec. The sampled wind magnitude (R) and wind direction (θ) are used to compute a one-minute running average ($\bar{R}$ and $\bar{\theta}$) by the following scheme: for

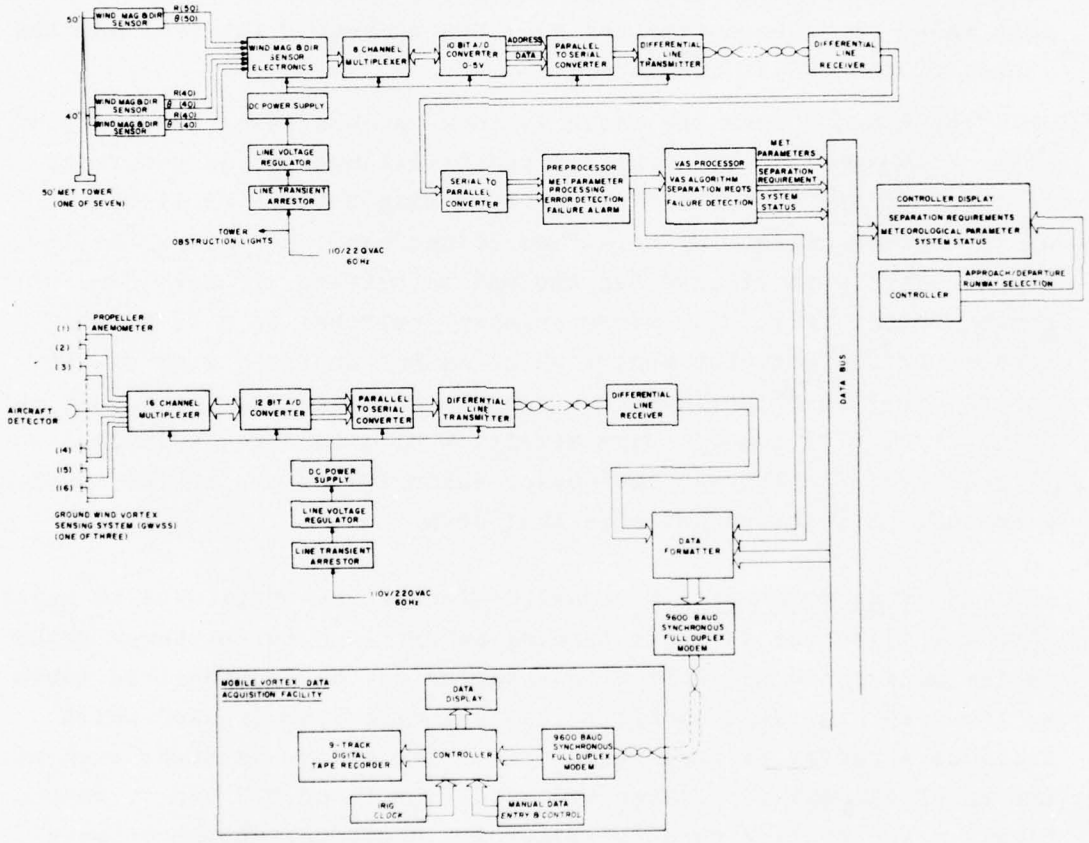


FIGURE 9-3. BLOCK DIAGRAM OF THE VAS.

each sample compute U=R sinθ and V=R cosθ, compute $\overline{U}$ and $\overline{V}$ using a running 128 sample average, and compute $\overline{R} = (\overline{U}^2+\overline{V}^2)^{\frac{1}{2}}$ and $\overline{\theta}= \tan^{-1}(\overline{V}/\overline{U})$.

A wind gust is defined using a 30-second interval. Within each 30-second interval, the sampled R is averaged using an 8-sample running average. Momentary peaks caused by high-frequency gusts which would not affect aircraft operations are filtered out by the 8-sample running average. (Transient spikes in the data are eliminated by a comparative process.) Any measured peak must be at least 9 knots above $\overline{R}$ to be considered a gust. The gust value is the peak value observed during each 30-second interval. At the end of each 30-second interval, the gust value is compared to the gust value observed during the previous 30-second interval and the larger of the two is displayed.

The R and θ from the three sensors on each tower are compared after each sampling interval. A sensor-failure bit is generated if the R of any sensor differs by more than 5 knots or if the θ of any sensor differs by more than 20 degrees. Normally, the 15-meter sensor data is used for the VAS algorithm. If the 15-meter sensor output fails, the microprocessor switches to a 12-meter sensor, and selects the sensor which is not in the shadow of the tower. Failure of at least two sensors to agree terminates all data output from that tower. Upon detection of a failure, a failure word is generated identifying the sensor which failed or, if two sensors disagree, which tower has been shut down.

9.1.1.5 VAS Processor - A separate microprocessor is used to calculate the allowable aircraft-landing separations for a runway based on the wind speed and direction measured by the instrumented tower. As shown in Fig. 9-4, an elliptical VAS algorithm is used which includes a buffer or transition zone. The major and minor axes of the inner and outer ellipses are 12, 14, 5.5 and 7.5 knots, respectively. The transition zone allows for a gradual change between states as opposed to an abrupt change which an aircraft controller working a line of approching aircraft could obviously not accommodate.

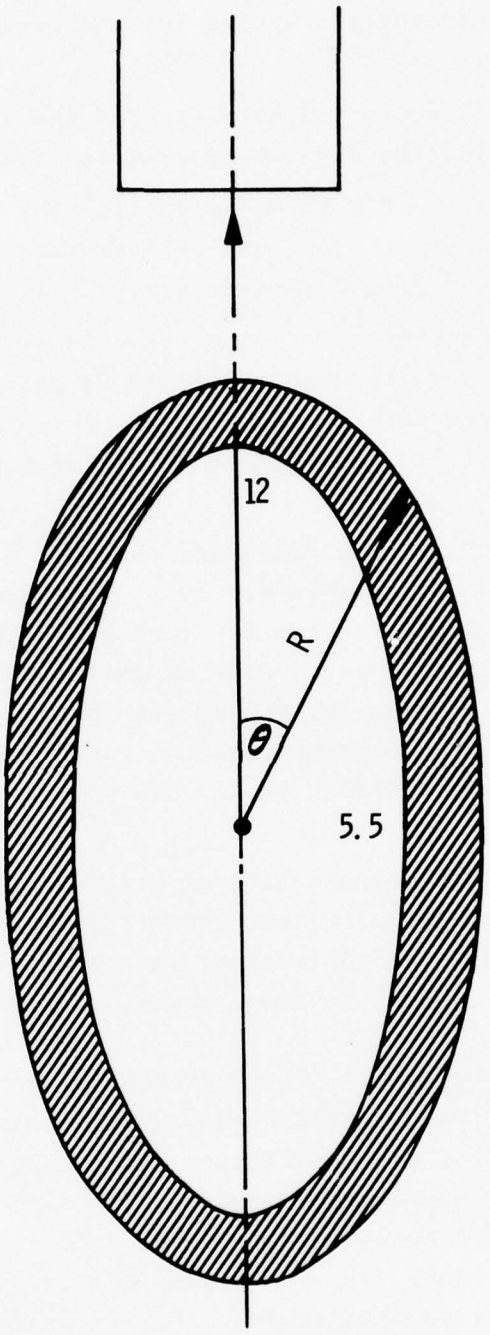


FIGURE 9-4. THE VAS WIND CRITERION.

The criteria for separation and for changing separations from one state to another are:

a. If the wind vector $(\overline{R},\overline{\theta})$ is inside the inner ellipse, the condition is RED, and the 3-4-5-6 separations apply.

b. If the wind vector $(\overline{R},\overline{\theta})$ is outside the outer ellipse, the GREEN condition exists, wherein all aircraft can be separated by 3 miles regardless of the type of aircraft leading or following.

c. If the condition is RED and the wind is increasing, the requirement exists for the wind vector to be outside the outer ellipse for 8 minutes before the GREEN light is turned on. If the wind vector only reaches the 2-knot buffer zone, the RED condition remains.

d. If the condition is GREEN and the wind starts decreasing and enters the transition or buffer zone, the GREEN light remains on, but the RED light is flashed for each of the 0.5-second intervals during which the wind vector is in the transition zone providing the controller with the indication that a possible change to RED may occur. If, however, the wind vector actually enters the inner ellipse region, a change to the RED condition takes place immediately.

The VAS processor outputs labeled data onto a data bus with the following information for each operating region: $\overline{R}$ to 1 knot, $\overline{\theta}$ to 10 degrees, gust (if applicable) to 1 knot, the vortex condition RED or GREEN for each landing runway, and failure messages.

9.1.1.6 Controller Display - The system interfaces with the air traffic controllers via the VAS Runway Monitor display (Fig. 9-5). The controller selects the operating corridor and designates either an arrival (A) or departure (D) runway. The display thereafter accepts data with the corresponding label from the data bus. As a very important byproduct, the controller display provides in digital form the wind direction, magnitude, and gust in the selected region. This should greatly improve the accuracy of the wind information relayed to the pilots by the controllers since, as indicated previously, a centrally located meteorological sensor does not provide

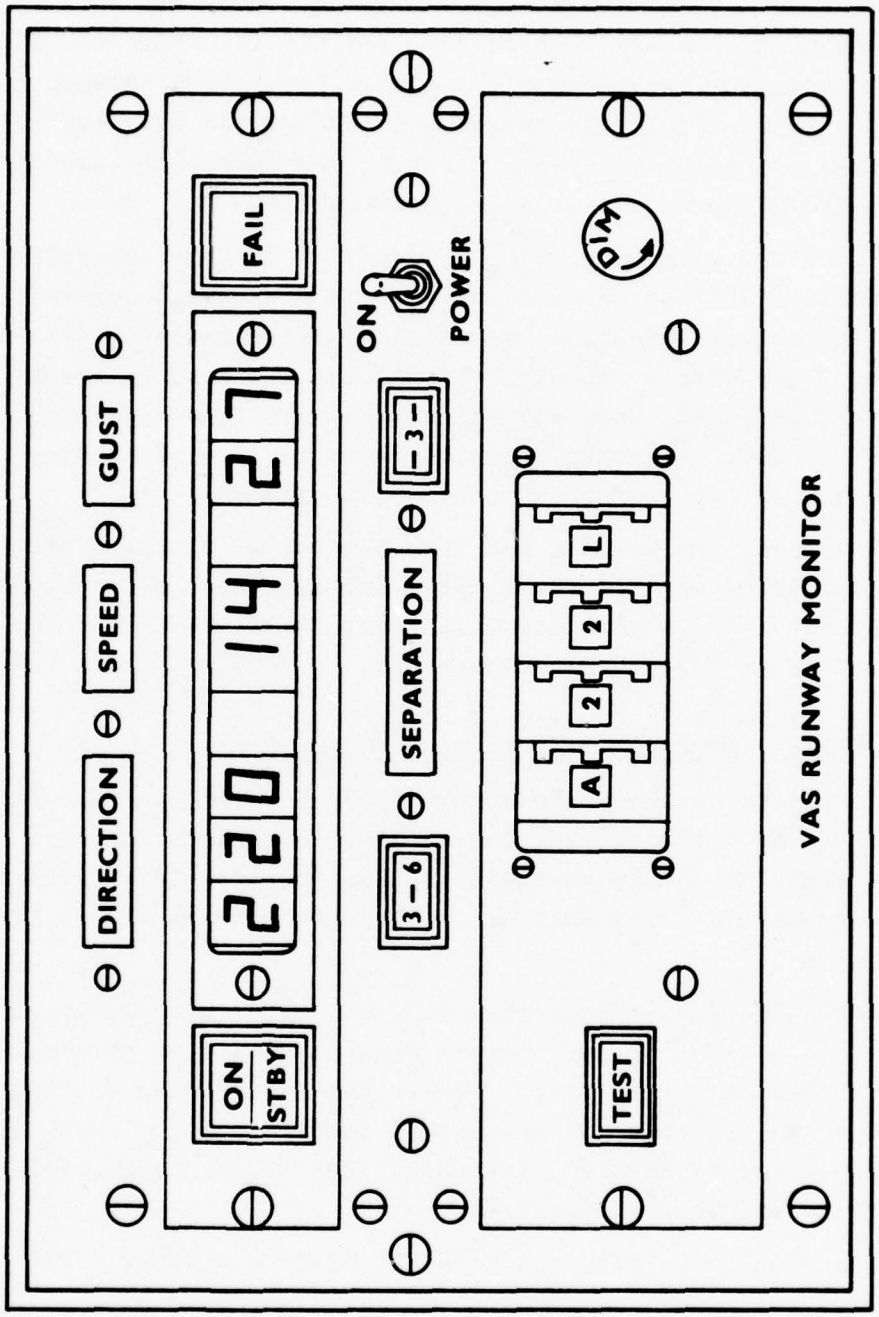


FIGURE 9-5. THE VAS RUNWAY MONITOR DISPLAY.

accurate wind information for widely dispersed points. If arrivals are being handled by the controller, the display indicates if the vortex conditions require a 3/4/5/6-mile separation between aircraft (RED), or if an all 3-mile separation (GREEN) may be used. If departures are being handled, only the wind conditions are displayed, and the RED/GREEN indications are blanked out.

A separate summary display is provided for the supervisor's console (Fig. 9-6) which displays the meteorological conditions across the entire airport as measured by the meteorological tower network. This display should greatly ease the task of runway selection, and also, show any major wind anomalies requiring controller/pilot attention, such as major local wind changes resulting from the passage of a front or thunderstorm.

At O'Hare, one summary and five controller displays are installed in the IFR room, and one summary and four controller displays in the tower cab. A separate display is installed in the equipment room for use in VAS system maintenance.

9.1.2 VAS Performance-monitoring and Evaluation

Evaluation of the performance of the VAS uses an independent monitor of the vortex motion and decay in the operating region. At O'Hare, three GWVSS are deployed for that purpose located on the approaches to the three most active landing runways (14R, 27R, and 32L).

Currently, Gill-type single-axis propeller anemometers are used in the GWVSS, the anemometers arrayed on a line perpendicular to the runway centerline. A 15-meter spacing between anemometers is used up to the lateral coverage of interest. At O'Hare, a 210-meter baseline is used, extending $\pm$105 meters to each side of the extended runway centerline.

Data from each GWVSS are transmitted to the central location in the control-tower equipment room, using a DAS-16 data-acquisition module and an LCS-111 and an LCR-211 data transmission-and-receiving unit. A separate microprocessor is used as a data formatter to collect all VAS and GWVAS data, and to to transmit them to a

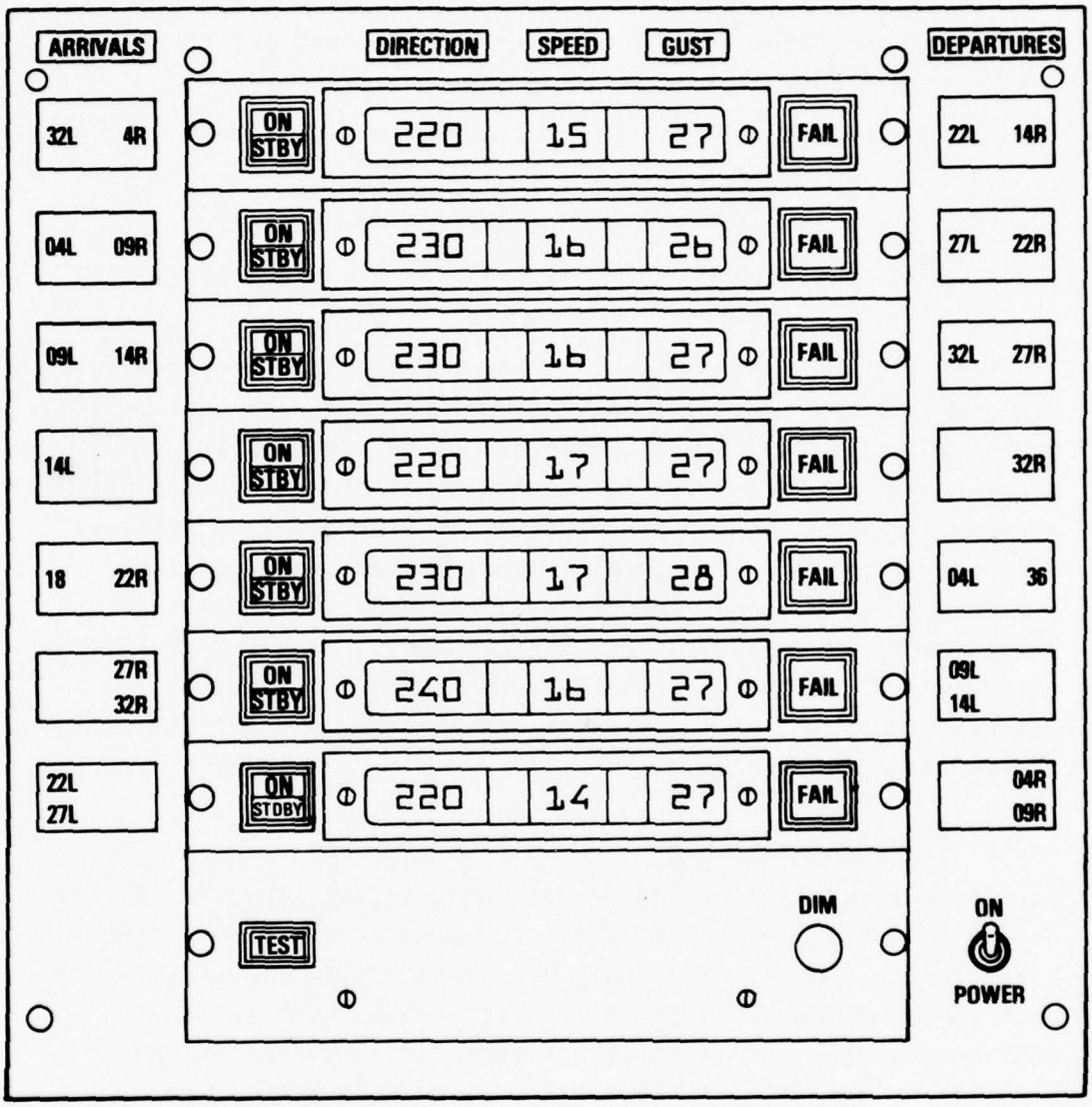


FIGURE 9-6. THE VAS SUPERVISOR DISPLAY.

data-acquisition van containing a minicomputer to format the data and record it on 9-track digital tape. The minicomputer also displays all the transmitted data. The transmitted data consist of:

a. All meteorological data-processor inputs and outputs consisting of the input samples at 2 samples/sec and all outputs to the VAS processor.

b. All VAS processor outputs (all data output onto the data bus to the controller displays).

c. All data collected from the three GWVSS lines.

The digital data tapes containing each day's run are sent daily to TSC for data reduction and analysis.

At TSC, the data are used to check that the microprocessors are operating as intended and that vortices are truly not posing a threat when the VAS display registers GREEN. Statistics are generated on how often RED and GREEN conditions occur, and projections are made on how the capacity of O'Hare could have been affected if the VAS were commissioned. Other quantities like atmospheric turbulence, temperature, and pressure are also being monitored. Studies are being conducted to ascertain if such meterological variables could be used in the VAS algorithm effectively to shrink the size of the ellipse, and thereby, gain a more effective system.

9.1.3 Suitability Tests

Upon completion of the development testing, the VAS will be turned over functionally to NAFEC to perform operational suitability tests on the system. The tests are primarily to evaluate the impact that the VAS will have on ATC personnel, operations, and environment when and if it is incorporated into the National Airspace System (NAS). The tests provide a foundation for changes in the ATC procedures which may be required effectively to integrate the VAS into the NAS. The results of the operational suitability tests along with the results of the development and

performance tests will become the technical foundation for a decision as to if the VAS should be incorporated into the NAS as an operational system.

Effectively to measure the operational suitability, several factors must be evaluated:

a. Practicality of the information provided by the VAS to approach control in an actual ATC environment, including human factors considerations.

b. Potential increase in air-traffic operations for all possible runway and approach scenarios using representative meteorological and traffic-flow conditions.

c. Workload imposed on the ATC system by the operation of the VAS and the effect of changes in the separation standards based on the VAS.

d. Maintenance support required for calibration and operation of the system.

e. Suitability of the VAS to the airport environment.

The operational suitability testing will provide the key answers as to the potential effectiveness and acceptance of the VAS in the NAS.

9.2 VORTEX-WARNING SYSTEM

The vortex-avoidance systems are designed to solve two of the major wake vortex problems; i.e., the reduction in capacity of an airport, and the possibility of the hazardous vortex encounter. In the United States, there are approximately 15 airports which have capacity problems which might be solved through the deployment of the VAS. The remaining airports which have a mix of commercial and general aviation traffic are only affected by the hazard of a following aircraft, particularly general aviation aircraft, encountering the vortex generated by a large aircraft preceding them.

The Vortex Warning System (VWS) is designed to monitor the critical approach region, and to provide the pilot of a landing aircraft with information on corridor status; i.e., is it clear of

vortices. Analysis and simulations of vortex encounters have resulted in the conclusion that a separation of 30 meters between aircraft and a vortex is sufficient to insure the aircraft's safety (see Section 5). Allowing a 15-meter lateral error in aircraft position during a landing resulted in the definition of a 90-meter wide corridor, centered on the extended runway centerline between the runway threshold and the middle marker which must be clear of vortices during an approach.

As shown in the block diagram of the VWS (Fig. 9-7), a vortex sensor is used to monitor the critical approach corridor and is located approximately 600 meters from the runway threshold. The sensor selected will be tailored to the specific site to be instrumented. Specifically, if adequate real estate is available, a GWVSS could be employed because of its low cost. However, if terrain limitations such as a dropoff at the end of the runway or water, etc. prohibit the use of a GWVSS, a point sensor such as the DAVSS or a LDVSS could be utilized.

The vortex sensor detects the vortices generated by each landing aircraft, and tracks their transport in the critical approach region. Vortex-position information is displayed to the following aircraft via lights installed at the landing-runway threshold.

Red and Green lights can be used to provide the approaching pilot with the approach corridor vortex status information. A green light would indicate that the approach corridor is free of the vortices generated by the preceding aircraft. Red light patterns could be used to provide the pilot lead-time information enabling him to make an early decision if to continue his approach. Thus, a "rippling" red light line could indicate a vortex is expected to persist in the corridor for more than 60 seconds; steady red, less than 60. The number of lights might even be used to indicate vortex strength. The information reported to the pilot would be sufficient to allow him to make a timely decision on if to proceed with the approach or to initiate a go-around.

Tests were run to determine the feasibility of using lights as a means to communicate to the pilot the corridor vortex status.

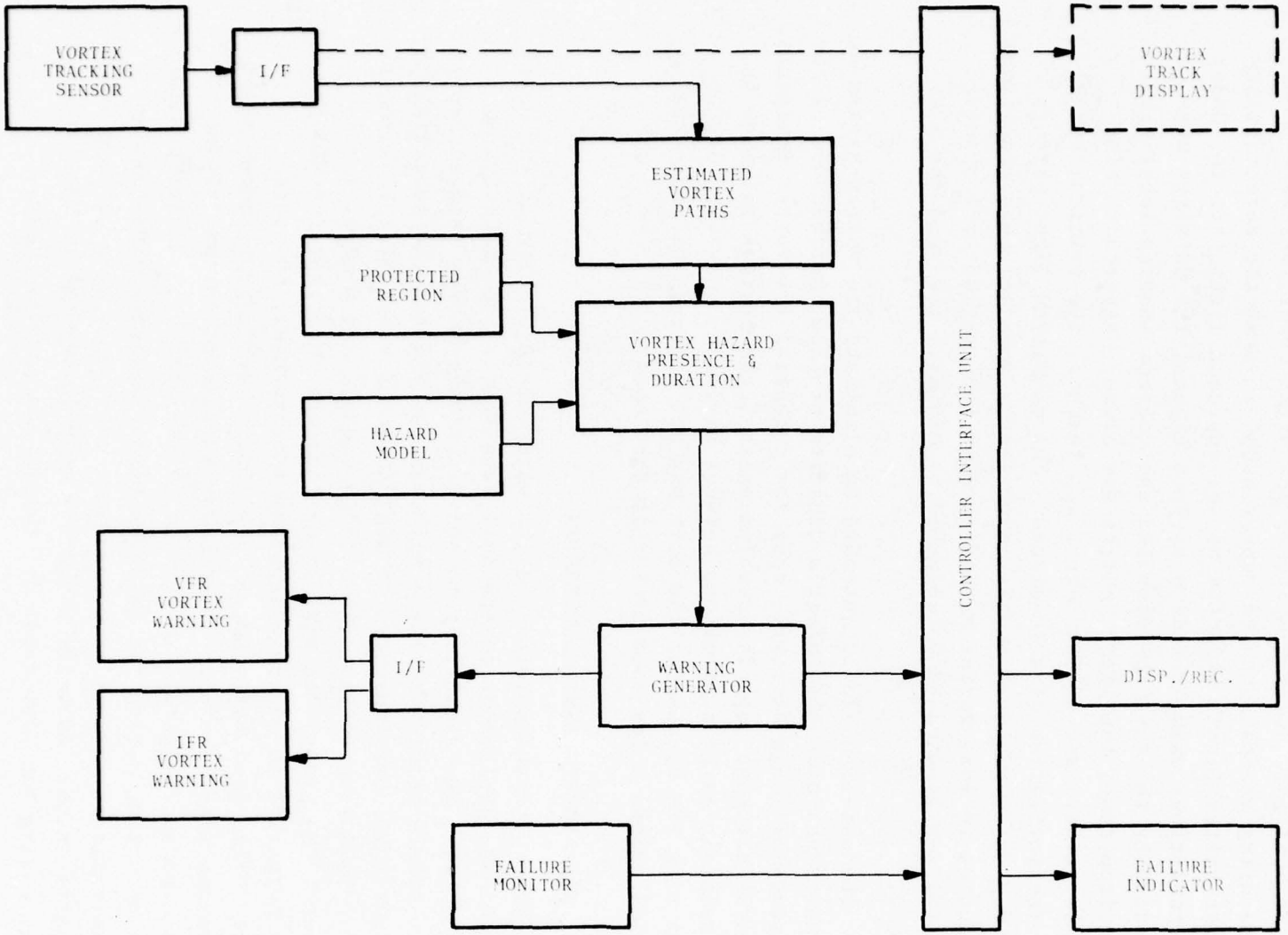


FIGURE 9-7. BLOCK DIAGRAM OF THE VORTEX WARNING SYSTEM.

Bright sunlight, adverse weather, and night conditions were simulated using an instrumented runway model to test the detectability of the vortex lights amid the normal approach light pattern. Under all conditions using standard airport lights, the patterns were detected by the test subjects and the correct meaning identified. Most important, the light pattern was always detected in time before an altitude of 100 meters was reached, the critical height for the initiation of a go-around. The displayed light pattern could also be repeated on the controller's console; when conditions conducive to long vortex persistence in the corridor are observed, the traffic flow could be adjusted to minimize the need for a go-around.

The use of a WVS is intended to eliminate the vortex hazard at airports which do not suffer a capacity problem, but because of the presence of large aircraft, have the potential for vortex incidents. Clearly since no capacity problem exists, the obvious solution is to maintain large separations between aircraft. However, deployment of a WVS because of the cost may not prove to be cost beneficial unless a low-cost sensor is developed.

9.3 WAKE VORTEX AVOIDANCE SYSTEM

The ultimate solution to the wake vortex problem is the development and deployment of the full Wake Vortex Avoidance System (WVAS) with the capability to solve the wake vortex related problems at all major airports. Although the VAS has the potential to increase airport capacity, it will do so only at selected airports and only during certain times (high winds). At O'Hare, for instance, the prevailing wind conditions are such that the VAS has the potential to increase capacity approximately 60 percent of the time. This does not occur at all times. During the summer months when low winds prevail, a reduction in separation can only be achieved approximately 20 percent of the time, the higher percentage occurring during the fall and winter periods. Los Angeles International Airport by comparison, exhibits a wind pattern which results in the VAS being effective only 20 percent of the time, thus making VAS unsuitable for use at Los Angeles.

An examination of the tens of thousands of vortex track histories collected by TSC indicates that 99 percent of the time a 3-mile separation between aircraft of any type could be safely used. The VAS, because of its wind-pattern dependence, is very conservative. Realization of reduced separations greater than 90 percent of the time requires the development and deployment of the WVAS.

A block diagram of the WVAS system is shown in Fig. 9-8. As can be seen, the WVAS incorporates the VAS and the VWS concepts but adds predictive capability to the system to provide adaptive separations, thus maximizing traffic flow for any given conditions. The WVAS must obviously take up the slack between the VAS performance and the demonstrated capability for the air traffic system to operate at reduced separations 99 percent of the time. This can be achieved by the WVAS with the following techniques:

a) Use of a meteorological prediction algorithm with forecasting techniques to predict vortex conditions in the corridor approximately 20 minutes ahead. The predictive algorithm is driven by a network of meteorological sensors deployed about the airport.

b) Use of a vortex behavior predictive model incorporating all pertinent meteorological parameters and aircraft types. The actual vortex tracks measured by the vortex-detection system are then used to update the predictive algorithm.

c) Use of a VWS at each runway approach for fail-safe operation.

d) As opposed to a fixed separation standard, the WVAS outputs an adaptive separation matrix which allows optimum separations and maximizes traffic flow for any set of conditions.

The WVAS thus achieves greater utilization of the available airport capacity by the replacement of fixed conservative separation standards with an adaptive standard permitting maximum traffic flow. This achievement is made possible through the use of accurate predictive algorithms and the fail-safe operations ensured by the presence of a VWS at each runway. Furthermore, the WVAS has a soft-failure mode; in the event of a main system failure,

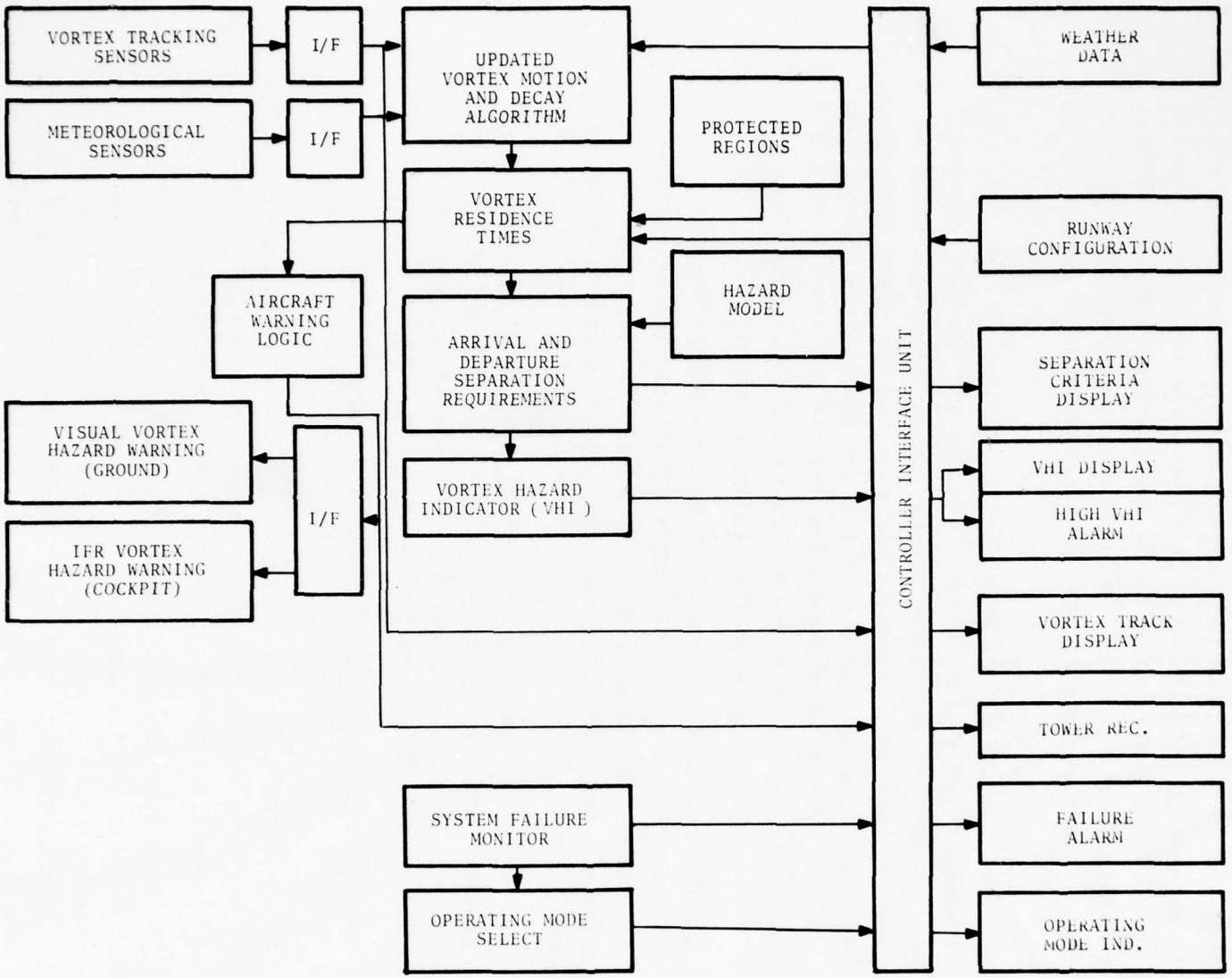


FIGURE 9-8. BLOCK DIAGRAM OF A WAKE VORTEX AVOIDANCE SYSTEM.

it reverts to a VAS and/or VWS operation. The WVAS is thus a highly safe concept for use at an airport for separation control.

The WVAS could allow operations below 3 nautical miles. For instance, the extensive data base shows that a 2 nautical-mile separation could be used 86 percent of the time. Obviously, the adaptive separations output by the WVAS will be continuously changed depending on traffic demand and meteorological conditions. It is fairly certain that a controller will not be capable of using these separations for the maximum efficiency of the system. This is borne out by the fact that most controllers do not utilize the present 3/4/5/6 separation standards, but instead use a 3/6 or an all 5 nautical-mile separation. Multiple separations cannot be adhered to by controllers at the major airports, particularly during high-traffic conditions.

The WVAS will, therefore, be used to its fullest capacity with the introduction of the metering-and-sequencing (M&S) algorithm into the ARTS-III system. The WVAS separation-requirements output would then go directly to the M&S system. Its operation would then be transparent to the controller, who would only assume direct control in case of an ARTS system failure. The WVAS would in that event fall back to a simple separation standard.

It must be emphasized that the introduction of the WVAS by itself will not solve the capacity problem of an airport. At O'Hare, for instance, operations at 2 nautical-mile separation for even a short time would quickly saturate the gate capacity of the terminal. However, the introduction of the full WVAS, the VAS, or the VWS will definitely remove the impediment wake vortices placed on the operation and efficiency of the air traffic system.

10. ON-GOING ACTIVITIES

The previous sections have reviewed wake vortex research-and-development programs conducted by the FAA and NASA. Although many questions have been answered and much has been learned about the phenomenon of wake vortices, considerable work is still underway. In this section, several of the current activities are discussed in terms of their objectives and schedules.

10.1 JOINT DOT/NASA FLIGHT TEST

The behavior of aircraft wake vortices has been studied in numerous ways: Wind tunnels and water channels have been used to simulate flight in the atmosphere, and various detection techniques (photographic, hot-wire anemometers, laser velocimeters, etc.) have been used to quantify vortex properties. The smoke-marked vortices of light general aviation aircraft have been photographed. Extensive airport tests involving vortex-tracking equipment have been, and are being, conducted to learn how vortices move and decay under various meteorological conditions. Aircraft have been deliberately flown into the wakes of other aircraft to study the ensuing response as a function of aircraft spacings. Each of the methods for studying wakes has yielded important information about the nature and life-cycle of vortices. A controlled flight test combining the essentials of each of the methods was deemed an important step to the unification of the plethora of sometimes conflicting data.

Four major objectives were set for the flight test: a study of vortex-alleviation techniques in ground effect, a study of vortex bursting, an investigation of full-scale experimental techniques, and the characterization of the B-747 wake.

10.1.1 Test Description

On 2 and 3 December 1975, a Boeing 747 aircraft flew 54 passes at low level over an array of ground-based sensors on the lakebed of Rosamond Dry Lake on Edwards Air Force Base, California. The

vortices of the B-747 were marked by Corvis oil smoke generators at eight spanwise locations on the wings to enable detailed visual analysis of the behavior of the flow field in various aircraft operational configurations.

The test was flown in six sorties, each of which consisted of eight runs (except for the third sortie, which had to be truncated because of aircraft hydraulic problems). The intervals between the sorties were used for meteorological measurements and for equipment adjustments.

Aircraft configuration varied from run to run, with dominant emphasis on as close to a normal landing configuration as operating conditions would allow. The clean configuration was also studied, and special flap and spoiler configurations were investgated for vortex-alleviation effectiveness. The Boeing 747 flew at 30 to 250 meters above the ground level. Runs were made in level flight as well as in descending and climbing flight. Descents were at about 250 m/min. A lift coefficient of about 1.4 was used for all flaps-down runs.

Of the 54 runs, 35 (or about 65 percent) were made with the inboard flaps lowered 30 degrees and the outboard flaps lowered 30 degrees (denoted 30/30); eight (approximately 15 percent) with 10/10 flaps and 5 (approximately 9 percent) with flaps retracted. The remaining six runs had the inboard flaps lowered 30 degrees and the outboard flaps lowered 1 degree, to test the effects of this configuration on vortex alleviation. For each flap-setting, runs were conducted with the gear down or retracted, and some had spoilers deployed (the extension angle was always 41 degrees) in addition to the flap.

Five types of instrumentation were used to record vortex behavior and to monitor the atmospheric conditions prevailing at the test site. Vortex-induced velocities were measured by a laser Doppler velocimeter (LDVSS), an array of monostatic acoustic sounders (MAVSS), and an array of propeller anemometers (GWVSS). Qualitative details of the visual behavior of the smoke-marked vortices were recorded photographically by an assortment of

motion-picture and still cameras on the ground and overhead in a helicopter. The atmospheric winds, turbulence, and stability were monitored by various sensors on the ground, suspended from a tethered balloon, and carried in a light aircraft.

10.1.2 Qualitative Summary of Results

Motion pictures and still photographs were made of the vortex motion and behavior over the array as long as the smoke trail was visible - typically 30 to 90 seconds. In 17 of the 54 filmed sequences, vortex breakdowns were observed during this period, and one of the cases showed sinuous linking of the vortex with its below-ground image. The remaining vortices maintained their columnar identity for the duration of the film. The distribution of the breakdown among the various configurations was practically in the same proportion as the number of runs in a particular configuration to the total number of runs, indicating that breakdowns were not preferential to any particular flap-setting. The time to breakdown, however, seems to be roughly correlated to the atmospheric turbulence, decreasing as turbulence increases. No trends for increase or decrease of vortex breakdown time were observed for the lowering or raising of the gear since the data are few and the scatter in the breakdown time is large. Two cases of spoiler deployment indicate an increase in time to breakdown over non-deployment, but this is probably not statistically significant.

For a number of cases, balloons were deployed and captured by the core. The flow in the cores, as illuminated by the balloon motion was generally jet-like -- i.e., away from the aircraft. This is consistent with the analysis of Brown (ref. 23) which shows that the wake flow should be jet-like initially if the aircraft configuration is such that $C_{Di}/C_{Do} > 0.5\pi^2$, where C_{Di} is the induced drag coefficient and C_{Do} is the profile drag coefficient.

The following observations or trends were noted:

a) The roll-up of the vortex sheet occurred rapidly within a few spans downstream of the aircraft.

b) The observed location, spacing, and strength of the multiple vortices were in general agreement with modified Betz roll-up calculations.

c) The peak tangential velocity and circulation of the merged vortices remained nearly constant in the near wake.

d) A decrease in the peak tangential velocity and circulation and an increase in the core radius were observed in the far wake.

e) Deployment of spoilers and flaps enhanced the vortex peak tangential velocity-decay process in the near wake while aircraft altitude, glideslope, and landing-gear deployment had little effect.

f) After the Corvis oil smoke had dissipated, there often remained a coherent rotary flow in the vortex.

g) After a vortex burst, a remnant vortex was often left behind.

h) There appeared to be no axial flow in the B-747 landing vortex when the aircraft was in level flight; jet-like flow when in descending flight.

i) The B-747 spoilers affected the vortices, producing vortices with large cores.

j) Vortices from the B-747 in takeoff configuration produced strong axial flows.

The data are still being analyzed. A report detailing the final results will be available in the summer of 1977.

10.2 ALLEVIATION WORK BY NASA

The deployment of spoilers on the B-747 produced significant vortex allievation when probed at altitude (see Section 4.2.6). However, the use of the spoilers is accompanied by some operational problems such as buffeting and noise. To reduce the buffeting, NASA considered perforating the spoilers; tests in a water channel indicated that holes placed in the spoilers significantly reduced the effectiveness of the spoilers in alleviating the vortex problem.

The usual flight-power settings and angle of attack must be altered to accommodate the extension of spoilers. The acceptability of these changes, particularly with respect to reconfiguring the aircraft for a missed approach at minimum altitude, and the increased noise level caused by the required increase in power, have yet to be evaluated.

Subsequent to the B-747 tests at Rosamond, wind-tunnel tests have been conducted on L-1011 and DC-10 configurations. Both aircraft indicated a requirement for different spoiler arrangements for alleviation than those used on the B-747. The difference in wing planform and engine placement suggest the reason for the changes. The concept of alleviation through spoiler deflection has shown indications that it may be effective until the vortex gets into ground effect. There are still many unanswered questions, including the cost benefit of implementing such alleviation techniques on the current air carrier fleet or considering alleviation techniques only for new aircraft design. The concept of alleviation is still in need of further testing to answer the existing questions and to demonstrate its validity for the current aircraft fleet in the total approach environment. Cost-benefit studies are being considered to determine the viability of operationally considering alleviation and detailed test planning is in process relative to testing the spoiler alleviation technique on the L-1011 and DC-10 aircraft.

10.3 WAKE VORTEX PREDICTIVE MODEL

The heart of any active vortex-avoidance system is a vortex-predictive model. Based on measured meteorological conditions and on certain aircraft parameters, the model should predict the motion and decay of vortices for the next 15 to 30 minutes (the time required to set up or alter aircraft spacings in the terminal environment without waveoffs or other interruptions in the smooth flow of traffic). If vortex conditions can be adequately predicted, then the possibility of using tailored spacings or even spacing of less than 3 nautical-miles may be considered. Such a system would

only be viable in the NAS if the system is combined with Metering and Spacing, and if capacity cannot be met by the VAS (see Section 9.1) now undergoing tests at Chicago O'Hare.

A predictive model has been defined (Section 3) and includes various fluid dynamic and meteorological mechanisms. Presently, measured vortex tracks obtained from various test sites (Section 7) are being compared with the corresponding predicted tracks to isolate the dominant mechanisms and to determine empirically the relevant numerical coefficients for each process.

10.3.1 Three Baseline Data

Three GWVSS are in operation at the JFK Airport. The system simultaneously monitors the motion of vortices in the approach corridor (see Fig. 7-1) to ascertain how vortices behave at three locations (near the runway threshold, approximately 600 meters from the threshold, and approximately 1200 meters from the threshold). Vortices are not straight; sinusoidal motions termed snaking occurs, such that a vortex could still be within the safety region (Section 8.1.1) at one of the baseline locations and outside at the other two. Before a WVAS system with a GWVSS or any other system using vortex sensors can be deployed, it must be verified that indeed a single baseline judiciously located is adequate to monitor vortex location as a function of time. The data collection using the three lines of JFK will be terminated in December of 1976 and the final analysis completed by the summer of 1977.

10.3.2 Extended Baselines

To increase capacity within the current airport system, one effort underway may provide significant benefits. The use of simultaneous operations on closely spaced parallel runways could provide increased operations. Tests are underway at JFK to determine how far vortices travel relative to a parallel runway. Extended ground wind lines to 1000 meters perpendicular to the runway centerline are being used to determine if parallel runways placed as close as 800 meters are safe vortex-wise for dual operations.

This data-collection effort will also be completed in December of 1976 with the final analytical conclusions completed by the fall of 1977.

10.4 RECATEGORIZATION OF AIRCRAFT

If the stretched versions of the DC-8 and B-707 aircraft now designated as heavies could be downgraded to the same category as the normal versions of these aircraft, considerable capacity gains can be attained at most large airports. A data system has been implemented at Chicago O'Hare using MAVSS to measure vortex-flow fields, and hence, allow the determination of vortex strength. A statistically significant sample of vortex-strength data from B-707 and DC-8 aircraft will be collected along with the landing weights of the same aircraft and detailed analysis performed to determine if the aircraft reporting "heavy" have vortices significantly different in strength from those same type of aircraft falling in the "light" category. As an example, the B-707 and DC-8 aircraft leaving Europe as "heavies," land in the United States with an actual landing weight less than many of the smaller B-707 and DC-8 aircraft on domestic flights landing at the same airport. It is planned that adequate data be obtained by March of 1977 and the analyses completed by the fall of 1977.

10.5 TAKEOFF TESTS AT TORONTO

In a joint program with the Canadian Ministry of Transport, DOT/TSC is collecting data on the vortices shed by aircraft departing the Toronto International Airport via runway 23L. Section 7.5 describes the test site and the location of the various sensors. Data collection began in August 1976 and is scheduled to continue for a period of six months.

Since the implementation of the rule governing intersection takeoffs in 1969, no accidents have been attributed to vortices formed by aircraft departing an airport. However, concern has surfaced about the possibility of a vortex encounter. Also, if systems such as the VAS are successful in increasing the capacity

of an airport for landing operations, can the identical VAS logic be used to permit more departure operations per hour? The trials and preliminary analyses have begun, but it is too premature to indicate any trends in the data.

10.6 VORTEX ADVISORY SYSTEM AT O'HARE

The major effort underway at this time relative to the vortex program is the collection of data and the evaluation of the VAS at Chicago O'Hare. The VAS in the first vortex system to be developed and installed for operational suitability testing. In parallel with the actual detailed vortex data and system performance comparisons, evaluations are being performed on controller work load, capacity effects, VFR and IFR implications, and possible maintenance and reliability considerations. The operational suitability testing is to be completed by June of 1977, such that a recommendation can be made to the FAA as to one of three options:

a) Implement the VAS as configured.

b) Implement the VAS with an expanded wind algorithm with attendant slight decreases in capacity gains.

c) Implement the VAS with the current algorithm and implement a backup safety system utilizing vortex sensors to warn of the presence of a vortex.

Early indications are that the current system will give the capacity gains needed. Cost-benefit analyses show extremely high benefit-to-cost ratios for implementation of the VAS at about 15 of the major United States air terminals. If the recommendation in June of 1977 is made to implement the VAS, the major vortex research and development effort will be complete. A system will have been demonstrated which solves the vortex problem relative to capacity as forecasted into the late 1980's, and will then enable the full use of the planned elements of the upgraded third generation ATC system.

11. REFERENCES

1. Israel, D.R., "Air Traffic Control: Upgrading the Third Generation," Technology Review, Vol. 77, No. 3, Jan. 1975, p. 14-24.

2. Gupta, V.P., "Vortex-Related Accidents Over the Ten Year Period 1964-1973," FAA-EM-75-6, April 1975, Mitre Corp., McLean, VA.

3. Prandtl, L., Essentials of Fluid Mechanics, Blackie & Sons Ltd., London, Third Edition, 1967.

4. Donaldson, C. duP. and Bilanin, A.J., "Vortex Wakes of Conventional Aircraft," AGARDograph No. 204, May 1975, Aero. Research Assoc. of Princeton, Princeton, NJ.

5. Westwater, F.L., "Rolling Up of the Surface of Discontinuity Behind an Aerofoil of Finite Span," R&M 1692, Aug. 1935, Aero. Research Council, Great Britain.

6. Takami, H., "A Numerical Experiment with Discrete Vortex Approximation with Reference to the Rolling Up of a Vortex Sheet," Report No. 202, 1964, Stanford University, CA.

7. Hackett, J.E. and Evans, M.R., "Vortex Wakes Behind High Lift Wings," J. Aircraft, Vol. 8, No. 5, May 1971, p. 334-340.

8. Chorin, A.J. and Bernard, P.S., "Discretization of a Vortex Sheet with an Example of Roll-Up," J. Comp. Physics, Vol. 13, 1973, p. 423-429.

9. Moore, D.W., "A Numerical Study of the Roll-Up of a Finite Vortex Sheet," J. Fluid Mech., Vol. 63, Part 2, April 1974, p. 225-235.

10. Bloom, A.M. and Jen, H., "Roll-Up of Aircraft Trailing Vortices Using Artificial Viscosity," J. Aircraft, Vol. 11, No. 11, Nov. 1974, p. 714-716.

11. Rossow, V.J., "Theoretical Study of Lift-Generated Vortex Sheets Designed to Avoid Roll-Up," AIAA J., Vol. 13, No. 4, April 1975, p. 476-484.

12. Kaden, H., "Augwicklung einer un-stabilen Unstetigkeitsflache," Ingenieur Archiv., Bd. II, 1931, p. 140-168.

13. Durand, W.F. (editor), Aerodynamic Theory, Vol. II, Div. E, Durand Reprinting Committee, California, 1943, p. 328-330.

14. Betz, A., "Behavior of Vortex Systems," Zeit. für angewandt Math. and Mech., Vol. 12, No. 3, June 1932, p. 164-174.

15. Howard, L.N., "Divergence Formulas Involving Vorticity," Arch. Rational Mech. Anal., Vol. 1, No. 1, 1957, p. 113-123.

16. Donaldson, C. duP., Snedeker, R.S., and Sullivan, R.D., "A Method of Calculating Aircraft Wake Velocity Profiles and Comparison with Full-Scale Experimental Measurements," J. Aircraft, Vol. 11, No. 9, Sept. 1974, p. 547-555.

17. Rossow, V., "On the Inviscid Rolled-Up Structure of Lift-Generated Vortices," J. Aircraft, Vol. 10, No. 11, Nov. 1973, p. 647-650.

18. Jordon, P., "Structure of Betz Vortex Cores," J. Aircraft, Vol. 10, No. 11, Nov. 1973, p. 691-693.

19. Verstynen, H.A., Jr. and Dunham, R.E., Jr., "A Flight Investigation of the Trailing Vortices Generated by a Jumbo Jet Transport," NASA TN D-7172, April 1973, NASA Langley Research Center, VA.

20. Snedeker, R.S. and Bilanin, A.J., "Analysis of the Vortex Wakes of the Boeing 727, Lockheed L-1011, McDonnell-Douglas DC-10 and Boeing 747 Aircraft," ARAP Report No. 245, July 1975, Aero. Research Assoc. of Princeton, Princeton, NJ.

21. Owen, P.R., "The Decay of a Turbulent Trailing Vortex," Aero. Quarterly, Vol. 21, Feb. 1970, p. 69-78.

22. Ciffone, D.L. and Orloff, K.L., "Far-Field Wake Vortex Characteristics of Wings," J. Aircraft, Vol. 12, No. 5, May 1975, p. 464-470.

23. Brown, C.E., "Aerodynamics of Wake Vortices," AIAA J., Vol. 11, No. 4, April 1973, p. 531-536.

24. Kuhn, G.D. and Nielsen, J.N., "Analytical Studies of Aircraft Trailing Vortices," AIAA Paper No. 72-42, San Diego, CA, 1972.

25. Hoffman, E.R. and Joubert, P.N., "Turbulent Line Vortices," J. Fluid Mech., Vol. 16, Part 3, July 1963, p. 391-411.

26. Marchman, J. F. and Marshall, J.R., "Vortex Age as a Wake Turbulence Scaling Parameter," AIAA Paper No. 74-36, Washington, DC, 1974.

27. Garodz, L.J., "Measurements of the Vortex Wake Characteristics of the Boeing 747, Lockheed C-5A and Other Aircraft," Data Report, Project 177-621-03X (Special Task No. 1), April 1970, NAFEC, Atlantic City, NJ.

28. Condit, P.M. and Tracy, P.W., "Results of the Boeing Wake Turbulence Test Program," In: Aircraft Wake Turbulence and Its Detection, 1st ed., Plenum Press, New York, 1971, p. 473-508.

29. Andrew, W.H., Robinson, G.H., Krier, G.E., and Drinkwater, F.J., "Flight Test Evaluation of the Wing Vortex Wake Generated by Large Jet Transport Aircraft," FWP-18, NASA Flight Research Center, Edwards, CA, 1970.

30. Spreiter, J.R. and Sacks, A.H., "The Rolling Up of the Trailing Vortex Sheet and Its Effect on the Downwash Behind Wings," J. Aerospace Sciences, Vol. 18, No. 1, Jan. 1951, p. 21-32.

31. Eisenhuth, J.J., McCormick, B.W., Nelson, R.C., and Garodz, L.J., "Analysis of Experimental Measurements of Trailing Vortex Systems of Large Jet Transport Aircraft," Proceedings of the National Aerospace Electronics Conf., IEEE, 1971, p. 28-35.

32. Garodz, L.J., Lawrence, D.M., and Miller, N.J., "The Measurement of the Boeing 747 Trailing Vortex System Using the Tower Fly-By Techniques," FAA-RD-73-156, June 1974, NAFEC, Atlantic City, NJ.

33. Garodz, L.J., Miller, N.J., and Lawrence, D.M., "The Measurement of the Boeing 707 Trailing Vortex System Using the Tower Fly-By Technique," FAA-RD-75-15, Feb. 1975, NAFEC, Atlantic City, NJ.

34. Garodz, L.J., "Investigation of the Relatively Long Time-History Vortex Characteristics of the CV880 Airplane in Terminal Area-Type Flight Operations," Data Report, Project 504-303-03X (Special Task No. 3), Nov. 1970, NAFEC, Atlantic City, N.J.

35. Garodz, L.J., "Abbreviated Full-Scale Flight Test Investigation of the Lockheed L-1011 Trailing Vortex System Using Tower Fly-By Technique," FAA-AFS-1-76-2, May 1976, NAFEC, Atlantic City, NJ.

36. Garodz, L.J., Lawrence, D.M., and Miller, N.J. "The Measurement of the Boeing 727 Trailing Vortex System Using the Tower Fly-By Technique," FAA-RD-74-90, Aug. 1974, NAFEC, Atlantic City, NJ.

37. Garodz, L.J., Lawrence, D.M., and Miller, N.J., "The Measurement of the McDonnell-Douglas DC-9 Trailing Vortex System Using the Tower Fly-By Technique," FAA-RD-74-173, Nov. 1974, NAFEC, Atlantic City, NJ.

38. Garodz, L.J., Lawrence, D.M., and Miller, N.J., "The Measurement of the DC-7 Trailing Vortex System Using the Tower Fly-By Technique," FAA-RD-73-141, Nov. 1973, NAFEC, Atlantic City, NJ.

39. Yates, J.E., "Calculation of Initial Vortex Roll-Up in Aircraft Wakes," J. Aircraft, Vol. 11, No. 7, July 1974, p. 397-400.

40. Maxworthy, T., "The Motion of Aircraft Trailing Vortices," Paper 75-APMW-58, Am. Soc. Mech. Engineers, Appl. Mech. Western Conf., Honolulu, HI, March 1975.

41. Zalay, A.D., White, R.P., and Balcerak, J.C., "Investigation of Viscous Line Vortices With and Without the Injection of Core Turbulence," RASA Report 74-01, Feb. 1974, Rochester Appl. Sci. Assoc., Rochester, NY.

42. Tombach, I.H., "Observations of Atmospheric Effects of Vortex Wake Behavior," J. Aircraft, Vol. 10, No. 11, Nov. 1973, p. 641-647.

43. Tombach, I.H., Bate, E.R., and MacCready, P.B., "Investigation of the Motion and Decay of the Vortex Wake of a Light Twin-Engine Aircraft," AV-FR-439, Oct. 1974, AeroVironment, Pasadena, CA.

44. Burnham, D.C., "Effect of Ground Wind Shear on Aircraft Trailing Vortices," AIAA J., Vol. 10, No. 8, Aug 1972, p. 1114-1115.

45. Brashears, M.R., Logan, N.A., and Hallock, J.N., "The Effect of Wind Shear and Ground Plane on Aircraft Wake Vortices," J. Aircraft, Vol. 12, No. 10, Oct. 1975, p. 830-833.

46. Tombach, I.H., "Influence of Meteorological Factors on the Vortex Wake of a Light, Twin-Engine Aircraft," AV FR-416, March 1974, AeroVironment, Pasadena, CA.

47. Lissaman, P.B.S., Crow, S.C., MacCready, P.B., Tombach, I.H., and Bate, E.R., "Aircraft Vortex Wake Descent and Decay Under Real Atmospheric Effects," FAA-RD-73-120, Oct. 1973, AeroVironment, Pasadena, CA.

48. Brashears, M.R. and Hallock, J.N., "Aircraft Wake Vortex Predictive Model," J. Aircraft, Vol. 11, No. 5, May 1974, p. 265-272.

49. Brashears, M.R. and Hallock, J.N., "Predictive Motion of Wake Vortices," Proceedings of Inst. of Elect. Engineers International Conf. on the Future of Aircraft All-Weather Operations, London, England, Nov. 1976.

50. Brashears, M.R. and Hallock, J.N., "Analysis of Predicted Aircraft Wake Vortex Transport and Comparison with Experiment," Vol. 12, No. 7, July 1975, p. 619-620.

51. Tombach, I.H., Crow, S.C., and Bate, E.R., "Investigation of Vortex Wake Stability Near the Ground," AFOSR-TR-75-1501, July 1975, AeroVironment, Pasadena, CA.

52. Sarpkaya, T., "On Stationary and Travelling Vortex Breakdowns," J. Fluid Mech., Vol. 45, No. 3, Feb. 1971, p. 545-559.

53. Tombach, I.H., "Transport and Stability of a Vortex Wake," MRI-72-FR-1010, April 1972, Meteorology Research Inc., Altadena, CA.

54. Hall, M.G., "The Structure of Concentrated Vortex Cores," In: Progress in the Aeronautical Sciences, Vol. VII, edited by D. Kucheman, Pergamon Press, 1966, p. 53-110.

55. Bossel, H.H., "Inviscid and Viscous Models of the Vortex Breakdown Phenomenon," Ph.D. Thesis, Report No. A.S. 67-14, Aug. 1967, Univ. California, Berkeley, CA.

56. Benjamin, T.B., "Theory of the Vortex Breakdown Phenomenon," J. Fluid Mech., Vol. 14, June 1962, p. 38-44.

57. Crow, S.C., "Stability Theory For a Pair of Trailing Vortices," AIAA J., Vol. 8, No. 12, Dec. 1970, p. 2172-2179.

58. Mager, A., "Dissipation and Breakdown of a Wing-Tip Vortex," J. Fluid Mech., Vol. 55, Part 4, Oct. 1972, p. 609-628.

59. Crow, S.C. and Bate, E.R., "Lifespan of Trailing Vortices in a Turbulent Atmosphere," J. Aircraft, Vol. 13, No. 7, July 1976, p. 476-482.

60. McGowan, W.A., "Aircraft Wake Turbulence Avoidance," Twelfth Anglo-American Aero. Conf., Paper 72/6, Calgary, Canada, July 1971.

61. Rossow, V.J., "Inviscid Modeling of Aircraft Trailing Vortices," In: NASA Symposium on Wake Vortex Minimization, NASA SP-409, Washington, DC, 1976.

62. Rossow, V.J., Corsiglia, V.R., Schwind, R.G., Frick, J.K.D., and Lemmer, O.J., "Velocity and Rolling Moment Measurements in the Wake of a Swept Wing Model in the 40- by 80-Foot Wind Tunnel," NASA TM-X-62414, April 1975, Ames Research Center, Moffett Field, CA.

63. Jones, R.T. and Cohen, D., "Aerodynamics of Wings at High Speeds," In: Aerodynamic Components of Aircraft at High Speeds, Vol. VII, edited by A.F. Donovan and H.R. Lawrence, Princeton Univ. Press, 1957.

64. Hough, G., "Remarks on Vortex-Lattice Methods," AIAA J., Vol. 10, No. 5, May 1973, p. 314-317.

65. Maskew, B., "Numerical Lifting Surface Methods for Calculating the Potential Flow about Wings and Wing-Bodies of Arbitrary Geometry," Ph.D. Thesis, Loughborough Univ. of Tech., Oct. 1972.

66. Stickle, J.W. and Kelly, M.W., "Ground-Based Facilities for Evaluating Vortex Minimization Concepts," In: NASA Symposium of Wake Vortex Minimization, NASA SP-409, Washington, DC, 1976.

67. Corsiglia, V.R., Rossow, V.J., and Ciffone, D.L., "Experimental Study of the Effect of Span Loading on Aircraft Wakes," NASA TM-X-62431, April 1975, Ames Research Center, Moffett Field, CA.

68. Smith, H., "A Flight Test Investigation of the Rolling Moments Induced on a T-37B Airplane in the Wake of a B-747 Airplane," NASA TM-X-56031, April 1975, Flight Research Center, Edwards, CA.

69. Schutz, C.M., "Flight in Jet Transport Wakes by C-141, CV-880, and C-135 Aircraft and Measurements in Convair 880 Wake by NAE (Canada) and NASA Turbulence Research T-33 Aircraft," Data Report, Feb. 1968, NAFEC, Atlantic City, NJ.

70. Barber, M.R., Kurkowski, R.L., Garodz, L.J., Robinson, G.H., Smith, H.J., Jacobsen, R.A., Stinnett, G.W., McMurtry, T.C., Tymczyszyn, J.J., Devereaux, R.L., and Bolster, A.J., "Flight Test Investigation of the Vortex Wake Characteristics Behind a Boeing 727 During Two-Segment and Normal ILS Approaches," NASA TM-X-62398 and FAA-NA-75-151, Jan. 1975, Edwards, CA.

71. Barber, M.R., Hastings, E.C., Champine, R.A., and Tymczyszyn, J.J., "Vortex Attenuation Flight Experiments," In: NASA Symposium on Wake Vortex Minimization, NASA SP-409, Washington, DC, 1976.

72. Rossow, V.J., "Theoretical Study of Lift-Generated Vortex Wakes Designed to Avoid Roll Up," AIAA J., Vol. 13, No. 4, April 1975, p. 476-484.

73. Corsiglia, V.R., Jacobsen, R.A., and Chigier, N., "An Experimental Investigation of Trailing Vortices Behind a Wing with a Vortex Dissipator," In: Aircraft Wake Turbulence and Its Detection, 1st edition, Plenum Press, New York, 1971, p. 229-242.

74. Croom, D.R., "Low-Speed Wind-Tunnel Investigation of Various Segments of Flight Spoilers as Trailing-Vortex Alleviation Devices on a Transport Aircraft Model," NASA TN-D-8162, 1976, Langley Research Center, Langley, VA.

75. Bernstein, S. and Iversen, J.D., "Dynamic Simulation of an Aircraft Under the Effect of Vortex Wake Turbulence," In: Proceedings of 2nd Atmospheric Flight Mech. Conf., NASA Ames Research Center, Sept. 1972, p. 29.1-29.9.

76. Harland, R.B. and Madden, S.J., "A Hazard Definition for Wake Turbulence Encounter During Terminal Area Operations," MSL-RE-81, March 1973, M.I.T., Cambridge, MA.

77. Johnson, W.A., Teper, G.L., and Rediess, H.A., "Study of Control System Effectiveness in Alleviating Vortex Wake Upsets," J. Aircraft, Vol. 11, No. 3, March 1974, p. 148-154.

78. Nelson, R.C., "The Response of Aircraft Encountering Aircraft Wake Turbulence," AFFDL-TR-74-29, June 1974, Air Force Flight Dynamics Lab., Wright-Patterson Air Force Base, OH.

79. Jenkins, M.W.M. and Hackett, J.E., "A Pilot-in-the-Loop, Visual Simulation of Trailing Vortex Encounters at Low Speed," AIAA Paper 75-104, Pasadena, CA, 1975.

80. Barrows, T.M., "Simplified Methods of Predicting Aircraft Rolling Moments due to Wake Vortex Encounters," AIAA Paper 76-61, Washington, DC, 1976.

81. Heaslet, M.A. and Spreiter, J.R., "Reciprocity Relations in Aeronautics," NACA Report No. 1119, 1953.

82. Eggleston, J.M. and Diederich, F.W., "Theoretical Calculation of the Power Spectra of the Rolling and Yawing Moments on a Wing in Random Turbulence," NACA Report No. 1321, 1957.

83. Sammonds, R.I. and Stinnett, G.W., "Hazard Criteria for Wake Vortex Encounters," NASA TM-X-62473, Aug. 1975, Ames Research Center, Moffett Field, CA.

84. Brown, C.E., "Pressure Field of a Vortex Wake in Ground Effect," J. Aircraft, Vol. 12, No. 2, Feb. 1975, p. 120-121.

85. Hallock, J.N. and Wood, W.D., "Joint US/UK Vortex Tracking Program at Heathrow International Airport," Vol. I, FAA-RD-76-58I, March 1976, DOT/Transportation Systems Center, Cambridge, MA.

86. Burnham, D.C., Hallock, J., Kodis, R., and Sullivan, T., "Vortex Sensing Tests at NAFEC," DOT-TSC-FAA-72-2, Jan. 1972, DOT/Transportation Systems Center, Cambridge, MA.

87. Hallock, J.N., "Pressure Measurements of Wake Vortices Near the Ground," J. Aircraft, Vol. 9, No. 4, April 1972, p. 311-312.

88. Sullivan, T., Burnham, D., and Kodis, R., "Vortex Sensing Tests at Logan and Kennedy Airports," FAA-RD-72-141, Dec. 1972, DOT/Transportation Systems Center, Cambridge, MA.

89. Harris, C.M., "Absorption of Sound in Air versus Humidity and Temperature," J. Acoustical Soc. Am., Vol. 40, No. 1, July 1966, p. 148-159.

90. Little, C.G., "Acoustic Methods for Remote Probing of the Lower Atmosphere," Proc. IEEE, Vol. 57, No. 4, April 1969, p. 571-578.

91. Balser, M., Nagy, A.E., and Proudian, A.P., "Vortex Observations by the Xonics Acoustic Radar at NAFEC," FAA-RD-71-103, Dec. 1971, Xonics Corp., Van Nuys, CA.

92. Balser, M., McNary, C., and Nagy, A., "Acoustic Analysis of Aircraft Vortex Characteristics," FAA-RD-72-81, July 1972, Xonics Corp., Van Nuys, CA.

93. Georges, T.M., "Acoustic Ray Paths through a Model Vortex with a Viscous Core," J. Acoustic Soc. Am., Vol. 51, No. 1 (Part 2), Jan. 1972, p. 206-209.

94. Burnham, D., Kodis, R., and Sullivan, T., "Observations of Acoustic Ray Deflection by Aircraft Wake Vortices," J. Acoustical Soc. Am., Vol. 52, No. 1 (Part 2), July 1972, p. 431-433.

95. Burnham, D.C. and Sullivan, T.E., "Influence of Flaps and Engines on Aircraft Wake Vortices," J. Aircraft, Vol. 11, No. 9, Sept. 1974, p. 591-592.

96. Balser, M., McNary, C.A., and Nagy, A.E., "Acoustic Backscatter Radar System for Tracking Aircraft Trailing Vortices," J. Aircraft, Vol. 11, No. 9, Sept. 1974, p. 556-562.

97. Burnham, D., Gorstein M., Hallock, J.N., Kodis, R., Sullivan, T., and McWilliams, I.G., "Aircraft Wake Vortex Sensing Systems," DOT-TSC-FAA-72-13, June 1971, DOT/Transportation Systems Center, Cambridge, MA.

98. Michanowsky, G., "Ultraviolet Reconnaissance as a Remote Detector and Tracker of Wake Turbulence," Final Report, Nov. 1972, Amazonia Foundation Inc., New York, NY.

99. Sonnenschein, C.M. and Horrigan, F.A., "Signal-to-Noise Relationships for Coaxial Systems that Heterodyne Backscatter from the Atmosphere," Applied Optics, Vol. 10, No. 7, July 1971, p. 1600-1604.

100. Huffaker, R.M., Jeffreys, H.B., Weaver, E.A., Bilbro, J.W., Craig, G.D., George, R.W., Gleason, E.H., Marrero, P.J., Reinbolt, E.J., and Shirey, J.E., "Development of a Laser Doppler System for the Detection, Tracking, and Measurement of Aircraft Trailing Vortices," FAA-RD-74-213, March 1975, NASA Marshall Space Flight Center, Huntsville, AL.

101. Brashears, M.R. and Hallock. J.N., "The Measurement of Wind Shear and Wake Vortices by Laser Doppler Velocimetry," Proc. of 7-th Conf. on Aerospace and Aeronautical Meteorology, Am. Met. Society, Nov. 1976, Melbourne, FL, p. 175-181.

102. Bilbro, J.W., Jeffreys, H.B., Weaver, E.A., Huffaker, R.M., Craig, G.D., George, R.W., and Marrero, P.J., "Laser Doppler Velocimeter Wake Vortex Tests," FAA-RD-76-11, March 1976, NASA Marshall Space Flight Center, Huntsville, AL.

103. Easterbrook, C.C. and Joss, W.W., "The Utility of Doppler Radar in the Study of Aircraft Wing-Tip Vortices, " In: Aircraft Wake Turbulence and Its Detection, 1st edition, Plenum Press, New York, 1971, p. 97-112.

104. Fridman, J.D., "Airborne Wake Vortex Detection," FAA-RD-74-46, March 1974, Raytheon Comp., Sudbury, MA.

105. Hallock. J.N., Wood, W.D., and Spitzer, E.A., "The Motion of Wake Vortices in the Terminal Environment," Proc. of 6-th Conf. on Aerospace and Aeronautical Meteorology, Am. Met. Society, Nov. 1974, El Paso, Texas, p. 393-398.

106. Hallock, J.N., Winston, B.P., Burnham, D.C., Sullivan, T.E., McWilliams, I. G., and Wood, W.D., "Joint US/UK Vortex Tracking Program at Heathrow International Airport," Vol. II, FAA-RD-76-58II, Dec. 1976, DOT/Transportation Systems Center, Cambridge, MA.

☆U.S. GOVERNMENT PRINTING OFFICE: 1977—701-111/31

300 copies